UNIVERSITÀ DEGLI STUDI DI CATANIA
Dipartimento di Fisica e Astronomia
Dottorato di ricerca in Fisica - XXVIII ciclo

Marina Giarrusso

LITHIUM AND AGE OF PRE-MAIN SEQUENCE STARS

PhD Thesis

Supervisor:
Chiar.mo Prof. S. Romano

Contents

ABSTRACT

The expectation to date the age of low mass pre-main sequence stars from lithium has been tested by comparing the observed lithium and the predicted abundance by evolutionary models. The test, in this thesis, has been applied on a sample of binary systems whose components have a well known mass or whose mass ratio has been exactly established. The common metallicity and the coevality of the two components of a system are strong constraints to determine the age on the basis of evolutionary codes.

To achieve reliable results, by an observational campaign, I have doubled the sample of stars presenting the necessary information for the analysis. Stellar parameters have been determined with the most precise and accurately tested techniques: high resolution spectroscopy along a very large wavelength range and numerical solution of the radiative transfer equation.

As to the evolutionary code, I have implemented FRANEC with the very accurate reaction rates as determined with the most reliable experimental technique, the Trojan Horse Method. Since for PMS stars the agreement between observed and predicted lithium abundance can be obtained just tuning the external convective efficiency, I have computed a database of models for different values of the mixing length parameter. Age determination of stars has been carried out by adopting what is nowadays believed to be the most powerful statistical method in the field, the Bayesian analysis. I have extended in an original way this statistical method from binary system with known masses to the most common double lined spectroscopic binaries.

Introduction

One of the most important unsolved problem in Astrophysics is the absolute determination of ages (Soderblom 2007). In such a context, the long living low mass stars represent the possibility to sample all epochs of the Universe, and the present thesis faces the problem of dating their initial phases.

The Pre-Main Sequence (PMS) represents the early stage of stellar life, at which the process of gravitational contraction with thermodynamical time scale of a totally convective structure takes place until the hydrogen burning starts into the core. As any other stage characterizing stellar evolution, its complete understanding comes from the comparison between *observational data* of stellar parameters and *theoretical predictions* of the same quantities from evolutionary models.

The observational information about stars is mainly based on spectroscopy and photometry. The analysis of stellar spectra provides an estimation for effective temperature, surface gravity, photospheric chemical composition, rotational velocity and stellar magnetic field. Photometry is related to the stellar brightness and it allows to establish the stellar type, from which it is possible to obtain a temperature estimation. Most of the stars in our Galaxy belongs to binary or multiple systems

(Batten 1973). Among these classes, the detached double-lined eclipsing binaries (EBs), the astrometric-spectroscopic binaries (ASs) and the spectroscopic binaries with circumstellar disc (DSKs) are those for which is possible to obtain an estimation of masses (dynamical masses).

Stellar models are the result of computational calculations performed by codes which involve the physics characterizing each evolutionary stellar phase. The result is the predicted time trend of physical variables into the whole stellar structure, for all the stellar evolutionary stages. For a fixed mass and initial chemical composition, the codes integrate the equations of stellar structure taking into account both the input physics of stellar plasma (e.g. equations of state, opacity coefficients, cross sections of nuclear burning, etc.) as well as the efficiency of physical mechanisms, such as energy transport or elements diffusion.

Then, the over mentioned comparison between observations and theoretical predictions allows not only to validate the models, but it is also the only method to derive not observable stellar properties, i.e. the *age*.

For this purpose, among the observational parameters surface lithium abundance is definitely of interest for *PMS late-type stars*. In their deep convective envelopes the continuous mixing brings the surface material to the inner regions, where the temperature of lithium burning is reached, and the processed one to the surface. Convection, which is then responsible for the observed lithium depletion, strongly depends on *mass* and *metallicity*. Since at fixed mass and chemical composition the depth of the convective envelope is age dependent, in principle the measured surface lithium abundance of PMS late-type stars can be used to derive the stellar age *lithium age*, if mass and metallicity are known.
Indeed the situation is not so simple, because, as stated before, the mass estimation is available and accurate enough only for a limited number of cases, while the chemical composition is in general not known with

extreme precision.More in detail, the metallicity (mass fractional abundance of elements heavier than helium) is obtained in general through the spectroscopic measurement of the iron abundance and then assuming a solar mixture of heavy elements, while the helium abundance is not observable and generally it is evaluated by assuming a linear relation between the helium and metallicity enrichment of the interstellar medium from which new generations of stars are formed.
Moreover at present the external convection efficiency cannot be calculated in a precise way, because a physically consistent and exhaustive treatment of convection would require non-linear and non-local equations whose solution in stellar condition is still not affordable. Thus we are not yet able to theoretically predict from first principles not only the PMS surface lithium abundance but also the T_{eff} and the radius of stars with an outer convective envelopes, such as PMS objects.
Since a fully consistent treatment of convection in superadiabatic conditions is still lacking, a common approach in stellar computation is to adopt the mixing length theory (Böhm-Vitense, 1958), where a single eddy replaces the spectral distribution of eddies typical of convective zones. In this framework the average convective efficiency depends on the mixing length $l = \alpha\, H_p$, where H_p is the pressure scale height and α is a free parameter to be calibrated through the comparison with observations.

In addition, the still present disagreement between theoretical predictions and observations of stellar surface lithium content (the so-called "lithium problem") could constitute a further and hardly predictable uncertainty source.
The quoted discrepancy is evident mainly for Main Sequence (MS) stars, for which several authors claim the introduction in the models of not standard physical mechanisms (as rotationally induced mixing, mixing due to gravity waves, etc. - Tognelli et al. 2012 and reference therein). For PMS stars the situation appears better; in general the agreement between theory and observations can be obtained just

tuning the external convection efficiency, which often results to be less efficient than in MS stars (Tognelli et al. 2012).

The main aim of this PhD thesis is to test the present capability of lithium in providing an estimation for stellar ages.
For the previous reasons my analysis has been restricted to PMS late-type stars.
The work is based on the comparison between theoretical stellar age estimation from evolutionary models and the age estimation related to the observed surface lithium abundance. I have obtained the former by means of a bayesian method, a well established statistical approach that allows to derive stellar properties by starting from observational data (Jørgensen & Lindegren 2005).
Since the knowledge of mass and chemical composition is fundamental in order to obtain a reliable theoretical predictions in this context, I have considered at first binary systems for which dynamical masses and measured iron content were available in literature, as well as, of course, the photospheric lithium content. After a complete data mining of *The Astrophysics Data System*, developed by the National Aeronautics and Space Administration, that lists more than eight million astronomy and physics papers, the number of PMS binary systems presenting all the necessary information were only eight. In order to enlarge the sample, I have reformulated the bayesian method to be applied to the more numerous double-lined spectroscopic binary systems, for which the mass ratio between the two components can be spectroscopically derived from radial velocities and represents a very accurate and distance-independent constraint.
Of course in the comparison between observational data and theoretical predictions a fundamental role is given by the reliability of the values to be compared. From the observational point of view, measurements are often largely uncertain mainly because of the instrumental limits, due, e.g., to low-resolution spectroscopy. Then in order to derive the stellar data with the accuracy required or not available in literature, I started

a high-resolution observational campaign at the Catania Astrophysical Observatory and Telescopio Nazionale Galileo (La Palma, Spain). Then, on the basis of spectral synthesis I have determined effective temperatures, surface gravities, photospheric abundances of chemical elements and radial velocities. Whenever it was possible, these radial velocities have been combined with literature data in order to obtain the orbital solutions, and so the mass ratio. As to the spectrograph of the Catania Astrophysical Observatory, the acquisition of the spectra has been preceded by a phase of validation of the instrumental characteristics.
The bayesian analysis has been applied to a database of stellar evolutionary models that I have computed with the Frascati Raphson Newton Evolutionary Code (FRANEC, Degl'Innocenti et al. 2008). From the theoretical point of view, the reliability of the stellar models resides in the accuracy of the adopted input physics. In particular for surface lithium abundance of PMS stars the lithium burning nuclear reaction rates at astrophysical energies are fundamental ingredients to obtain reliable theoretical predictions. So I have implemented the code with nuclear reaction rates obtained through the Trojan Horse Method (THM, Baur 1986, Spitaleri 1999, 2011) for reactions involving light elements. The THM is a powerful indirect technique which allows to derive the bare-nucleus S-factor for charged-particle-induced reactions at astrophysical energies without invoking both Coulomb penetrability and electron screening effects (Tumino et al. 2007, 2008).

The thesis is organized as it follows:
A description of PMS phase and binary systems is in Chapter 1.
The present experimental status of reaction rates is in Chapter 2.
The importance of lithium in understanding the evolution of stars and the observed discrepancies are in Chapter 3.
Present capability and limits of stellar structure and evolutionary codes are described in Chapter 4.
Current methods and the here proposed extention to infer mass and

ages of stars on the basis of the bayesian analysis are described in Chapter 5.
The adopted observational strategy and methods to determine the temperature, surface gravity, chemical composition and lithium abundances of stars are in Chapter 6.
Inferred stellar parameters and results of the bayesian analysis are in Chapter 7 and 8 respectively.
For a better reading, there are three appendices. The first reports the massive bayesian output. A second one describes the high resolution spectrographs used for the observations and the last appendix is dedicated to the details of the data reduction.

Publications:

1. Li I 6708A Blend in the Spectra of Strongly Magnetic Star HD166473" Shavrina, A. V.; Khalack, V.; Glagolevskij, Y.; Lyashko, D.; Landstreet, J.; Leone, F.; Polosukhina, N. S.; Giarrusso, M. 2013, Odessa Astronomical Publications, 26, 112

2. "PAOLO: a Polarimeter Add-On for the LRS Optics at a Nasmyth focus of the TNG" S. Covino, E. Molinari, P. Bruno, M. Cecconi, P. Conconi, P. D'Avanzo, L. di Fabrizio, D. Fugazza, M. Giarrusso, E. Giro, F. Leone, V. Lorenzi, S. Scuderi 2014, Astronomische Nachrichten, 335, 117

3. "HD 161701, a chemically peculiar binary with a HgMn primary and an Ap secondary" J.F. Gonzalez, C. Saffe, F. Castelli, S. Hubrig, I. Ilyin, M. Scholler, T. A. Carroll, F. Leone and M. Giarrusso 2014, Astronomy & Astrophysics, 561, 63

4. "The chemical abundances of the Ap star HD94660" M. Giarrusso 2014, AIP Conference Proceedings, 1595, 234

5. "The magnetic field in HD 161701, the only binary system identified to consist of an HgMn primary and an Ap secondary" Hubrig, S.; Carroll, T. A.; González, J. F.; Schöller, M.; Ilyin, I.; Saffe, C.; Castelli, F.; Leone, F.; Giarrusso, M. 2014, Monthly Notices of the Royal Astronomical Society: Letters, 440, 6

6. "The analysis of Li i 6708A line through the rotational period of HD166473 taking into account Paschen-Back magnetic splitting" Shavrina, A. V.; Khalack, V.; Glagolevskij, Y.; Lyashko, D.; Landstreet, J.; Leone, F.; Giarrusso, M. 2014, Magnetic Fields throughout Stellar Evolution, Proceedings of the International Astronomical Union, IAU Symposium, 302, 274

7. "A polarimetric unit for HARPS-North at the Telescopio Nazionale Galileo: HANPO" Leone, Francesco; Cecconi, Massimo; Cosentino,

Rosario; Ghedina, Adriano; Giarrusso, Marina; Gonzalez, Manuel; Lorenzi, Vania; Munari, Matteo; Perez Ventura, Hector; Riverol, Luis; San Juan, Jose; Scuderi, Salvatore 2014, Proceedings of the SPIE, 9147, 2

8. "Short timescale photometric and polarimetric behavior of two BL Lacertae type objects" Covino, S.; Baglio, M. C.; Foschini, L.; Sandrinelli, A.; Tavecchio, F.; Treves, A.; Zhang, H.; Barres de Almeida, U.; Bonnoli, G.; Böttcher, M.; Cecconi, M.; D'Ammando, F.; di Fabrizio, L.; Giarrusso, M.; Leone, F.; Lindfors, E.; Lorenzi, V.; Molinari, E.; Paiano, S.; Prandini, E.; Raiteri, C. M.; Stamerra, A.; Tagliaferri, G. 2015, Astronomy & Astrophysics, 578, 68

9. "CAOS spectroscopy of Am stars Kepler targets" Catanzaro, G.; Ripepi, V.; Biazzo, K.; Busá, I.; Frasca, A.; Leone, F.; Giarrusso, M.; Munari, M.; Scuderi, S. 2015, Monthly Notices of the Royal Astronomical Society, 451, 184

10. "Kepler observations of A-F pre-main sequence stars in Upper Scorpius: Discovery of six new δ Scuti and one γ Doradus stars" Ripepi, V.; Balona, L.; Catanzaro, G.; Marconi, M.; Palla, F.; Giarrusso, M. 2015, accepted on Monthly Notices of the Royal Astronomical Society

CHAPTER 1

Pre-Main Sequence stars

1.1 From gas to stars

The space between stars is not empty, but contains the *InterStellar Medium* (ISM). In spiral galaxies, as the Milky Way, it mostly lies on the galactic plane and consists of matter in the form of dust, gas of mainly hydrogen, helium and traces of heavier elements which in astrophysics are called "metals"[1]. In addition it is permeated by cosmic rays (i.e. relativistic charged particles) and magnetic fields.
The star formation process starts from gravitational collapse of a cloud of interstellar matter. By neglecting as a first approximation the presence of magnetic fields, gas turbulence and rotation, the initial contraction occurs when the self-gravity exceeds the thermal pressure of the gas. It is therefore easy to intuit how stars should be formed in high density and low temperature regions of the ISM. These regions are called *molecular clouds*, since at their physical conditions the hydrogen gas is in form of molecules.

In this thesis I have analyzed Pre-Main Sequence (PMS) stars but,

[1]The mass-fraction of hydrogen, helium and metals are indicated as X, Y and Z respectively, being X + Y + Z = 1.

for completeness, I just shortly resume the previous history from the cloud to the star formation. First of all it's worth mentioning that star formation mechanism are not still understood in detail and thus we can define only a rough general scenario. The stars born inside molecular clouds and until the radiation pressure of the new formed star has sweeped out residual gas of the original cloud the stellar surface is not directly visible.

From the initial gravitational contraction to a stellar structure sustained by the central hydrogen nuclear burning, three main phases follow one another: *isothermal collapse*, *protostellar* and *pre-main sequence* phase.

Let a gas cloud of mass M be spherical for simplicity. If R is the radius, T the temperature and μ the molecular weight, by indicating with m_p and k_B respectively the proton mass and the Boltzmann constant, the total energy E can be written as the sum of the gravitational energy Ω and the thermal on K:

$$E = K + \Omega = \frac{3}{2} k_B T \frac{M}{\mu m_p} - G\frac{M^2}{R} \tag{1.1}$$

where G is the gravitational constant.
As stated before, in the most simple scenario the necessary condition for a cloud-collapse is that the gravitational energy of the gas overcomes the thermal one, or, equivalently, that the total energy becomes negative. This condition can be translate into a mass condition, so that the collapse starts when M exceeds the so-called *Jeans Mass* M_J:

$$M > M_J = \left(\frac{3k_B T}{2G\mu m_p}\right)^{\frac{3}{2}} \left(\frac{4\pi\rho}{3}\right)^{-\frac{1}{2}} \tag{1.2}$$

As the gravitational contraction begins, triggered by a compression due to supernova shocks or stellar winds, it proceeds in free-fall mode. If the contraction proceeds not-uniformly, the density of the gas cloud locally increases, let the Jeans Mass locally decreasing, so that the cloud fragments, allowing the formation of low-mass stars *hierarchical fragmentation*, Hoyle 1953). In the early stages of the collapse, the gas

cloud is optically thin to the developed gravitational energy. The energy is radiated and the temperature remains almost constant, so that this phase is assumed to be *isothermal*. As the collapse proceeds, the density in the inner part of the cloud increases until the gas becomes optically thick to the gravitational energy. The energy cannot be radiated and let the material heats up. As a result, a central core in quasi-hydrostatic equilibrium develops, surrounded by an envelope of gas and dust which is still falling on it. The core contraction proceeds in *adiabatic* conditions. When the core temperature reachs ∼2000 K, molecular hydrogen dissociates. This causes a further increase of density, resulting in an increase of pressure. A consequent non-isothermal collapse occurs to counterbalance the internal pressure, until the core reaches the hydrostatic equilibrium. A *protostar* is now born.
At the same time, an accretion disk forms. The matter of the disk falls onto the central object in constant and/or time dependent accretion episodes (see e.g., Vorobyov & Basu, 2006; Cesaroni et al., 2007).
A protostar evolves into a formed star gaining mass from the original cloud where it is born.
The details of the protostar formation have been recently investigated thanks to the development of hydrodynamical codes of collapsing clouds. The resulting models predict how the fragmentation and the subsequent accretion processes might occur in different environments (see e.g, Masunaga et al., 1998; Masunaga & Inutsuka, 2000; Vorobyov & Basu, 2005, 2006; Machida et al., 2010; Tomida et al., 2010; Vorobyov & Basu, 2010; Dunham & Vorobyov, 2012; Tomida et al., 2013).
On the other hand, the presence of the accretion disk has been confirmed by the observations of star-forming regions that have been collected during the few tens of years (Masunaga et al., 1998; Masunaga & Inutsuka, 2000; Vorobyov & Basu, 2005, 2006; Machida et al., 2010; Tomida et al., 2010; Vorobyov & Basu, 2010; Dunham & Vorobyov, 2012; Tomida et al., 2013). Several observations of young star-forming regions collected in the past few tens of years have revealed the presence of a circumstellar accretion disks around objects younger than few

Myr, with a possible dependence on stellar mass.
The accretion rate has been largely investigated too, resulting between $\sim 10^{-7} - 10^{-9}$ $M_\odot$ yr^{-1} for stars of about 0.1-1 Myr, although a large dispersion is present (Manara et al. 2012), so that lower (Rigliaco et al. 2011) and higher values have been observed. The highest one has been $\sim 10^{-4}$ $M_\odot$ yr^{-1} for the star FU Ori.
Regarding to the mass accretion geometries, at present two configurations have been hypothesized, i.e. the *spherical accretion* and the *disk accretion*. As to the former, all the stellar surface is interested by the accretion, since the matter is supposed to fall almost radially on the star.
In the latter scenario, the matter is supposed to fall onto a central object from an accretion disk. The accretion can interest a small portion of the central object (i.e. polar accretion caused by magnetic fields), or a large part of the stellar surface, depending on the structure of the disk. If the matter angular momentum in the protostellar core isn't high enough to break the spherical gravitational contraction of the collapsing region, the accretion occurs radially. This is probably most likely to take place at the beginning of the contraction of the cold cloud, which eventually leads to the formation of the protostar (see e.g., Larson, 1969; Tomida et al., 2013, and references therein). In the other case, an accretion disk will form.
A subclass of the disk-accretion is represented by the *thin-disk accretion*; in this case the fraction of the stellar surface where matter is accreted is very small compared to the total surface, thus allowing the star to radiate almost freely. This approximation is supported by observations (Hartigan et al. 1991) on large sample of young accreting formed stars, for which 1 - 10% of the total surface is actually affected by the matter infall, thus confirming the adoption of a thin-disk accretion-like scenario. As confirmed by observations (e.g. Lada et al., 2000, Luhman et al., 2008), in fact, disk structures are still present in formed stars.

1.1.1 The Pre-Main Sequence phase

The Hertzsprung-Russel (HR) diagram is a powerful tool for studying stellar evolution and consists on a diagram in which the abscissa represents the effective temperature and the ordinate represents the bolometric luminosity.
During the protostellar phase the accretion rate is very strong, so that the stellar surface is not at thermal equilibrium. Moreover the emitted radiation is strongly absorbed by the external envelope. For these reasons $T_{\rm eff}$ and $L_{\rm bol}$ are undetermined and the protostar evolution cannot be showed on the HR diagram.

The Pre-Main Sequence (PMS) phase starts when almost all the surrounded material is fallen onto the protostar, so that the accretion rate becomes almost negligible. At this phase the star has already sweeped out the residual gas of the original cloud so that the stellar surface is directly visible. Luminosity and effective temperature ($\sim$3000 K) are now determined and one can trace the stellar evolution on the HR diagram.
Since the emitted radiation is not balanced by an internal energy source, the star contracts in quasi-hydrostatic equilibrium on thermodynamical time scale. For this reason, during the PMS phase, its position on the HR diagram rapidly changes with age, describing a path (*evolutionary track*) that depends on mass and is reproduced by stellar structure and evolutionary models.
Figure **??** shows PMS tracks for stars of different masses in the range 0.1-6.0 $M_\odot$ (Stahler & Palla, 2005) The tracks start from the so called *Birthline* (Stahler, 1983), where lie the first stellar structures optically visible, and end on the *Zero Age Main Sequence* (ZAMS), where lie the first stellar structures held up by the nuclear hydrogen burning in the core. The light grey lines represent the *isochrones*, i.e. where lie stars with the same age (*coeval* stars).
A PMS star evolves through two stages:

- a contraction phase, in which the stellar structure is initially to-

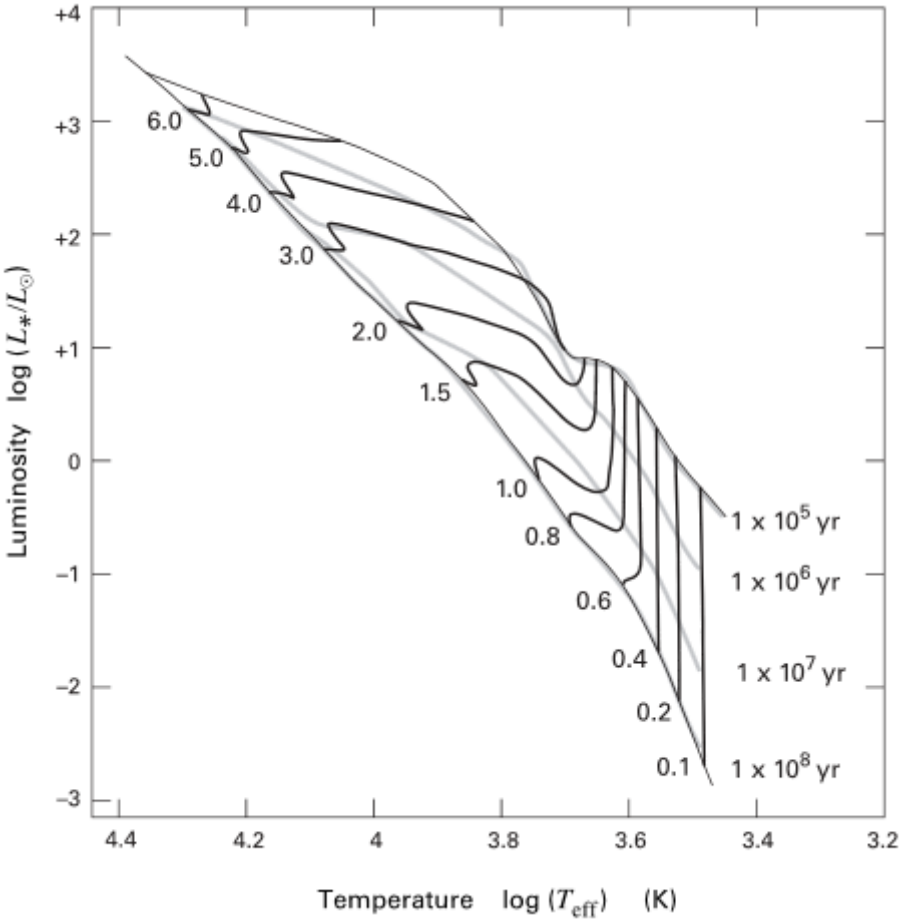

Figure 1.1: Evolutionary tracks from Stalher & Palla (2005).

tally *convective*. Because of the contraction, the decreasing radius results in a progressively less-extensive radiating surface, responsible for a decreasing luminosity, while the effective temperature remains almost constant. This phase corresponds to the quite-vertical line on the HR diagram, the so-called *Hayashi Track*;

- the contraction let the central temperature T_c increase and the opacity decrease, removing the convection instability. As a consequence, a *radiative* core develops and grows up, at the expense of the convective zone. This phase corresponds to the quite-horizontal line on the HR diagram, the so-called *Henyey Track*.

Both the size of the radiative core and the relative duration of the two phases strongly depend on stellar mass.
High-mass ($M \geq 6.0 M_\odot$) are not observed in PMS stage, because they are believed to start the central hydrogen burning while still in the protostellar accretion phase (SHU ET AL. 1987 ARAA and reference therein), so that they are Main Sequence (MS) object when become visible. The study of PMS stars is primarily restricted to low-mass ($M \leq 2.0 M_\odot$) stars, named T Tauri stars, and to the less numerous intermediate mass ($2.0 M_\odot < M < 6.0 M_\odot$) stars, the Herbig Ae/Be stars. Stars belonging to the latter class are of spectral type A-B and show strong Balmer lines emission (Perreira et al. 2003). Since they early experience an extended radiative core, the photospheric lithium content is not depleted and cannot provide any informations about stellar age.
The T Tauri stars (TTSs) are the youngest visible objects of spectral type between late F and middle M, with ages in the range $\sim 10^5 - 10^7$ yr (Strom et al., 1975). From the observational point of view, these stars show very intriguing features, being characterized by strong emission lines (H_α line, H & K Ca ii and iron lines), weak photospheric absorption lines, strong infrared (IR) and strong ultraviolet (UV) excess, irregular optical variability, optical polarization and presence of lithium absorption line.

Anyway, it's possible to distinguish between two mainly classes of T Tauri objects, on the basis of differences in observational features. The classification also reflects the evolutionary stage of the star:

- *Classical T Tauri Stars (CTTSs)* show an equivalent width of the H_α emission line $EW_{H_\alpha} \geq 10$ Å and more generally strong line emission, strong infrared (IR) and strong ultraviolet (UV) excess. These characteristics are well explained with the model of magnetospheric accretion (Stempels & Piskunov (2003) and references therein): the stellar magnetic field couples to the circumstellar disk and controls the accretion flow from disk to star. Once the matter impacts to the stellar surface, shocks heats the photosphere locally. Hard X-ray radiation from these areas heats and ionized the matter of the accretion flow, so explaining the strong emissions. The validity of the model has been confirmed by several observational evidences (Rice & Strassmeier (1996), Johns-Krull & Hatzes (2001), Muzerolle et al. (2001)). In particular, the UV excess originated from the disk represent an additional continuum superimposed to the stellar photospheric spectrum, resulting in a weakening of the absorption lines. This effect is known as *veiling*.

- *Weak T Tauri Stars (WTTSs)* show an equivalent width of the H_α emission line $EW_{H_\alpha} < 10$ Å and, although exhibit magnetic activity and photospheric lithium content, don't reveal strong emission line as well as IR and UV excess (Stempels & Piskunov, 2003). The *Naked T Tauri Stars (NTTSs)* are considered as a subclasses of the WTTSs showing an equivalent width of the H_α line $EW_{H_\alpha} < 5$ Å in emission the cooler stars and H_α line in absorption in the hotter ones. No signatures of circumstellar material have been detected for these objects (Walter, 1986).
  WTTSs are supposed to be evolved CTTSs.

1.2 Binary systems

Most (70%-80%) of the stars in our Galaxy belongs to binary or multiple systems (Batten 1973).

A binary system consists of two stars moving around their common center of mass in a keplerian orbit. In a binary system the more massive star is referred as *primary* component and the less massive is called *secondary* component. Very rare is to observe stars tracing their orbit in the sky, visual binaries. Much more common is to observe the periodic wavelength shift of spectral lines due to the Doppler effect. Binary systems have a fundamental role in astrophysics since from the calculation of orbits it is possible to exactly determine, without any assumption, the fundamental parameter of a star, the mass. Obviously, masses can be inferred only combining the apparent orbit and the radial velocity variation of the visual binaries. However, for a particular class of binary systems whose spectrum shows the spectral lines of both components, the so called Spectroscopic Binary of type 2 (SB2), it is possible to determine the mass ratio of the two components as equal to the inverse amplitudes of velocity curves. Thanks to the very recent optical interferometry, it is nowadays possible to resolve the circum binary disks and to infer the cumulative mass of the binary system. In these cases, it is still possible to measure the absolute masses of a binary system with a single assumption on their distance (Mathieu 2007). A further lucky case, is the coincidence of the line of sight with the orbital plane. For these eclipsing binary systems, masses of components are straightly measured and timing of the eclipses gives the relative length of stellar radii.

Binary systems have two properties that strongly impact theories about their formation. First, the typical separation between the two components is small, i. e. much less than one to several thousands Astronomic Unit (AU). Second, for stars in a binary system with an orbital period P shorter than $\sim$100 yr the mass of the secondary is close to the primary one and it is thought that the formation of the secondary

component has been influenced by the formation of the primary (Abt & Levy, 1976, Abt, 1983). Then it's reasonable to assume that they have the same chemical composition.
Different scenarios have been proposed to describe binary formation (Shu et al. 1987 and reference therein, Tohline 2002):

- *Fission* consists of the split of a cloud in unstable equilibrium. Although first coarse evolutionary simulations seemed to confirm the validity of this process (Lucy & Ricco 1979), subsequent studies (Durisen et al. 1986; see also reference in Shu et al. 1987) demonstrated that fission from quasi-static configurations into two bodies with orbital separations of AU scales would seem to be impossible.

- *Capture* of a star by a second one. A star cannot capture another star unless kinetic energy is expelled from the system. A third star can be sink for this kinetic energy, but in the open clusters of the Galactic disk (which contain sparse youngest stars) the probability that three stars would come together at the same time leaving two of them in a bound configuration is very low. Even with the higher stellar densities in stars-forming regions, the rate of capture is too low to produce a high number of binary systems with young stars. This scenario can explain binary formation in the denser and older globular clusters of the Galactic Halo.

- *Hierarchical Fragmentation*, which occurs when the isothermal collapse of a single Jeans mass of (non-rotating and non-magnetic) gas followed by successive rounds of dynamical fragmentation (Hoyle, 1953).

- *Collapse of the accretion disk* if the disk around a young stars is massive enough, it can collapse in a second star, forming a binary system with short period (Abt 1983).

By considering the last two scenarios as possible ones for young binary formations, in both cases the two components can be assumed with the

same age, or at least with an age difference less than 1 Myr (i.e., the time to form a star from a protostar with a constant mass accretion rate of 10^{-5} $M_{\odot}$ yr^{-1} ranges from 0.1 to 0.6 Myr, Stahler & Palla 2004).

Among these classes, the detached double-lined eclipsing binaries (EBs), the astrometric-spectroscopic binaries (ASs) and the spectroscopic binaries with circumstellar disc (DSKs) are those for which is possible to obtain an estimation of masses (dynamical masses).

CHAPTER 2

Light element burning rates

2.1 Nuclear reactions inside stars

The introduction of nuclear physics into astronomy allows scientists to strongly improve their knowledge about stellar evolution. The nucleosynthesis explains how atomic species are formed in the Universe through nuclear processes. The primordial nucleosynthesis tells us how the light elements ^{2}H, He, Li, Be, B have been formed in the early Universe. The heavier elements up to ^{56}Fe are produced in stars by nuclear burnings, while elements heavier than iron are sinthetyzed through $s-$ and $r-$processes.

The presence of nuclear reactions inside stars has been confirmed by several observative evidences. One of the earliest direct proofs dates from 1952, when the astronomer Paul W. Merrill identified technetium lines in red giant star spectra. All the isotopes of this element are unstable and the longest lived one has a half-life ~ 4.2 Myr, a value smaller than the age of the Universe. Then it must be formed in situ. In addition, since neutrinos are produced in nuclear processes, the detection on the Earth of a solar neutrino flux (Bahcall 1989) can be considered also

a strong direct evidence of the presence of nuclear reactions in stars. Moreover, our present understanding of the observed stellar populations in the Galaxy is enterly based on the assumption of nucleosynthesis. No alternative explanation for a such large variety of phenomena has been found. The classification of stellar populations is based on age, location and metal content (Z). The Sun belongs to the population I, which identifies metal-rich ($Z \sim 10^{-2}$) stars formed within the past few billion years and located in the galactic disk. Extreme population I stars are the youngest and most metal-rich stars of the Galaxy, observed in the spiral arms. Contrarily, population II includes older and metal-poor ($Z \sim 10^{-3} - 10^{-4}$) stars of the bulge and halo of the Galaxy, while the extreme population II stars, the eldest and most metal-poor ones, are found in the halo and in globular clusters. Since there are no reason to assume a not-uniform initial composition of our Galaxy as well as a mechanism that concentrated the metals in the galactic disk, this evidence suggests that stellar nucleosynthesis naturally occurs inside stars as them evolve, modifying their chemical composition. So, the youngest objects are formed after the metal enrichment of the ISM due to stellar winds, mass loss of evolved stars and supernovae explosions.

2.2 Reaction rates in stellar environments

The reaction rate tells us how many reactions occur per units of volume and time. It depends on the probability that the reaction proceeds after a collision of two nuclei and on the number of collisions per second. In a nuclear collision, the cross section σ represents a geometrical area associated with each nucleus and is related to the probability that a projectile interacts with that particle.
Since in a stellar plasma the kinetic energy of nuclei is due to their thermal motion, we can refer to the nuclear reactions in stellar environments as *thermonuclear reactions*.

Let us consider a stellar gas composed by two different species of

nuclei, X and Y, and denote respectively with n_X and n_Y the number of particles per unit of volume. We can refer to the relative motion in which, e.g., X is the projectile and Y the target, since the cross section for a reaction between nuclei is only a function of their relative velocity v. Then, the collision probability per unit of area of a single projectile X will be given by the product between the cross section for a single target Y and the total number of target nuclei, $\sigma(v)n_Y$. The reaction rate per units of volume and time can be obtained by multiplying this quantity for the total flux of incident particles X, $n_X v$:

$$r_{XY} = n_X n_Y \sigma(v) v \tag{2.1}$$

The term $\sigma(v)v$ can be interpreted as the reaction probability per pair and per second, while $n_X n_Y$ represents the total number of pairs of non-identical nuclei. In the case of identical particles it must be divided by 2, in order to count each pair once only. Then the precedent equation can be rewritten by means of the Kronecker delta:

$$r_{XY} = \frac{1}{1+\delta_{XY}} n_X n_Y \sigma v \tag{2.2}$$

For a non-relativistic and non-degenerate gas, as it is the stellar plasma in the most of cases, the particle velocities follows the Maxwell-Boltzmann distribution. By referring to the reduced mass m, it results:

$$\phi(v) = 4\pi \left(\frac{m}{2\pi k_B T}\right)^{3/2} v^2 exp\left(-\frac{mv^2}{2k_B T}\right) \tag{2.3}$$

and has the normalization $\int_0^\infty \phi(v)dv = 1$. Since $\phi(v)dv$ indicates the probability that a pair of interacting nuclei has velocity between v and $v + dv$, the total reaction rate per units of volume and time can be obtained by means of $\sigma(v)v$ averaged over the velocity distribution, $< \sigma v >$

$$r_{XY} = \frac{1}{1+\delta_{XY}} n_X n_Y < \sigma v > \tag{2.4}$$

with

$$\begin{aligned} < \sigma v > &= \int_0^\infty \phi(v) v \sigma(v) dv \\ &= 4\pi \left(\tfrac{m}{2\pi k_B T}\right)^{3/2} \int_0^\infty v^3 \sigma(v) exp\left(-\tfrac{mv^2}{2k_B T}\right) dv \end{aligned} \tag{2.5}$$

and making use of the relative energy $E = 1/2\, mv^2$

$$< \sigma v >= \sqrt{\frac{8}{\pi m}} \left(\frac{1}{k_B T}\right)^{3/2} \int_0^\infty E\sigma(E) exp\left(-\frac{E}{k_B T}\right) dE \qquad (2.6)$$

where $\sigma(E)$ is the cross section as a function of energy and we can refer to the exponential term as the Maxwell-Boltzmann factor.

Of particular interest for astrophysical applications are the non-resonant charged-particle-induced reactions.
Let us consider two particles of charge $Z_1 e$ and $Z_2 e$ respectively. The Coulomb potential between them is $\sim$MeV, while in stellar interiors the energy of the plasma is $\sim$keV. Anyway the Coulomb barrier can be crossed via Tunnel Effect and the cross section can be written as

$$\sigma(E) = \frac{1}{E} exp(-2\pi\eta) S(E) \qquad (2.7)$$

This equation defines the astrophysical S-factor $S(E)$, which contains all the strictly nuclear effects. For non resonant reactions, $S(E)$ varies smoothly with energy as compared to the cross-section, which drops sharply with decreasing energy (Rolfs & Rodney, 1988). The exponential term, named Gamow factor, gives the penetration probability of the Coulomb barrier and includes η, the Sommerfield parameter:

$$\eta = \frac{Z_1 Z_2 e^2}{\hbar} \sqrt{\frac{m}{2E}} \qquad (2.8)$$

By inserting $\sigma(E)$ into the Eq.(2.6):

$$< \sigma v >= \sqrt{\frac{8}{\pi m}} \left(\frac{1}{k_B T}\right)^{3/2} \int_0^\infty S(E)\, exp\left[-\frac{E}{k_B T} - \sqrt{\frac{E_{\rm G}}{E}}\right] dE \qquad (2.9)$$

where

$$E_{\rm G} = (2\pi\eta\sqrt{E})^2 = \left(\pi \frac{Z_1 Z_2 e^2}{\hbar} \sqrt{2m}\right)^2 \qquad (2.10)$$

is called Gamow energy. Given the smooth energy behavior of $S(E)$, the exponential term is the main responsible for the energy trend of

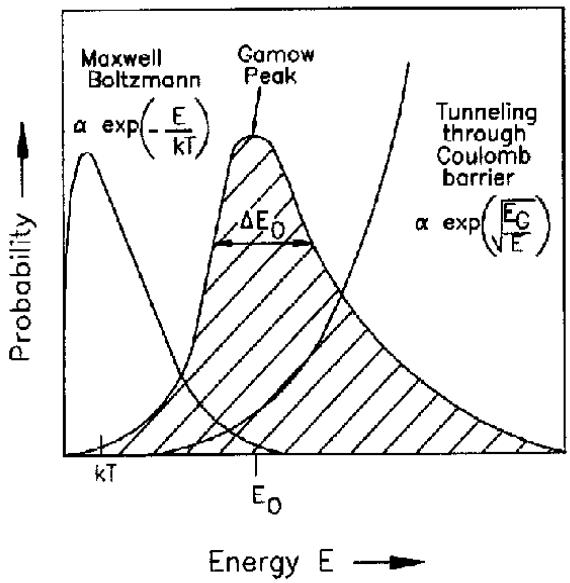

Figure 2.1: The Gamow-peak.

the integrand function. It is the product of the Maxwell-Boltzmann factor, which decreases for increasing energy, and the Gamow factor, which increases for increasing energy. The maximum of the resulting probability distribution is called Gamow peak and corresponds to the energy E_0 (Fig. 2.1). The reaction effectively proceeds in stars only for energy values in an interval around E_0 (Gamow window), typically ranging from few to hundred keV.

2.3 Measuring cross section at astrophysical energies

The reaction rate per particle pair and per second can be expressed in units of cm^3 mol^{-1} s^{-1} by multiplying $< \sigma v >$ for the Avogadro constant, N_A, and can be determined by solving Eq.(2.6) once that the cross section $\sigma(E)$ is measured or theoretically estimated.
By taking into account the presence of electrons in stellar plasma, it

can be written as

$$\sigma_{pl}(E) = \sigma_b(E) f_{pl}(E) \approx \sigma_b(E) e^{\frac{\pi\eta U_{pl}}{E}} \tag{2.11}$$

where $\sigma_b(E)$ is the bare-nucleus cross section and $f_{pl}(E)$ is the stellar electron screening enhancement factor defined by means of the plasma potential U_{pl}. If $f_{pl}(E)$ is estimated within the framework of the Debey-Hückel radius and $\sigma_b(E)$ can be measured at the ultra-low Gamow energy, then it's possible to obtain $\sigma_{pl}(E)$.
Anyway, at the energies at which the most of nuclear reactions proceed in stellar environments (from few keV to hundred keV, as stated before) direct measurements of cross sections are difficult, because of the presence of Coulomb barrier (of the order of MeV) between the interacting charged particles, which is responsible for a strong exponential decreasing of the reaction cross-section values to nano or picobarn. In such a case it's possible to estimate the bare-nucleus astrophysical factor $S_{\mathrm{b}}(E)$ by means of *extrapolation procedures* on direct measurements made at energies greater than the astrophysical ones

$$S_{\mathrm{b}}(E) = E\sigma_b(E) e^{2\pi\eta} \tag{2.12}$$

because, as stated before, it varies smoothly with energy (Fig.**??**) since the inverse of the Gamow factor, $e^{2\pi\eta}$, removes the dominant energy dependence of $\sigma_b(E)$.

Despite the recent improvements of detection tecniques and the availability of high-current low-energy accelerators make today possible a *direct evaluation* of $\sigma_{\mathrm{b}}(E)$ in the Gamow window, this laboratory measurements are affected by electron screening phenomena due to electron clouds surrounding the interacting ions, so that the measured cross-section results

$$\sigma_s(E) = \sigma_b(E) f_{lab}(E) \approx \sigma_b(E) e^{\frac{\pi\eta U_e}{E}} \tag{2.13}$$

Here $f_{lab}(E)$ and U_e are respectively the electron screening enhancement factor and the electron screening potential measured in the laboratory.

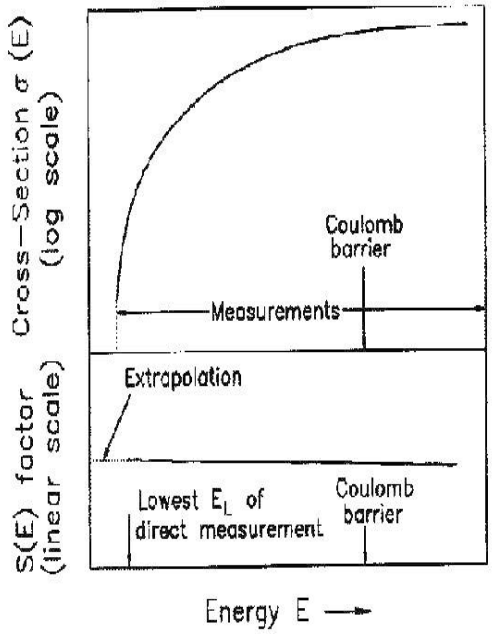

Figure 2.2: From Rolfs & Rodney (1988). The upper panel shows the energy trend of the cross section $\sigma(E)$ of a charged-particle-induced nuclear reaction: it drops sharply as the energy decreases below the Coulomb barrier E_C, providing a lower limit E_L of the beam energy for experimental measurements. The smooth trend to the S-factor (lower panel) makes the extrapolation to lower energies more reliable.

An accurate knowledge of U_e (which differs from U_{pl}) is required to calculate $\sigma_b(E)$ from Eq.(2.13) or, alternatively, to better understand U_{pl}, needed to determine $\sigma_{pl}(E)$ (Tumino et al.2014).
Given the trend of f_{lab} with respect to E, the electron screening phenomena are not negligible at low energies and lead to an increasing in measured cross-sections with respect to the case of bare nuclei, making the estimations of $\sigma_s(E)$ very uncertain.

2.3.1 The Trojan Horse Method

The Trojan Horse method (THM; Baur 1986; Cherubini et al. 1996; Spitaleri et al. 1999, 2011) is a powerfull indirect technique to measure the $S_{\rm b}(E)$ factor for charged-particle-induced reactions at astrophysical energies without invoking both the Coulomb penetrability and the electron screening effects (Tumino et al. 2007, 2008).
The basic idea is to study the two-body reaction a(x,c)C of astrophysical interest by means of the so-called TH-reaction, an appropriate two-body to three-body process a(A,cC)s in quasi-free (QF) kinematics regime, where the TH-nucleus A has a cluster structure x$\oplus$s. The QF-process can be described in the Impulse Approximation (based essentially on the assumption of negligible interaction between s and the outgoing particles c and C) by means of the pole diagram showed in Fig. **??**. The QF-kinematics implies that the relative x-s momentum is approximately zero, a condition that minimize the interaction between the two cluster particles resulting in the maximum distance between them (Tribble et al. 2014).
In the entry channel a+A the relative kinetic energy is chosen to be higher than the electrostatic potential, so that the probability to find A very near to a is not suppressed by the Coulomb barrier. When in proximity of a, the TH-nucleus virtually breaks down leaving x (the *participant*) to induce the binary reaction and s (the *spectator*) to fly away. The interaction between x and a takes place inside the short range nuclear field, so that the two-body reaction is free from Coulomb suppression as well as from electron screening effects. Nevertheless, the quasi-free a+x process can occur even at very low sub-Coulomb energies, since the method requires that the a+x relative motion is compansated for by the x-s binding energy, determining the so-called "quasi-free two-body energy", E_{QF}:

$$E_{QF} = E_{a-x} - B_{x-s} \tag{2.14}$$

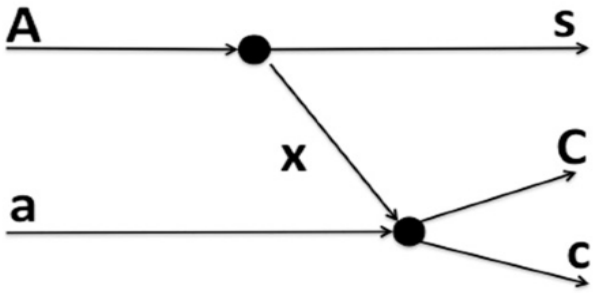

Figure 2.3: Pole diagram for the QF-reaction a(A,cC)s. The upper pole describes the break up of the TH-nucleus A into the clusters x and s, the latter being the spectator of the virtual binary reaction a(x,c)C taking place in the lower pole.

Here E_{a-x} and B_{x-s} indicate the relative energy in the two-body entrance channel and the x-s binding energy, respectively.
The accessible astrophysical energy region is then determined by the x-s inter-cluster motion and corresponds to a cutoff in the momentum distribution of s of few tens of MeV/c.

Under the Plane Wave Impulse Approximation (PWIA), the cross section of the TH-reaction can be factorized into the terms corresponding to the poles of Figure **??** and is given by

$$\frac{d^3\sigma}{dE_c d\Omega_c d\Omega_C} \propto KF \cdot |\Phi(p_{sx})|^2 \cdot \left[\frac{d\sigma}{d\Omega}\right]^{HOES} \tag{2.15}$$

where

- KF is a kinematical factor containing the final-state phase space factor and is a function of the masses, momenta, and angles of the outgoing particles;
- $|\Phi(p_{sx})|^2$ is the momentum distribution for the x-s inter-cluster motion, usually described in terms of Hänkel, Eckart, or Hulthén functions depending on the x-s system properties;
- $\left[\frac{d\sigma}{d\Omega}\right]^{HOES}$ is the half-off-energy-shell (HOES) differential cross-section for the two-body a(x, c)C reaction at the center of mass

energy E_{cm} given in post-collision prescription by

$$E_{cm} = E_{c-C} - Q_{2b} \tag{2.16}$$

where E_{c-C} is the relative energy of the outgoing particles c and C, and Q_{2b} is the Q-value of the binary reaction.

If KF is calculated and $|\Phi(p_{sx})|^2$ is known, then it's possible to extract the two-body cross section from the measured three-body one:

$$\left[\frac{d\sigma}{d\Omega}\right]^{HOES} \propto \left[\frac{d^3\sigma}{dE_c d\Omega_c d\Omega_C}\right] \cdot [KF \cdot |\Phi(p_{sx})|^2]^{-1} \tag{2.17}$$

The Coulomb barrier in HOES cross section is suppressed due to the virtuality of particle x. Then, in order to relate the HOES cross section to the relevant on-energy-shell (OES) one, the Coulomb suppression must be replaced by means of an appropriate penetration factor, P_l, so that:

$$\left[\frac{d\sigma}{d\Omega}\right]^{THM} \propto \left[\frac{d\sigma}{d\Omega}\right]^{HOES} \cdot P_l \tag{2.18}$$

The approach gives only the energy dependence of the two-body cross section. Then, in order to obtain its absolute value, a normalization to direct data available at energies above the Coulomb barrier is required (Spitaleri et al. 2004, Spitaleri et al. 2015).
By introducing the TH cross section into Eq.(2.12) it's possible to obtain the bare-nucleus $S_b(E)$-factor and then also a model-independent estimation for the U_e potential from Eq.(2.13).

2.4 Trojan Horse reaction rates

Although in a PMS star the central H burning (dominating the most of stellar life) is not yet started, when the inner temperature reaches a few 10^6 K nuclear burnings of light elements occur. From the astrophysical point of view, these reactions are of particular interest to determine properties of low-mass PMS stars, which have deep convective envelopes that reach the burning regions and thus that are responsible for the observed depletion of the surface light element abundances. Then, in this

contest the accuracy of theoretical predictions largely relies on both the treatment of convection and the adopted nuclear reaction rates.
The database of stellar models that I have computed for my analysis has been obtained with nuclear reaction inputs from the Nuclear Astrophysics Compilation of Reaction Rates (NACRE, Angulo et al.1999) and JINA REACLIB database, but for the following reactions involving the light elements ^{2}H, ^{6}Li and ^{7}Li, that have been determined via the Trojan Horse Method:

- ^{2}H(d,p)^{3}H and ^{2}H(d,n)^{3}He
  I implemented the FRANEC evolutionary code with the reaction rates of the two $d + d$ burning channels obtained via THM by means of the QF-reaction ^{2}H(^{3}He,p^3H)^{1}H and ^{2}H(^{3}He,n^3He)^{1}H, respectively (Tumino et al., 2014).
  In PMS stars deuterium can be destroyed both by direct proton capture and in $d + d$ channels. The former is the most efficient burning channel, so that the inclusion of the two $d + d$ into the code do not affect the predictions for global properties of the star in a significant way (Tumino et al., 2014).

- ^{6}Li(p,α)^{3}He
  The ^{6}Li(p,α)^{3}He cross section at astrophysical energies has been obtained by applying the Trojan Horse Method to the ^{2}H(^{6}Li,α^3He)n QF-reaction, with ^{2}H as a TH-nucleus (Lamia et al. (2013)). The TH reaction rate can be written by means of a correction factor f_{corr} for the JINA REACLIB reaction rate:

$$N_A < \sigma v >_{THM} = N_A < \sigma v >_{REACLIB} \cdot f_{corr} \tag{2.19}$$

  where

$$\begin{aligned} f_{corr}(T_9) = 1.09 &- 0.48 \times 10^{-1} \cdot lnT_9 - 0.50 \times 10^{-2} \cdot (lnT_9)^2 \\ &+0.38 \times 10^{-2} \cdot (lnT_9)^3 + 0.99 \times 10^{-3} \cdot (lnT_9)^4 \\ &+0.68 \times 10^{-4} \cdot (lnT_9)^5 \end{aligned}$$

with T_9 temperature in billions of Kelvin.
Fig.**??** shows the relative trend of the two reaction rates: the TH one is more efficient and deviates by ∼15% at $T_9 = 10^{-3}$ and by ∼5% at $T_9 = 1$ with respect to the JINA REACLIB rate.
I updated the FRANEC reaction rate by introducing the TH correction factor, as in Eq.(2.19).

- ^{7}Li(p,α)^{4}He
  The ^{7}Li(p,α)^{4}He cross section at astrophysical energies has been obtained from Lamia et al. (2012) by applying the Trojan Horse Method to the ^{2}H(^{7}Li,$\alpha\alpha$)n QF-reaction, using ^{2}H as a TH-nucleus.
  The TH reaction rate can be written by introducing a correction factor f_{corr} in the analytical expression given in the NACRE compilation (Angulo et al.1999):

$$N_A < \sigma v >_{THM} = N_A < \sigma v >_{NACRE} \cdot f_{corr} \tag{2.20}$$

  where

$$f_{corr}(T_9) = 0.966 - 0.184 \times 10^{-1} \cdot lnT_9 + 0.545 \times 10^{-3} \cdot (lnT_9)^2$$

  with T_9 temperature in billions of Kelvin.
  Fig.**??** shows the relative trend of the two reaction rates: the TH one is less efficient and deviates by ∼13% at $T_9 = 10^{-3}$ and by ∼5% at $T_9 = 1$ with respect to the NACRE rate.
  I introduced the TH correction factor in the FRANEC code, as in Eq.(2.20).

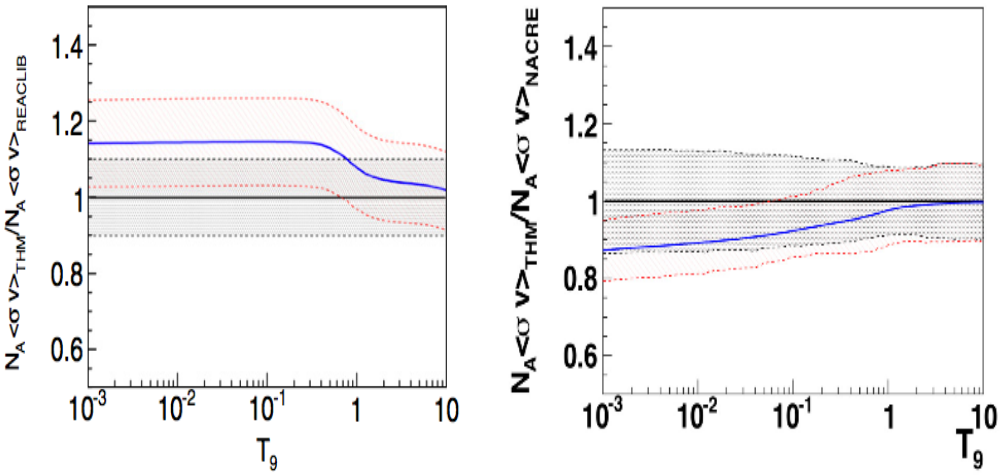

Figure 2.4: **Left**. From Lamia et al. (2013). The solid blue line represents the trend of the ratio between the adopted THM ^{6}Li(p,α)^{3}He reaction rate and the rate reported in the JINA REACLIB (Cyburt et al.2010). The red dashed line shows the upper and lower limits for the TH rate, the black dashed area indicates the upper and lower limits of the JINA REACLIB rate with the same uncertainties given in the NACRE compilation (Angulo et al.1999). **Right**. From Lamia et al. (2012), the solid blue line represents the trend of the ratio between the adopted THM ^{6}Li(p,α)^{3}He reaction rate and the rate reported in the NACRE compilation (Angulo et al.1999). The red dashed line shows the upper and lower limits for the TH rate, the black dashed area indicates the upper and lower limits of the NACRE rate.

CHAPTER 3

The lithium problem

Theoretical predictions from the Standard Stellar Models[1] (SSMs) tell us that during the PMS stages low-mass stars ($M \leq 1.3\ M_{\odot}$) are fully convective or have deep convective envelopes . As a consequence of the PMS contraction, their interiors heat up and when the temperature at the base of the convective zone, T_{BCZ}, reaches that of Li burning, $T_{LB} \sim 2.5 \times 10^6$ K, lithium is here destroyed via (p,α) reactions. Convection is then responsible for the observed lithium depletion, by bringing the processed material to the stellar surface and the not yet processed one to the inner regions.

The efficiency of this process strongly depends on stellar metallicity and mass. Li-burning is faster in metal-rich stars, since the higher opacity and the consequent deeper convective envelope result in a higher T_{BCZ}. This statement is well shows in Figure **??**: at a fixed age (10 Myr), the predictions from two different classes of models for the logarithmic surface ^{7}Li abundace of PMS

[1]Standard Stellar Models assume a spherically symmetric structure and convection and diffusion as the only processes that mix surface elements with the interior.

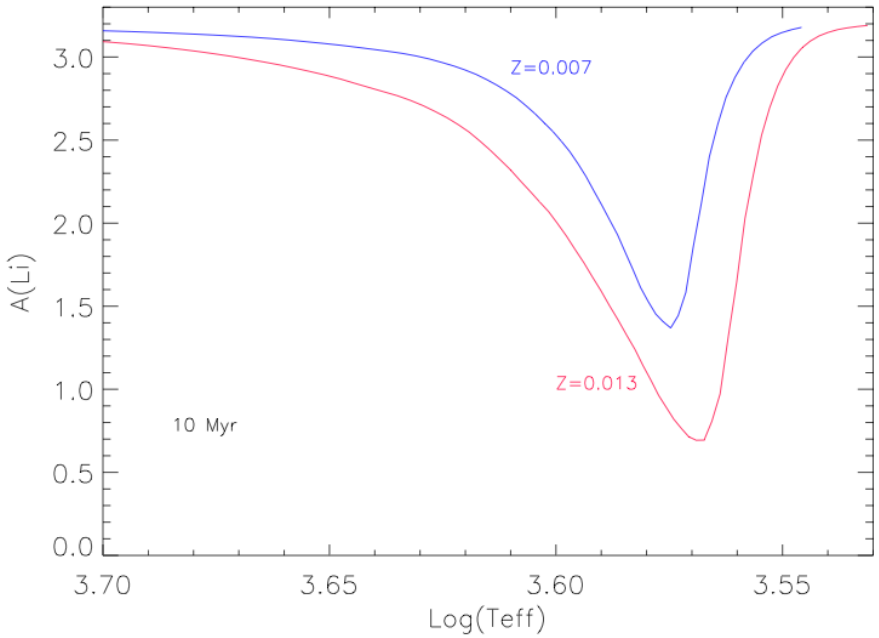

Figure 3.1: At the age of 10 Myr, the logarithmic surface ^{7}Li abundances are plotted for PMS stars with masses between 0.2-2.5 $M_\odot$ and different metallicity. Any star is identified by its effective temperature, T_{eff}. The two set of models have been computed with the same mixing-length parameter value α=1.74 and Trojan Horse reaction rates for reactions involving lithium.

stars are plotted. Any star is identified by its effective temperature. The two set of FRANEC models have been computed in the mass range 0.2 - 2.5 $M_\odot$ with the same input physics, but for metallicity.

As to the mass, when a fully convective PMS stars ($M \leq 0.4\ M_\odot$ for solar metallicity) reaching T_{LB} it completely destroyed the initial lithium content in few tens-hundreds of Myr (see e.g. Sestito et al. 2008 and reference therein, Tognelli et al. 2015) in dependence on the mass: the smaller the stellar mass, the greater the time to reach T_{LB}, the longer the timescale of Li-burning phase.

In the interiors of more massive stars a radiative core develops and

grows up as faster as larger is the stellar mass. As a consequence the convective envelope becomes progressively less extended until $T_{BCZ} < T_{LB}$ and the Li-burning is stopped.

It is therefore clear how, *for a fixed metallicity*, the photospheric lithium content of PMS late-type stars is related to their *mass* and *age*. This has been confirmed by the large amount of ^{7}Li observations collected for isolated stars, binary systems, and open clusters, from pre-MS to the late-MS phase (see e.g. Sestito & Randich, 2005), that showed the strong dependence of ^{7}Li depletion on mass and age. Then, in principle, the observed surface lithium abundance can be used to derive their (*lithium*) age, if metallicity and mass are known, by means of theoretical evolutionary models.

Unfortunately, despite the well known capability of the current stellar models in reproducing the main evolutionary parameters, up to now comparison between theoretical lithium predictions and observational data may be not in good agreement (Tognelli et al. 2012, hereafter T12, and references therein). This disagreement, refers to *the lithium problem*, is present in both PMS and MS stars. See, e.g., the case of Pleiades (Fig.3.1), for which the large lithium dispersion observed for stars with (same) effective temperature $T_{eff} < T_{\odot}$ is not reproduced from models (T12; Somers & Pinsonneault 2014a,b, hereafter SP14a,b). Moreover theoretical predictions for PMS lithium depletion from SSMs tend to underestimate the observed one, while the opposite trend is found for MS stars (Jeffries 2000;T12).

The match between lithium theoretical prediction and observations for MS stars is worst and several authors claimed the introduction in the models of not standard physical mechanisms,

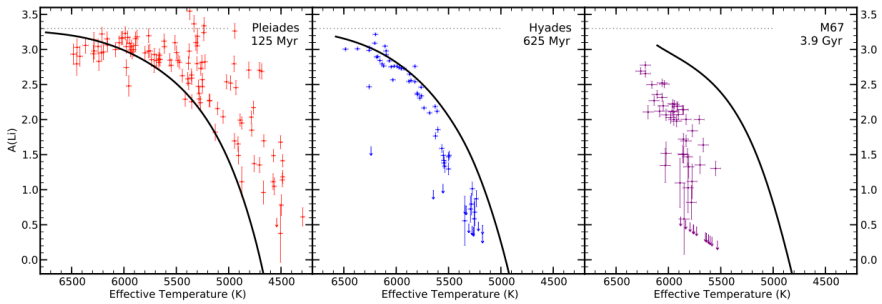

Figure 3.2: From Somers & Pinsennault 2014. Observed (dots) lithium for Pleiades, Hyades and M67 are compared to Standard Stellar Model lithium patterns (solid lines). SSMs under-predict the lithium abundance for the PMS stars (Pleiades), and over-predict the oldest one.

as rotationally induce mixings, magnetic fields, etc. (Tognelli et al. 2012 and reference therein). For PMS stars the situation appears better; in general the agreement between theory and observations can be obtained just tuning the external convection efficiency, which often results to be less efficient than in MS stars (Tognelli et al. 2012).

3.1 Lithium and age of PMS stars

Keeping this in mind, in my thesis I test the present capability of lithium to provide an estimation of the age for a sample of PMS stars.

In principle, by exactly knowing metallicity and mass of a star, the values of a set of observational quantities (as effective temperature, surface gravity, luminosity, radius) and the observed photospheric lithium abundance, it's possible to compute the model with the known values of metallicity and mass. Then, one can search into this model for the age at which the values of the observational parameter appear all together (*theoretical age*) and, independently, for the age at which the observed surface lithium

value appears in the model (*lithium age*). However, *all* the parameters (including metallicity and mass) are affected by errors and one may be in a mistake in choosing exactly the estimated mass and the central value of the observed quantities. Therefore, in order to taking into account all these uncertainties at the same time, I have applied a Bayesian analysis for deriving theoretical estimation for mass ($M_{\rm mod}$) and age ($\tau_{\rm mod}$) (Jörgensen & Lindegren 2005 hereafter JL05). From the resulting model I have derived the lithium age related to the observed lithium abundance and compared it with the theoretical one.

In the comparison between observational data and theoretical predictions a fundamental role is given of course by the reliability of the values to be compared. From the observational point of view, the measurements are often largely uncertain, because of the dependence on other observational quantities and so approximated estimation (i.e., the absolute magnitude depends on the assumed distance) and/or because of the instrumental limits (e. g., low-resolution spectroscopy). Fig. 3.2 shows the case of the binary system V773 Tau A. Boden et al. (2007) carried out a spectroscopic determination of effective temperature and surface gravity for both components, from a spectrum with resolution R=35000. However, Kurucz synthetic spectrum as computed by assuming the authors results doesn't match the high resolution (R=115000) high signal-to-noise (S/N = 68) HARPS-North spectrum.
From the theoretical point of view, it has to be noted that the adoption of different physical inputs (such as equation of state, radiative opacity, nuclear cross sections, convection efficiency, etc) in computation of stellar evolutionary models lead to different predictions for surface lithium abundance at a fixed mass and age. In particular, the convection efficiency in super adiabatic regions (i.e. the mixing length parameter) and the cross sections for nu-

clear reactions involving lithium are fundamental ingredients to obtain reliable theoretical predictions. An example is showed in Fig. 3.3: the logarithmic surface ^{7}Li abundace is plotted at a fixed age ($\sim$10 Myr) by means of two classes of models with solar metallicity and mixing length parameter α=1 (in red) and 1.74 (in purple). Each class has been computed with the same assumptions on the adopted input physics, but for nuclear reaction rates for reactions involving lithium, that are from Trojan Horse (empty circles) and NACRE compilation (filled circles).

A constraints for theoretical model results are the binary systems, which have same metallicity and age. Bayesian determinations of stellar mass and age has yet been successfully applied by Gennaro et al. (2012, hereafter GPT12) to a sample of stars including detached, double lined, eclipsing (EB) binaries, astrometric-spectroscopic (AS) binaries and spectroscopic binaries with circumstellar disk (DSK). These classes are the only for which the dynamical mass ($M_{\rm dyn}$) of both components are determined. $M_{\rm dyn}$ is distance-independent, then it represent a reliable observational estimation, useful in deriving theoretical bayesian results.
Unfortunately the number of known objects belonging to these classes and for which lithium surface abundance is available is small. Anyway, since the radial velocities are nowadays between the most accurate measurements, I suggest to enlarge the sample by applying the method to PMS double lined spectroscopic binaries (SB2) by means of the mass-ratio of the two components, which directly follows from their radial velocities.

The use of mass-ratio, however, doesn't allow to derive the age of each star, but only provides an estimation for the age of the system (*coevality*). Anyway, the hypothesis of coevality is a good assumption for a binary system.

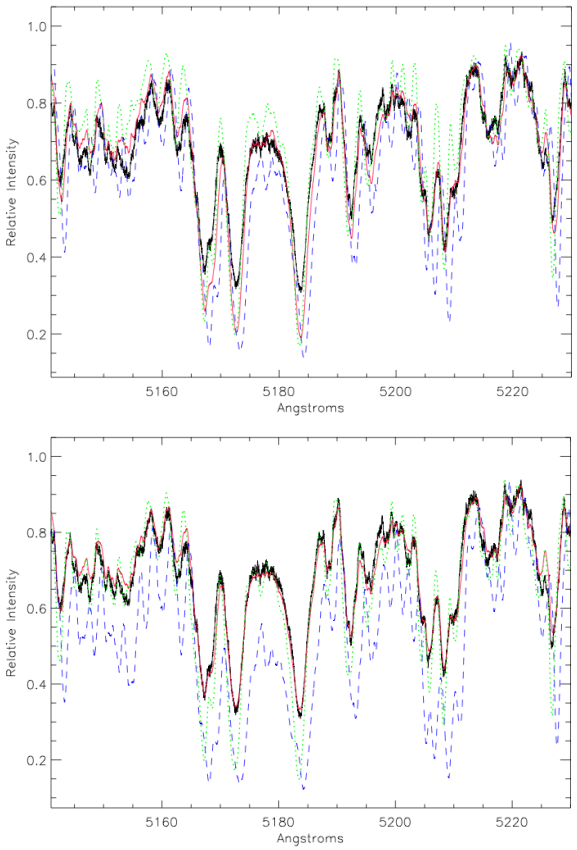

Figure 3.3: *Upper panel*: HARPS-North spectrum (R=115000, S/N=68) of the binary system V773 Tau A and synthetic one (red) computed with no veiling, T_{eff}=4900 and 4700 K and log$g$=3.9 and 4.1 for primary (green) and secondary (blue) component respectively. These values have been determined by Boden et al. (2007) from spectroscopy at R=35000, S/N=35. - *Lower panel*: synthetic spectrum computed with a veiling of 15%, T_{eff} = 4700 and 4100 K and log$g$ = 3.7 and 3.7 for primary and secondary component fits the observed one at the best.

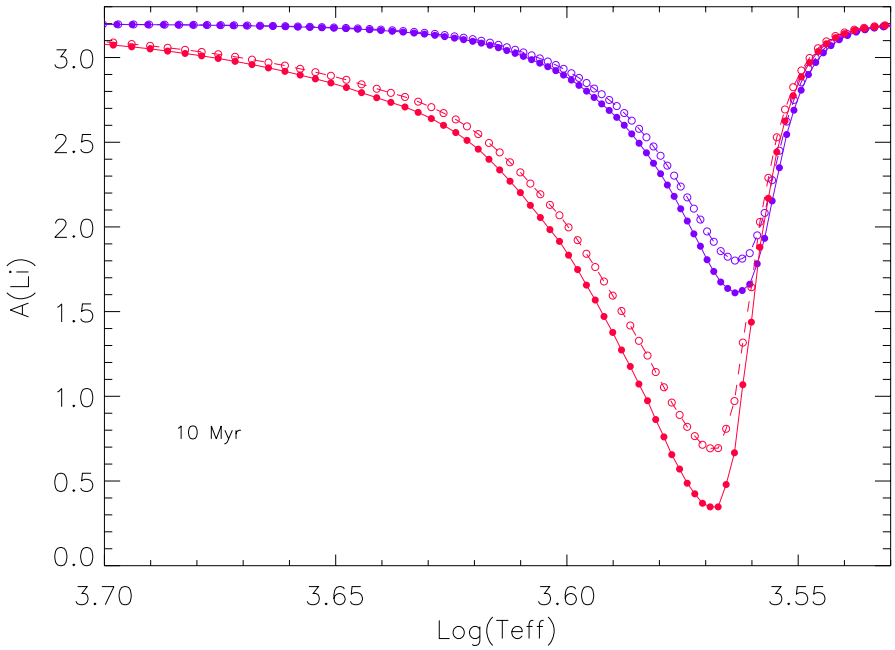

Figure 3.4: Logarithmic surface ^{7}Li abundace is plotted against T_{eff}, at the same age, for two classes of models with solar metallicity and mixing-length parameter α=1 (purple), α=1.74 (red). Each class has been computed with different inputs for cross sections of reaction involving lithium, i.e. THM (empty circles) and NACRE (filled circles).

CHAPTER 4

Stellar evolution modeling

4.1 Stellar structure equations

A star can be defined as a self-gravitational gaseous structure in hydrostatic equilibrium. Under the assumption of spherical symmetry and by neglecting the effects of magnetic fields as a first approximation, the internal stellar structure is described by the following system of four differential equations (see, e.g., Castellani 1985):

$$\frac{dP}{dr} = -\frac{GM_r\rho}{r^2} \tag{4.1}$$

$$\frac{dM_r}{dr} = 4\pi\rho r^2 \tag{4.2}$$

$$\frac{dL_r}{dr} = 4\pi\epsilon\rho r^2 \tag{4.3}$$

$$\frac{dT}{dr} = f(M_r, r, L_r, T, P) \tag{4.4}$$

where

– r indicates the distance from the center of the star

- P is the total pressure
- M_r is the mass contained inside a shell of radius r
- L_r represents the energy through a surface of radius r (it indicates the luminosity when r is equal to the stellar radius R)
- T is the gas temperature
- the function $f(M_r, r, L_r, T, P)$ defines the temperature gradient in each region of the star depending on the energy transport mechanism (i.e. radiative/convective heat transport).
- ρ is the gas density
- ϵ represents the total energy production per gram and per second

Density and energy production are functions of r, M_r, P, T and L_r. Generally the mass M is assumed as independent variable, so that the unknowns are the four quantities P, T, r and L.

The solution of the system allows to derive the trend of the quantities characterizing stellar interiors as a function of the mass and for a fixed chemical composition, then representing a powerful tool to explore stellar structure and evolution. This is what stellar evolutionary codes do.
In order to solve the equations system, a code needs the following *input physics*:

- *Equation of state*, which provides all the thermodynamical quantities required for the integration of a model, such as the density ρ, specific heat at a constant pressure c_P , molecular weight μ, and the adiabatic gradient Δad
- *Radiative and conductive opacity coefficients.* The opacity coefficients determine the transparency level of the stellar

gas to the energy transport.
The radiative opacity, due to the interaction between radiation and matter, depends on several photon absorption processes or scattering on molecules, atoms, ions, or electrons present in the stellar gas. Although the most of these processes strongly depend on the frequency, stellar evolutionary codes make use of a mean value (Rosseland mean opacity) obtained by averaging the frequency-dependent opacity over the frequency distribution (approximated to a black body).
The conductive opacity is related to the electron conduction, which is not negligible when the free electron densities are high and the electrons begin to become degenerate. It mainly regards (low mass stars) and stars in more advanced post-main sequence phases.

– *Energy production.* The total stellar energy production coefficient can be written as the sum of three quantities

$$\epsilon = \epsilon_g + \epsilon_n - \epsilon_\nu \tag{4.5}$$

where the first term is related to the energy generated by thermodynamical transformations of the gas (gravitational energy), the second one indicates the energy production by nuclear burnings and the third (important in post main-sequence phases) represents the energy-loss due to thermo-neutrinos, that are neutrinos produced not in nuclear fusions (i.e. photon-, pair-, and bremsstrahlung- production).

together with the *convection treatment*, which is the formalism adopted to treat the convective heat transport inside a star and in particular in the outermost stellar envelopes, and the *boundary conditions*, that are the physical quantity values at the stellar center and surface. Of course, at the center of a star ($M = 0$) the boundary conditions can be expressed by setting both radius and luminosity equal to zero, so that $r(M = 0) = L(M = 0) = 0$.

For what concerns stellar surface, the usual approach consists in adopting the physical quantities at the base of the atmosphere as boundary condition values.

For this work, I have computed a database of stellar models by means of the Frascati Raphson Newton Evolutionary Code (FRANEC, Degl'Innocenti et al. 2008). The models have been evolved from the early PMS phase up to the end of the central MS H-burning and however not longer than an age of 20 Gyr.
FRANEC solves the set of equations by considering two stellar regions: the *interiors* (from the center to a fraction of the total mass $\sim$99.98%) in which the mass is adopted as independent variable, and the *sub-atmospheric region*, which represents the remaining $\sim$0.02% of fractional mass and where the adopted independent variable is the total pressure. The integration procedure adopted by the code is briefly described below.

- Computation of a *starting model* through the *fitting method*, which consists, given four boundary conditions, two at the surface (luminosity and effective temperature), and two at the center (central pressure and temperature), in integrating the stellar structure equations from the surface downward and from the center upward. The interior and exterior solutions have to match in a given point, *the fitting point*. With an iterative procedure, the four boundary conditions are adjusted until the convergence at the fitting point is achieved within a specified tolerance.
  Such a model represents the one at time zero (t = 0).
- *Evolution.* The model obtained from the fitting method (t = 0) or the model computed for each time-step (t $\neq$ 0) is then evolved. The evolution consists in computing the structure at the next time-step t + Δt, where t is the age of the current model. The time does not appear explicitly in the structure equations, given the hydrostatic nature of the code, but it

appears in the equations that define the chemical evolution (through nuclear burning, diffusion, mixing) and in the computation of the gravitational energy, which contains the time derivatives of the physical quantities (i.e. pressure, temperature, and molecular weight). The new model (i.e. the new structure) is then computed with the *Henyey method* (Henyey et al., 1964): the physical quantities obtained from the previous model are used as initial guess. Since both the chemical composition and the gravitational energy have changed, the equations of stellar structure are no longer satisfied adopting the initial guess. Thus, in each mesh of the structure the physical quantities have to be adjusted with an iterative procedure based on a Raphson-Newton method. The convergence of the model is reached if in each mesh the structure equations are verified within a given tolerance.

I supplied the following input physics and assumptions to the code:

Equations of state - The adopted equations of state have been that provided in 2006 by the Opacity Project at Livermore (OPAL) group (see e.g., Rogers & Nayfonov 2002).

Opacity - For the inner regions ($\log T(\mathrm{K}) > 4.5$) I have adopted the OPAL high-temperature radiative opacity released in 2005 by the Opacity Project at Livermore group (see e.g. Iglesias & Rogers 1996), while for the outer regions ($\log T(\mathrm{K}) \leq 4.5$) the low-temperature radiative opacities of Ferguson et al. (2005). The radiative opacity tables at all temperatures are computed by assuming the solar-scaled heavy-element mixture by Asplund, Grevesse & Sauval (2009).

Atmosphere models - It's necessary to introduce atmosphere models in the code in order to integrate the stellar structure equations.

For $\log T_{\rm eff}(\mathrm{K}) > 4$ I have chosen the atmosphere models computed by Castelli & Kurucz (2003), for $\log T_{\rm eff}(\mathrm{K}) \leq 4$ the ones by Brott & Hauschildt (2005).

Convection - I have introduced the convection by adopting the Mixing-Length theory (Böhm-Vitense 1958) under the formalism of Cox & Giuli (1968) and the classical Schwarzschild criterion. I have computed models with five values of mixing-length parameter, that are $\alpha = 0.80, 1.00, 1.25, 1.50, 1.74$, for exploring as much as possible cases of mixing, since this quantity is unknown. The value $\alpha = 1$ has been found to be suitable for PMS stars (T12), while $\alpha = 1.74$ is the solar-calibrated one.

Nuclear reaction rates - As stated in Chapter 2, I have adopted the code reaction rates from NACRE compilation and JINA REACLIB database, but for the following ones involving light elements, that have been derived by the Trojan Horse Method (THM, Spitaleri 1997):

d(d,p)t	Tumino et al. (2014)
d(d,n)^{3}He	Tumino et al. (2014)
^{6}Li(p,α)^{3}He	Lamia et al. (2013)
^{7}Li(p,α)^{4}He	Lamia et al. (2012)

Chemical composition - The initial abundances of helium, light elements and metals, i.e. the elements content of the starting model, must be set in the code. The aim has been to compute models with chemical compositions reflecting the ones of my sample of stars. From the observational point of view, however, only the $[Fe/H]$ value is available.
It must be outlined that all species are considered to diffuse inside the stellar structure, so that their abundances could locally vary even if they are not created or destroyed via nuclear processes. However, the microscopic diffusion is inefficient on time-scales

typical of PMS evolution. Moreover, diffusion efficiency decreases as the depth of the convective envelope increases, thus in almost fully convective stars (as in the case of PMS) such effect can be safely neglected.

By assuming for population I stars a solar-scaled heavy elements distribution (valid for solar-like metallicity stars, see e.g., Asplund et al., 2009), i.e. the relative abundances of each element heavier than helium is the same in the analyzed star and in the Sun, the metallicity value currently present at the stellar surface can be directly inferred from the observed $[Fe/H]$ (see equation below) and can be safely adopted as a good approximation of the initial metallicity over the whole structure (see Tognelli et al. 2012 for details), since the effect of microscopic diffusion is negligible.

As to the helium content, it cannot be spectroscopically measured for PMS late-type stars, since their low temperature not allows helium transitions. In this case the following relation between initial metals content (Z) and helium abundance (Y), involving the primordial helium abundance value (Y_p) and the helium-to-metals enrichment ratio (Δ Y/Δ Z) can be adopted (Gennaro et al., 2010, and references therein):

$$Y = Y_P + Z\frac{\Delta Y}{\Delta Z} \tag{4.6}$$

with

$$Z = \frac{1 - Y_p}{1 + \frac{\Delta Y}{\Delta Z} + (Z/X)_\odot \times 10^{-[Fe/H]}} \tag{4.7}$$

I have adopted Y_p=0.2485 (see e.g. Cyburt, Fields & Olive 2004), $\Delta Y/\Delta Z = 2$ (Casagrande et al. 2007) and $(Z/X)_\odot$=0.0181 (Asplund et al. 2009).

In order to cover the full range of the observed $[Fe/H]$ of the examined sample, I have computed models for six different values of metallicity Z, that are 0.00700, 0.00800, 0.00900, 0.01000, 0.01291 (the solar one), 0.01550 and 0.01800.

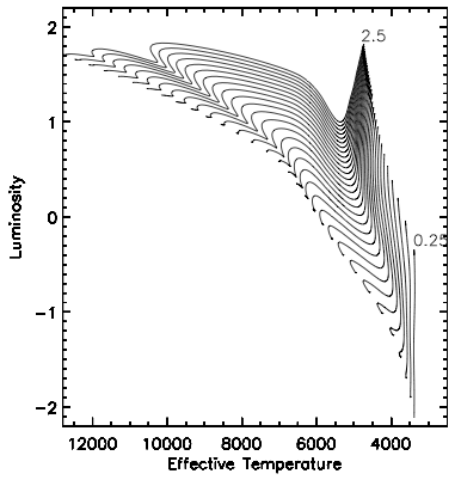

Figure 4.1: FRANEC evolutionary tracks.

Regarding to the initial abundances of of light elements at different metallicities, I have set the initial deuterium mass fraction abundance $X_{\rm D} = 2 \times 10^5$ that is suitable for Population I stars (see e.g. Linsky et al. 2006), while for ^{6}Li, Be, B I have adopted the values given in Prantzos (2012). Finally, I have set the logarithmic initial ^{7}Li abundance A(^{7}Li)[1]=3.2 (Jeffries 2006, Lodders et al. 2009).

In order to obtain a high precision in my analysis, I computed a very fine grid of models in the mass range [0.25, 2.50] $M_\odot$ as follows. The models have initially been obtained with a spacing of 0.25 $M_\odot$. Then I have interpolated the grid with a spacing of 0.0125 $M_\odot$ and 0.005 Myr in the full mass range.

4.2 Pre-Main Sequence models

As already stated in chapter 1, the Pre-Main Sequence (PMS) phase starts when accretion rate onto the protostar becomes neg-

[1] A(^{7}Li) $= 12 + log N_{Li}/N_H$ where N_{Li} and N_H indicate respectively the lithium and hydrogen numerical abundance.

ligible and the residual gas of the original cloud has almost all been sweeped out, so that the mass of the central object is well defined and the stellar surface is optically visible. Luminosity and effective temperature are well determined and one can trace the stellar evolution on the HR diagram. In 1983 Stahler defined the *Birthline* as *the locus in the HR diagram where PMS stars of various masses should first appear as visible objects* (Stahler 1983). Since the emitted radiation is not balanced by an internal energy source, the star contracts in quasi-hydrostatic equilibrium on thermodynamical time scale. For this reason, its position on the HR diagram rapidly changes with time, describing a path (evolutionary track) which depends on mass and is reproduced by stellar structure and evolutionary models.

For this purpose the choice of the starting model of the evolutionary code is of fundamental importance. A realistic PMS models starting from the Birthline implies to take as a starting model the structure left at the end of the previous hydrodynamical evolution of the protostar. However, the hydrodynamical protostellar evolution is still largely debated and not yet settled. The most of authors (Baraffe et al. 1998; Siess et al. 2000; Yi et al. 2001; Dotter et al. 2007; Di Criscienzo et al. 2009) follows the standard approach outlined by Iben (1965) which consists in choosing as a starting model a fully convective structure of very large radius and luminosity (i.e. a point along the Hayashi track) from which the star begins its quasi-static contraction at constant mass (i.e. neglecting any mass accretion episode). The problem is to understand if this simplistic approach significantly affects the whole evolution of PMS models or only the very early stages. Many works agree in predicting that after the end of the main mass-accretion phase, the evolution quickly converge to that of standard hydrostatic models (Stahler 1983; Palla & Stahler 1991, 1992). However, there is not yet complete agreement with

this conclusion (Wuchterl & Tscharnuter 2003). Fig. 4.2 shows FRANEC standard stellar PMS tracks for masses between 0.2 - 6.0 $M_\odot$ in the HR diagram with the superimposed birthline of Stahler & Palla (2005) and isochrones of 0.5 and 1 Myr (Tognelli et al. 2011). The tracks intersect the Birthline at different ages in dependence on the mass, i.e. before 0.5 Myr for masses up to 1 $M_\odot$ and and before 1 Myr for more massive stars. So, in standard approximation the FRANEC Birthline starts from an age $\sim$ 0.5 - 1 Myr.

A further approximation of the standard PMS models that in principle could affect the early PMS evolution is the assumption that the initial deuterium abundance is the same as that of the ISM. Theoretical predictions from models taking into account protostellar accretion (Stahler & Palla 2005) state that in a protostar the deuterium burning start when a mass of 0.3 $M_\odot$ is reached, under the assumption of constant mass accretion rate of 10^{-5} $M_\odot$ yr^{-1}. This implies that the initial deuterium abundance on the Birthline for stars of mass lower than 0.3 $M_\odot$ is the same of the ISM, while for more massive stars the value significantly decreases as the mass increases. That is stars with a mass $M > 1M_\odot$ should almost completely deplete the deuterium during the protostellar phase. However, since in standard models the deuterium burning occurs at luminosities much higher than corresponding Birthline ones, when the model reaches it the deuterium depletion agrees with that provided by protostellar computations (Tognelli et al. 2011). So the assumptions of standard models about the initial deuterium abundance has a negligible effect on the PMS evolution.

Finally, the definition of starting model may also has implication on the stellar age determination. As stated by Tognelli et al. 2011, *the age assigned to pre-MS stars by means of standard models is simply the interval of time required for the model to attain*

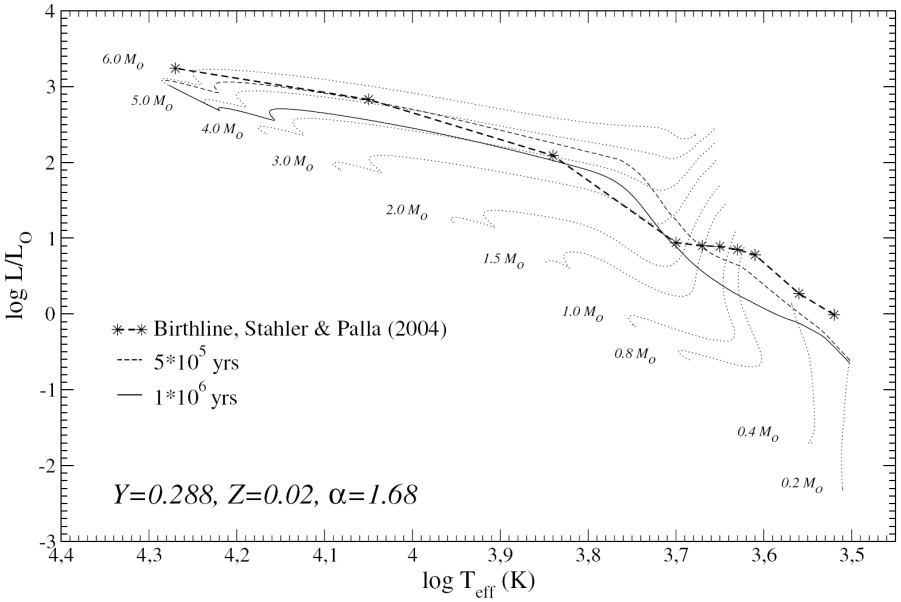

Figure 4.2: From Tognelli et al. 2011. The dotted lines represent the FRANEC PMS evolutionary tracks for masses between 0.2-6.0 $M_\odot$, while the dashed line and the dotted line are respectively 0.5 Myr and 1 Myr isochrones. Star-dashed line is the Birthline by Stahler & Palla (2005).

the observed radius and luminosity starting from the arbitrary initial conditions of high luminosity and large radius. Anyway, this estimation is inaccurate particularly for low mass stars, since it neglects the protostellar phase. A more reliable age estimation may be obtained by adding the protostellar age to the PMS one, measured from the Birthline (Stahler 1983). However, the time to form a star from a protostar with a constant mass accretion rate of 10^{-5} $M_\odot$ yr^{-1} (Stahler & Palla 2005) ranges from 0.1 to 0.6 Myr, so that the inaccuracy can be assumed negligible.

CHAPTER 5

The bayesian method

5.1 Theoretical age and mass determinations: the Bayesian method

Theoretical age and mass determinations of the stellar sample have been obtained by applying a bayesian analysis. The method allows to derive an estimation for a stellar parameter (e.g. mass and age) by comparing observational evidence of other quantities (such as effective temperature, surface gravity, luminosity, radius) with models' predictions for the same quantities, and including the "*a priori*" informations (by means of the so-called *prior probability*) about the parameters to be determined.

By following the notation in GPT12, I define the vector $\mathbf{q}$ as the set of *stellar observational quantities*, e.g. $\mathbf{q}$=($T_{\rm eff}$,log$g$) (effective temperature and surface gravity) and the vector $\mathbf{p}$=(τ,μ,Z) as the set of *model parameters* (age, mass and metallicity). I also define the different values of mixing-length ($\alpha_{\rm j}$) as *meta-*

parameters, which identify a class of models.

Briefly, from the Bayes' theorem the probability $f(\mathbf{p}|\mathbf{q})$ of getting p-values given the observed q-data (*posterior probability* of $\mathbf{p}$) is related to the probability $f(\mathbf{q}|\mathbf{p})$ of observing the q-data given the p-values and the probability $f(\mathbf{p})$ of getting p-values independently from q-data (*prior probability* of $\mathbf{p}$) as follows:

$$f(\mathbf{p}|\mathbf{q}) = \frac{f(\mathbf{q}|\mathbf{p})f(\mathbf{p})}{f(\mathbf{q})} = \frac{f(\mathbf{q}|\mathbf{p})f(\mathbf{p})}{\int f(\mathbf{q}|\mathbf{p})f(\mathbf{p})d\mathbf{p}} \tag{5.1}$$

where $f(\mathbf{q}|\mathbf{p})$ is proportional to the *likelihood* $L(\mathbf{p}|\mathbf{q})$ of the parameters $\mathbf{p}$ given the evidence $\mathbf{q}$. The normalizing factor f($\mathbf{q}$) (*marginal distribution* of $\mathbf{q}$) is the probability of observing $\mathbf{q}$ under *all* possible values for $\mathbf{p}$, so it requires the introduction in our analysis of all models for all possible parameters and meta-parameters, that isn't possible. Anyway, if we are looking only for the most probable *p-values* within a single class of models or we want to compare two different classes of models, normalization can be removed by taking the probability ratios (see GPT12). Then

$$f(\mathbf{p}|\mathbf{q}) \propto L(\mathbf{p}|\mathbf{q})f_p(\mathbf{p}) \tag{5.2}$$

The likelihood $L(\mathbf{p}|\mathbf{q})$ represents the comparison between empirical data and theoretical predictions for the observational quantities, that in this case are $T_{\rm eff}$ and log$g$.
As in JL05, by assuming independent Gaussian errors σ_i ($i = 1, .., dim(\mathbf{q})$) for the observed quantities $\mathbf{q}$, the likelihood function is defined as:

$$L(\mathbf{p}|\mathbf{q}) = (\Pi \frac{1}{(2\pi)^{1/2}\sigma_i}) \times exp(-\chi^2/2) \tag{5.3}$$

where

$$\chi^2 = \Sigma(\frac{q_i^{ob} - q(\mathbf{p})_i}{\sigma_i})^2 \tag{5.4}$$

Here q_i^{ob} and $q(\mathbf{p})_i$ are the measured value of the observable q_i and the vector of model-values for the same quantity, respectively.

The prior probability f($\mathbf{p}$) allows the introduction in the procedure of the available information (if any) about the model parameters, i.e. metallicity, mass and age of the star.

As to metallicity, it has been here introduced by a Gaussian function (GPT12) centered on the known metallicity-value Z_{ob} (*metallicity prior distribution*):

$$f_p(Z) \propto \exp[-(1/2)[(Z - Z_{ob})/\sigma_{Zob}]^2] \tag{5.5}$$

For each system Z_{ob} has been obtained from the observed $[Fe/H]_{ob}$ by the formula (Gennaro et al. 2010):

$$Z_{ob} = \frac{1 - Y_p}{1 + \frac{\Delta Y}{\Delta Z} + \frac{1}{(Z/X)_\odot} \times 10^{-[Fe/H]_{ob}}} \tag{5.6}$$

As stated in previous chapter, I adopted Y_p=0.2485 for the primordial helium abundance (see e.g. Cyburt, Fields & Olive 2004), $\Delta Y/\Delta Z$=2 for helium-to-metals enrichment ratio (Casagrande et al. 2007) and $(Z/X)_\odot$=0.0181 (Asplund et al. 2009).
Actually, f_p(Z) could be very asymmetric and the equation above is strictly valid only if the errors on [Fe/H] are distributed as gaussian. Anyway, we are in the same conditions of GPT12, i.e. typical [Fe/H] uncertainties in our data $\sim$0.1, so the departure from gaussian function is negligible, as the authors showed.

Regarding to the masses, for the EB, AS and DKS systems the $M_{\rm dyn}$ estimation is introduced into the procedure by means of a Gaussian function:

$$f_p(\mu) \propto \exp[-(1/2)[(\mu - M_{\rm dyn})/\sigma_{M_{\rm dyn}}]^2] \tag{5.7}$$

In absence of accurate information about the single masses of the systems in exam but having their accurate mass-ratio value, I have considered the binary as a single object, for which I wanted to determine the two theoretical models, i.e. the two masses μ_1 and μ_2, having the observed mass-ratio, MR_{ob}, and the same age from the observational data $\mathrm{T}_{\mathrm{eff}\,j}$, $\log g_j$, for j=1,2. I then define the *mass-ratio prior distribution*:

$$f_p(MR) \propto \exp[-(1/2)[((\mu_2/\mu_1) - MR_{ob})/\sigma_{MRob}]^2] \qquad (5.8)$$

The "*a priori*" information about the age of a binary system is the *coevality*, that is implicitly taken into account in the analysis of SB2, since I was looking for the same age. In the other cases it is imposed by multiplying the age marginal distributions of the two stars (see below).

The integration of the equation (1) with respect to all parameters but one, p_i, yields the *marginal distribution* for p_i, the mode of which provides the most probable value for p_i and its confidence interval. I was interested in deriving mass μ_j and age τ_j (j=1,2) of the components of each binary system in exam. When M_{dyn} was available, I have obtained the mass marginal distribution $H(\mu)$ and the age marginal distribution $G(\tau)$ for each star. By explicitly writing the vector $\mathbf{p}$:

$$H_j(\mu) = \iint L_j(\tau, \mu, Z|\mathbf{q}_j) f_p(Z) f_p(\mu) d\tau dZ \qquad (5.9)$$

$$G_j(\tau) = \iint L_j(\tau, \mu, Z|\mathbf{q}_j) f_p(Z) f_p(\mu) d\mu dZ \qquad (5.10)$$

and the coevality τ_c for the two stars has been imposed by multiplying their age marginal distributions:

$$G_c(\tau) = G_1(\tau) \times G_2(\tau) \qquad (5.11)$$

For the case of SB2, in general to treat the binary system as unique object (dependent on) implies that the likelihood is a function of the model parameters related to both stars. However, given its simple structure (Eq. ...), in this case it can be factorized as the product of the likelihood of the single stars:

$$L(\tau_1, \mu_1, Z_1, \tau_2, \mu_2, Z_2|\mathbf{q}_1\mathbf{q}_2) = L_1(\tau_1, \mu_1, Z_1|\mathbf{q}_1) \times L_2(\tau_2, \mu_2, Z_2|\mathbf{q}_2) \tag{5.12}$$

and the integrand function becomes

$$L_1(\tau_1, \mu_1, Z_1|\mathbf{q}_1)L_2(\tau_2, \mu_2, Z_2|\mathbf{q}_2) \\ f_p(Z_1)f_p(\mu_1)f_p(\tau_1)f_p(Z_2)f_p(\mu_2)f_p(\tau_2) \tag{5.13}$$

The assumptions of coevality and same metallicity for both stars can be provided by adopting Dirac delta for τ_1,τ_2 and Z_1,Z_2, respectively. Moreover, the mass prior of each star can be replaced by the mass-ratio prior defined above.
Then, for $i, j = 1, 2$, $i \neq j$, and by considering through $f_p(Z)$ a possible available metallicity information, the mass marginal distributions of the two stars and their common age marginal distribution can be written as follows:

$$H_j(\mu_j) = \iiint L_j(\tau, \mu_j, Z|\mathbf{q}_j)L_i(\tau, \mu_i, Z|\mathbf{q}_i)f_p(MR)f_p(Z)d\mu_i d\tau dZ \tag{5.14}$$

$$G(\tau) = \iiint L_1(\tau, \mu_1, Z|\mathbf{q}_1)L_2(\tau, \mu_2, Z|\mathbf{q}_2)f_p(MR)f_p(Z)d\mu_1 d\mu_2 dZ \tag{5.15}$$

The mode of the marginal distributions gives an estimation of masses, coevality and (when $M_{\rm dyn}$ is available) single ages. The confidence interval, that is the uncertainty on the obtained estimation, has been obtained as in GPT12: if A is the total area under the generic marginal distribution curve, F(x), the confidence interval $[x_{min}, x_{max}]$ is given by:

$\int_{x_l}^{x_{min}} F(x)dx = \int_{x_{min}}^{x_u} F(x)dx = 0.16$ A

where I have assumed that the variable x is defined in the interval $[x_l, x_u]$. In this way 16 per cent of the total probability is rejected on each side of the confidence interval. This definition coincides with that of a 1σ interval in the case of a Gaussian distribution.

CHAPTER 6

The Spectroscopic Data

6.1 Overview

Only few of the known PMS binary systems present well known orbit parameters, as well stellar parameters: temperature gravity, chemical composition and lithium abundance. In order to enlarge this sample, I started an high resolution observational campaign with particular attention for the SB2 systems.

Observations were driven by an accurate exploration of all database to look for already available high resolution spectra useful for our goal, namely the *European Southern Observatory*, *Anglo Australian Observatory* and *Canadian French Hawaii Telescope* archives. I have obtained spectra of AK Scorpii, CD-39 10292, GSC06213-00306, HD 34700 A from the European Southern Observatory (ESO) Archive and of V4046 Sgr from the Canadian French Hawaii Telescope (CFHT) Archive. The ESO spectra have been obtained with the Fiber-fed Extended Range Optical Spectrograph (FEROS), an Échelle spectrograph with resolution R = 48000 and

covering a wavelength range between 3700 and 8600 Å. The CFHT spectra have been obtained with the Échelle SpectroPolarimetric Device for the Observation of Stars (ESPaDOnS), which has a resolution R = 68000 and covers a wavelength range between 3700 and 10500 Å.

6.2 Observations

About twenty observing nights have been dedicated to the collection of data. Most of the spectra were obtained with the *Catania Astrophysical Observatory Spectropolarimeter*, plus a three nights observing run with HARPS-North at the Telescopio Nazionale Galileo.

A total of fifteen systems have been monitored. As it was expected, only two systems presented the all the necessary characteristics for my goals. Most of the systems were not presenting the typical SB2 composed spectrum and only few stars had a detactable lithium line.

Please refer to Appendix B for details on the data reduction. Please refer to Appendix C for a description of used instrumentation.

6.3 Determination of stellar parameters

In astrophysics, the stellar parameters: temperature, surface gravity, radial velocity, rotational velocity and atmosphere velocity fields of a star are at the best inferred by minimizing the difference between observed and synthetic high resolution spectra.

Following Catanzaro, ... Giarrusso et al. (2015), and Ripepi ... Giarrusso (2015), for this purpose I have then computed a grid of synthetic spectra in local thermodynamic equilibrium (LTE) approximation, by means of the SYNTHE code (Kurucz & Avrett

1981). The atmosphere models given at the input of the code have been obtained with the ATLAS9 program (Kurucz 2005), while the atomic line list distributed by Kurucz (1993) has been adopted in order to identify the spectral lines. All models assume the solar metallicity, no macroturbulence and microturbulence of 2 km s^{-1}, after the Magazzú et al. (1991) and Martín (1997) determination for PMS stars. Effective temperature of the synthetic spectra ranges from 3500 to 10000 K with a step of 100 K. For each temperature value, the logarithmic surface gravity varies between 3.2 and 4.6 with a step of 0.1 dex.

In the case of binary systems, the two set of stellar parameters have to be determined simultaneously appearing the spectral lines of any component reduced in strength because of the companion additional luminosity. In order to estimate *effective temperature* ($T_{\rm eff}$) and *surface gravity* ($\log g$) for the stars of each system:

1) At first, I chose wavelength intervals useful for my analysis of late-type stars, i.e. spectral frames containing the Mg I b lines $\lambda\lambda$5167.3, 5172.7, 5183.6 Å, the Na I D lines $\lambda\lambda$5889.950, 5895.924 Å, and the Ca I λ6162 Å line, all mainly sensitive to gravity variations (Deeming 1960, Gray 1992). Regarding to the effective temperature I selected where possible the spectral region around λ6252 Å, since the line depth ratio of V I λ6251.83 Å and Fe I λ6252.57 Å is temperature-sensitive (Gray 1992). Anyway, Na I D lines are sensitive to temperature too (Stempels et al. 2008).

2) A quantitative comparison between observed and synthetic spectra has been done as:

$$\chi^2 = \frac{1}{n}\Sigma_{\lambda=\lambda_1}^{\lambda_2}\left(\frac{S^{obs}(\lambda)N(\lambda) - S^{th}(\lambda)}{\sigma(\lambda)}\right)^2 \qquad (6.1)$$

where:

a) $S^{th}(\lambda) = \frac{S_p(\lambda(1-v^p_{\rm rad}/c))+S_s(\lambda(1-v^s_{\rm rad}/c))w}{C_p(\lambda(1-v^p_{\rm rad}/c))+C_s(\lambda(1-v^s_{\rm rad}/c))w}$

is the spectrum obtained by adding the SYNTHE spectra of the primary (S_p) and secondary (S_s) components and normalizing to the sum of their continua (C_p and C_s). The weight $w = \frac{M_s}{M_p}\frac{g_p}{g_s}$ takes into account for the generally different contribution of the two stars of masses M_p, M_s to the composed luminosity L due to their generally different radius R, since for each star $L \propto SR^2$ and $R^2 \propto \frac{M}{g}$. The S_p and S_s spectra are broadened according to both a gaussian instrumental profile and a stellar rotation profile with the input $v^p \sin i$ and $v^s \sin i$ projected rotation velocities. A Doppler shift was applied to the spectra of the primary and secondary star according to the input $v^p_{\rm rad}$ and $v^s_{\rm rad}$ radial velocities;

b) $N(\lambda)$ represents a normalization factor for the observed spectrum S^{obs} (the continuum of observed late-type star spectra cannot reliably be set a priori), which has also been corrected for the barycentric velocity γ;

c) $\sigma(\lambda)$ is the estimated error on the observed spectra;

d) n is the total number of points within [λ_1,λ_2].

3) This procedure selects the pair of synthetic spectra S_p and S_s which best match the observed one, that is to an estimation of ($T_{\rm eff}$,log$g$)$_p$ and ($T_{\rm eff}$,log$g$)$_s$.

It has to be noted that PMS stars can be characterized by *veiling*, an effect that lets spectral lines appear weaker because of continuum emission imposed over the photospheric flux (Joy 1949). The origin of this additional flux is ascribed to circumstellar matter

and/or to heating of the outer atmosphere. If no combination of SYNTHE spectra matches the observation satisfactorily, the reason could be attributed to a sub-solar metallicity of the system or to the presence of veiling. Since the six examined stars are near to the Sun, it is reasonable to hypothesize that they have a solar chemical composition, so that the latter possibility should be the most probably one. I developed a procedure which takes into account for the veiling contribution. However, I computed a further grid of synthetic spectra with sub-solar metallicity, i.e. [M/H] = -0.5 according to the opacity table of Kurucz.

4) *Lithium abundance* (A(Li)) has been derived for each star by measuring the observed equivalent widths ($EW^{\rm obs}$) of the LiI 6707.82 Å doublet. As in Conti (1970) and Catanzaro et al. (2003), I converted these values into the intrinsic ones ($EW^{\rm intr}$), that are equivalent widths corrected for the light ratio $l = \frac{L_p}{L_s} = \frac{S_p}{S_s w}$ of the synthetic spectra resulting in the preview step

$$EW_p^{\rm intr} = \frac{1+l}{l} EW_p^{\rm obs} \tag{6.2}$$

$$EW_s^{\rm intr} = (1+l) EW_s^{\rm obs} \tag{6.3}$$

From these, Non-LTE curve of growths calculations from Pavlenko & Magazzú (1996) for the $T_{\rm eff}$ range $[3500, 6000]$ K or the most recent ones from Lind et al. (2009) for the $T_{\rm eff}$ range $[4000, 8000]$ K directly provide the corresponding logarithmic lithium abundance (in the scale log$N$(H)=12)

$$A_{p,s}({\rm Li}) = log(\frac{N({\rm Li})}{N({\rm H})})_{p,s} + 12 \tag{6.4}$$

where N(Li) and N(H) indicate respectively the number of lithium and hydrogen absorbing atoms.

All these derived quantities are summarized in Table 6.1.

6.3.1 Orbital parameters

As a by product of the previous procedure devoted to the determination of stellar parameters, the radial velocity of stellar components of any binary system has been measured. These values have been combined with data from the literature to derive the orbital parameters.

According to a classical description, orbits are defined by:

a	semi-major axis
e	eccentricity
P	period
i	inclination angle
ω	longitude of periastron
T_o	time of periastron passage

and the expected radial velocities are

$$v_{\rm rad} = K[\cos(\theta + \omega) + e\cos\omega] \tag{6.5}$$

where

$$K = \frac{2\pi a \sin i}{P\sqrt{1-e^2}} \tag{6.6}$$

and θ is the angular position of the star measured from the center of mass at a given instant.

Orbital elements have been determined by a least-squares fitting of observed radial velocities to Eq. (6.2) with the following steps: one degree for ω, 0.5 $\mathrm{km\,s^{-1}}$ for velocities and 0.01 for e. Errors have been estimated as the variation in the parameter which increases the rms deviation of the observed radial velocities with respect to the fitted curve by $1\,\sigma$.

6.3.2 Lithium abundances

Spectral lines in stellar spectra present a shape and a strength depending on the physical and thermodynamical conditions in the most external layer, that is the atmosphere. In addition to the abundance of elements, there exists a large variety of phenomena occurring in the formation of spectral lines: the temperature that sets the population of electron levels, the pressure (e.g. surface gravity) that determines the local electric field and with it the importance of the Stark effect, the velocity fields (microturbulence and macroturbulence), the magnetic fields. As a consequence of so many dependences, the most reliable way to determine the chemical abundance of stars is based on the numerical solution of the radiative transfer equation. Stellar parameters are chosen in order to reproduce the observed flux distribution and abundances are adopted as those values matching the spectral line profiles (Gray 1992).

To derive the Lithium abundance in stars the LiI6708 Å resonance line is commonly considered. This is one of the three lithium line present in the visible range and it is preferred for its strength and for being not blended with other spectral lines.

For our goals, I have measured the equivalent width, that is the flux absorbed by an atomic transition, and numerical equal to:

$$EW = \int \frac{F_{\rm c} - F_{\lambda}}{F_{\rm c}} d\lambda \tag{6.7}$$

of the observed LiI6708 Å lines and converted them in abundances following the methods suggested by Pavlenko & Magazzú (1996) and Lind et al. (2009). All these authors include in the calculations the effects of *Non Local Thermodinamical Equilibrium*. That is the influence of the radiation field in populating the electron levels.

6.4 The examined pre-main sequence binaries

In the following, a brief description of each examined binary system. Where not specified, the errors associated to the equivalent width are 20 mÅ.
All the data used in the analysis are summarized in Tables 5.2 and 5.3.

6.4.1 AK Sco

AK Sco (= CD-36 11056 = HD 152404 = HIP 82747) is a PMS double-lined spectroscopic binary characterized by Li I 6708 Å absorption line and H_α emission with a deep central reversal (Herbig & Rao 1972). Strong infrared excess, irregular light variations and no evidence for Ca I H & K lines emission have been found by Andersen et al. (1989) (hereafter A89), which highlighted how this intriguing system shares characteristics with both CTTSs and earliest-type NTTSs. The system consists of two almost identical stars of spectral type F5IVe and presence of an extended surrounding environment has been confirmed by several authors (A89, Jensen & Mathieu 1997, Alencar et al. 2003 hereafter A03). The Hipparcos distance $D = 145^{+38}_{-25}$ pc of AK Sco is consistent with that of both Upper Scorpius and Upper Centaurus Lupus star forming region (de Zeeuw et al. 1999, hereafter dZ99). dZ99 established that the system is located in the former with a probability of 57%. Upper Scorpius (age ∼11±3 Myr) and Upper Centaurus Lupus (age ∼16±1 Myr) are subgroups of the OB Association Scorpius-Centaurus, together with Lower Centaurus Crux (age ∼17±1 Myr) (Pecaut et al. 2012). More recently Czekala et al. (2015) located AK Sco in the older Upper Centaurus Lupus, on the basis of age derived from models.
From spectroscopy A89 estimated effective temperature T_{eff}=6500

K and surface gravity log$g$=3.9 for both components. As to orbital solutions, the authors found a high eccentricity, $e = 0.47$, and a period $P = 13.6$ days.
A03 provided an estimation for barycenter velocity $\gamma = -1.97 \pm 0.10$ km s^{-1}, velocity semi-amplitudes $K_{\rm A} = 64.45 \pm 0.23$ km s^{-1} and $K_{\rm B} = 65.32 \pm 0.24$ km s^{-1}, anomaly $\omega = 185.40^{\rm o} \pm 0.33^{\rm o}$, T0 and no eclipse by photometry.

I have spectroscopically analyzed five FEROS spectra of AK Sco from the ESO Archive, obtained between 28 July and 03 August 2007.

Orbital solutions - From a gaussian fit of the line Fe I λ6065.492 Å, I derived rotational velocities, $v_{\rm A} \sin i = 30 \pm 0.5$ km s^{-1} and $v_{\rm B} \sin i = 30.5 \pm 0.5$ km s^{-1}, and radial velocities of the two components in the five spectra. These measurements together with the ones in A03 are plotted in Fig. 6.1. From all the data I determined an orbital period $P = 13.609$ days, barycenter velocity $\gamma = -1.9 \pm 0.5$ km s^{-1}, velocity semi-amplitudes $K_{\rm A} = 64.5 \pm 0.9$ km s^{-1} and $K_{\rm B} = 65.4 \pm 0.9$ km s^{-1}, anomaly $\omega = 185.2 \pm 0.5^{\rm o}$, eccentricity $e = 0.47 \pm 0.05$ and T0 = 46654.366 days.

Physical parameters - The spectrum showing a best line separation of the two components has signal-to-noise $S/N = 200$ and has been obtained in the night 2007 July, 28. I selected this one to measure
From comparison with the synthetic spectra of solar metallicity, I obtained $T_{\rm eff} = 6600$ K and log$g = 4.5$ for primary, $T_{\rm eff} = 6500$ K and log$g = 4.6$ secondary component. No veiling I have detected. Fig. 6.2 and Fig. 6.3 show the observed spectrum fitted with the synthetic one for both Andersen1989 parameters and values I measured.
From a gaussian fit of the Li I λ6708 Åline I derived the observed

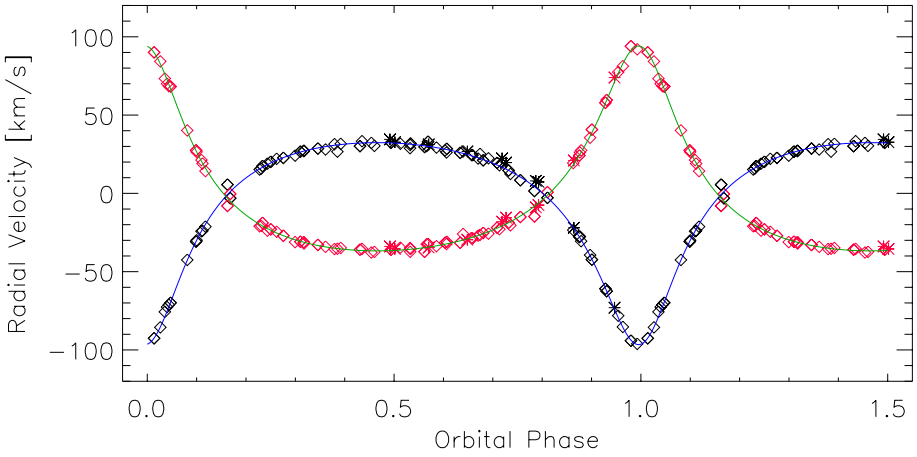

Figure 6.1: AK Sco radial velocity curve. Data for primary (black) and secondary (red) component are from Alencar et al.2003. The star symbol indicate values I obtained from the FEROS spectra.

equivalent widths for the two components, $EW_{\rm A}^{\rm obs} = 69$ mÅ and $EW_{\rm B}^{\rm obs} = 61$ mÅ. As a result of correction for luminosity ratio I obtained the intrinsic values $EW_{\rm A}^{\rm intr} = 120$ mÅ and $EW_{\rm B}^{\rm intr} = 143$ mÅ which I converted to lithium abundances $A_{\rm A}({\rm Li}) = 3.36{\pm}0.60$ and $A_{\rm B}({\rm Li}) = 3.41 \pm 0.60$ by means of the NLTE computations by Lind et al. (2009).

6.4.2 ASAS J052821+0338.5

ASAS J052821+0338.5 (= 2MASS J05282082+0338327) is a PMS detached eclipsing (Pojmański et al. 2005) and double-lined spectroscopic (Stempels et al. 2008, hereafter S08) binary system of spectral type K1/K3.

It was spectroscopically and photometrically analyzed by S08, which estimated a distance $D = 280 \pm 30$ pc and located the system in the 11.4 Myr old Orion OB1 subassociation. The authors found deep Li I 6708 Å absorption lines of the two components in

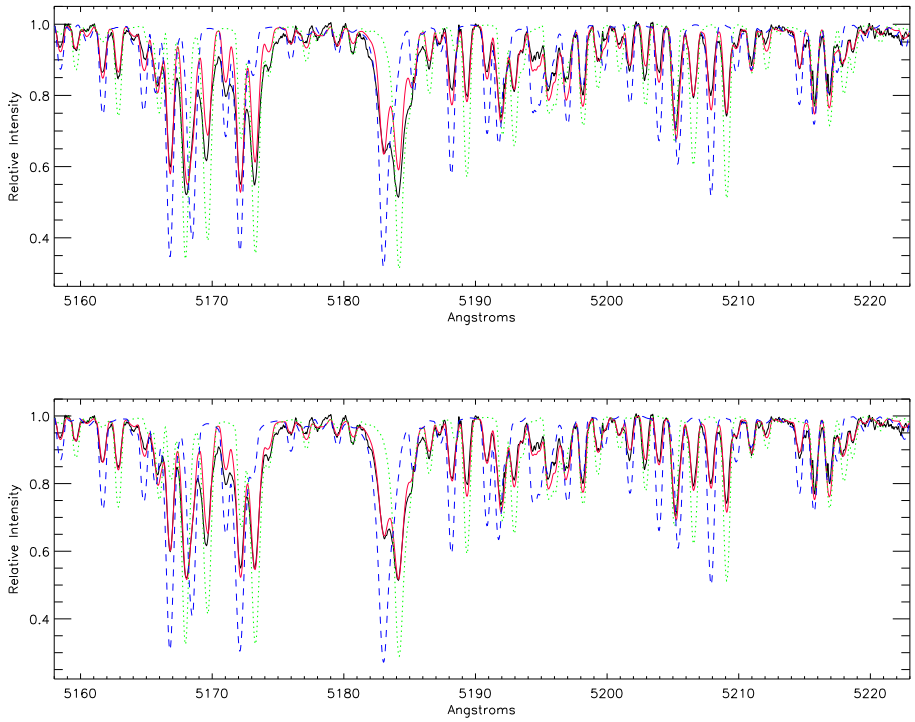

Figure 6.2: AK Sco. Observed (black) FEROS spectrum in the Mg I b lines region. - *Upper panel*: synthetic (red) spectrum computed with Andersen1989 parameters, see text, for primary (green) and secondary (blue) component. - *Lower panel*: synthetic spectrum computed with here determined parameters:T_{eff} = 6600 K and log$g$ = 4.5 for the primary component, T_{eff} = 6500 K and log$g$ = 4.6 for the secondary.

its spectra, corresponding to near-primordial lithium abundances $A_A(Li) = 3.10$ and $A_B(Li) = 3.35$, as well as H_α emission and no other emission lines. S08 derived metallicity slightly lower than the solar one, i. e. $[M/H] = -0.2 \pm 0.2$ and -0.1 ± 0.2 for primary and secondary component. In this work I adopted the mean central value -0.15, as in Gennaro et al. 2012. The orbit is almost circular ($e = 0.02$), with period $P = 3.87$ days.

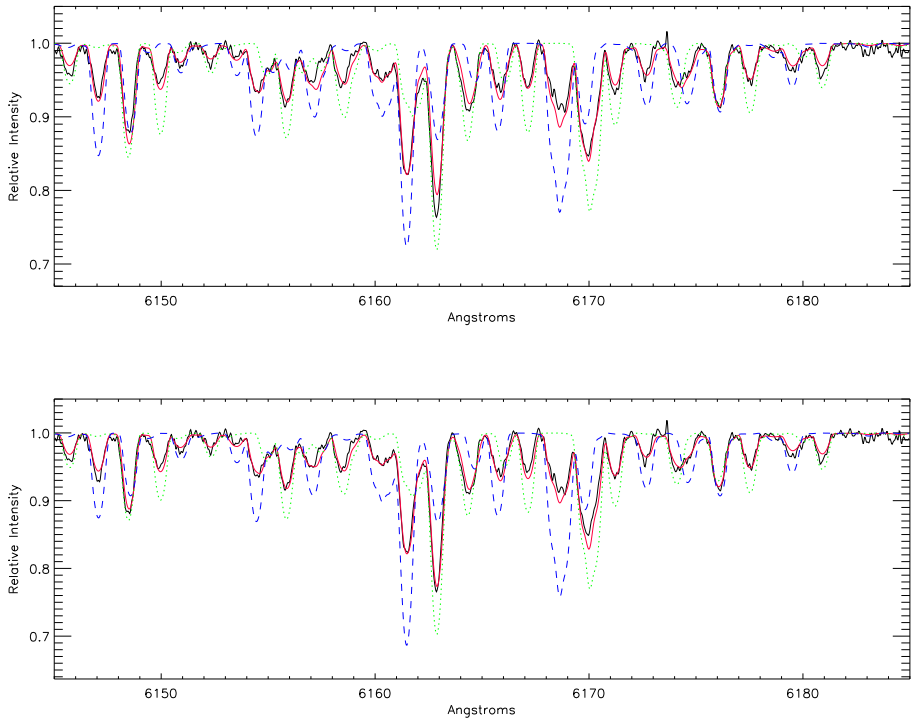

Figure 6.3: AK Sco. Observed (black) FEROS spectrum in the Ca I λ6162 Å region. - *Upper panel*: synthetic (red) spectrum computed with Andersen1989 parameters, see text, for primary (green) and secondary (blue) component. - *Lower panel*: synthetic spectrum computed with here determined parameters:$T_{\rm eff}$ = 6600 K and log$g$ = 4.5 for the primary component, $T_{\rm eff}$ = 6500 K and log$g$ = 4.6 for the secondary.

6.4.3 CD-39 10292

CD-39 10292 (= RX J1603.9-3938) is a PMS binary system classified as a SB2 by Wichmann et al. (1999) and located at a distance of ≈70 pc. It consists of two WTTS stars, both of spectral type between K3 and K4 Guenther et al. (2001) (hereafter G01). The system was independently studied by Melo et al. (2001) (hereafter M01) and G01. Both authors determined a circular orbit with a period of about 7.5 days and a mass ratio of ∼0.936. From the

evolutionary models by D'Antona & Mazzitelli, M01 attributed 1.1 $M_\odot$ and 0.9 $M_\odot$ at primary (A) and secondary (B) component, respectively, and a system age of 7 Myr. Moreover, M01 measured the Li I λ6708 $\mathring{A}$ intrinsic equivalent widths $EW(\mathrm{Li})_\mathrm{A}$ = 420 m$\mathring{A}$ and $EW(\mathrm{Li})_\mathrm{B}$ = 390 m$\mathring{A}$, corresponding to $\mathrm{A(Li)_A} \sim$ 3.2 and $\mathrm{A(Li)_B} \sim$ 2.9.
Under the hypothesis of $\mathrm{M_A}$=1.0 $M_\odot$, G01 gave an age estimation from Siess et al. (2000) evolutionary models of 10-20 Myr for the primary and ∼30 Myr for the secondary.

I have analyzed six FEROS spectra of CD-39 10292 from the ESO Archive, obtained on April, 2007.

Orbital solutions - From a gaussian fit of the line FeI λ6663.447 Å, I derived rotational velocities v sin i = 10 and 7 km $\mathrm{s^{-1}}$ for primary and secondary component respectively, and radial velocities plotted in Fig. 6.4 together with G01 measurements. I derived for this system an orbital period P = 7.56 days, barycenter velocity γ = 1.8 km $\mathrm{s^{-1}}$, velocity semi-amplitudes $K_\mathrm{A} = 40.6 \pm 0.9$ km $\mathrm{s^{-1}}$ and $K_\mathrm{B} = 43.4 \pm 0.90$ km $\mathrm{s^{-1}}$, anomaly $\omega = 0.0^\mathrm{o}$, eccentricity e = 0.0 and T0 = 51208.47 days.

Physical parameters - From the spectrum obtained during the night 2007 April 9, having S/N = 35, I estimated $\mathrm{T_{eff}}$ = 4600 and 4300 K for primary and secondary component respectively, and log$g$ = 4.0 for both. A veiling of ∼20% has been detected. In Fig. 6.5 and Fig. 6.6 is shown a comparison between the spectrum fitted with my data and the values from M01.
Through a gaussian fit of the Li I λ6708 Åline I derived the lithium observed equivalent widths for the two components, $EW_\mathrm{A}^\mathrm{obs}$ = 233 mÅ and $EW_\mathrm{B}^\mathrm{obs}$ = 178 mÅ̇The correction for luminosity ratio led to the intrinsic values $EW_\mathrm{A}^\mathrm{intr}$ = 387 mÅ and $EW_\mathrm{B}^\mathrm{intr}$ = 448 mÅ which correspond to lithium abundances $A_\mathrm{A}(\mathrm{Li}) = 2.84 \pm 0.13$

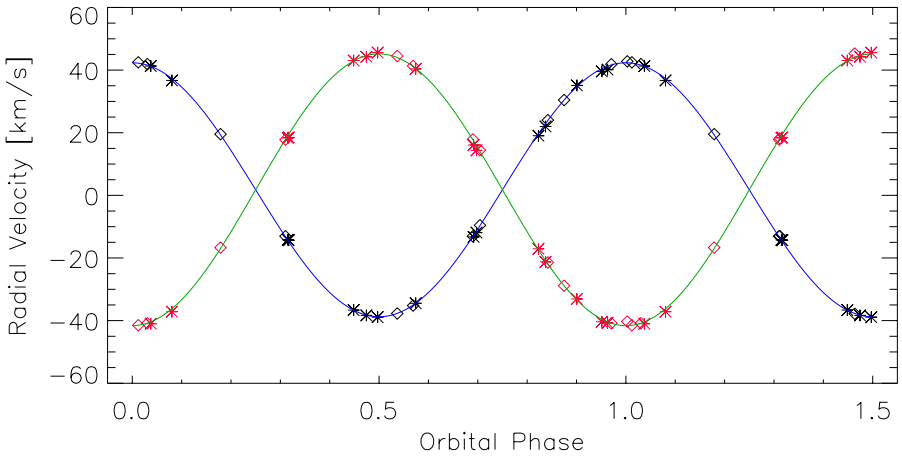

Figure 6.4: CD-39 10292 radial velocity curve. Data for primary (black) and secondary (red) component are from Guenther et al. (2001). The star symbols indicate values I obtained from the FEROS spectra.

and $A_{\rm B}$(Li) = 2.76 ± 0.15 according to the NLTE computations by Lind et al. (2009).

6.4.4 CoRoT 223992193

CoRoT 223992193 (= 2MASS J06414422+0925024) is a double-lined, detached eclipsing binary systems, consisting on two PMS stars of spectral type M2 and belonging to the 3Myr old NGC 2264 star-forming region (Gillen et al. 2014, hereafter Gil14). King et al. (2000) deduced an iron abundance of ∼ -0.15 ± 0.09 for NGC 2264, so I assumed this value to derive the metallicity of the system. Gil14 derived a period P∼3.87 days and dynamical masses 0.67 and 0.495 for primary and secondary component, respectively. The authors measured the equivalent width of the LiI 6708 Å line, i.e. $EW(\mathrm{Li})_{\rm A}$ = 560 ± 10 mÅ and $EW(\mathrm{Li})_{\rm B}$ = 550 ± 20. I converted these quantities into A(Li) by means of the NLTE computations by Pavlenko & Magazzú (1996), obtaining

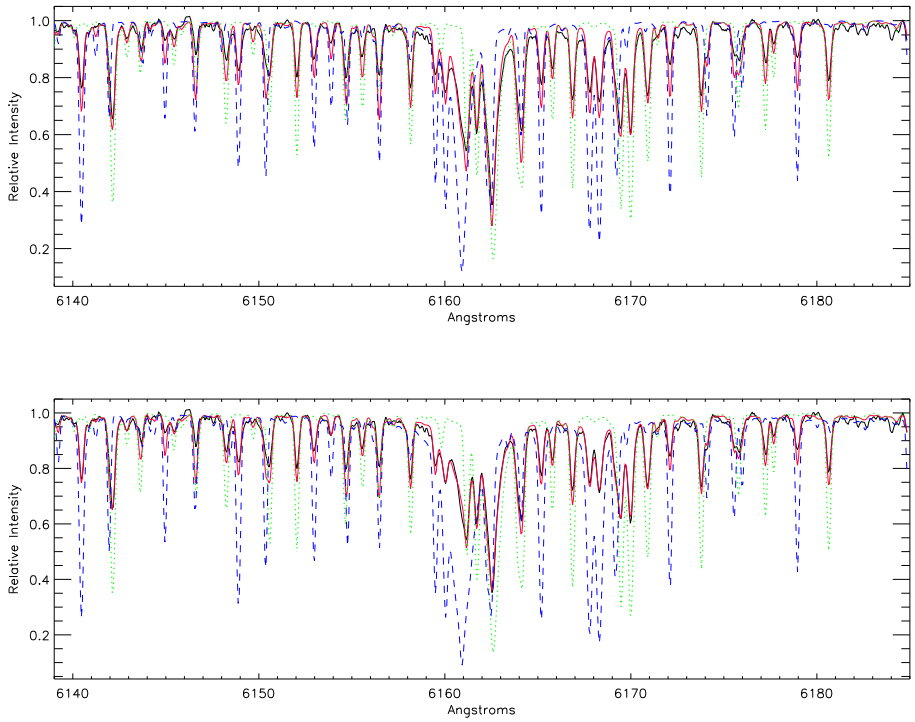

Figure 6.5: CD-39 10292. Observed (black) FEROS spectrum in the Ca I λ6162 Å region. - *Upper panel*: synthetic (red) spectrum computed with Melo et al. (2001) parameters, see text, for primary (green) and secondary (blue) component. - *Lower panel*: synthetic spectrum computed with here determined parameters: ∼20% veiling, T_{eff} = 4600 K and log$g$ = 4.0 for the primary component, T_{eff} = 4300 K and log$g$ = 4.0 for the secondary.

∼2.3 and 1.8 for primary and secondary component, respectively.

6.4.5 GSC 06213-00306

GSC 06213-00306 (= BD-21 4301) is a PMS double-lined spectroscopic binary system, classified as a Weak T-Tauri Star (WTTS) and located in the Scorpius Centaurus star forming region (age ∼ 11 - 17 Myr). The spectrum of this system shows Li I 6708 Å absorption line and variable filled Hα-line, as reported by Guenther

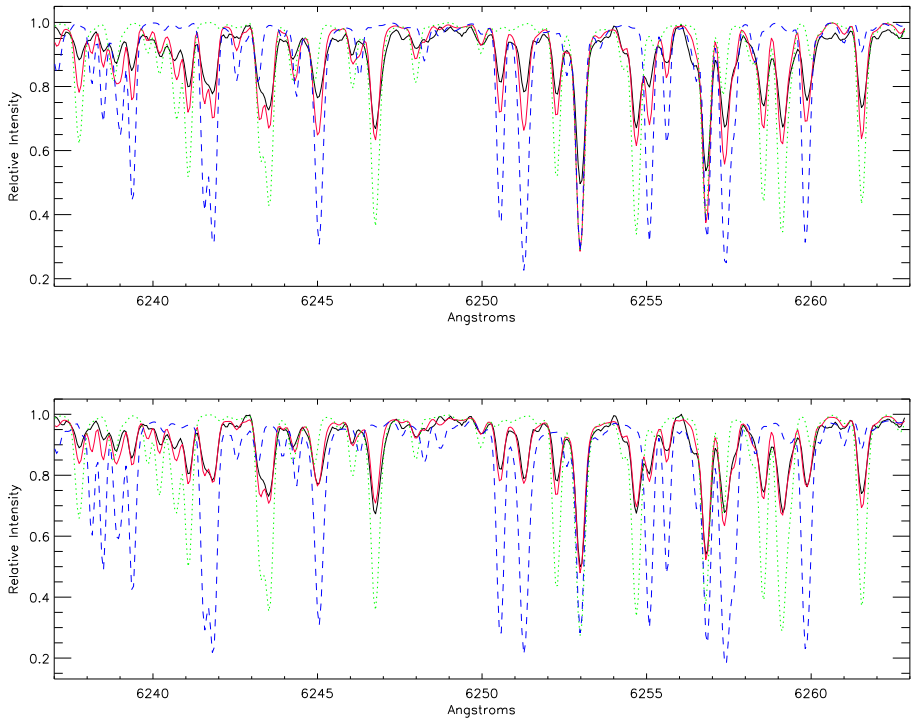

Figure 6.6: CD-39 10292. Observed (black) FEROS spectrum the range including V I λ6251.83 Å and Fe I λ6252.57 Å lines. - *Upper panel*: synthetic (red) spectrum computed with Melo et al. (2001) parameters, see text, for primary (green) and secondary (blue) component. - *Lower panel*: synthetic spectrum computed with here determined parameters: $\sim$20% veiling, $T_{\rm eff}$ = 4600 K and log$g$ = 4.0 for the primary component, $T_{\rm eff}$ = 4300 K and log$g$ = 4.0 for the secondary.

et al. (2007, hereafter G07). The authors observed $EW(\mathrm{Li})_{\mathrm{A}} = 241 \pm 4$ mÅ and $EW(\mathrm{Li})_{\mathrm{B}} = 180 \pm 4$ mÅ, while the Hα-line appears sometimes as an emission line with $EW(\mathrm{H}\alpha)$ = -0.1 and other times as an absorption line with $EW(\mathrm{H}\alpha) = 0.1$.

G07 also determined the orbital elements of both components, founding a period of 166.9 ± 0.1 days and a mass ratio $\sim 0.97 \pm 0.01$. The authors don't provide an estimation for physical parameters.

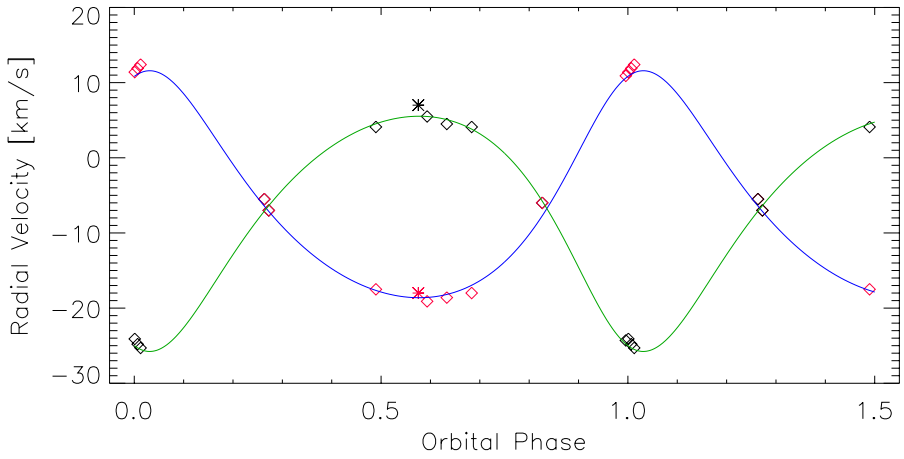

Figure 6.7: GSC 06213-00306 radial velocity curve. Data for primary (black) and secondary (red) component are from Guenther et al. 2007. The star symbol indicate the values I measured from the FEROS spectrum.

I have taken from the ESO Archive the only available FEROS spectrum of GSC 06213-00306, obtained on May 2, 2007.

Orbital solutions - From a gaussian fit of the line Fe I λ6663.447 Å, the rotational velocities result 19.6 km s^{-1} for primary and 13.4 km s^{-1} for secondary component. I derived the orbital period $P = 168.7 \pm 0.1$ days, barycenter velocity $\gamma = -6.49$ km s^{-1}, velocity semi-amplitudes $K_{\rm A} = 15.3 \pm 0.1$ km s^{-1} and $K_{\rm B} = 15.4 \pm 0.1$ km s^{-1}, anomaly $\omega = 162.5^{\rm o}$, eccentricity $e = 0.23$ and T0 = 52124.607 days.
Fig. 6.7 shows the radial velocity curve of GSC 06213-00306 with data from G07 and this work.

Physical parameters - The spectrum I analyzed, of $S/N = 123$, allows me to estimate for the primary star $T_{\rm eff} = 5500$ K and log$g$ = 4.6, while for the secondary $T_{\rm eff} = 5100$ K and log$g = 4.5$. The system has solar metallicity and the spectrum presents a veiling

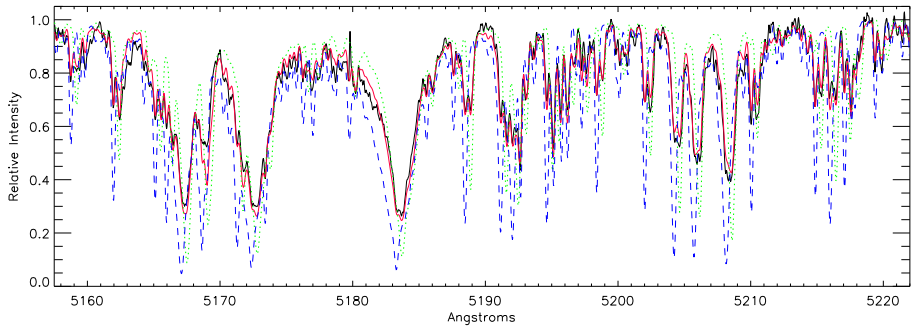

Figure 6.8: GSC 06213-00306. Observed (black) FEROS spectrum in the Mg I b lines region. The synthetic (red) spectrum is computed with here determined parameters: ∼5% veiling, T_{eff} = 5500 K and log$g$ = 4.6 for the primary (green) component, T_{eff} = 5100 K and log$g$ = 4.5 for the secondary (blue).

of ∼5%. The spectrum fitted with my data is shown in Fig. 6.8 and Fig. 6.9.

A double gaussian fit of the Li I λ6708 Åline provided $EW_{\rm A}^{\rm obs}$ = 216 mÅ and $EW_{\rm B}^{\rm obs}$ = 185 mÅ̇The corrected values $EW_{\rm A}^{\rm intr}$ = 411 mÅ and $EW_{\rm B}^{\rm intr}$ = 390 mÅ correspond to very high abundances $A_{\rm A}$(Li) = 3.88 ± 0.09 and $A_{\rm B}$(Li) = 3.40 ± 0.11 according to the NLTE table of Lind et al. (2009).

6.4.6 HD 34700 A

HD 34700 (= HIP 24855 = IRAS 05170+0535 = SAO 112630) is a quadruple system consisting of a central double-lined spectroscopic binary (Arellano et al. 2003) with both stars of spectral type G0 IVe (Mora et al. 2001) and two faint, young, visual stars of spectral type M1-2 and M3-4 (Sterzik et al. 2005, hereafter S05) .

By referring to the central SB2 system (here Aa and Ab components), its membership to the PMS stage is spectroscopically

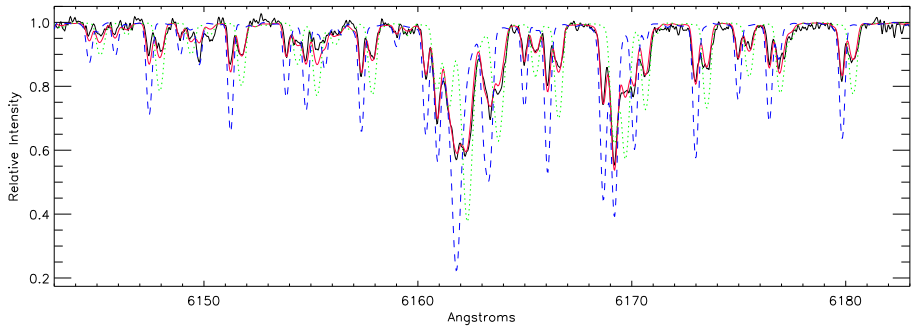

Figure 6.9: GSC 06213-00306. Observed (black) FEROS spectrum in the Ca I λ6162 Å region. The synthetic (red) spectrum is computed with here determined parameters: $\sim$5% veiling, T_{eff} = 5500 K and log$g$ = 4.6 for the primary (green) component, T_{eff} = 5100 K and log$g$ = 4.5 for the secondary (blue).

inferred from a strong infrared excess, presence of the Li I λ6708 absorption line, strong X-ray emission and Hα emission line of equivalent width 0.6 $\mathring{A}$ (both emissions characteristics of Weak-lined T Tauri stars, WTTSs). The equivalent width of Li I λ6708 line (0.15 $\mathring{A}$ by S05, 0.17 $\mathring{A}$ by Torres 2004, hereafter T04) is weaker than the typical values for T Tauri. This is justified by the higher $T_{\rm eff}$ with respect to the T Tauri one and by a probable presence of veiling.

The system is located in the direction of Orion, but its distance has not yet been measured and so it is not possible to determine the age from model isochrones. Anyway, a maximum limit of 10 Myr was suggested by Zuckerman, Forveille, & Kastner (1995) on the basis of circumstantial evidences.

T04 tried to derive the age from A(Li) only, by comparing diagrams of lithium equivalent width versus temperature and found an upper limit of about 100 Myr. This implies that the system could be at the end of the T Tauri stage.

The two stars move in a very eccentric orbit, e = 0.2501, with period P = 23.4877 days (see T04). S05 have given projected

rotational velocity v $\sin i = 23.3 \pm 0.6$ km s^{-1} and 21.7 ± 0.6 km s^{-1} for primary and secondary component respectively.
I observed this system at the 0.91 m telescope of Serra la Nave with CAOS spectrograph, for six night between October and November 2014, obtaining four useful spectra.
In addition, I took one FEROS spectrum from the ESO Archive, obtained on 4 February, 2008.

Orbital solutions - From a gaussian fit of the line Ca I λ6122.213 Å, I determined rotational velocities of 46 km s^{-1} for the primary and 35 km s^{-1} for the secondary star. The radial velocities I measured for all five spectra, together with the ones in T04, allowed me to derive orbital period $P = 23.48$ days, barycenter velocity $\gamma = 21.2$ km s^{-1}, velocity semi-amplitudes $K_{\rm Aa} = 38.8$ km s^{-1} and $K_{\rm Ab} = 39$ km s^{-1}, anomaly $\omega = 359.6^{\rm o}$, eccentricity $e = 0.24$ and T0 = 51072.668.
Fig. 6.10 shows the radial velocity curve of HD 34700 A obtained by data from this work together with measurements from T04.

Physical parameters - From the spectrum I selected and analyzed ($S/N = 75$) I estimate for the primary component $T_{\rm eff} = 6400$ K and log$g = 4.0$, and for the secondary star $T_{\rm eff} = 6300$ K and log$g = 4.0$. The system has solar metallicity and no veiling has been detected. Observed spectrum and synthetic one with physical parameters derived here and from T04 is shown in Fig. 6.11 and Fig. 6.12.
Observed equivalent width of the Li I λ6708 Åline, $EW^{\rm obs}_{\rm Aa} = 41$ mÅ and $EW^{\rm obs}_{\rm Ab} = 59$ mÅ have been corrected, $EW^{\rm intr}_{\rm Aa} = 79$ mÅ and $EW^{\rm intr}_{\rm Ab} = 122$ mÅ providing lithium abundances $A_{\rm Aa}({\rm Li}) = 3.00 \pm 0.07$ and $A_{\rm Ab}({\rm Li}) = 3.19 \pm 0.07$ from the NLTE table of Lind et al. (2009).

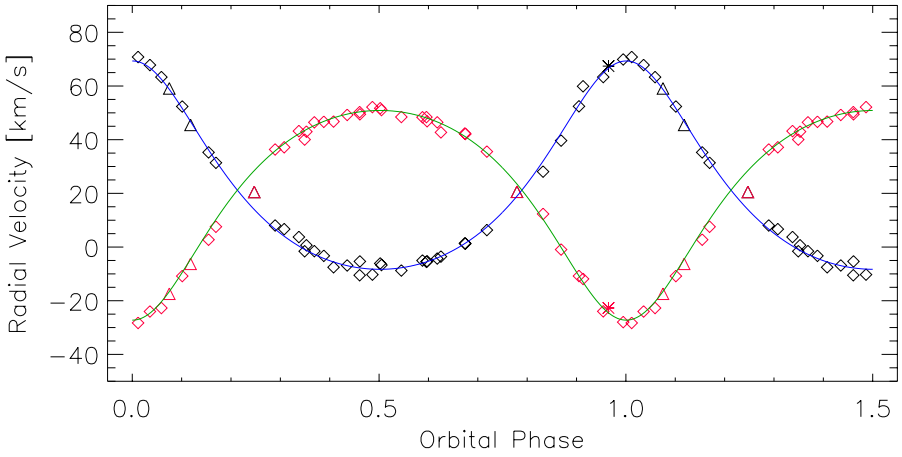

Figure 6.10: HD 34700 A radial velocity curve. Data for primary (black) and secondary (red) component are from this work (star symbol for FEROS spectrum, triangle for CAOS spectra) and Torres (2004).

6.4.7 HD 98800 B

HD 98800 (= HIP 55505 = TWA 4) is a quadruple system located at a distance of 44.9 ± 4.6 pc (van Leeuwen 2007, Boden et al. 2005) and belonging to the TW Hydra association (Kastner et al. 1997).

It appears as a visual binary (Innes 1909) with separation of components of 0.848 arcsec in 2001 (Prato et al. 2001) and orbital period $P \sim$ 300 - 430 yr (Tokovinin 1999). Each component is itself a binary system: the southern, brighter one, HD 98800 A, is a single-lined spectroscopic binary with orbital period $P_A \sim$ 262 days (Torres et al. 1995); the northern, fainter one, HD 98800 B, is a double-lined spectroscopic binary with orbital period $P_B \sim$ 315 days (Torres et al. 1995; Boden et al 2005, hereafter B05; Laskar et al. 2009, hereafter L09). As a result, the spectrum of HD 98800 is the sum of the spectra of the three components Aa, Ba, Bb. Soderblom et al. (1998) derived lithium abundance A(Li)$_{Aa}$ ∼3.1, A(Li)$_{Ba}$ ∼2, A(Li)$_{Bb}$ ∼3. On the basis of A(Li),

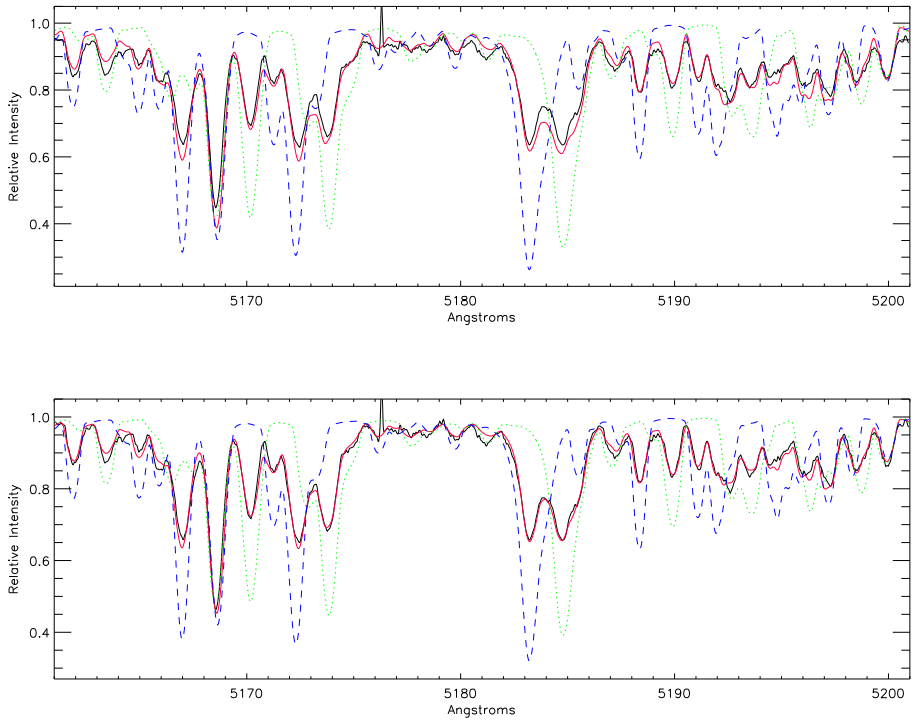

Figure 6.11: HD 34700 A. Observed (black) CAOS spectrum in the Mg I b lines region. - *Upper panel*: synthetic (red) spectrum computed with T04 parameters, see text, for primary (green) and secondary (blue) component. - *Lower panel*: synthetic spectrum computed with here determined parameters: T_{eff} = 6400 and log$g$ = 4.0 for the primary component, T_{eff} = 6300 K and log$g$ = 4.0 for the secondary.

the authors claimed a system age between 5-20 Myr, with a most probable value of 10 Myr.

Anyway, the system doesn't exhibit strong activity as well as H_α emission despite its youth. The authors also measured rotational velocity v sin i = 5.0, 3.0, 0.0 km s^{-1} for Aa, Ba and Bb component respectively. L09 derived a subsolar metallicity [M/H] = -0.20 $\pm$ 0.10.

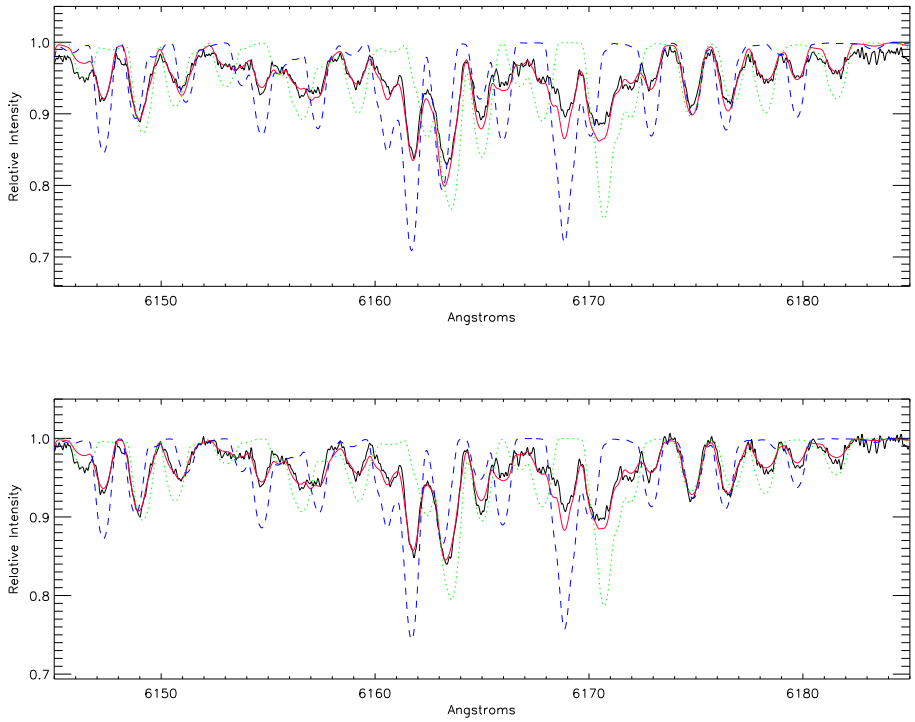

Figure 6.12: HD 34700 A. Observed (black) CAOS spectrum in the Ca I λ6162 Å region. - *Upper panel*: synthetic (red) spectrum computed with T04 parameters, see text, for primary (green) and secondary (blue) component. - *Lower panel*: synthetic spectrum computed with here determined parameters: T_{eff} = 6400 and log$g$ = 4.0 for the primary component, T_{eff} = 6300 K and log$g$ = 4.0 for the secondary.

6.4.8 HD 155555

HD 155555 (= IRAS 17121-6653 = HIP 84586 = V824 Ara) is a double-lined short-period (P = 1.68 days) PMS binary system. It consists on primary star of spectral type G5 IV and secondary star of spectral type K0 IV with solar metallicity (Dunstone et al. 2008, hereafter D08).

Both components present H_α and strong Ca II H and K emission (e.g. Dempsey et al. 1993), and very high Li I λ6708 $\AA$ abundance, quantified by D08 as log$N$(Li) = 3.16 and 3.15 for primary

and secondary respectively. These values allowed the authors to confirm the youth of this system and to estimate an age between 0 and 30 Myr.
An age of 18 Myr was previously inferred from Stessmeier & Rice (2000) by means of Hipparcos distance (31 pc) and PMS evolutionary tracks of D'Antona & Mazzitelli (1997).

6.4.9 MML 53

MML 53 (= CD-35 9931 =RX J1458.6-3541 = TYC 7310-503-1) is a young low mass triple system of spectral type K2IVe, located in the 16±1 Myr old Upper Centaurus Lupus (UCL) subassociation (with a probability of 93%), at a distance of 136^{+16}_{-13} pc from us (Mamajek et al. 2002). James et al. inferred for UCL $[Fe/H] = -0.10 \pm 0.04$.
Spectroscopic observations (Hebb et al. 2010, hereafter H10) show a strong Li I λ6708 $\mathring{A}$ absorption (from which A(Li) = 3.2, 2.3 and 3.0 for primary, secondary and tertiary components, respectively) and Hα emission for the secondary and tertiary, leading to classify the system as a PMS object.
MML 53 is spatially unresolved; however the photometric data obtained by the SuperWASP survey together with the analysis of a single FEROS spectrum allowed H10 to discover a central eclipsing binary of mass ratio $q \sim 0.8$, in a circular orbit with period $P \approx 2.1$ days. Stempels & Hebb (2011) provided dynamical masses $M_A = 0.99\ M_\odot$ and $M_B = 0.86\ M_\odot$, and A(Li) = 3.1 and 3.2 for primary and secondary components, respectively.

6.4.10 PAR 1802

Parenago 1802 is a double lined, detached eclipsing binary belonging to the ∼1 Myr Orion Nebula Cluster (ONC). (Cargile et al. (2008) hereafter Carg08, Chew et al. (2012)) hereafter Gom12). Carg08 measured the orbital period P∼4.7 days and the equivalent width of Liı λ6708 $\mathring{A}$ line corrected for the difference in continuum fluxes, $EW_{\rm A}^{\rm corr} \sim 330$ mÅ and $EW_{\rm B}^{\rm corr} \sim 300$ mÅİ have converted these values into lithium abundances, A(Li) = 1.48 and 0.57 for primary and secondary component respectively, by means of the NLTE computations by Pavlenko & Magazzú (1996). In my analysis I have assumed the most recent physical parameters and dynamical mass estimations (∼0.39 $M_\odot$ and 0.38 $M_\odot$ for primary and secondary components, respectively) provided by Gom12.

6.4.11 RX J0529.4+0041 A

I have examined RX J0529.4+0041 A, an eclipsing binary that is part of the triple system RX J0529.4+0041. All the three stars belongs with an high probability to the Orion region and present high lithium abundance, so it's plausible to affirm that they are coeval stars in the PMS phase (Covino et al. 2004, hereafter C04). C04 estimate dynamical masses $M_{\rm A}$=1.27 $M_\odot$ and $M_{\rm B}$=0.93 $M_\odot$, a system distance of 325±15 pc and from the isochrone of the Swenson et al.'s derived an age of about 10 Myr. Covino et al. (2000) provided the corrected equivalent widths of the Liı λ6708 $\mathring{A}$ line, $EW_{\rm A}^{\rm corr} \sim 380$ mÅ and $EW_{\rm B}^{\rm corr} \sim 300$ mÅ that I have converted into lithium abundances A(Li) = 3.48 and 3.02 for primary and secondary component respectively, by means of the NLTE computations by Lind et al. (2009).

6.4.12 RX J0530.7-0434

RX J0530.7-0434 is a double lined spectroscopic binary located in the general direction of the Orion star forming region. Cov01 spectroscopically analyzed the system and derived very similar characteristics for the two components, which are probably two almost equal stars of spectral type between K2 and K3. The authors determined an orbital period of 13.5 days and amplitudes of radial velocity variations $K_{\rm A} = 47.51 \pm 0.21$ and $K_{\rm B} = 47.59 \pm 0.15$. Moreover, they derived a primordial lithium abundance A(Li) = 3.3 and 3.2 for primary and secondary component respectively. From their spectroscopic and photometric results, by comparing the position on the HR diagram of the two stars with isochrones from different authors, Cov01 concluded that this is a young bona fide PMS system with age of few Myr.

6.4.13 RX J0532.1-0732

RX J0530.7-0434 is a double lined spectroscopic binary located in the eastern edge of the Orion cloud A. Cov01 derived an orbital period of about 47 days, an orbital eccentricity e=0.47 and spectral type K2-K3 for the primary component, K3 for the secondary. The authors measured amplitudes of radial velocity variations $K_{\rm A} = 43.25 \pm 0.18$ and $K_{\rm B} = 45.61 \pm 0.15$ and lithium abundance A(Li) = 3.2 and 3.1 for primary and secondary component respectively. From their spectroscopic and photometric results, by comparing the position on the HR diagram of the two stars with isochrones from different authors, Cov01 claimed that this is a bona fide PMS binary with age between 3 and 5 Myr.

6.4.14 RX J0541.4-0324

RX J0530.7-0434 is a double lined spectroscopic binary that is seen projected very close to the Orion Nebula. Cov01 determined a circular orbit for the system with an orbital period of nearly 5 days and spectral type G8 for the primary component, K3 for the secondary. The authors measured amplitudes of radial velocity variations $K_{\rm A} = 65.16 \pm 0.10$ and $K_{\rm B} = 96.63 \pm 0.56$ and lithium abundance A(Li) = 3.1 and 2.9 for primary and secondary component respectively. From their spectroscopic and photometric results, by comparing the position on the HR diagram of the two stars with isochrones from different authors, Cov01 estimate for this system an age between 5 and 10 Myr and concluded that only the secondary component would be classified as a PMS star.

6.4.15 V773 Tau A

V773 Tau (= HD 283447 = HIP 19762 = IRAS 04111+2804) is a PMS quadruple system located at a distance of 136.2 ± 3.7 pc in the Taurus-Auriga star-forming region (Boden et al. 2007, hereafter B07). It was at first classified as a K2 spectral type (Herbig & Rao 1972) single T Tauri star on the basis of photometric variability, H_α and Ca II H and K emission and high surface lithium content (Rydgren et al. 1976). However, the star showed features of both Classical and Weak-lined T Tauri stars. Further studies revealed the multiplicity of the object, consisting of a central double-lined spectroscopic binary (V773 Tau A) with orbital period of 51 days (Welty 1995, hereafter W95) and of two additional components, here designed with B and C. V773 Tau A and B form a visual binary system (Ghez et al. 1993, Leinert et al. 1993). Duchene et al. (2003) classified both B and C components as CTTSs from their IR excess, while the optically brighter A component as a WTTS.

In this work I examined the SB2 subsystem V773 Tau A. It is a highly variable radio source (Kutner et al. 1987) and has been well studied from B07. By assuming solar metallicity and from analysis of low resolution (R = 35000) and low signal-to-noise ratios (S/Ns = 16-35) spectra, the authors derived effective temperature T_{eff}=4900 and 4700 K and surface gravity log$g$ = 3.9 and 4.1 for primary (Aa) and secondary (Ab) component respectively, and projected rotational velocity $v \sin i = 38 \pm 4$ km s^{-1} for Aa only (in agreement with the value by W95, i.e. $\sim$ 41 km s^{-1} for both stars). From radial velocity curve they obtained velocity semi-amplitudes $K_{\rm Aa}$ = 35.95 km s^{-1} and $K_{\rm Ab}$ = 41.6 km s^{-1}, which result in a mass ratio $M_{\rm Ab}/M_{\rm Aa}$ = 0.865. No presence of veiling has been claimed in their work.

By means of optical and radio interferometry the authors resolved the two stars and studied V773 Tau A as an astrometric system. Derived dynamical masses, 1.540 $M_\odot$ and 1.332 $M_\odot$ for primary and secondary component respectively, together with isochrones from Yonsei-Yale (Demarque et al. 2004) and Montalban & D'Antona models (2006), allowed B07 to infer an age of 3 $\pm$ 1 Myr.

By SED modeling, taking into account the derived effective temperatures, they obtained an estimation for radii ($R_{\rm Aa} = 2.22 \pm 0.20 R_\odot$, $R_{\rm Ab} = 1.74 \pm 0.19 R_\odot$) and luminosities ($L_{\rm Aa} = 2.56 \pm 0.35 L_\odot$, $L_{\rm Ab} = 1.37 \pm 0.15 L_\odot$) of each component.

Regarding to lithium abundance W95 measured intrinsic equivalent widths $EW_{\rm Aa}$ = 422 mÅ and $EW_{\rm Ab}$ = 483 mÅ of the Li I λ6708 absorption line.

Anyway, in my work I considered this system as a SB2, since the mass determinations from Boden et al. (2007) rely on their measured physical parameters, which are very different from those I have obtained, as showed below.

I spectroscopically analyzed V773 Tau A by means of a high-

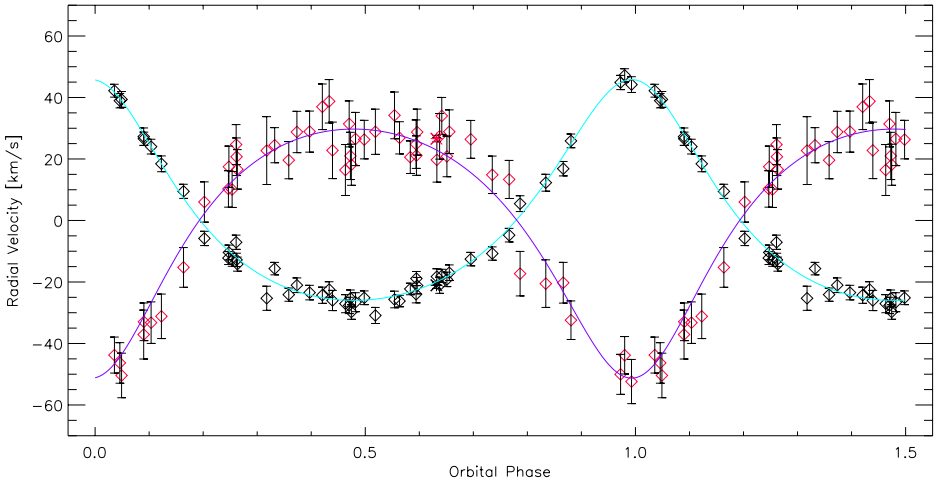

Figure 6.13: V773 Tau A radial velocity curve. Data for primary (black) and secondary (red) component are from Boden et al. (2007). The star symbol indicate values I obtained from the HARPS-North spectrum.

resolution HARPS-N spectrum that I obtained at TNG on August 4, 2014.

Orbital solutions - I determined radial velocities of the two components from the HARPS-North spectrum that are showed in Fig. 6.13 together with the data of Boden et al. (2007). As claimed by the authors, this system has orbital period $P = 51.1$ days, baricenter velocity $\gamma = 0.02$ km s^{-1}, velocity semiamplitudes $K_{\rm Aa} = 35.9$ km s^{-1} and $K_{\rm Ab} = 41.5$ km s^{-1}, anomaly $\omega = 63.5^{\rm o}$, eccentricity $e \sim 0.27$ and T0 =53059.73.

Physical parameters - I measured rotational velocities $v_{\rm Aa} \sin i = 68.1 \pm 0.5$ km s^{-1} and $v_{\rm Ab} \sin i = 63.1 \pm 0.5$ km s^{-1}. From the best fitting between observed and synthetic spectra with solar metallicity I obtained effective temperature $T_{\rm eff}$= 4700 K and 4100 K for primary and secondary component respectively, and surface gravity $\log g = 3.7$ for both stars. A veiling of ∼15% has been estimated. I measured the equivalent widths of the Li I λ6708

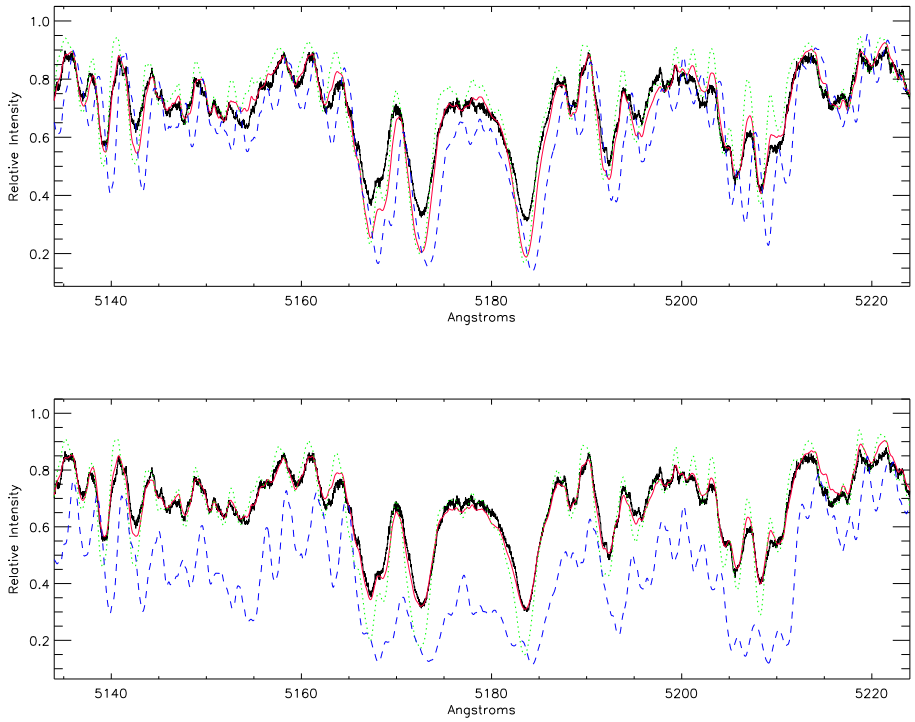

Figure 6.14: V773 Tau A. Observed (black) HARPS-North spectrum in the Mg I b lines region. - *Upper panel*: synthetic (red) spectrum computed with Boden et al. (2007) parameters, see text, for primary (green) and secondary (blue) component. - *Lower panel*: synthetic spectrum computed with here determined parameters: ∼15% veiling, $T_{\rm eff}$ = 4700 and log$g$ = 3.7 for the primary component, $T_{\rm eff}$ = 4100 K and log$g$ = 3.7 for the secondary.

line from a double-gaussian fit, $EW^{\rm obs}_{\rm Aa}$ = 381 mÅand $EW^{\rm obs}_{\rm Ab}$ = 162 mÅ. Correction for luminosity ratio of the two best resulting synthetic spectra leads to the intrinsic values $EW^{\rm intr}_{\rm Aa}$ = 545 mÅand $EW^{\rm intr}_{\rm Ab}$ = 539 mÅ, which correspond to lithium abundances $A_{\rm Aa}$(Li) = 3.65±0.42 and $A_{\rm Ab}$(Li) = 2.89±0.21 according to the NLTE computations by Lind et al. (2009).

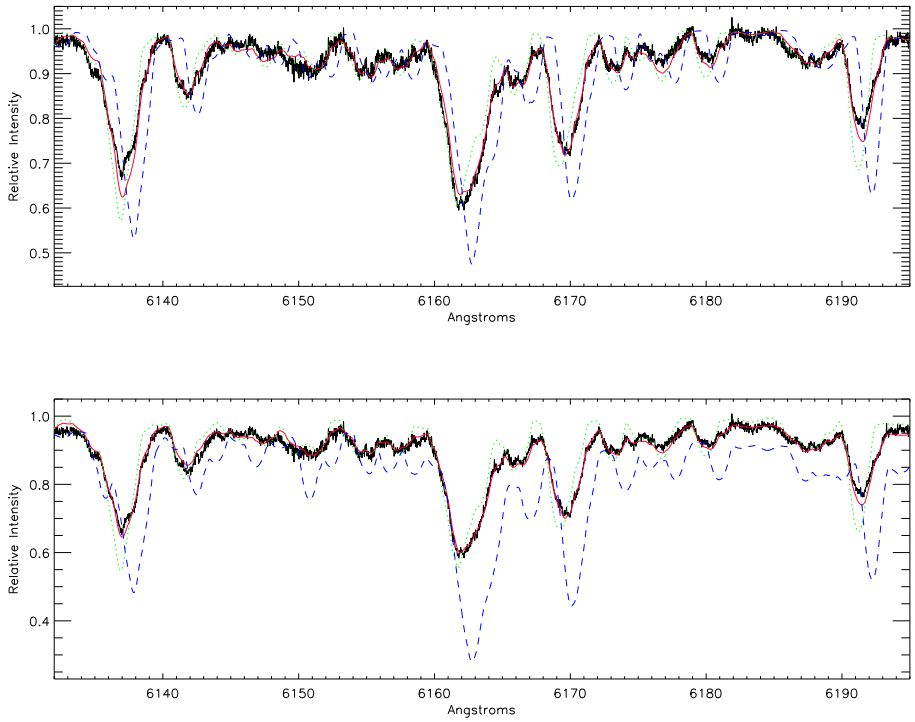

Figure 6.15: V773 Tau A. Observed (black) HARPS-North spectrum in the Ca I λ6162 Å region. - *Upper panel*: synthetic (red) spectrum computed with Boden et al. (2007) parameters, see text, for primary (green) and secondary (blue) component. - *Lower panel*: synthetic spectrum computed with here determined parameters: ∼15% veiling, $T_{\rm eff}$ = 4700 K and log$g$ = 3.7 for the primary component, $T_{\rm eff}$ = 4100 K and log$g$ = 3.7 for the secondary.

6.4.16 V1174 Ori

V1174 Ori (= RX J053425.7-054133) is a double-lined, spectroscopic, PMS eclipsing binary located in the Orion star-forming region (Stassun et al. (2004), hereafter S04) . From spectroscopic and photometric analysis, the authors attributed spectral types K4.5 and ∼M1.5 to primary (A) and secondary (B) components, respectively. They also derived a period of 2.634727 days, a distance of ∼400 pc and distance-independent measurements

for mass and radius ($\sim$ 1.01 $M_\odot$ and 1.34 $R_\odot$ for the primary, 0.73 $M_\odot$ and 1.06 $R_\odot$ for the secondary).
Authors provided the corrected equivalent widths of the LiI λ6708 $\AA$ line, $EW_{\rm A}^{\rm corr} \sim 480$ mÅ and $EW_{\rm B}^{\rm corr} \sim 537$ mÅ that I have converted into lithium abundances $A_{\rm A}({\rm Li}) = 3.11$ and $A_{\rm B}({\rm Li}) = 2.07$ by means of the NLTE computations by Pavlenko & Magazzú (1996).
By comparing the empirically derived stellar dimensions with a variety of PMS evolutionary models, S04 attributed to the system an age in the range $\sim$5-10 Myr. Moreover, they noted that models with lower convection parameter (i.e. $\alpha = 1$) better agreed with their measurements.

6.4.17 V4046 Sgr

V4046 Sagittarii is a double-lined spectroscopic binary system, classified as a CTTS. Quast et al. (2000) derived a short period of $\sim$2.42 days and an age between 4-7 Myr, as well as $K_{\rm A} = 51.82$ km s^{-1} and $K_{\rm B} = 54.89$ km s^{-1} from radial velocity curve. Stempels et al. (2004) derived $T_{\rm eff}$ = 4370 K and log$g$=4.0 for primary component, $T_{\rm eff} = 4100$ K and log$g$=4.0 for secondary component, and claimed a veiling of about $\sim$5-15% in the red part of the spectrum ($\lambda \sim 6000 - 6700$ Å). Recently Rosenfeld et al. (2012) estimate disk-based dynamical masses of 0.90 $M_\odot$ and 0.85 $M_\odot$ for primary and secondary component, respectively.

I spectroscopically analyzed this V4046 Sgr by means of an ESPaDONs spectrum taken from the CFHT Archive. The spectrum has been obtained on September 9, 2009.
Since no radial velocities data are reported from Quast et al. (2000), I could not derive orbital parameters.

Physical parameters - I measured rotational velocities $v_{\rm A} \sin i =$

22.0 ± 0.5 km s^{-1} and $v_{\rm Ab} \sin i = 21.4 \pm 0.5$ km s^{-1}. From the best fitting between observed and synthetic spectra with solar metallicity I obtained effective temperature $T_{\rm eff}$= 4400 K and 4100 K for primary and secondary component respectively, and surface gravity $\log g = 4.0$ for both stars, values in good accord with Stempels et al. (2004). I estimated a veiling between ∼15% and 20%. I measured the equivalent widths of the Li I λ6708 Å line from a double-gaussian fit, $EW_{\rm A}^{\rm obs} = 260$ mÅ and $EW_{\rm B}^{\rm obs} =$ 194 mÅ. Correction for luminosity ratio of the two best resulting synthetic spectra leads to the intrinsic values $EW_{\rm Aa}^{\rm intr} = 431$ mÅ and $EW_{\rm A}^{\rm intr} = 488$ mÅ, which correspond to lithium abundances $A_{\rm Aa}({\rm Li}) = 2.82$ and $A_{\rm B}({\rm Li}) = 2.65$ according to the NLTE computations by Lind et al. (2009).

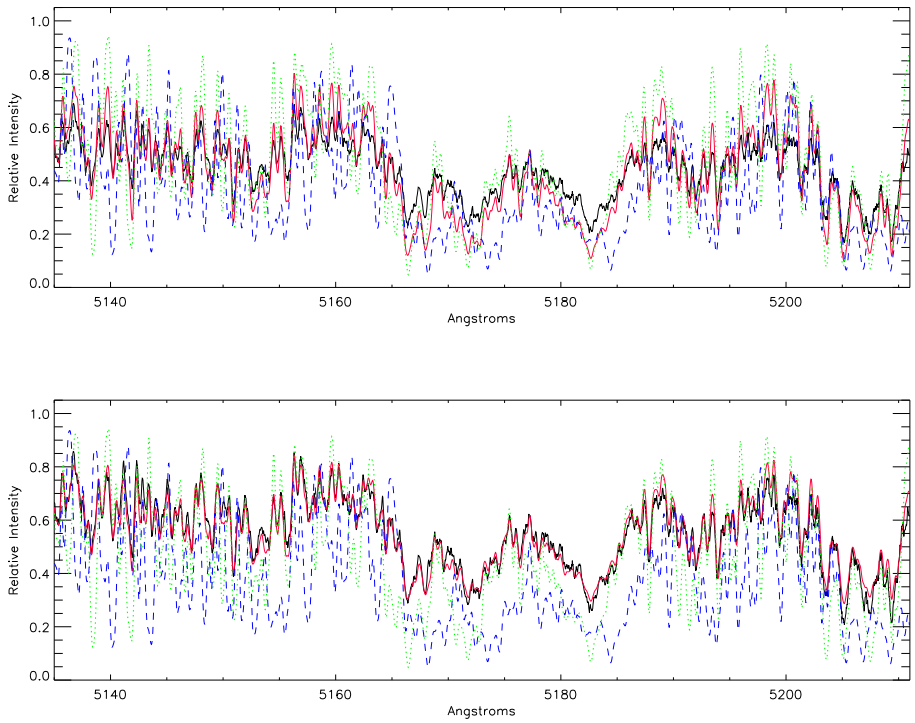

Figure 6.16: V4046 Sgr. Observed (black) HARPS-North spectrum in the Mg I b lines region. - *Upper panel*: synthetic (red) spectrum computed with Stempels et al. (2004) parameters, see text, for primary (green) and secondary (blue) component. - *Lower panel*: synthetic spectrum computed with here determined parameters: ∼15% veiling, T_{eff} = 4400 and log$g$ = 4.0 for the primary component, T_{eff} = 4100 K and log$g$ = 4.0 for the secondary.

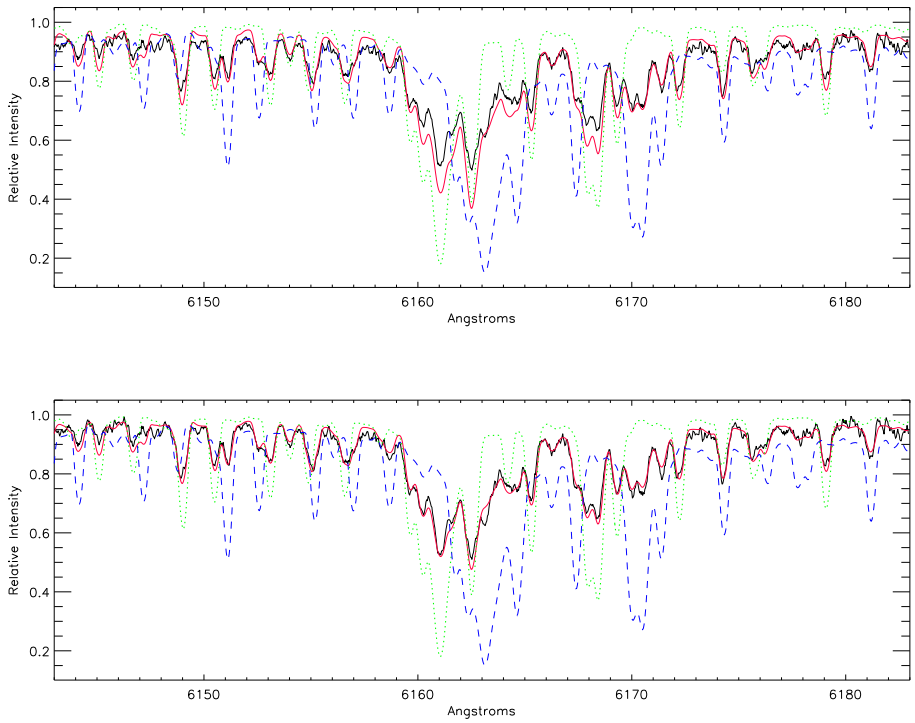

Figure 6.17: V4046 Sgr. Observed (black) HARPS-North spectrum in the Ca I λ6162 Å region. - *Upper panel*: synthetic (red) spectrum computed with Stempels et al. (2004) parameters, see text, for primary (green) and secondary (blue) component. - *Lower panel*: synthetic spectrum computed with here determined parameters: $\sim$15% veiling, $T_{\rm eff}$ = 4700 K and log$g$ = 4.0 for the primary component, $T_{\rm eff}$ = 4100 K and log$g$ = 4.0 for the secondary.

CHAPTER 7

Results

In this chapter I present star by star the results of the bayesian analysis.

Since for the SB2 systems the masses of the two components are not known *at priori*, applying the bayesian analysis with the mass ratio, on models computed with different mixing lengths, different values of age are expected. For the first time, it appears possible to determine this invisible parameter as the one whose age is in agreement with the lithium age. The associated masses are assumed as representative of the system.

Graphical outputs is here presented only for a system whose dynamical masses are known, CoRoT 223992193, and the SB2 system CD-39 10292. For an easier reading of this chapter, graphycs for the other stars are shown in Appendix A with the same layout.

Tables 6.3 and 6.5 list bayesian results for the mass of each star, at different values of mixing length, together with the limits from the confidence interval.

Tables 6.4 shows bayesian results for the age of systems whose dynamical masses are known. The single age of the star each system, together with the age system (coevality) are listed. Any value is reported with the limits from the confidence interval.
Tables 6.6 shows bayesian results for the coevality of the SB2 systems in exam, together with the limits from the confidence interval.

7.1 CD-39 10292

The bayesian estimations for the masses of primary and secondary components for different mixing lenght range between ∼1-1.5 $M_\odot$ and ∼0.95-1.4 $M_\odot$ respectively, with decreasing values for increasing α.The bayesian estimation for the age-system ranges in the interval ∼2-6 Myr, with decreasing values for increasing α.
For the primary component, mass values obtained for low mixing lenght, i.e. α= 0.80, 1.00 and 1.25 are too high for strongly deplete lithium (Fig. 7.3). The depletion is slightly stronger for the mass 1.14 $M_\odot$ found for α=1.50, but there is yet no macth with the observed lithium. The better case appears for mixing lenght 1.74: the upper limit of the observed lithium abundance provides an age of ∼8 Myr. This values, anyway, doesn't match with the bayesian one, that is between 2-3 Myr.
A similar trend is shown in Fig. 7.4 for the secondary component. In this case, however, for α=1.74 the central value of the observed lithium also provides an age estimation of ∼10 Myr for the lower mass limit (0.89 $M_\odot$).
Such a situation suggests to increase the mixing lenght value, in contrast to what claimed in literature (Tognelli et al. 2012), in order to find a real accord between theoretical and lithium age.

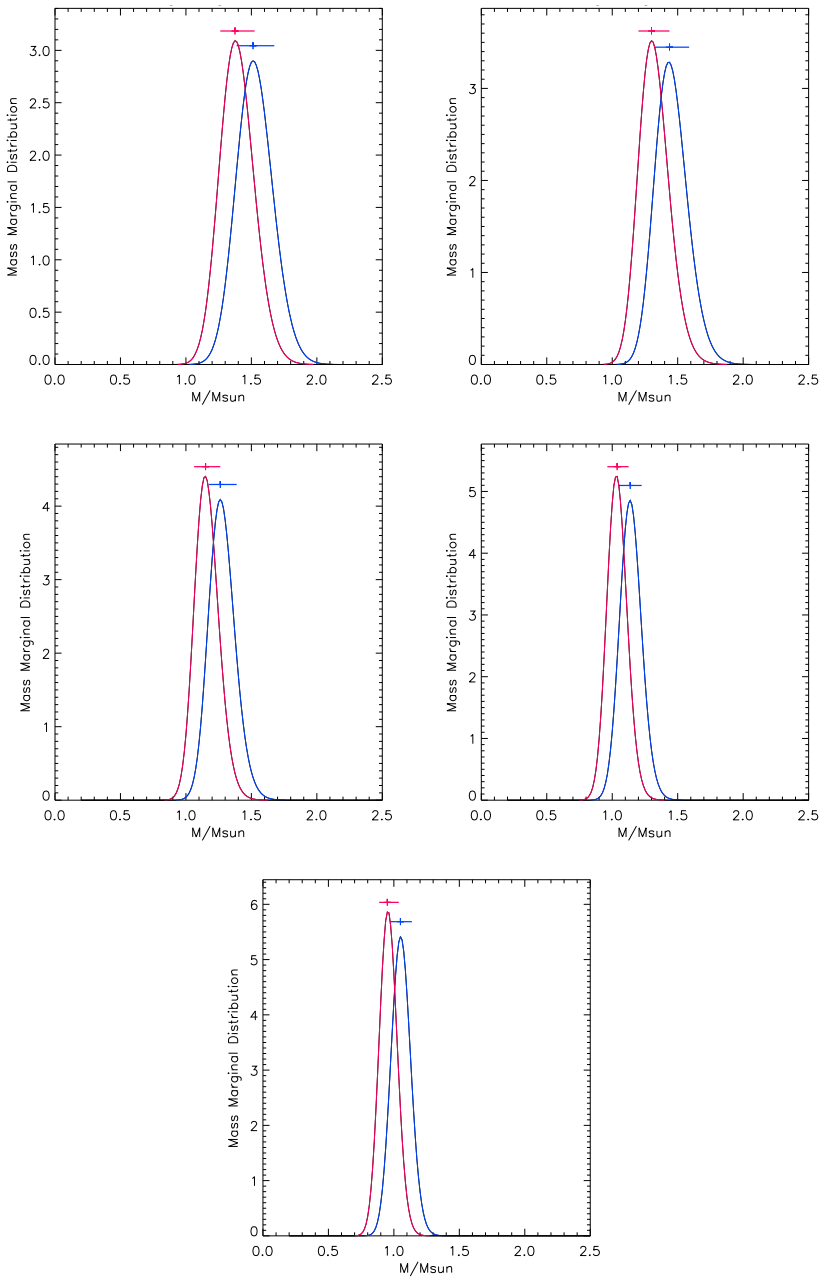

Figure 7.1: CD-39 10292 Mass Marginal Distribution for primary (blue) component and secondary (red) component. Top left panel shows the results for mixing length $\alpha = 0.80$, top right for $\alpha = 1.00$, middle left for $\alpha = 1.25$, middle right for $\alpha = 1.50$ and bottom panel for $\alpha = 1.74$. Horizontal line represents the confidence interval.

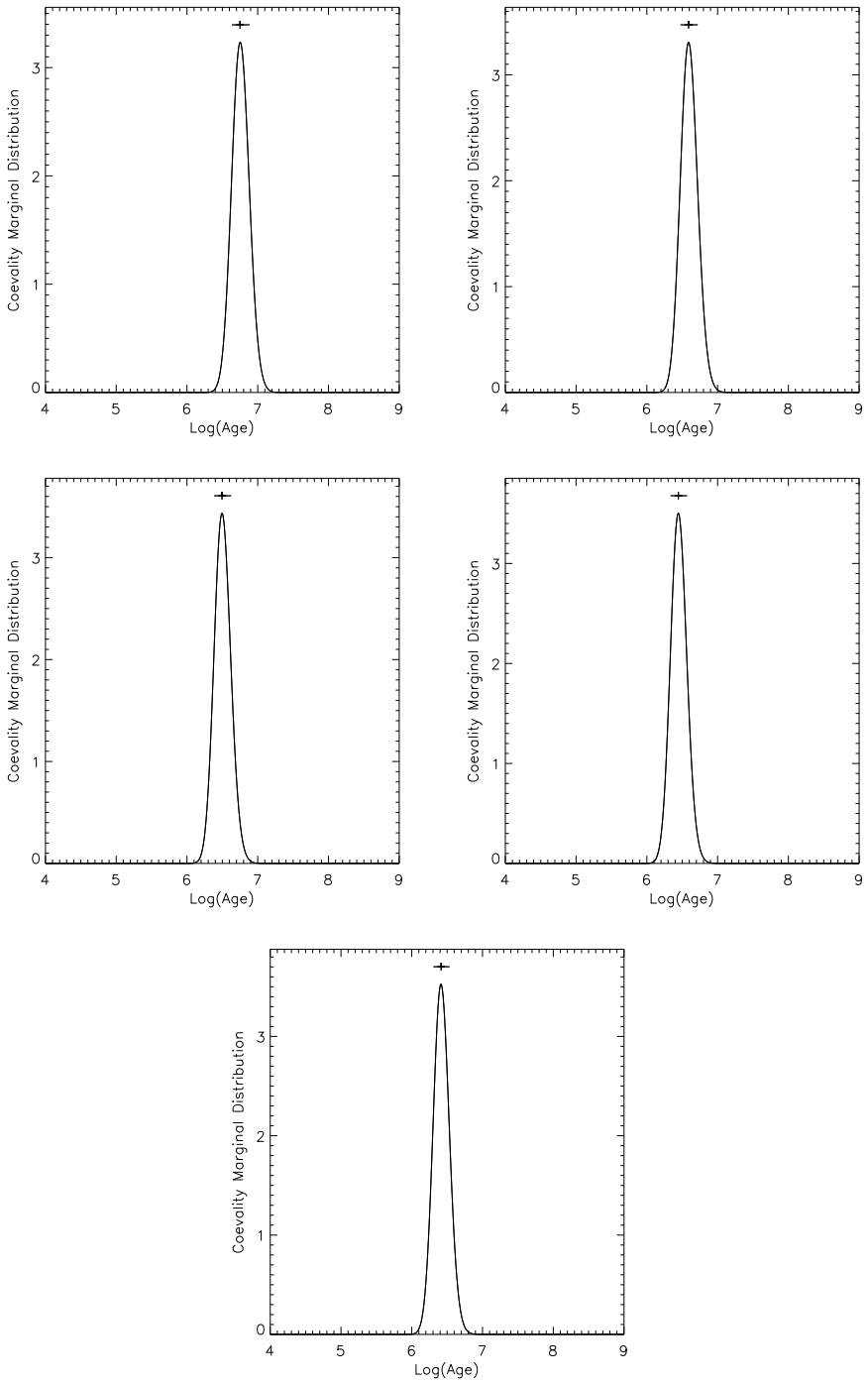

Figure 7.2: CD-39 10292 Age Marginal Distribution. Horizontal line represents the confidence interval. The order of panels is as in Fig.7.1.

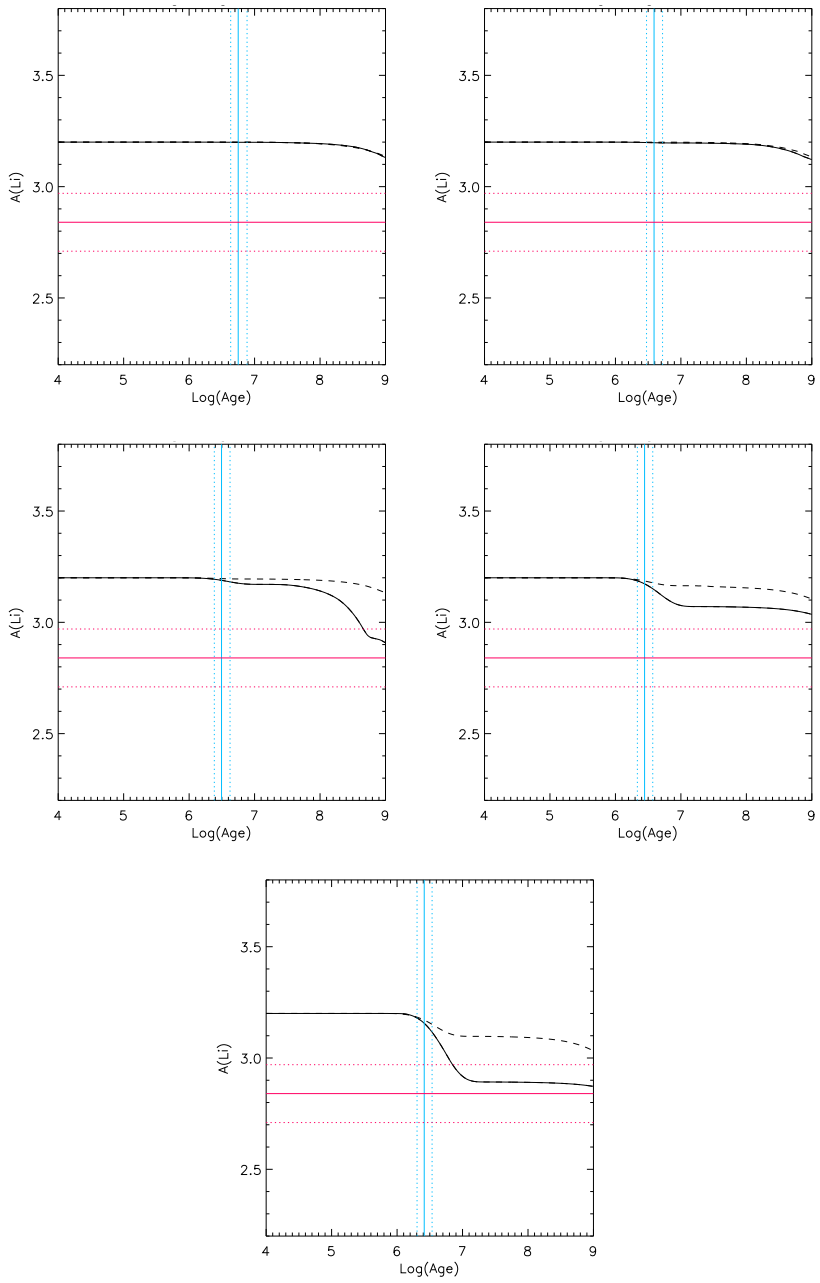

Figure 7.3: CD-39 10292 lithium results for primary component. Lithium depletion for the estimated mass is represented in black solid line, dashed the propagation of mass error from confidence interval. Blue vertical solid line marks the bayesian system age (coevality), dotted the associated error from the confidence interval. Red horizontal solid line represents the observed lithium abundance, dotted the associated error. The order of panels is as in Fig. 7.1.

7.2 CoRoT 223992193

For all the mixing lenght values, bayesian analysis returns masses consistent with the dynamical ones. The coevality ranges between ∼3.3-4.6 Myr, with decreasing values for increasing α. This is in good agreement with the age ∼3 Myr attributed to the NGC 2264 star-forming region, which hosts this system.
As to lithium age, except for α=0.80, the central value of observed lithium for the primary star (Fig. 7.7) provides an age estimation of ∼20 Myr (α=1.00), ∼16 Myr (α=1.25) and ∼12.5 Myr for both α=1.50 and 1.74. However, the lithium age is not in accord with the bayesian one.
The same situation occurs for the secondary (Fig. 7.8), for which the lithium age ranges from ∼10 Myr for α=1.25, 1.50 and 1.74, to ∼12 Myr and ∼12.5 Myr respectively for α=1.00 and 0.80.

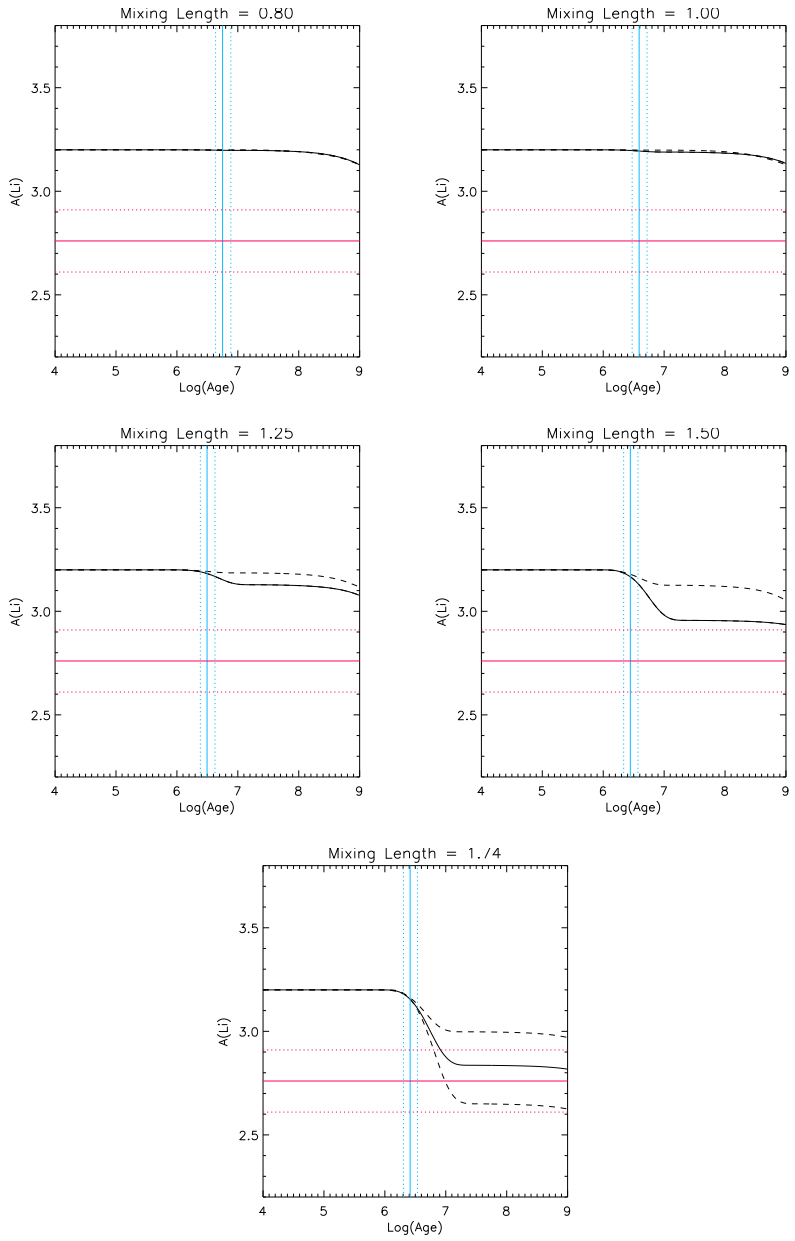

Figure 7.4: CD-39 10292 lithium results for secondary component. Lithium depletion for the estimated mass is represented in black solid line, dashed the propagation of mass error from confidence interval. Blue vertical solid line marks the bayesian system age (coevality), dotted the associated error from the confidence interval. Red horizontal solid line represents the observed lithium abundance, dotted the associated error. The order of panels is as in Fig. 7.1.

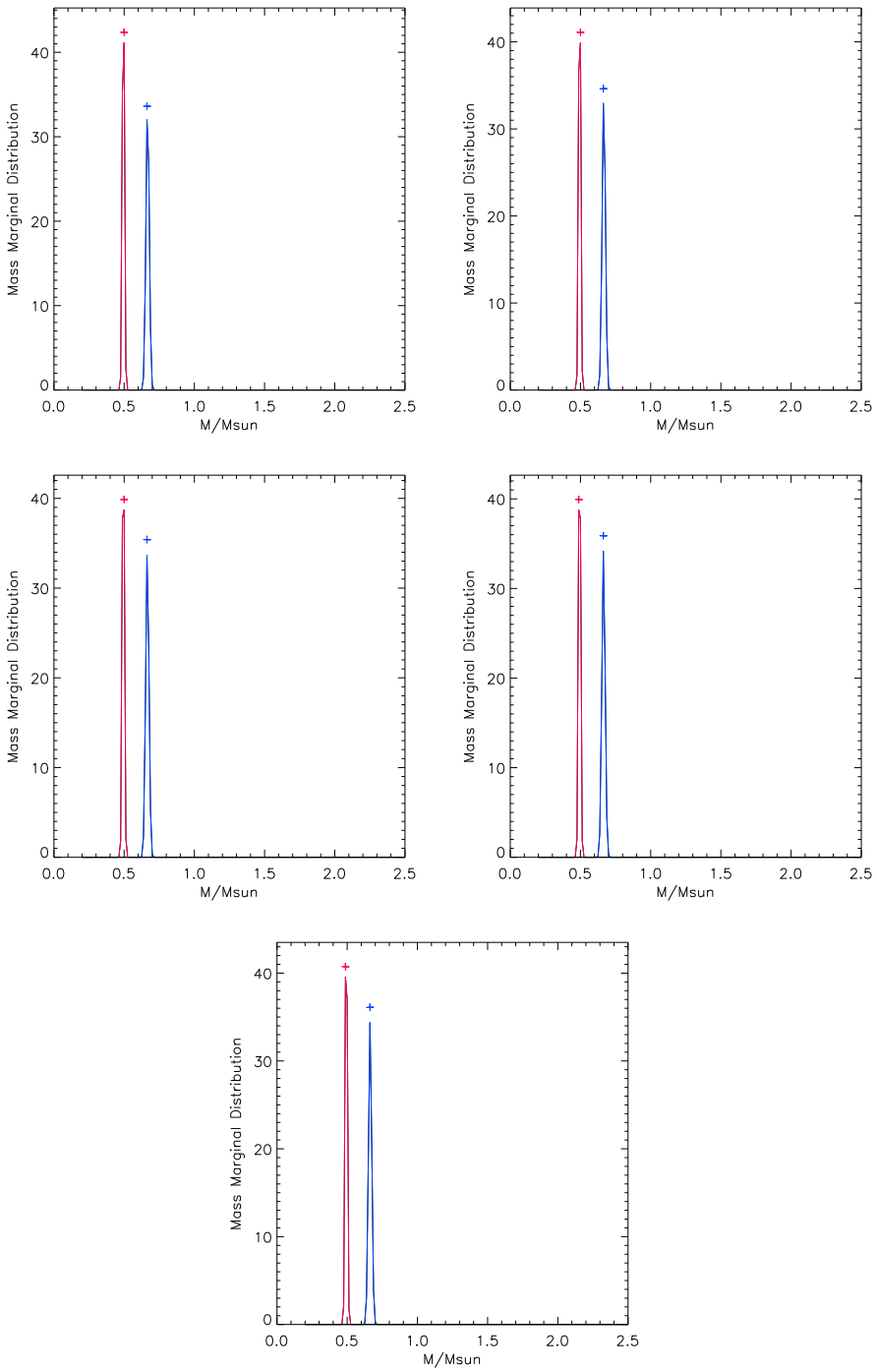

Figure 7.5: CoRoT 223992193 Mass Marginal Distribution for primary (blue) component and secondary (red) component. Horizontal line represent the confidence interval. The order of panels is as in Fig. 7.1.

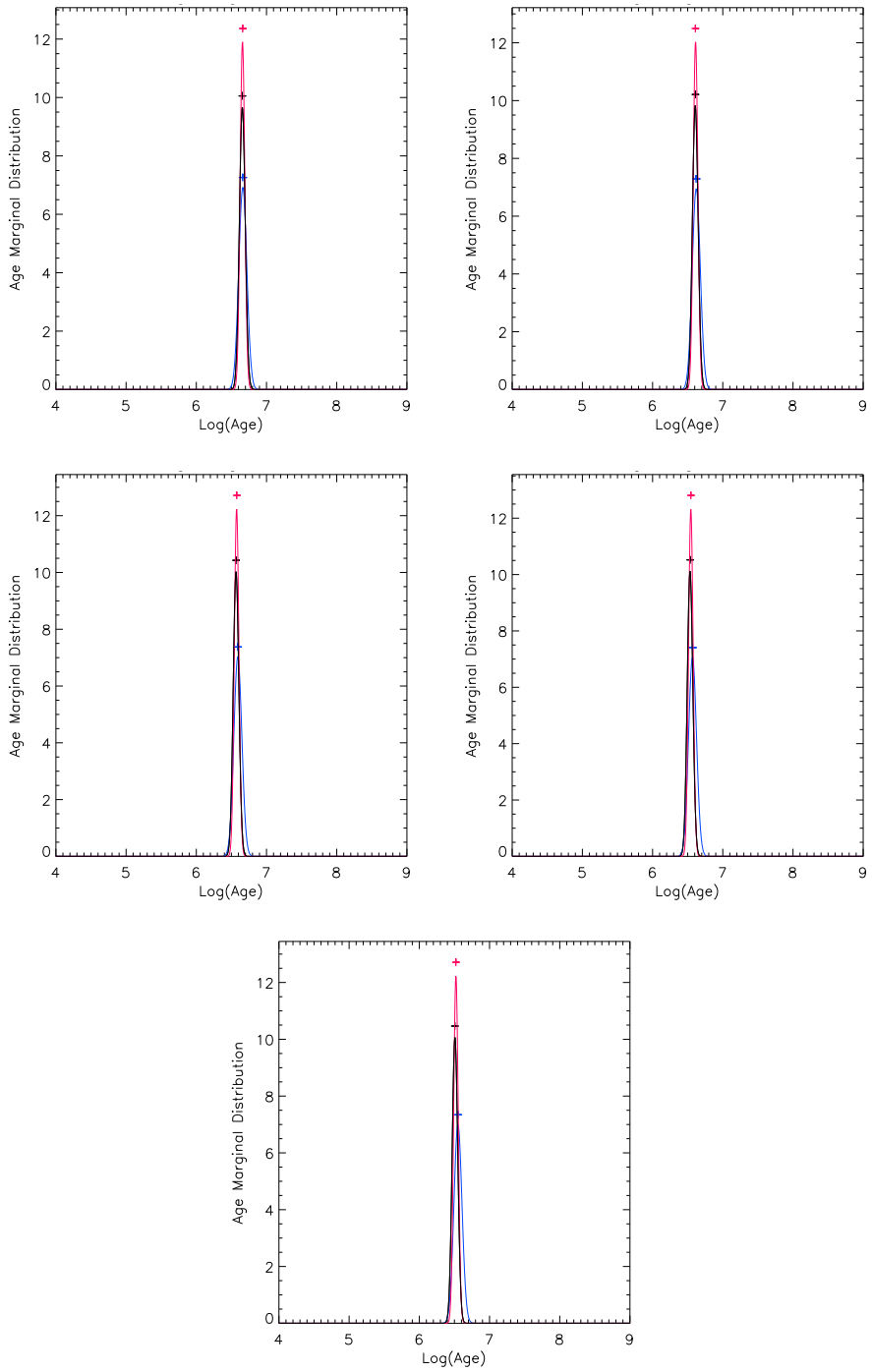

Figure 7.6: CoRoT 223992193 Age Marginal Distribution for primary (blue) component, secondary (red) component and for coevality (red). Horizontal line represent the confidence interval. The order of panels is as in Fig.7.1.

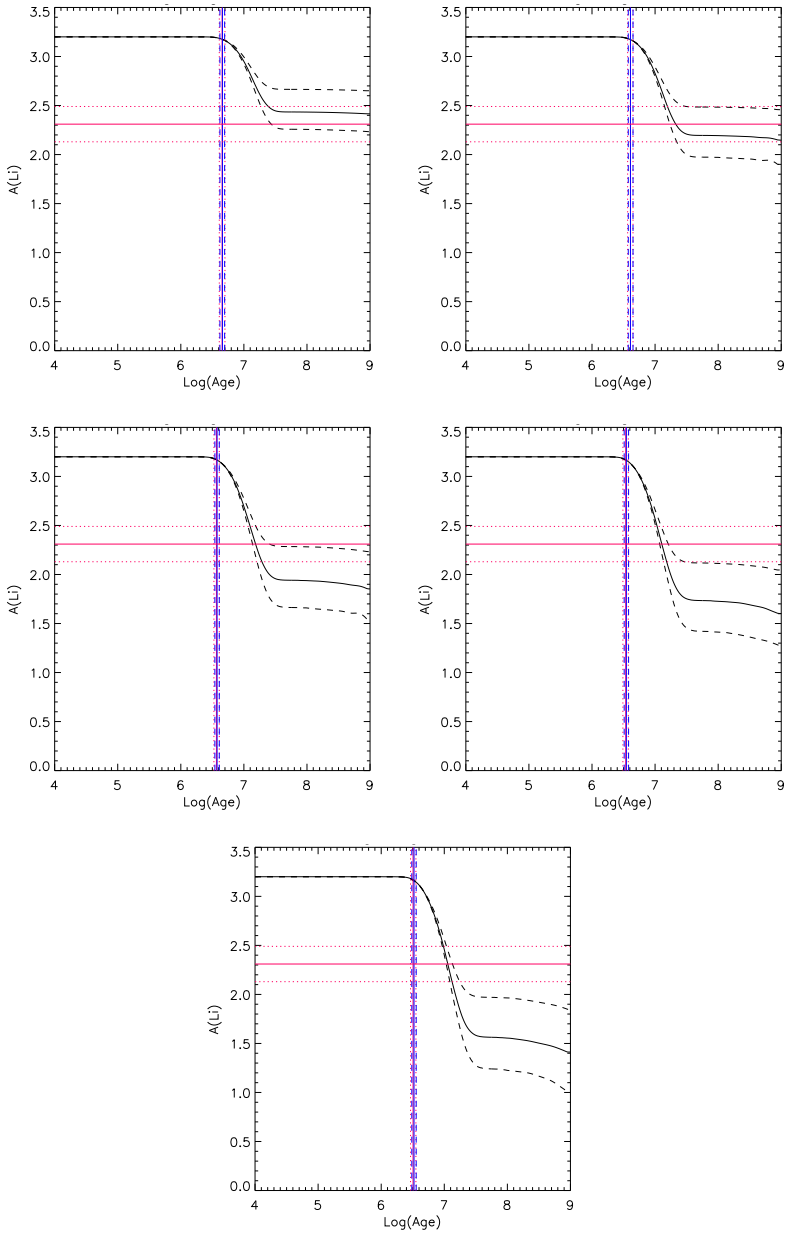

Figure 7.7: CoRoT 223992193 lithium results for primary component. Lithium depletion for the estimated mass is represented in black solid line, dashed the propagation of mass error from confidence interval. Blue vertical solid line marks the bayesian age of the single star, dashed the associated error from the confidence interval. Red vertical solid line marks the system age (coevality), dotted the associated error from the confidence interval. Red horizontal solid line represents the observed lithium abundance, dotted the associated error. The order of panels is as in Fig. 7.1.

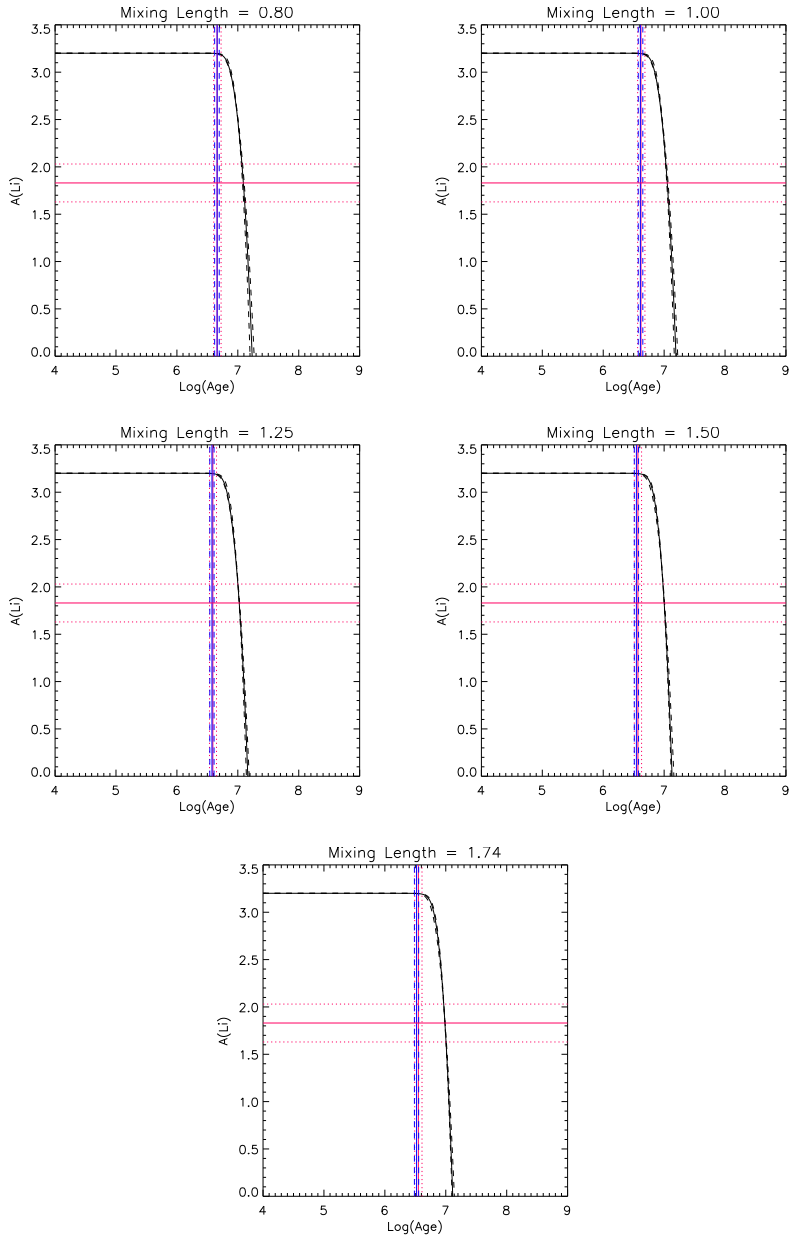

Figure 7.8: CoRoT 223992193 lithium results for secondary component. Lithium depletion for the estimated mass is represented in black solid line, dashed the propagation of mass error from confidence interval. Blue vertical solid line marks the bayesian age of the single star, dashed the associated error from the confidence interval. Red vertical solid line marks the system age (coevality), dotted the associated error from the confidence interval. Red horizontal solid line represents the observed lithium abundance, dotted the associated error. The order of panels is as in Fig. 7.1.

7.3 AK Sco

Bayesian mass results for different α-values range between ∼1.25-1.30 $M_\odot$ for primary and ∼1.20-1.30 $M_\odot$ for secondary component, with decreasing values for increasing α. Bayesian estimation for the coevality has a central value of ∼50 Myr with a very large confidence interval, higher than the literature estimation of ∼16 Myr for Upper Centaurus Lupus. However, this large indetermination is not a consequence of large errors in the stellar parameters, but it is due to the proximity of the star to the main sequence where for a very long time stars do not change their properties.
By referring to Fig. A.3 and A.4, for both stars the lithium age remains undefined, since the observed value is higher even than the primordial one.
Moreover, the bayesian derived masses at the solar metallicity do not give a strong lithium depletion.

7.4 ASAS J052821+0338.5

For this system, th bayesian coevality ranges between ∼2.7-10.6 Myr, with decreasing values for increasing α. Except for α=0.80, bayesian analysis returns masses consistent with the dynamical ones. As shown in Figures A7 and A8, the lithium age is undefined for all mixing lenght values for both component.

As for AK Sco, the masses of ASAS J052821+0338.5 components are to large to deplete lithium at the subsolar metallicity of the system. Morover the secndary shows a lithium abundance also higher than the primordial one.

7.5 GSC 06213-00306

For this system, the bayesian mass estimations of primary and secondary components, for different mixing lenght, range between $\sim$0.86-0-98 $M_\odot$ and $\sim$0.85-0.96 $M_\odot$ respectively, with decreasing values for increasing α. The bayesian estimation for the age-system has a central value of $\sim$40 Myr with a very large confidence interval. As in the case of AK Sco, this large indetermination is not due to large errors in the stellar parameters, but to the proximity of the star to the main sequence where for a very long time stars do not change their properties.
As to the lithium abundance, no match can be reached between models and observations (see Figures A.11 and A.12) being the observed value for both components also higher than the primordial lithium abundance.

7.6 HD 155555

Figure A.13 shows the Mass Marginal Distribution of each component of HD 155555, for different mixing lenght values. Note that more than one peak are present in the curves, indicating that more than one mass value is possible for the star, although less probable. Anyway, the bayesian mass estimation for primary ranges between $\sim$1.15-1.58 $M_\odot$ and for secondary $\sim$1.05-1.44 $M_\odot$ with increasing values for increasing α. The system age ranges between $\sim$3.6-16 Myr with decreasing values for increasing α. For both components, the small lithium depletion and the relatively large errors in the observed lithium values, it is not possible to draw any conclusion. (see Fig. A.15 and A.16).

7.7 HD 34700 A

For both components, bayesian mass estimations ranges between ∼1.34-1.45 $M_{\odot}$, while the system age is estimated between ∼10-16 Myr, with decreasing values for increasing α.
For both primary and secondary component the lithium age remains undefined. However, we find a difference, the primary present an underabundance of lithium as compared to the theoretical prediction. While the secondary star shows a lithium abundance well in agreement. Age cannot be determined for this large mass star showing then no lithium depletion (Fig. A.19 and A.20). q

7.8 HD 98800 B

For higher α-values bayesian analysis returns masses more consistent with the dynamical ones than for lower mixing length. Regarding the system age, bayesian estimation ranges between ∼8.5-13 Myr with decreasing values for increasing α.
For primary component, it's no possible to estimate the lithium age, since the low observed value with respect to the theoretical predictions (Fig. A23). For secondary component, an age between ∼20 Myr (α=0.80, 1.00, 1.25) and ∼25 Myr (α=1.50, 1.74) is deduced (Fig. A.24).

7.9 MML 53

For all the mixing lenght values, bayesian analysis returns masses consistent with the dynamical ones. Bayesian result for the coevality ranges between ∼10-23.5 Myr, with decreasing values for increasing α. This result is in good agreement with the age ∼16 Myr of Upper Centaurus Lupus sub-association, in which the system is very probably located.

For the primary star, the lithium age is undefined, but for the mass corresponding to α=1.74, from which an age of $\sim$180 Myr is deduced. For the secondary star, instead, an upper limit of $\sim$3 Myr is provided by the central lithium observed value. Alternatively, an age of $\sim$4 Myr can be deduced by the lithium low limit (Fig. A27, A28).

7.10 PAR 1802

The bayesian analysis estimates masses consistent with the dynamical ones, for all the mixing length values. The bayesian estimation of coevality ranges between $\sim$0.8-1.3 Myr, with decreasing values for increasing α.
Moreover, for both primary and secondary components (Fig. A31, A32) observed lithium abundance provides an age of $\sim$13 Myr for all mixing length values. Then, there is no match between the theoretical age estimation and the lithium age.

7.11 RXJ0529.4+0041 A

For this system, bayesian analysis provides masses consistent with the dynamical ones, for all the mixing lenght values. It has to be noted that the bayesian results for the ages of the single stars are in good agreement as the mixing lenght increases. It is indicative of a better choice in α=1.74, that is the solar value, for which the coevality results $\sim$5.4$\pm$0.3 Myr.
As to the lithium abundance, for the primary component no match is found between the observed value and the theoretical predictions for different mixing lenght. This is being the observed lithium more abundant than in the primordial universe. For the secondary one, instead, the lithium age is in perfect agreement in the case of both α=1.50 and 1.74 (Fig. A35, A36).

7.12 RX J0530.7-0434

Bayesian mass results range between ∼1.12-2.25 $M_\odot$ for both components, while the coevality estimation ranges between ∼0.35-1.80 Myr, with decreasing values for increasing α.
No lithium age can be derived for both components for small mixing length values, because of the large bayesian masses and almost negligible lithium depletion.

Differently if α=1.74 an upper limit for the age of both components is ∼4 Myr (Fig. A39, A40).

7.13 RX J0532.1-0732

Bayesian mass results for different α-values range between ∼1.10-1.50 $M_\odot$ for primary and ∼1.05-1.45 $M_\odot$ for secondary component, while estimation for the coevality ranges between ∼1.6-3.9 Myr, with decreasing values for increasing α.

For the primary component, given the small depletion and the large error in the lithium determination (Fig. A43), it is not possible to draw any conclusion. Anyway, an upper limit ∼1 Myr is given in the case of both α=1.50 and 1.74. Also for the secondary component (Fig. A44), given the small depletion and the large error in the lithium determination, it is in general not possible to draw any conclusion. Only for the solar value mixing length (1.74) the observed lithium corresponds to an age of ∼4 Myr.

7.14 RX J0541.4-0324

For this system, bayesian analysis provides masses in the range ∼1.85-2.00 $M_\odot$ for primary and ∼1.25-1.30 $M_\odot$ for secondary

component, coevality in the range ∼3.55-3.75 Myr, with decreasing values for increasing α.
For both components, given the small depletion due to the high mass value and the large error in the lithium determination, it is not possible to draw any conclusion. Anyway, for the solar mixing lenght value (1.74), may be possible to attribute a lithium age of 1 Gyr to the secondary component (Fig. A47, A48).

7.15 V773 Tau A

For this system, bayesian analysis provides masses between ∼0.95-2.15 $M_\odot$ for primary and ∼0.8-1.8 $M_\odot$ for secondary component, with decreasing values for increasing α. As to the coevality, bayesian estimation ranges between ∼0.95-2.2 Myr, with decreasing values for increasing α.
As to the lithium age, for primary star it is not defined, since the higher value to the observed lithium abundance with respect the primordial one.
For the secondary component, the observed lithium provides an age of ∼8 Myr for both cases α=1.50 and 1.74 (Fig. A51, A52).

7.16 V1174 Ori

For all the mixing lenght values, bayesian analysis returns masses consistent with the dynamical ones. The coevality ranges between ∼6.7-10.5 Myr, with decreasing values for increasing α.
For the primary component, a perfect agreement arises between bayesian and lithium age estimations for the case of α=1.25, while for α=1.50 and α=1.74 the lithium age estimations are ∼6 Myr and ∼5 Myr respectively, anyway in good agreement with the corresponding bayesian ones. For the secondary component, a lithium age between ∼25 Myr (for α=1.00, bayesian coevality ∼9

Myr) and ∼12 Myr (for α=1.74, bayesian coevality ∼6.7 Myr) is derived, so that, for the secondary, not a good agreement is found (Fig. A55, A56).

7.17 V4046 Sgr

For this system, the bayesian analysis provides masses consistent with the dynamical ones for the solar mixing lenght value, α=1.74. The coevality estimation ranges between ∼2.75-4.50 Myr with decreasing values for increasing α.
For the primary component, only for α=1.74 it is possible to obtain an estimation from the observed lithium, that is ∼10 Myr. For the secondary one, a lithium age of ∼12 Myr is derived in the case α=1.50 and ∼9 Myr for α=1.74, both higher than the bayesian estimations (Fig. A59, A60).

Component		Type	$M_{dyn}(M_\odot)$	K_A/K_B	$T_{\rm eff}(K)$	Log$g$	Radius($R_\odot$)	Log($L/L_\odot$)	[Fe/H]	A(Li)	Ref.
ASAS J0528	A B	EB	1.387±0.017 1.331±0.011	0.972±0.009	5103 ±100 4599 ±100	4.0±0.1 3.9±0.1	1.84±0.01 1.78±0.01	0.314±0.034 0.107±0.034	-0.15±0.20	3.10±0.20 3.35±0.20	Stemp08, Dor09
CoRoT 223	A B	EB	0.668±0.012 0.4953±0.0073	0.74±0.01	3750±100 3500±100	4.038±0.026 4.045±0.040	1.295±0.040 1.107±0.050	- -	-0.15±0.09	2.31±0.18 1.83±0.20	Gil14, K00
HD 98800 B	a b	AS	0.699±0.064 0.582±0.051	0.83±0.03	4200±150 4000±150	4.21±0.12 4.21±0.12	1.09±0.14 1.09±0.14	-0.481±0.099 0.777±0.099	-0.15±0.09	1.44±0.14 0.97±0.15	Bod05, Lask09
MML 53	A B	EB	1.02±0.05 0.88±0.05	0.862±0.017	4910±100 4400±100	4.27±0.10 4.37±0.10	1.19±0.07 1.05±0.07	- -	-0.10±0.04	3.10±0.10 3.20±0.10	SH11, Jam06
PAR 1802	A B	EB	0.391±0.032 0.385±0.032	0.984±0.085	3675±150 3365±150	3.55±0.04 3.61±0.04	1.73±0.02 1.62±0.02	- -	-0.01±0.04	1.48±0.21 0.57±0.22	Carg08, Gom12 Dor09
RX J0529.4 A	a b	EB	1.27±0.01 0.93±0.01	0.730±0.003	5200±150 4220±150	4.22±0.02 4.14±0.02	1.44±0.05 1.35±0.05	0.14±0.08 -0.28±0.15	-0.01±0.04	3.48±0.10* 3.02±0.16*	Cov04, Dor09
V1174 Ori	A B	EB	1.009±0.015 0.731±0.008	0.724±0.007	4470±120 3615±100	4.19±0.01 4.25±0.01	1.339±0.015 1.065±0.011	−0.193±0.048 −0.761±0.058	-0.01±0.04	3.00±0.05 1.98±0.09	Sta04, Dor09
V4046 Sgr	A B	DKS	0.90±0.05 0.85±0.04	0.944±0.011	4400±100 4100±100	4.0±0.1 4.0±0.1	- -	- -	0.00±0.05	2.82±0.14 2.65±0.16	tw

Table 7.1: Observed data for binary systems with dynamical masses. References: Stemp08 = Stempels et al. (2008), Cov04 = Covino et al. (2004), Car08 = Cargile et al. (2008), Jams06 = James et al. (2006), Dor09 = D'Orazi et al. (2009), Gil14 = Gillen et al. (2014), K00 = King et al. (2000), Sta04 = Stassun et al. (2004), K00 = King et al. (2000), Bod05 = Boden et al. (2005), Lask09 = Laskar et al. (2009), tw = this work

Component		K_A/K_B	$T_{\rm eff}(K)$	Log$g$	Radius($R_\odot$)	Log($L/L_\odot$)	[Fe/H]	A(Li)	Ref.
HD 155555	A	0.912±0.003	5300±100	4.05±0.10	-	-	0.00±0.05	3.16±0.15	Dun08
	B		5050±100	4.10±0.10	-	-		3.15±0.15	
RX J0530.7	A	0.9983±0.0076	4600±200	-	-	0.73±0.02	-0.01±0.04	3.30±0.20	Cov01, Dor09
	B		4600±200	-	-	0.73±0.02		3.20±0.20	
RX J0532.1	A	0.9483±0.0071	4600±200	-	-	0.185±0.014	-0.01±0.04	3.20±0.30	Cov01, Dor09
	B		4500±200	-	-	0.167±0.015		3.10±0.30	
RX J0541.4	A	0.6743±0.0049	5100±200	-	-	0.672±0.009	-0.01±0.04	3.10±0.20	Cov01, Dor09
	B		4500±200	-	-	0.079±0.036		2.90±0.30	
AK Sco	A	0.986±0.030	6600±100	4.50±0.10	-	-	0.00±0.05	3.36±0.06	tw
	B		6500±100	4.60±0.10	-	-		3.41±0.06	
CD-39 10292	A	0.934±0.044	4600±100	4.00±0.10	-	-	0.00±0.05	2.84±0.13	tw
	B		4300±100	4.00±0.10	-	-		2.76±0.15	
GSC 06213	A	0.993±0.013	5500±100	4.60±0.10	-	-	0.00±0.05	3.88±0.09	tw
	B		5100±100	4.50±0.10	-	-		3.40±0.11	
HD 34700 A	a	0.994±0.051	6400±100	4.00±0.10	-	-	0.00±0.05	3.00±0.07	tw
	b		6300±100	4.00±0.10	-	-		3.19±0.07	
V773 Tau A	a	0.865±0.042	4700±100	3.70±0.10	2.22±0.20	-	0.00±0.05	3.65±0.42	tw
	b		4100±100	3.70±0.10	1.74±0.19	-		2.89±0.21	

Table 7.2: Observed data for the examined SB2 binary systems. References: Cov01 = Covino et al. (2001), Dor09 = D'Orazi et al. (2009), Dun08 = Dunstone et al. (2008),- tw = this work.

Component		M_{bayes}					M_{dyn}
		α=0.80	α=1.00	α=1.25	α=1.50	α=1.74	
ASAS J0528	A	$1.32^{+0.02}_{-0.02}$	$1.38^{+0.01}_{-0.02}$	$1.40^{+0.02}_{-0.01}$	$1.40^{+0.02}_{-0.02}$	$1.39^{+0.02}_{-0.02}$	1.39±0.02
	B	$1.32^{+0.02}_{-0.01}$	$1.32^{+0.02}_{-0.01}$	$1.32^{+0.02}_{-0.01}$	$1.32^{+0.02}_{-0.01}$	$1.32^{+0.02}_{-0.01}$	1.33±0.01
CoRoT 223	A	$0.66^{+0.02}_{-0.01}$	$0.66^{+0.02}_{-0.01}$	$0.66^{+0.02}_{-0.01}$	$0.66^{+0.02}_{-0.01}$	$0.66^{+0.02}_{-0.01}$	0.67±0.01
	B	$0.50^{+0.01}_{-0.02}$	$0.50^{+0.01}_{-0.02}$	$0.50^{+0.01}_{-0.02}$	$0.49^{+0.02}_{-0.01}$	$0.49^{+0.02}_{-0.01}$	0.50±0.01
HD 98800 B	a	$0.77^{+0.05}_{-0.06}$	$0.76^{+0.05}_{-0.08}$	$0.74^{+0.06}_{-0.06}$	$0.74^{+0.05}_{-0.06}$	$0.72^{+0.06}_{-0.06}$	0.70±0.06
	b	$0.62^{+0.05}_{-0.06}$	$0.61^{+0.05}_{-0.05}$	$0.61^{+0.05}_{-0.06}$	$0.60^{+0.05}_{-0.05}$	$0.60^{+0.05}_{-0.05}$	0.58±0.05
MML 53	A	$0.96^{+0.04}_{-0.04}$	$1.00^{+0.04}_{-0.04}$	$1.02^{+0.04}_{-0.04}$	$1.04^{+0.04}_{-0.04}$	$1.04^{+0.04}_{-0.04}$	1.02±0.05
	B	$0.88^{+0.04}_{-0.04}$	$0.89^{+0.04}_{-0.04}$	$0.89^{+0.04}_{-0.04}$	$0.88^{+0.04}_{-0.04}$	$0.88^{+0.04}_{-0.04}$	0.88±0.05
PAR 1802	A	$0.40^{+0.02}_{-0.02}$	$0.40^{+0.02}_{-0.04}$	$0.39^{+0.04}_{-0.02}$	$0.39^{+0.04}_{-0.02}$	$0.39^{+0.04}_{-0.02}$	0.39±0.03
	B	$0.39^{+0.02}_{-0.02}$	$0.39^{+0.02}_{-0.04}$	$0.38^{+0.04}_{-0.02}$	$0.38^{+0.04}_{-0.02}$	$0.38^{+0.02}_{-0.02}$	0.38±0.03
RXJ 0529.4 A	a	$1.26^{+0.01}_{-0.02}$	$1.25^{+0.02}_{-0.05}$	$1.25^{+0.05}_{-0.02}$	$1.26^{+0.05}_{-0.04}$	$1.25^{+0.06}_{-0.02}$	1.27±0.01
	b	$0.92^{+0.02}_{-0.01}$	$0.91^{+0.02}_{-0.04}$	$0.92^{+0.02}_{-0.04}$	$0.92^{+0.04}_{-0.02}$	$0.92^{+0.04}_{-0.04}$	0.93±0.01
V1174 Ori	A	$1.04^{+0.01}_{-0.02}$	$1.02^{+0.01}_{-0.02}$	$1.01^{+0.02}_{-0.01}$	$1.01^{+0.02}_{-0.02}$	$1.01^{+0.01}_{-0.02}$	1.01±0.02
	B	$0.72^{+0.02}_{-0.01}$	$0.72^{+0.02}_{-0.01}$	$0.72^{+0.01}_{-0.01}$	$0.72^{+0.01}_{-0.01}$	$0.72^{+0.01}_{-0.01}$	0.73±0.01
V4046 Sgr	A	$0.96^{+0.05}_{-0.05}$	$0.96^{+0.05}_{-0.05}$	$0.95^{+0.05}_{-0.05}$	$0.93^{+0.05}_{-0.04}$	$0.91^{+0.05}_{-0.05}$	0.90±0.05
	B	$0.87^{+0.04}_{-0.05}$	$0.86^{+0.04}_{-0.05}$	$0.85^{+0.04}_{-0.05}$	$0.84^{+0.04}_{-0.04}$	$0.82^{+0.04}_{-0.04}$	0.85±0.05

Table 7.3: Bayesian mass results for systems with dynamical masses.

System		Age$_{\rm bayes}$ (Myr)									
		α=0.80		α=1.00		α=1.25		α=1.50		α=1.74	
		star	coevality	star	coevality	star	coevality	star	coevality	star	coevality
ASAS J0528	A	$13.49^{+1.65}_{-2.40}$	$10.59^{+1.29}_{-0.71}$	$7.85^{+2.38}_{-0.61}$	$7.00^{+0.59}_{-0.62}$	$5.37^{+1.24}_{-0.58}$	$4.62^{+0.39}_{-0.41}$	$3.94^{+0.85}_{-0.43}$	$3.43^{+0.29}_{-0.30}$	$3.13^{+0.63}_{-0.31}$	$2.69^{+0.26}_{-0.21}$
	B	$7.16^{+1.75}_{-0.85}$		$4.68^{+1.01}_{-0.51}$		$3.09^{+0.76}_{-0.24}$		$2.43^{+0.46}_{-0.26}$		$1.97^{+0.37}_{-0.21}$	
CoRoT 223	A	$4.52^{+0.44}_{-0.40}$	$4.57^{+0.33}_{-0.35}$	$4.03^{+0.44}_{-0.35}$	$4.07^{+0.34}_{-0.27}$	$3.67^{+0.35}_{-0.32}$	$3.76^{+0.31}_{-0.29}$	$3.43^{+0.33}_{-0.30}$	$3.51^{+0.29}_{-0.27}$	$3.20^{+0.35}_{-0.25}$	$3.31^{+0.28}_{-0.26}$
	B	$4.57^{+0.68}_{-0.54}$		$4.17^{+0.62}_{-0.50}$		$3.89^{+0.58}_{-0.46}$		$3.71^{+0.50}_{-0.48}$		$3.55^{+0.53}_{-0.42}$	
HD 98800 B	a	$10.96^{+4.70}_{-3.02}$	$13.18^{+3.80}_{-2.71}$	$8.91^{+3.82}_{-2.38}$	$11.22^{+3.23}_{-2.31}$	$7.50^{+3.34}_{-1.94}$	$9.77^{+2.82}_{-1.92}$	$6.76^{+2.90}_{-1.75}$	$9.02^{+2.60}_{-1.85}$	$6.24^{+2.78}_{-1.61}$	$8.51^{+2.45}_{-1.75}$
	b	$15.85^{+7.32}_{-4.37}$		$13.96^{+6.45}_{-3.85}$		$12.59^{+5.82}_{-3.47}$		$11.75^{+5.43}_{-3.14}$		$11.22^{+5.19}_{-3.09}$	
MML 53	A	$25.12^{+3.72}_{-3.49}$	$23.44^{+2.86}_{-2.79}$	$18.41^{+1.54}_{-2.92}$	$17.58^{+2.37}_{-2.09}$	$13.65^{+2.76}_{-2.03}$	$13.65^{+2.02}_{-1.76}$	$11.09^{+2.40}_{-1.65}$	$11.35^{+1.83}_{-1.35}$	$9.66^{+1.95}_{-1.62}$	$10.00^{+1.61}_{-1.29}$
	B	$20.65^{+4.76}_{-3.47}$		$16.40^{+3.78}_{-2.92}$		$13.49^{+3.30}_{-2.52}$		$11.75^{+3.04}_{-2.20}$		$10.59^{+2.90}_{-1.98}$	
PAR 1802	A	$1.23^{+0.13}_{-0.15}$	$1.29^{+0.11}_{-0.11}$	$1.05^{+0.11}_{-0.11}$	$1.10^{+0.09}_{-0.08}$	$0.93^{+0.09}_{-0.09}$	$0.99^{+0.07}_{-0.08}$	$0.83^{+0.08}_{-0.07}$	$0.88^{+0.06}_{-0.06}$	$0.75^{+0.08}_{-0.07}$	$0.79^{+0.07}_{-0.05}$
	B	$1.35^{+0.15}_{-0.16}$		$1.16^{+0.13}_{-0.14}$		$1.03^{+0.11}_{-0.09}$		$0.93^{+0.10}_{-0.08}$		$0.85^{+0.08}_{-0.08}$	
RXJ0529.4A	a	$27.86^{+0.98}_{-2.16}$	$19.50^{+2.38}_{-3.09}$	$19.95^{+2.18}_{-3.73}$	$11.09^{+2.09}_{-1.54}$	$12.88^{+2.25}_{-1.79}$	$7.08^{+0.77}_{-0.47}$	$9.66^{+1.69}_{-1.25}$	$5.96^{+0.50}_{-0.40}$	$7.76^{+1.25}_{-0.84}$	$5.37^{+0.32}_{-0.36}$
	b	$7.50^{+1.21}_{-0.58}$		$6.38^{+0.62}_{-0.49}$		$5.49^{+0.46}_{-0.37}$		$4.90^{+0.41}_{-0.33}$		$4.52^{+0.38}_{-0.30}$	
V1174 Ori	A	$13.49^{+2.54}_{-2.01}$	$10.47^{+0.49}_{-0.47}$	$8.51^{+0.82}_{-0.57}$	$9.12^{+0.43}_{-0.31}$	$6.92^{+0.41}_{-0.39}$	$8.03^{+0.28}_{-0.27}$	$6.03^{+0.28}_{-0.34}$	$7.33^{+0.26}_{-0.33}$	$5.43^{+0.26}_{-0.24}$	$6.68^{+0.31}_{-0.30}$
	B	$10.23^{+0.61}_{-0.35}$		$9.33^{+0.44}_{-0.42}$		$8.51^{+0.40}_{-0.38}$		$7.94^{+0.37}_{-0.36}$		$7.50^{+0.35}_{-0.25}$	
V4046 Sgr	A	$4.84^{+2.57}_{-1.45}$	$4.47^{+1.42}_{-0.96}$	$3.51^{+1.80}_{-1.02}$	$3.54^{+1.13}_{-0.76}$	$2.95^{+1.46}_{-0.84}$	$3.13^{+0.95}_{-0.67}$	$2.69^{+1.29}_{-0.76}$	$2.88^{+0.87}_{-0.62}$	$2.54^{+1.17}_{-0.74}$	$2.75^{+0.83}_{-0.62}$
	B	$4.17^{+1.93}_{-1.15}$		$3.63^{+1.62}_{-1.03}$		$3.31^{+1.47}_{-0.97}$		$3.09^{+1.38}_{-0.90}$		$2.95^{+1.36}_{-0.88}$	

Table 7.4: Bayesian age results for systems with dynamical masses.

Star		M_{bayes}					K_A/K_B
		α=0.80	α=1.00	α=1.25	α=1.50	α=1.74	
AK Sco	A	$1.31^{+0.02}_{-0.05}$	$1.31^{+0.02}_{-0.06}$	$1.29^{+0.02}_{-0.06}$	$1.26^{+0.02}_{-0.06}$	$1.24^{+0.02}_{-0.06}$	0.934±0.044
	B	$1.30^{+0.02}_{-0.06}$	$1.29^{+0.02}_{-0.06}$	$1.26^{+0.02}_{-0.06}$	$1.24^{+0.02}_{-0.06}$	$1.20^{+0.04}_{-0.05}$	
CD-39 10292	A	$1.51^{+0.16}_{-0.12}$	$1.44^{+0.15}_{-0.11}$	$1.26^{+0.12}_{-0.09}$	$1.14^{+0.09}_{-0.09}$	$1.05^{+0.09}_{-0.07}$	0.934±0.044
	B	$1.38^{+0.11}_{-0.15}$	$1.30^{+0.14}_{-0.10}$	$1.15^{+0.11}_{-0.09}$	$1.04^{+0.09}_{-0.08}$	$0.95^{+0.09}_{-0.06}$	
GSC 06213	A	$0.98^{+0.02}_{-0.05}$	$0.94^{+0.02}_{-0.04}$	$0.90^{+0.04}_{-0.02}$	$0.89^{+0.02}_{-0.04}$	$0.86^{+0.04}_{-0.02}$	0.993±0.013
	B	$0.96^{+0.02}_{-0.05}$	$0.92^{+0.02}_{-0.04}$	$0.89^{+0.04}_{-0.04}$	$0.86^{+0.04}_{-0.02}$	$0.85^{+0.04}_{-0.02}$	
HD 34700 A	a	$1.34^{+0.12}_{-0.02}$	$1.34^{+0.12}_{-0.02}$	$1.36^{+0.12}_{-0.05}$	$1.41^{+0.12}_{-0.09}$	$1.45^{+0.14}_{-0.09}$	0.99±0.05
	b	$1.34^{+0.12}_{-0.04}$	$1.34^{+0.12}_{-0.04}$	$1.34^{+0.15}_{-0.04}$	$1.39^{+0.14}_{-0.08}$	$1.44^{+0.14}_{-0.09}$	
HD 155555	A	$1.15^{+0.18}_{-0.04}$	$1.30^{+0.20}_{-0.05}$	$1.56^{+0.14}_{-0.18}$	$1.58^{+0.21}_{-0.11}$	$1.58^{+0.21}_{-0.10}$	0.912±0.003
	B	$1.05^{+0.16}_{-0.04}$	$1.19^{+0.19}_{-0.05}$	$1.41^{+0.14}_{-0.14}$	$1.44^{+0.20}_{-0.10}$	$1.44^{+0.20}_{-0.09}$	
RX J0530.7	A	$2.25^{+0.02}_{-0.14}$	$2.18^{+0.01}_{-0.32}$	$1.76^{+0.21}_{-0.31}$	$1.36^{+0.31}_{-0.21}$	$1.12^{+0.29}_{-0.18}$	0.9983±0.0076
	B	$2.24^{+0.02}_{-0.14}$	$2.18^{+0.01}_{-0.32}$	$1.76^{+0.21}_{-0.31}$	$1.36^{+0.31}_{-0.21}$	$1.12^{+0.28}_{-0.18}$	
RX J0532.1	A	$1.52^{+0.01}_{-0.10}$	$1.48^{+0.00}_{-0.18}$	$1.34^{+0.06}_{-0.20}$	$1.18^{+0.14}_{-0.16}$	$1.09^{+0.15}_{-0.16}$	0.9483±0.0071
	B	$1.45^{+0.01}_{-0.10}$	$1.40^{+0.01}_{-0.16}$	$1.28^{+0.05}_{-0.19}$	$1.11^{+0.14}_{-0.15}$	$1.05^{+0.12}_{-0.16}$	
RX J0541.4	A	$1.98^{+0.04}_{-0.06}$	$1.94^{+0.04}_{-0.05}$	$1.90^{+0.04}_{-0.05}$	$1.88^{+0.04}_{-0.05}$	$1.85^{+0.04}_{-0.04}$	0.6743±0.0049
	B	$1.32^{+0.04}_{-0.04}$	$1.30^{+0.04}_{-0.04}$	$1.28^{+0.04}_{-0.02}$	$1.26^{+0.02}_{-0.04}$	$1.25^{+0.02}_{-0.04}$	
V773 Tau A	a	$2.15^{+0.18}_{-0.19}$	$1.75^{+0.28}_{-0.19}$	$1.30^{+0.20}_{-0.12}$	$1.08^{+0.14}_{-0.09}$	$0.96^{+0.11}_{-0.08}$	0.865±0.042
	b	$1.78^{+0.16}_{-0.18}$	$1.45^{+0.24}_{-0.16}$	$1.06^{+0.18}_{-0.09}$	$0.89^{+0.12}_{-0.08}$	$0.79^{+0.10}_{-0.06}$	

Table 7.5: Bayesian results for masses of the SB2 systems.

System	Coevality (Myr)				
	α=0.80	α=1.00	α=1.25	α=1.50	α=1.74
AK Sco	$51.28^{+194}_{-13.3}$	$49.54^{+199}_{-12.8}$	$50.12^{+216}_{-13.4}$	$50.70^{+241}_{-13.9}$	$51.29^{+276}_{-14.6}$
CD-39 10292	$5.62^{+1.96}_{-1.31}$	$3.89^{+1.36}_{-0.90}$	$3.13^{+1.04}_{-0.70}$	$2.79^{+0.93}_{-0.62}$	$2.60^{+0.83}_{-0.58}$
GSC 06213	$42.66^{+430}_{-0.00}$	$43.65^{+493}_{-0.00}$	$43.65^{+531}_{-0.00}$	$42.66^{+539}_{-0.00}$	$38.90^{+529}_{-0.00}$
HD 34700 A	$16.60^{+1.19}_{-3.86}$	$14.79^{+1.80}_{-3.04}$	$13.33^{+1.80}_{-2.74}$	$11.35^{+2.14}_{-2.23}$	$9.88^{+2.00}_{-2.12}$
HD 155555	$16.03^{+5.10}_{-4.28}$	$10.35^{+2.83}_{-2.85}$	$6.46^{+2.05}_{-1.83}$	$4.42^{+1.68}_{-1.10}$	$3.55^{+1.35}_{-0.89}$
RX J0530.7	$1.80^{+0.83}_{-0.52}$	$1.17^{+0.46}_{-0.38}$	$0.74^{+0.33}_{-0.24}$	$0.48^{+0.24}_{-0.16}$	$0.34^{+0.17}_{-0.12}$
RX J0532.1	$3.89^{+0.79}_{-1.07}$	$3.13^{+0.72}_{-0.86}$	$2.40^{+0.76}_{-0.68}$	$1.82^{+0.81}_{-0.45}$	$1.64^{+0.60}_{-0.50}$
RX J0541.4	$3.76^{+0.36}_{-0.37}$	$3.80^{+0.27}_{-0.45}$	$3.67^{+0.35}_{-0.36}$	$3.59^{+0.35}_{-0.35}$	$3.55^{+0.34}_{-0.39}$
V773 Tau A	$2.21^{+0.36}_{-0.48}$	$1.43^{+0.43}_{-0.29}$	$1.16^{+0.33}_{-0.24}$	$1.04^{+0.30}_{-0.21}$	$0.95^{+0.28}_{-0.20}$

Table 7.6: Bayesian results for coevality of the SB2 systems.

CHAPTER 8

Conclusion

The expectation to date the age of low mass pre-main sequence stars from lithium has been tested by comparing the observed lithium and the predicted abundance by evolutionary models. The test, in this thesis, has been applied on a sample of binary systems whose components have a well known mass or whose mass ratio has been exactly established. The common metallicity and the coevality of the two components of a system are strong constraints to determine the age on the basis of evolutionary codes. To achieve reliable results, by an observational campaign, I have **doubled** the sample of stars presenting the necessary information for the analysis. Stellar parameters have been determined with the most precise and accurately tested techniques: high resolution spectroscopy along a very large wavelength range and numerical solution of the radiative transfer equation. As to the evolutionary code, I have implemented FRANEC with the very accurate reaction rates as determined with the most reliable experimental technique, the Trojan Horse Method. Since for PMS stars the agreement between observed and predicted lithium abundance

can be obtained just tuning the external convective efficiency, I have computed a database of models for different values of the mixing length parameter. Age determination of stars has been carried out by adopting what is nowadays believed to be the most powerful statistical method in the field, the Bayesian analysis. I have extended in an original way this statistical method from binary system with known masses to the most common double lined spectroscopic binaries.

Despite of all my efforts, the stellar ages determined from lithium are, with very few exceptions, different from the theoretical estimations. Indeed the trend of my results is not consistent with the literature. For some of the 17 selected systems the lithium age cannot be defined at all for two reasons. Often, derived bayesian masses are too large to experience the lithium depletion. Furthermore, many systems show a lithium abundance larger than the primordial value. As to MML 53, RXJ0529.4+0041 A, RX J0530.7-0434, RX J0532.1-0732, V773 tau A, V1174 Ori and V4046 Sgr the lithium age is defined only for a mixing length as large as the solar value. In particular for V1174 Ori, a perfect match between lithium and bayesian ages is obtained for the primary component in the case of a mixing length equal to 1.25, while no match exists for the secondary. Moreover, for the secondary component of RXJ0529.4+0041 A a perfect accord between lithium and bayesian ages is obtained for a mixing length equal to 1.50 and 1.74, while no match is found for the primary.

Since for the SB2 systems the masses of the two components are not known *at priori*, applying the bayesian analysis with the mass ratio, on models computed with different mixing lengths, different values of age are expected. For the first time, I tried then to determine this invisible parameter as the one whose age is in agreement with the lithium age. The associated masses are assumed as representative of the system. Unfortunately, I never reached

the good agreement. Anyway, I found, as a general trend, a better agreement between lithium age and bayesian age estimation for the highest mixing length values, in contrast with commonly reported in the literature for the PMS stars.

One of the main discrepancies comes from the observed lithium abundance. Not only it can be larger than expected from evolutionary codes, but even much larger then the value commonly ascribed to the primordial nucleo-synthesis. There are two possible explanations for such a large values. Lithium appear to be more abundant because of surface effects in the stellar photosphere. Leone (2007) has quantified the increment in the equivalent width of lithium lines in presence of few kilo gauss (solar spot) magnetic fields. Another possibility is related to the production of lithium. In this case, the initial lithium value of the cloud would be unknown and its depletion unpredictable. Such very old hypothesis has proved just this year by Tajitu et al. (2015) that have discovered the presence of the lithium lines in the spectrum of the classical nova V339 Del.

APPENDIX A

Graphical outputs of Bayesian analysis

The huge graphical output of the bayesian analysis, however necessary to understand the behavior of single objects, has been here stacked.

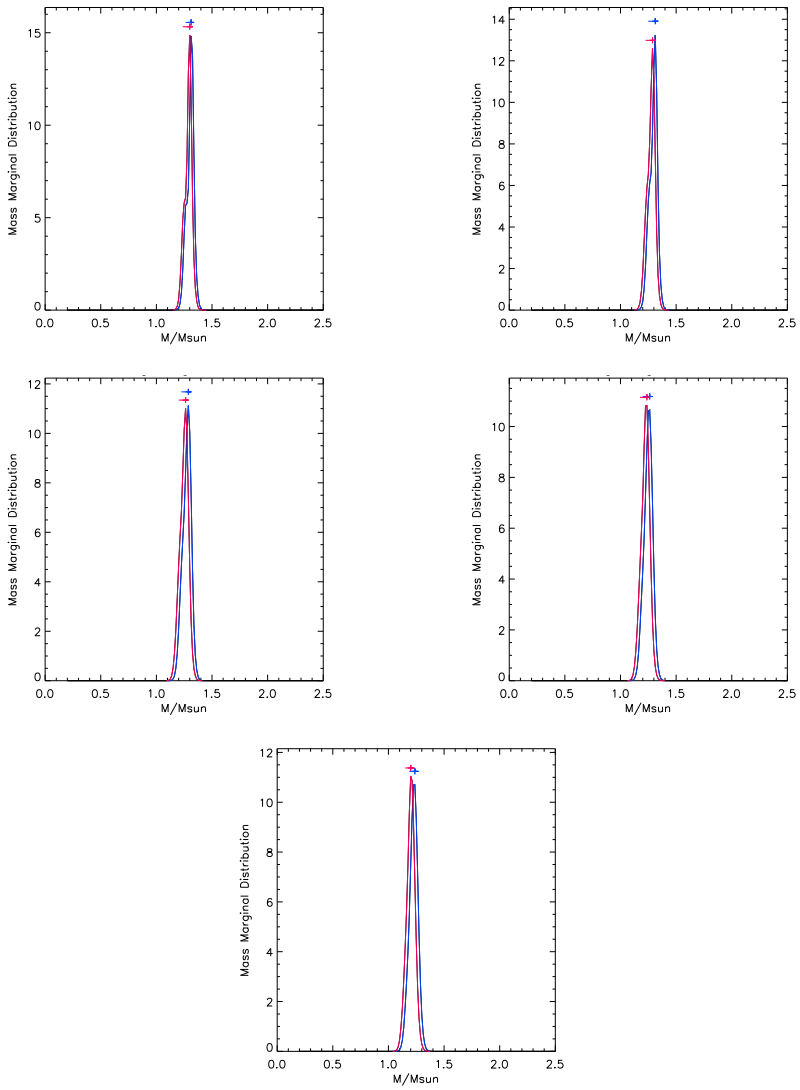

Figure A.1: AKSco Mass Marginal Distribution for primary (blue) component and secondary (red) component.

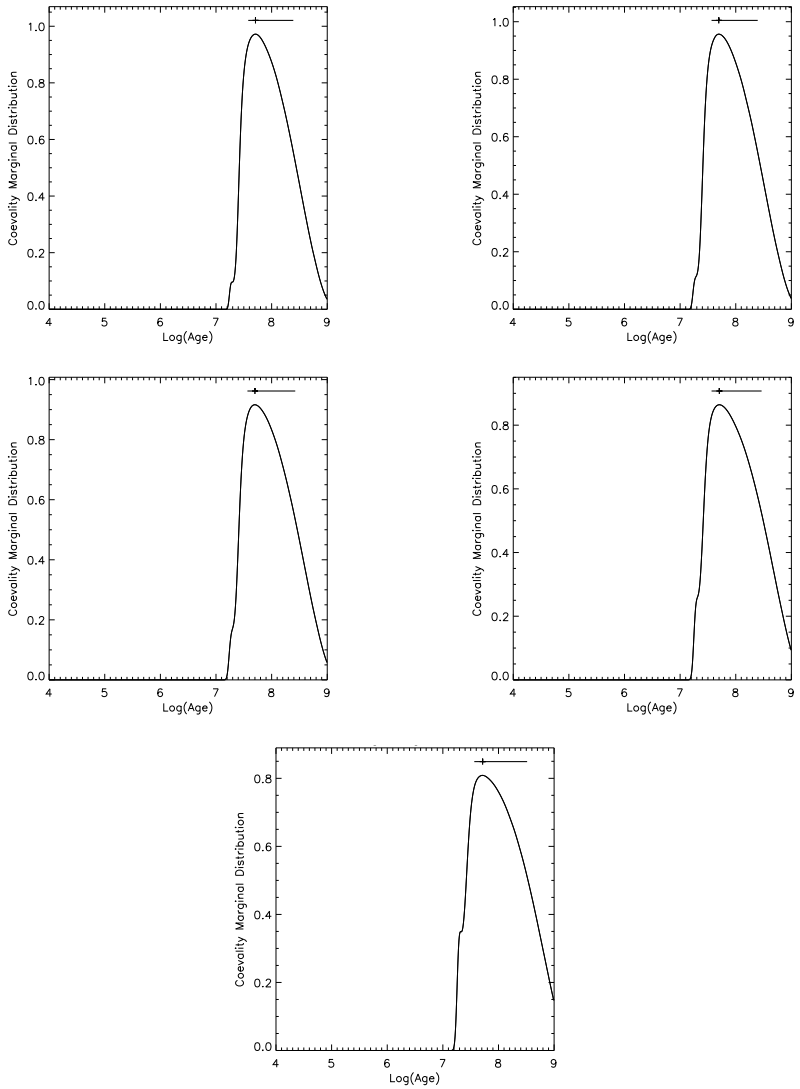

Figure A.2: AK Sco Age Marginal Distribution

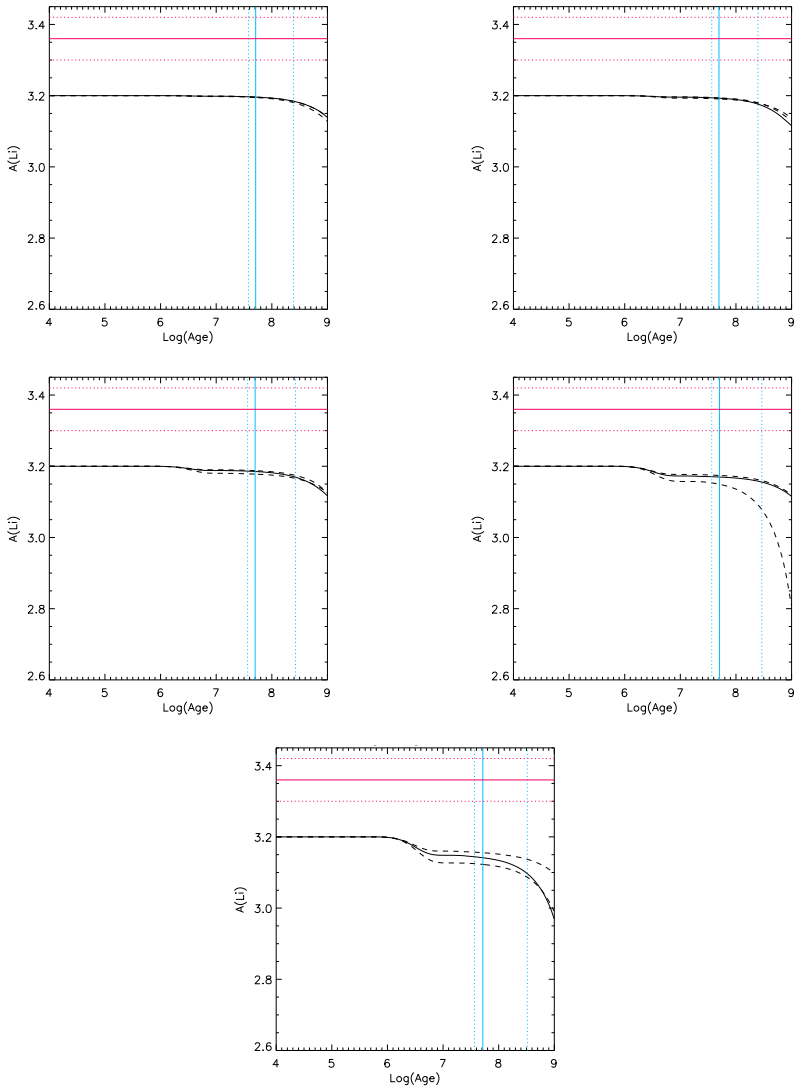

Figure A.3: AK Sco lithium results for primary component.

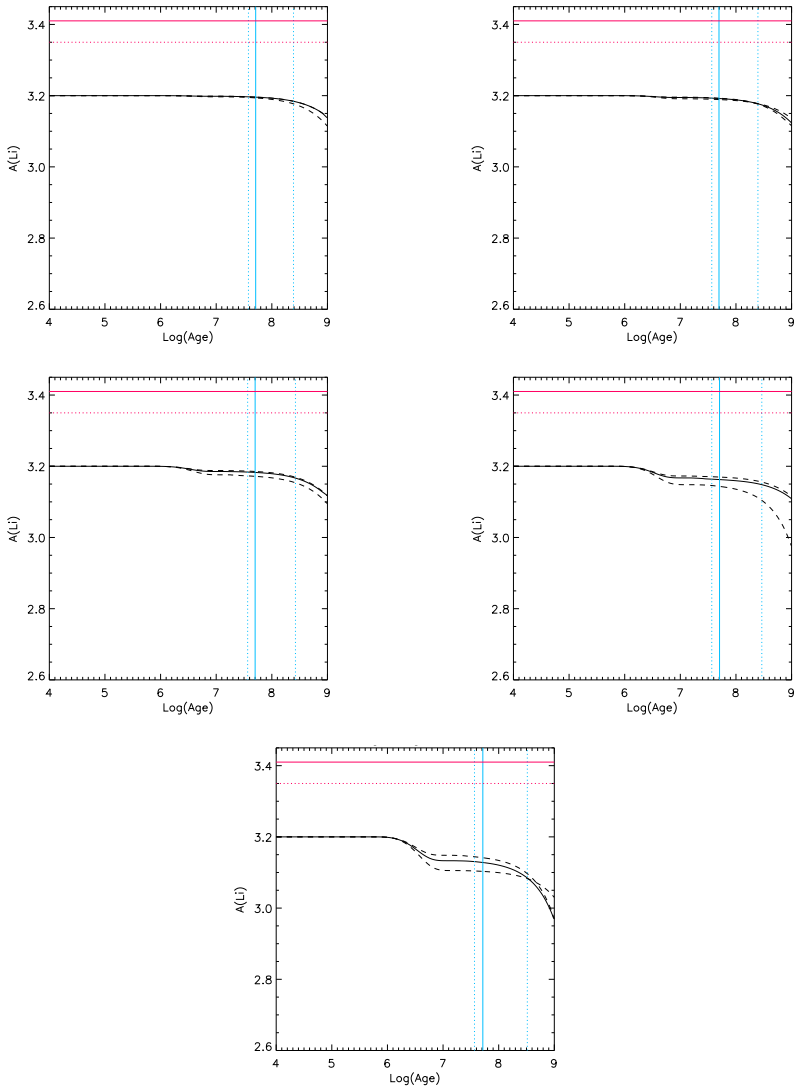

Figure A.4: AK Sco lithium results for secondary component.

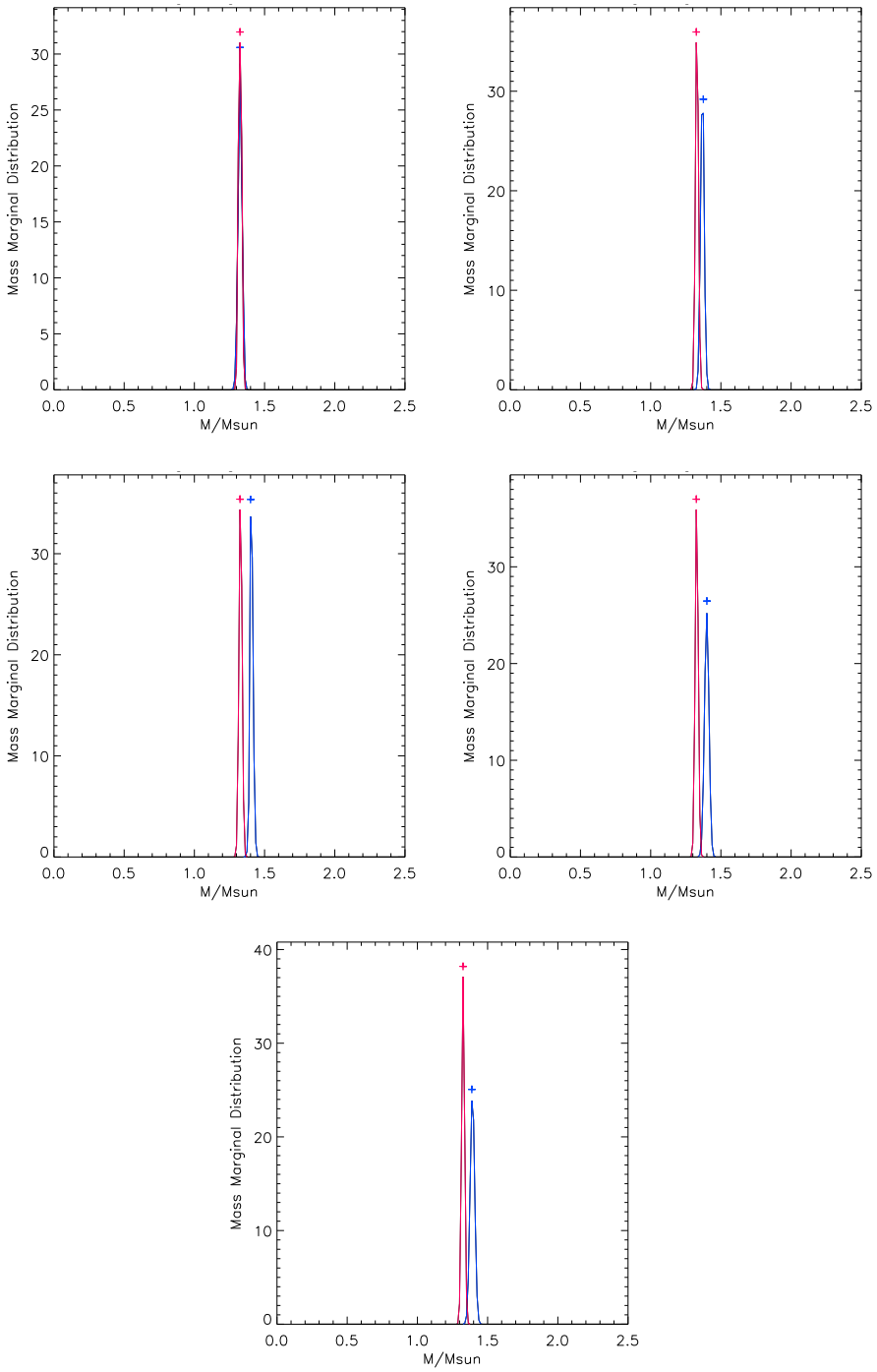

Figure A.5: ASASJ052821+0338.5 Mass Marginal Distribution for primary (blue) component and secondary (red) component.

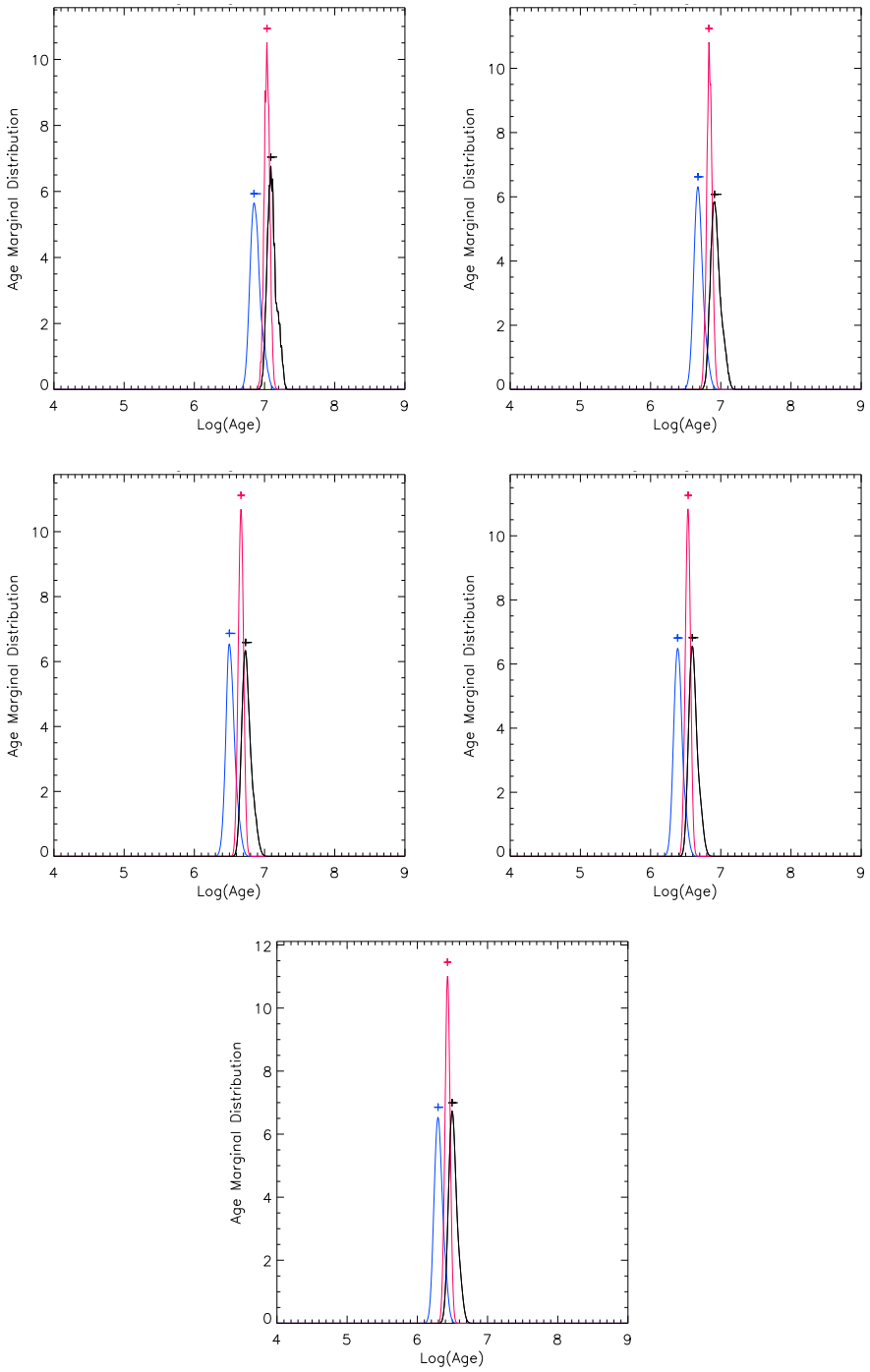

Figure A.6: ASASJ052821+0338.5 Age Marginal Distribution for the primary (blue) component, the secondary (yellow) component and for coevality (red).

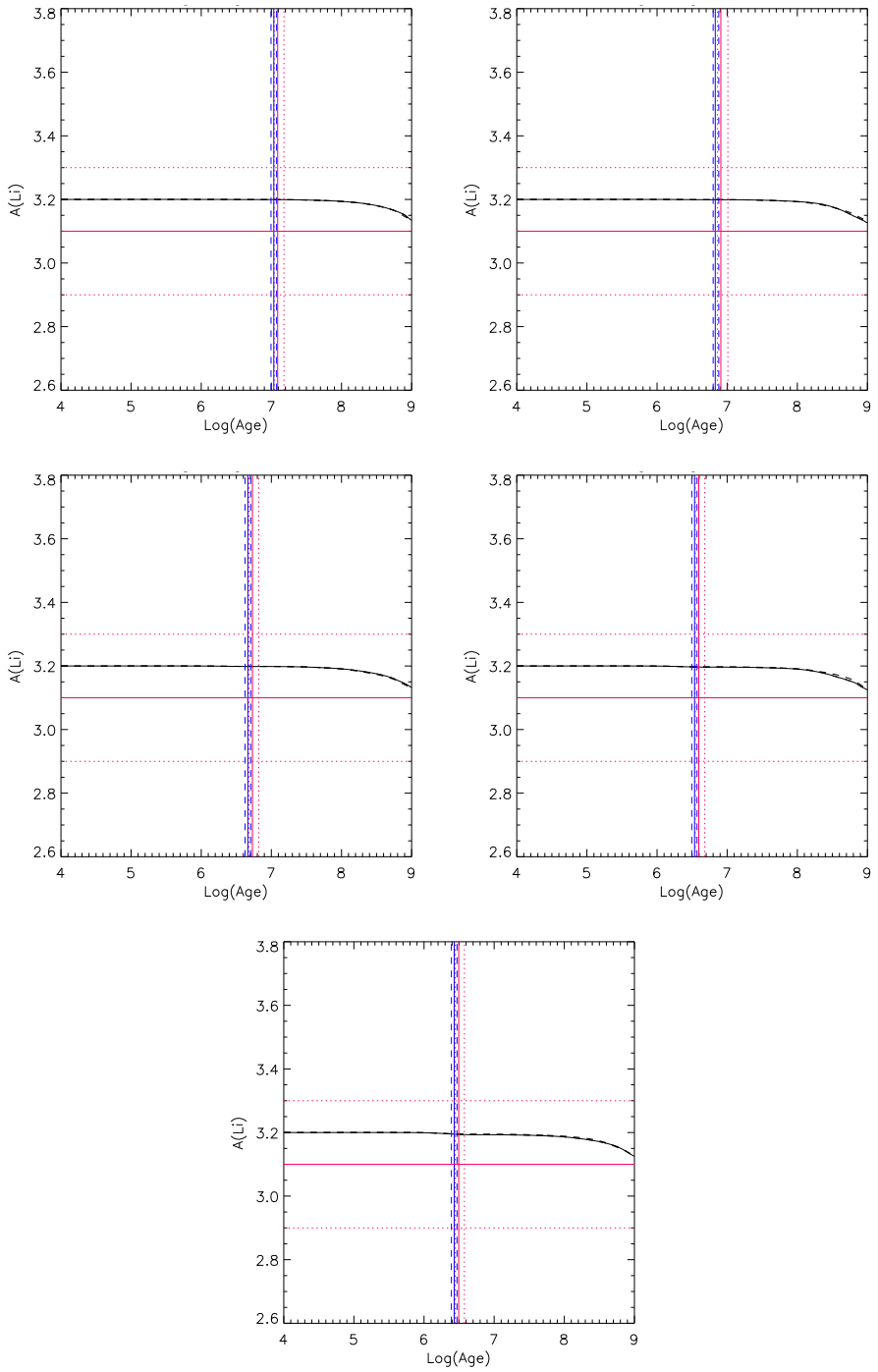

Figure A.7: ASASJ052821+0338.5 lithium results for primary component

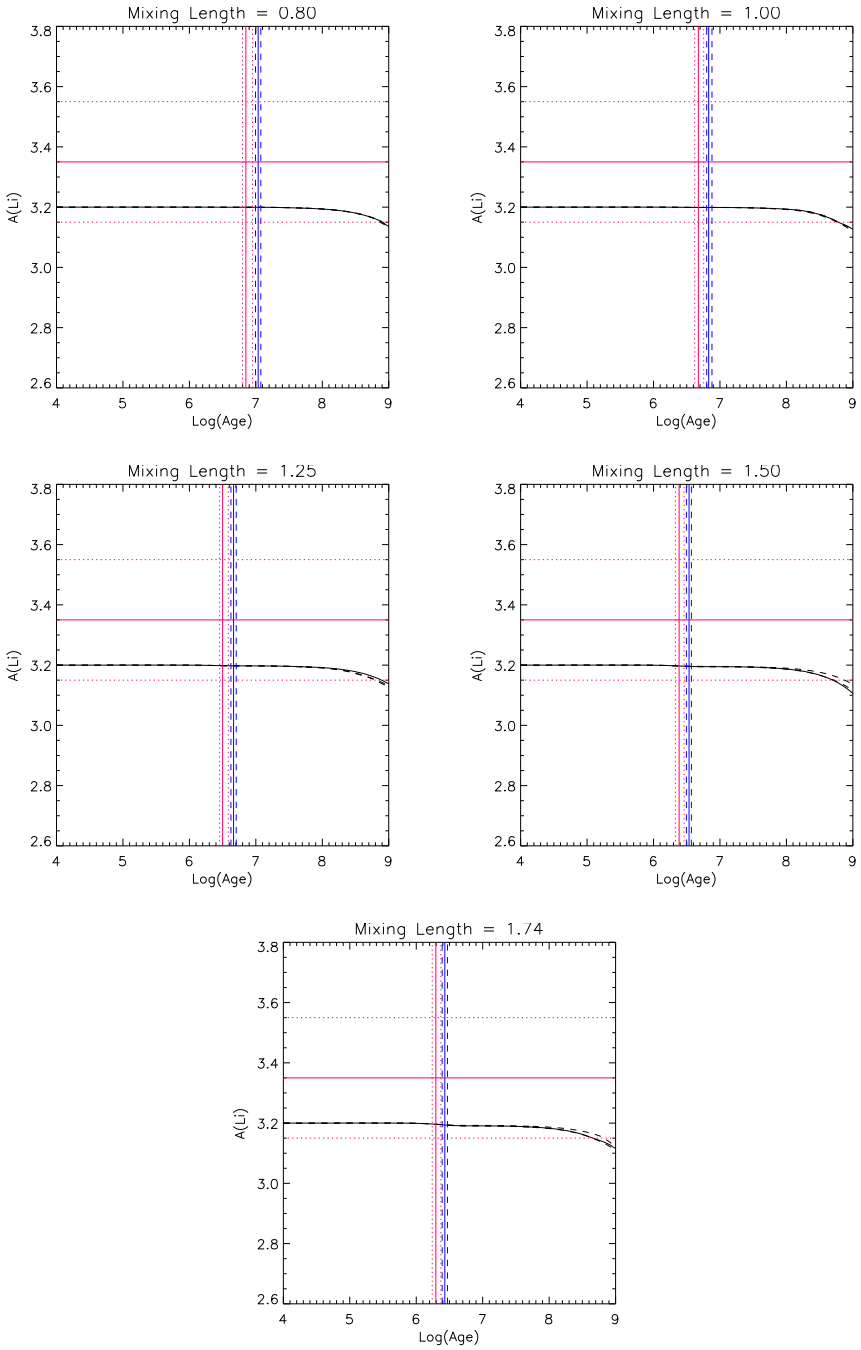

Figure A.8: ASASSJ052821+0338.5 lithium results for secondary component

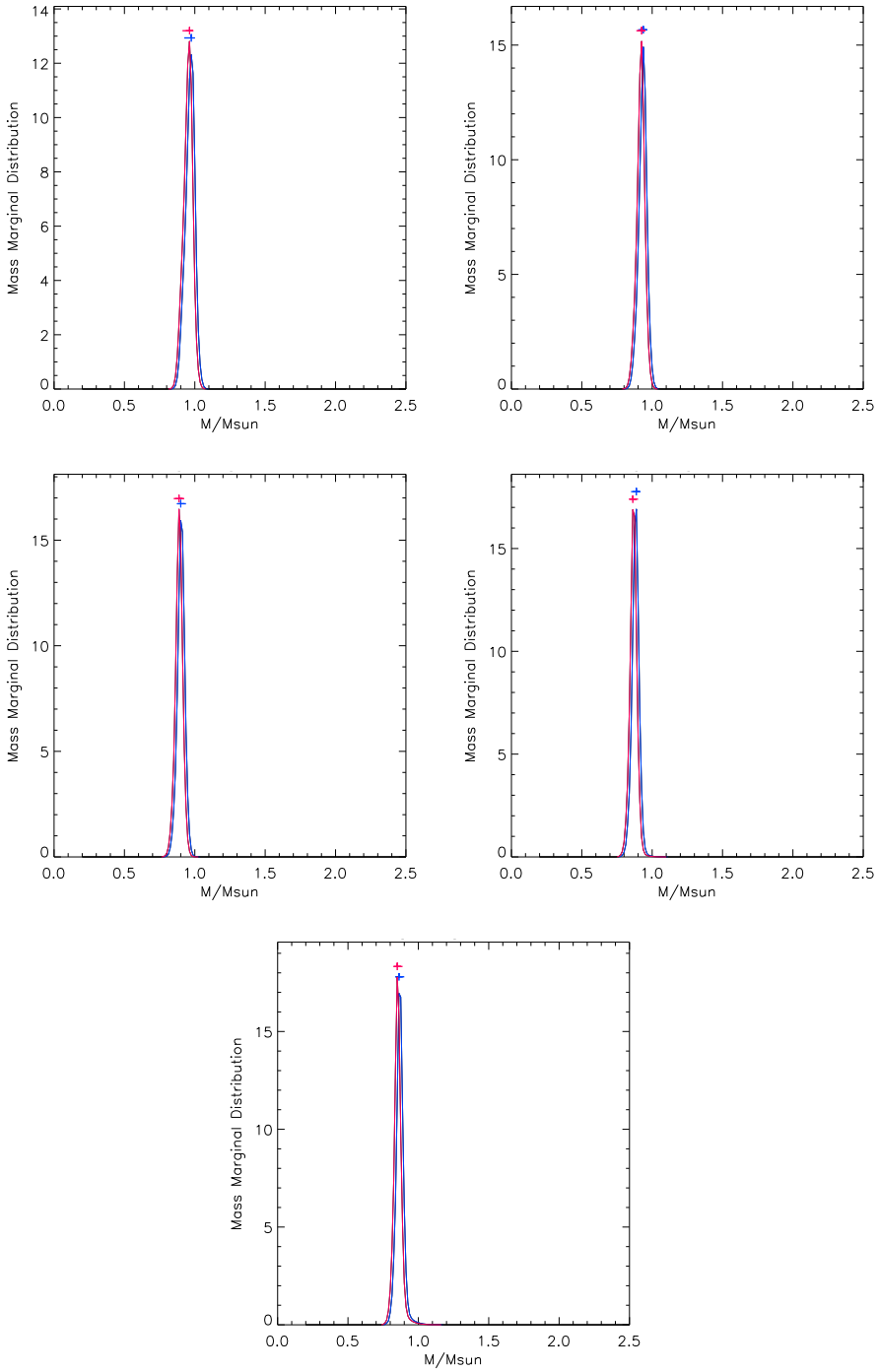

Figure A.9: GSC 06213-00306 Mass Marginal Distribution for primary (blue) component and secondary (red) component.

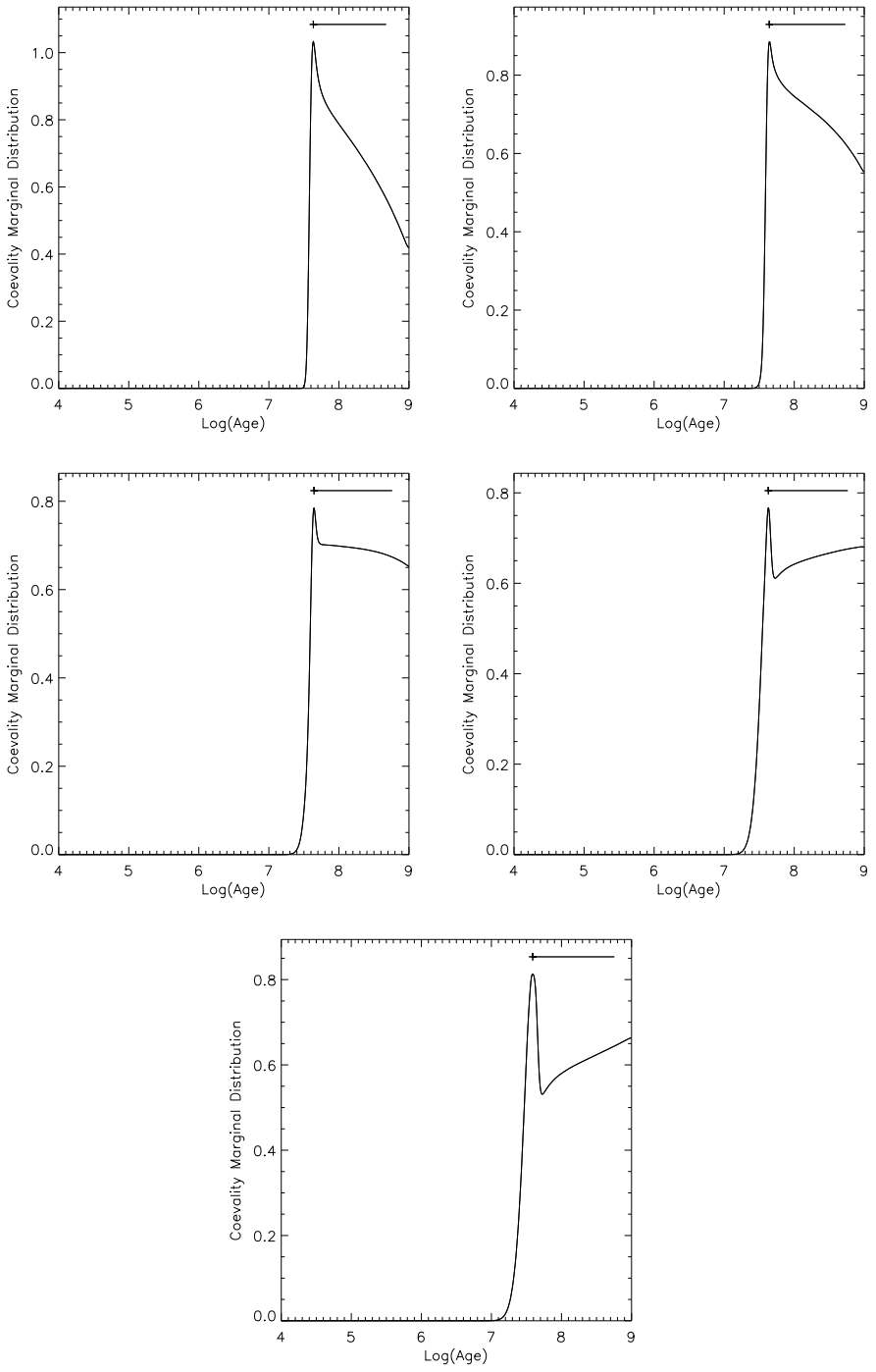

Figure A.10: GSC 06213-00306 Age Marginal Distribution for the primary (blue) component, the secondary (yellow) component and for coevality (red).

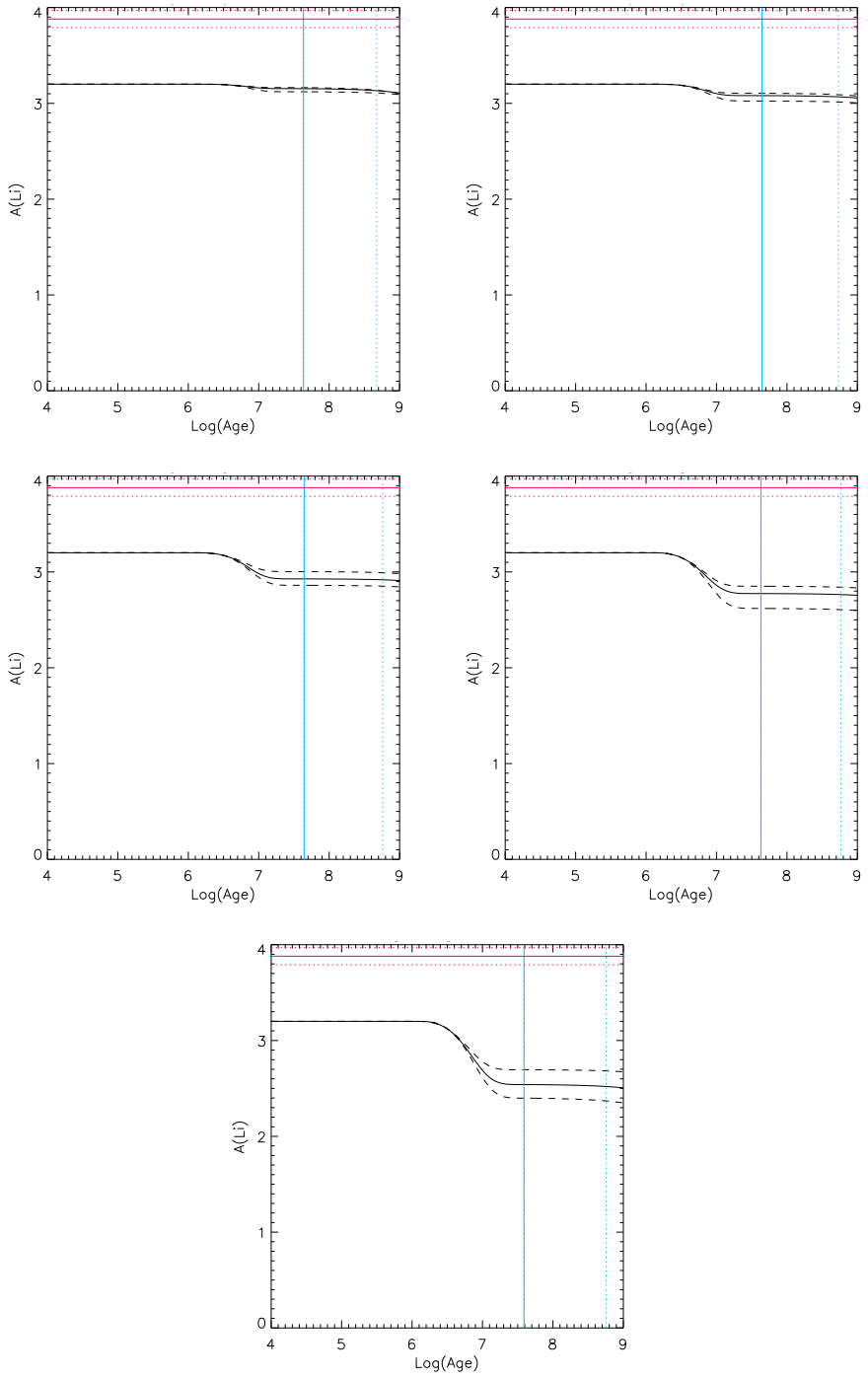

Figure A.11: GSC 06213-00306 lithium results for primary component

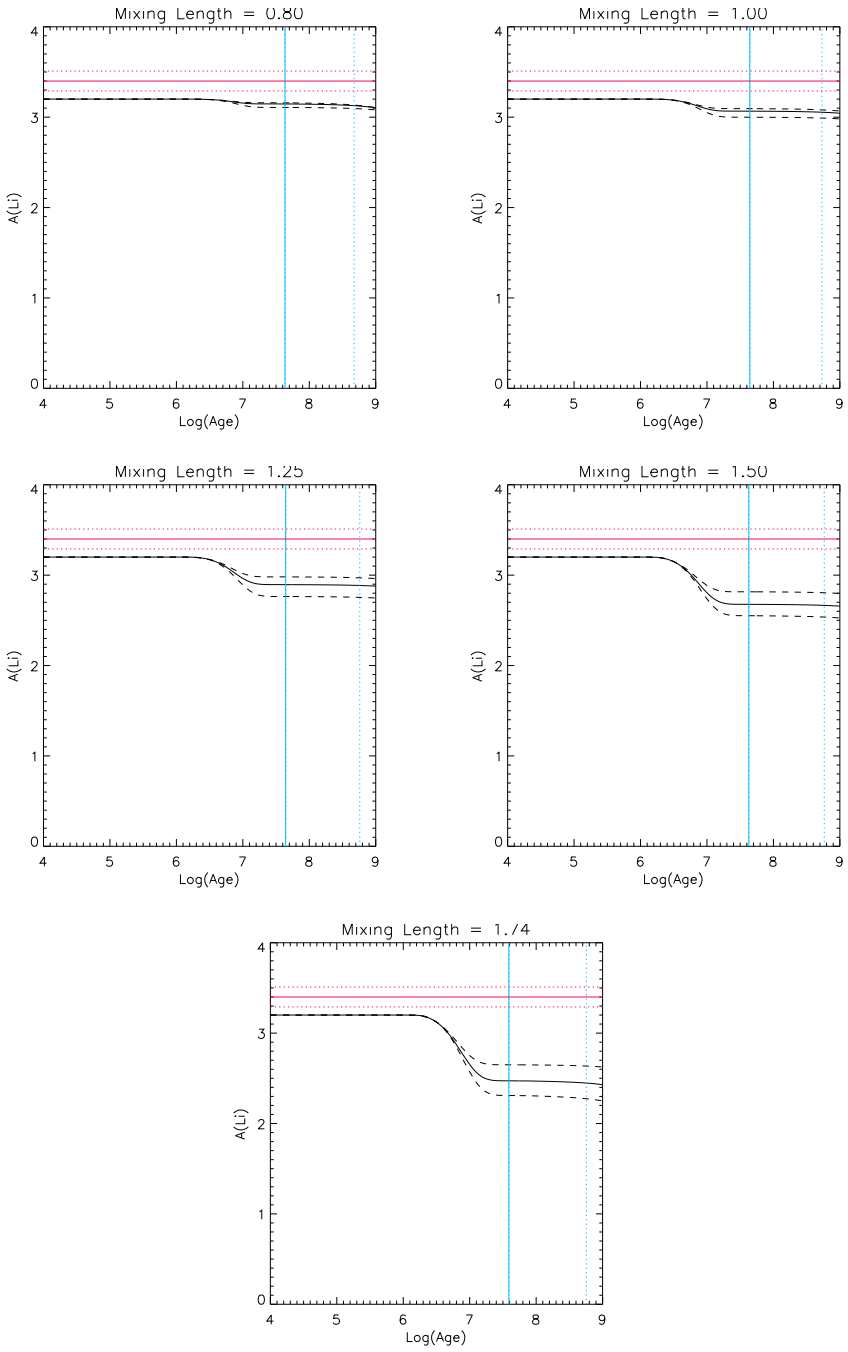

Figure A.12: GSC 06213-00306 lithium results for secondary component

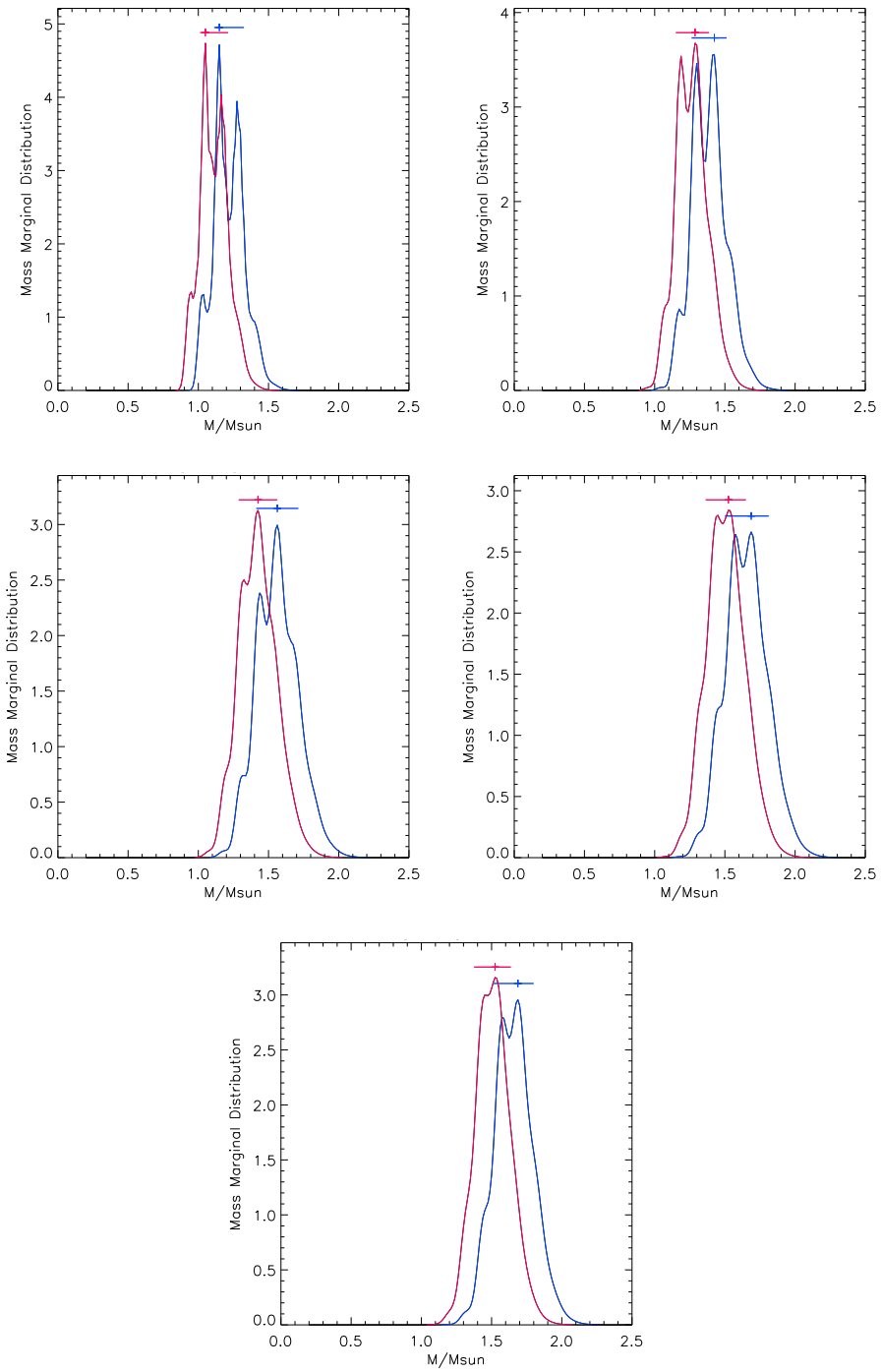

Figure A.13: HD155555 Mass Marginal Distribution for primary (blue) component and secondary (red) component.

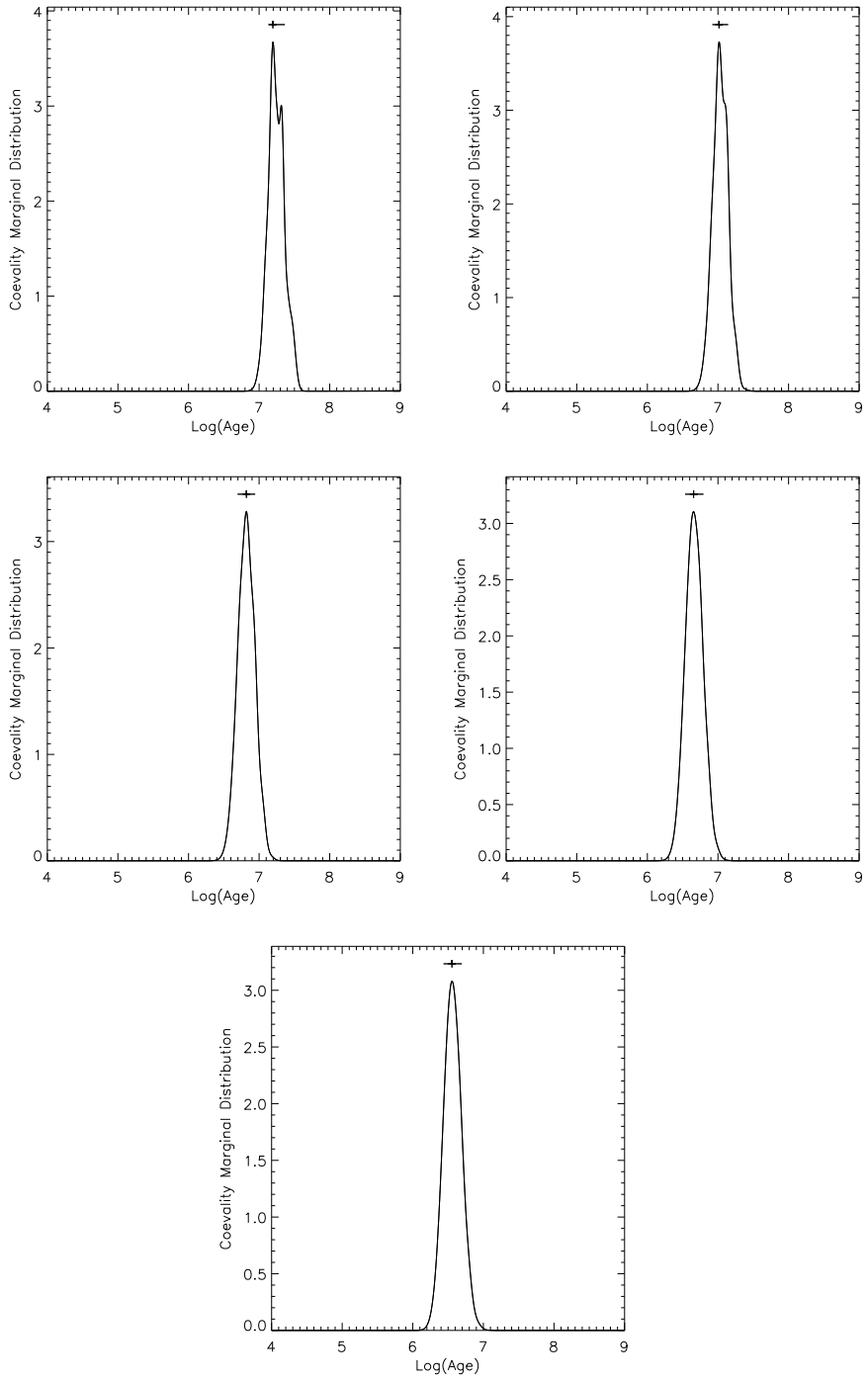

Figure A.14: HD155555 Age Marginal Distribution for the primary (blue) component, the secondary (yellow) component and for coevality (red).

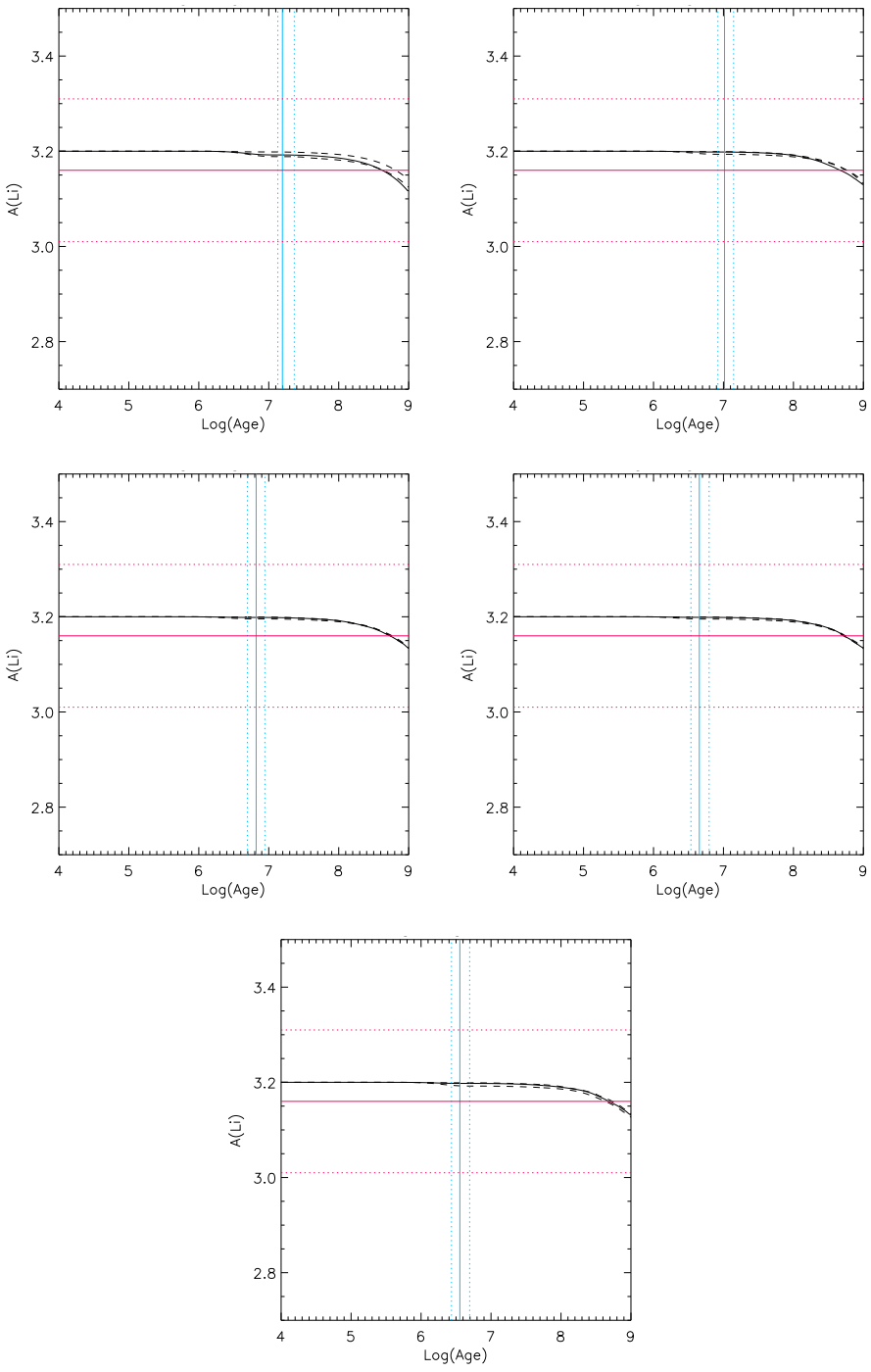

Figure A.15: HD155555 lithium results for primary component

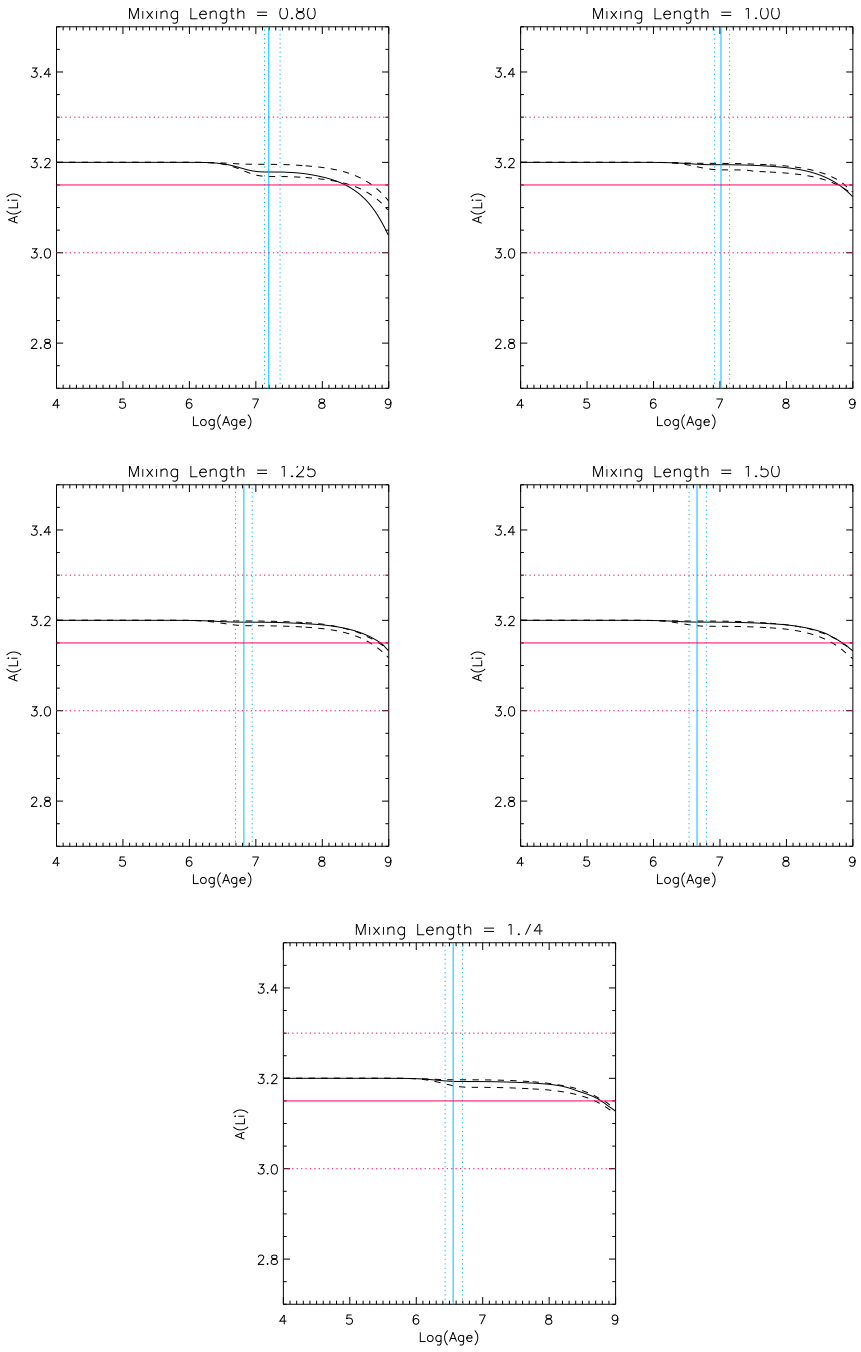

Figure A.16: HD155555 lithium results for secondary component

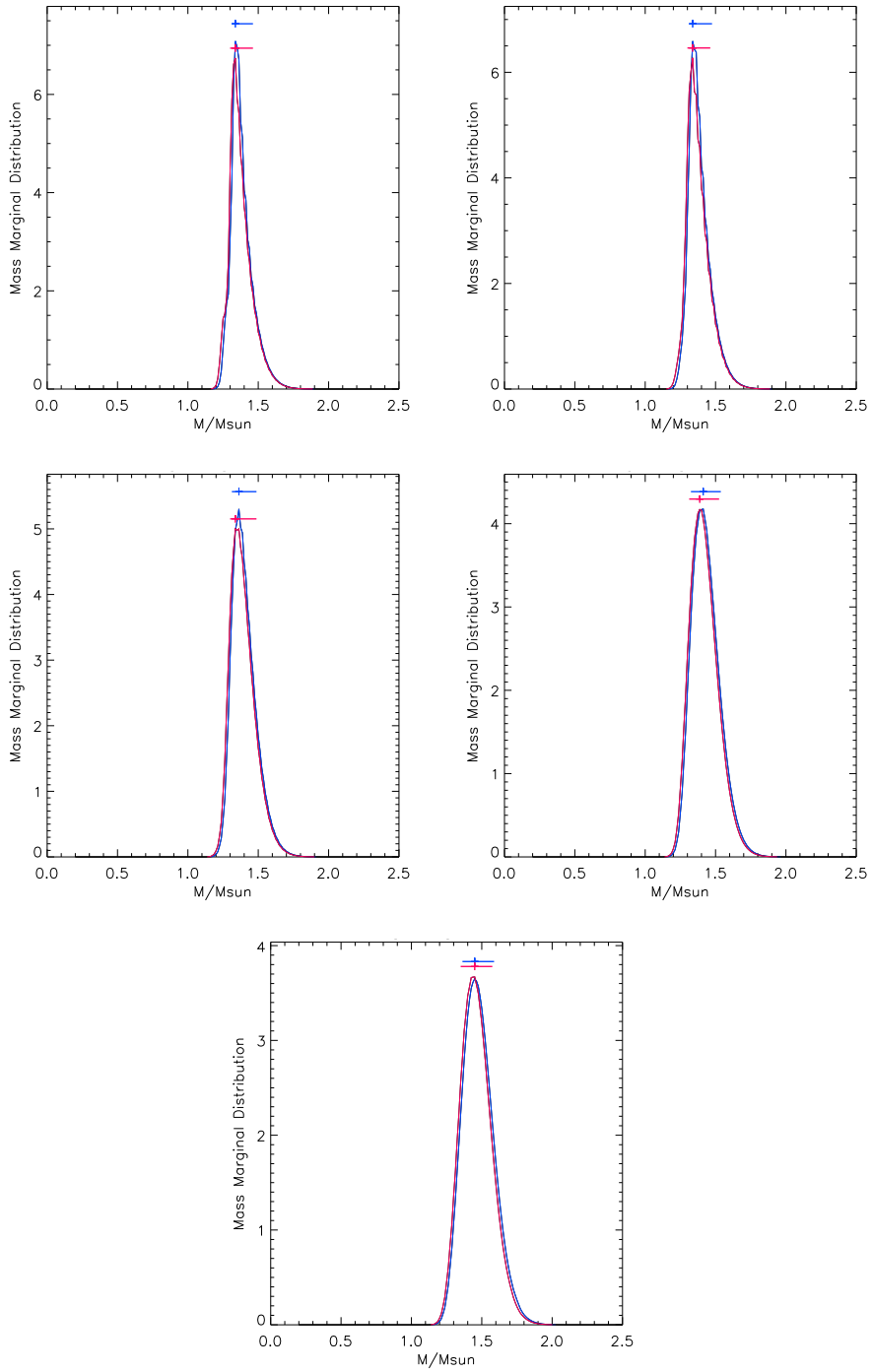

Figure A.17: HD34700A Mass Marginal Distribution for primary (blue) component and secondary (red) component.

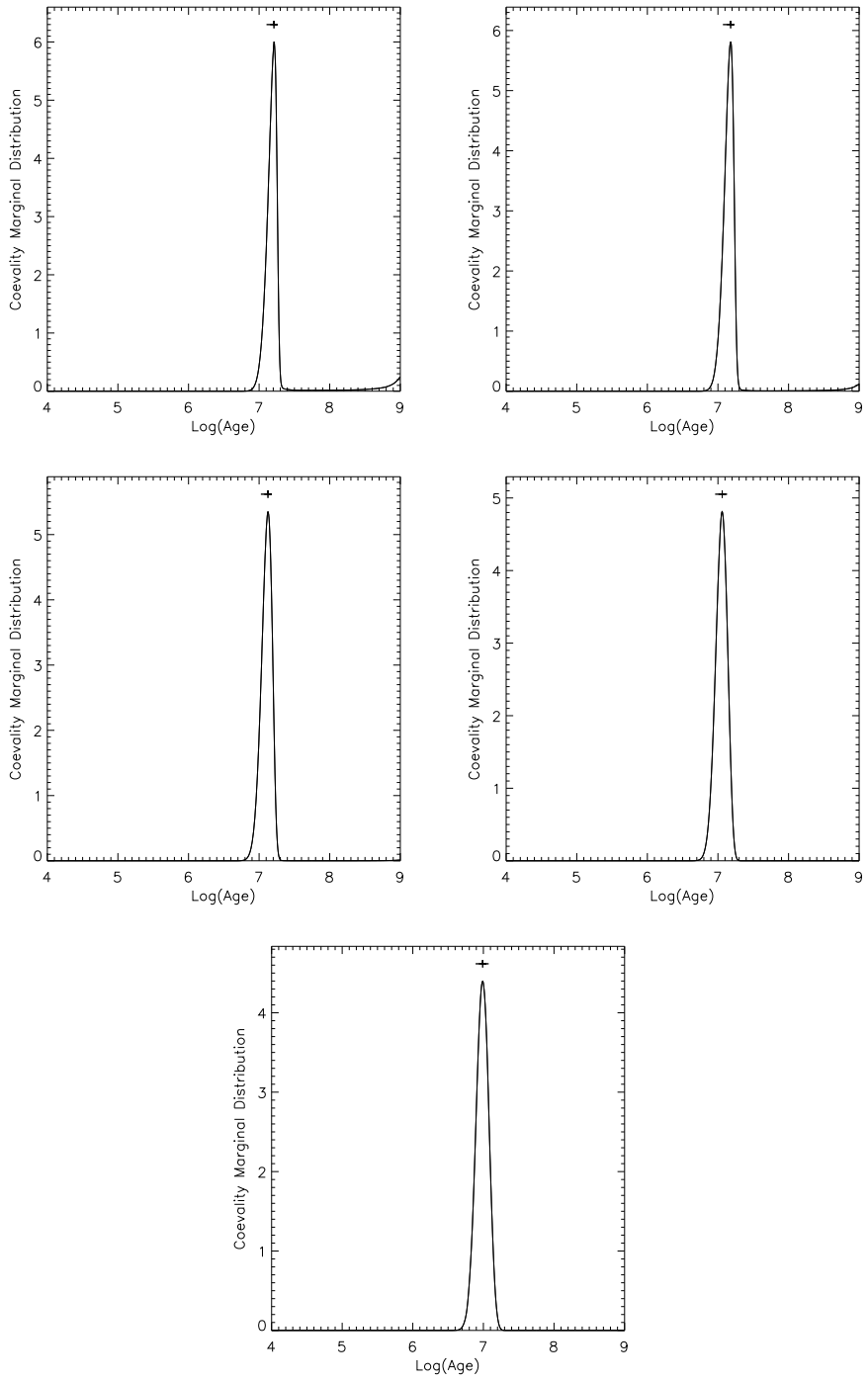

Figure A.18: HD34700A Age Marginal Distribution for the primary (blue) component, the secondary (yellow) component and for coevality (red).

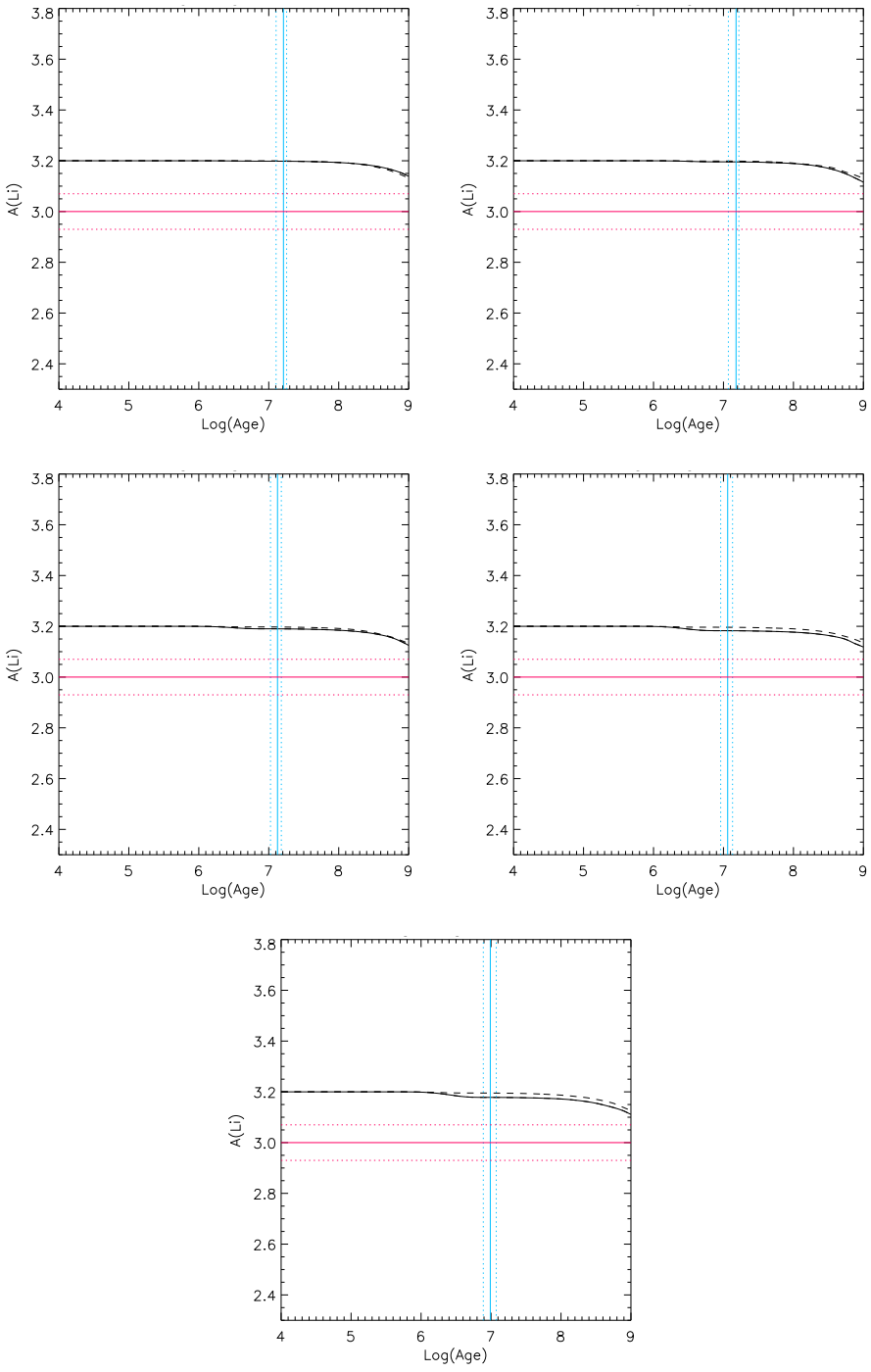

Figure A.19: HD34700A lithium results for primary component

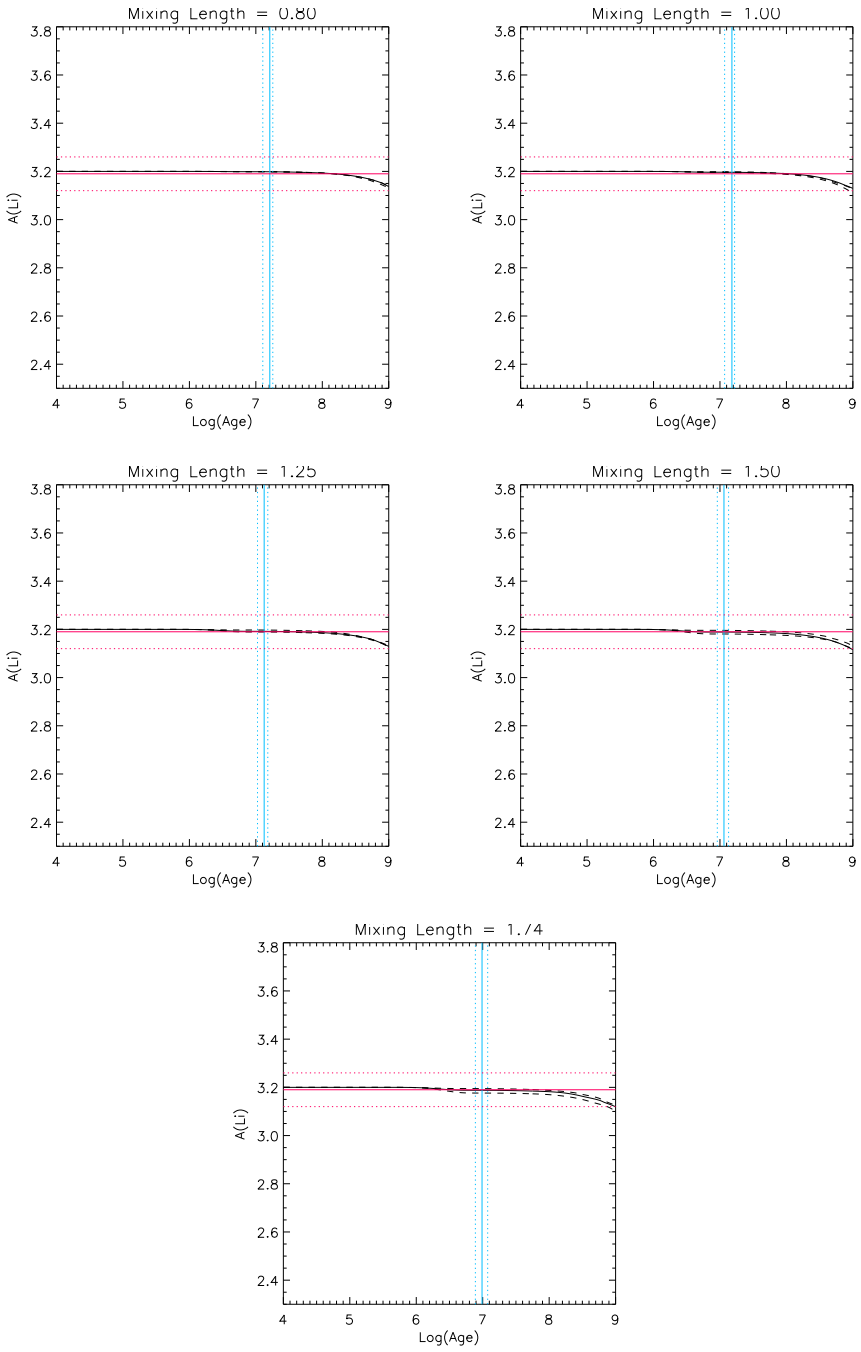

Figure A.20: HD34700A lithium results for secondary component

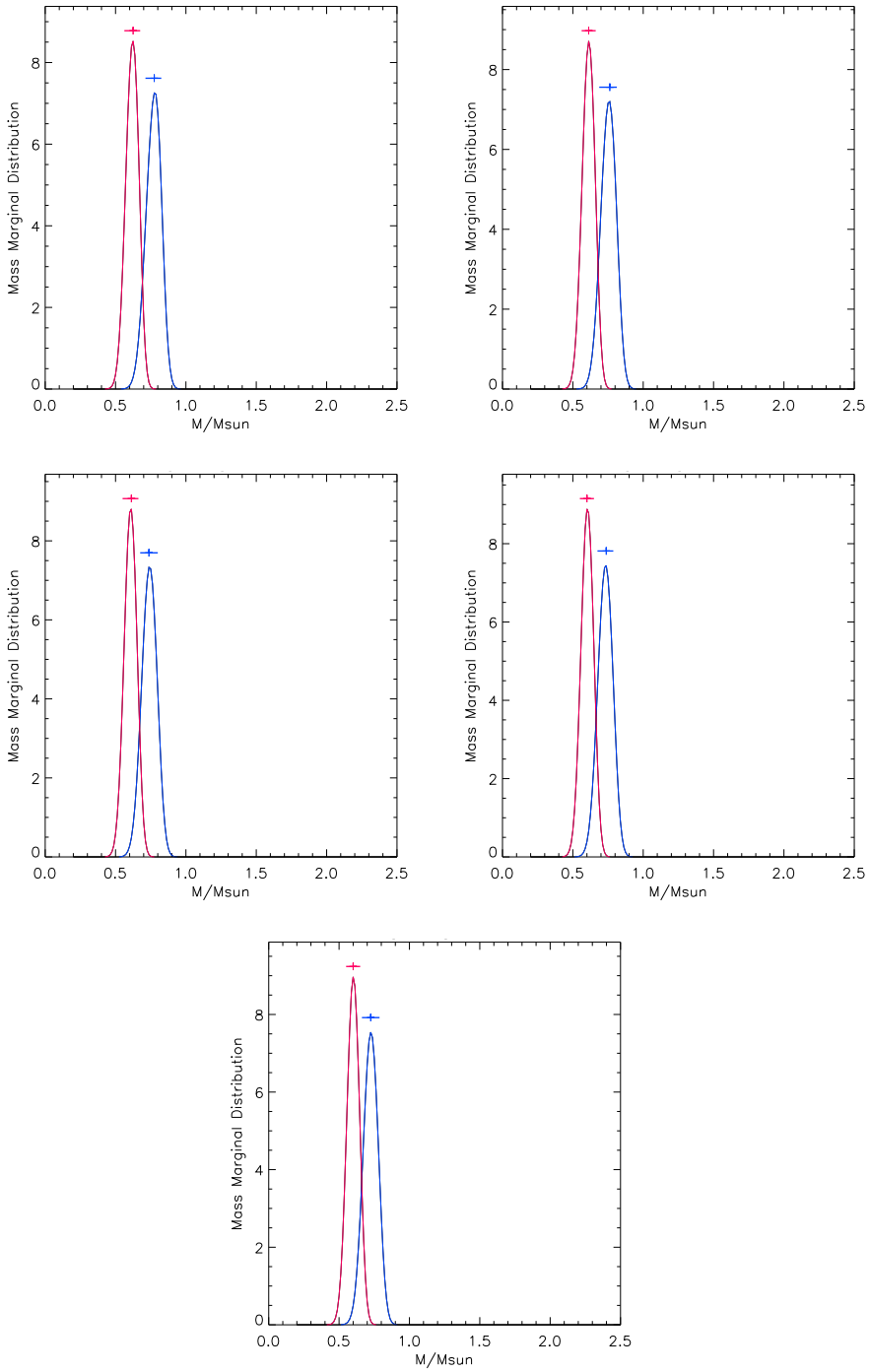

Figure A.21: HD98800 B Mass Marginal Distribution for primary (blue) component and secondary (red) component.

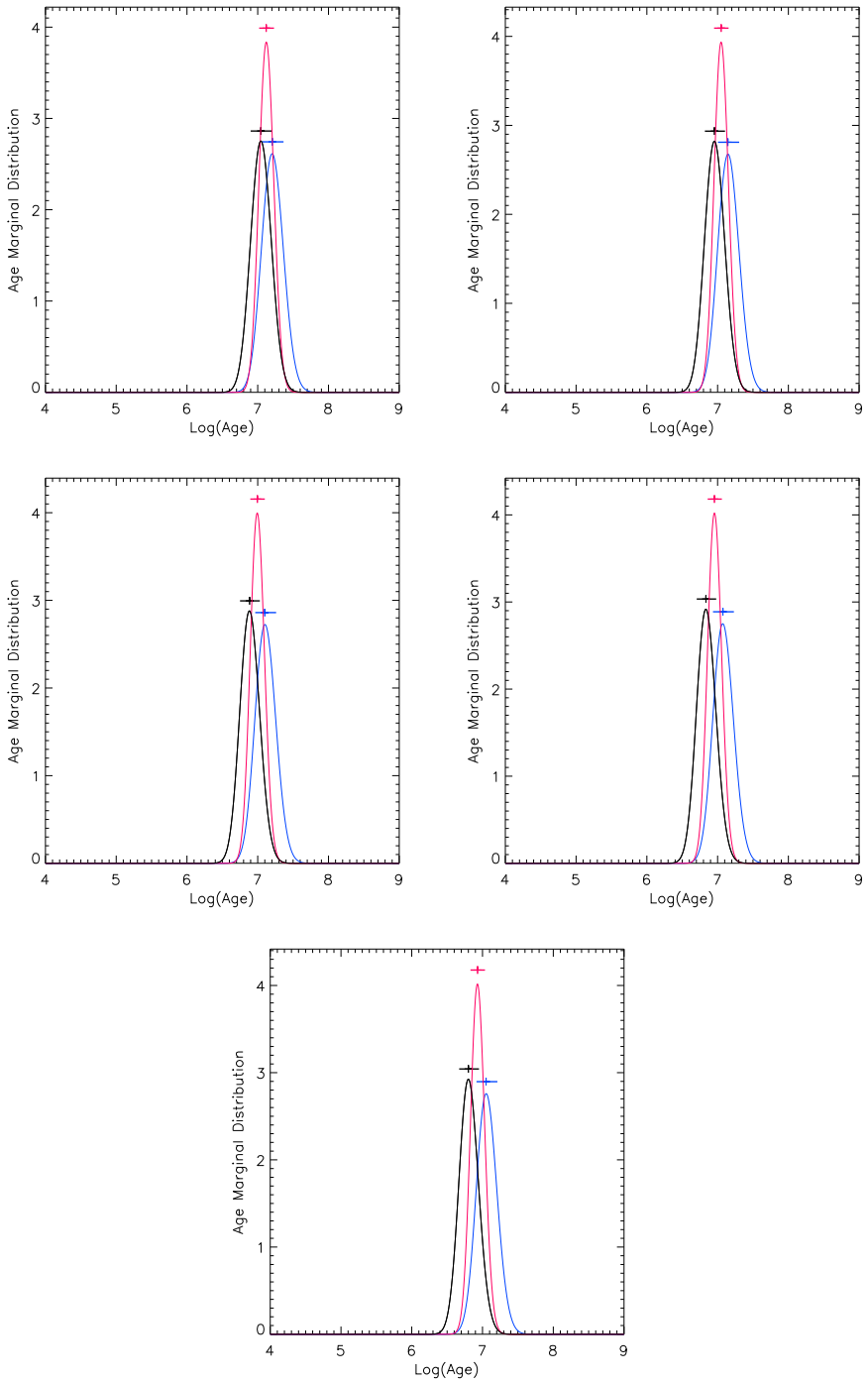

Figure A.22: HD98800 B Age Marginal Distribution for the primary (blue) component, the secondary (yellow) component and for coevality (red).

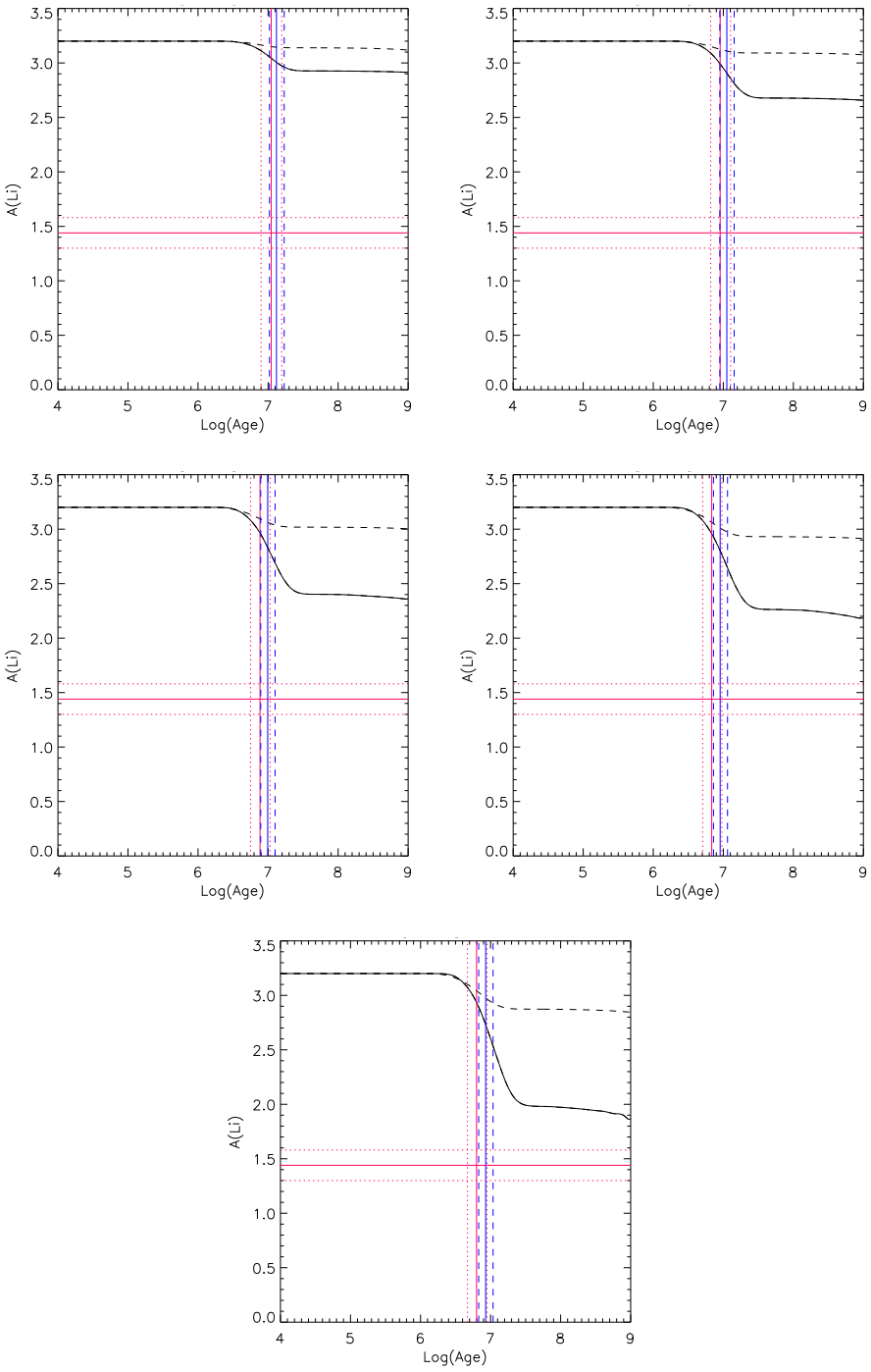

Figure A.23: HD98800 B lithium results for primary component

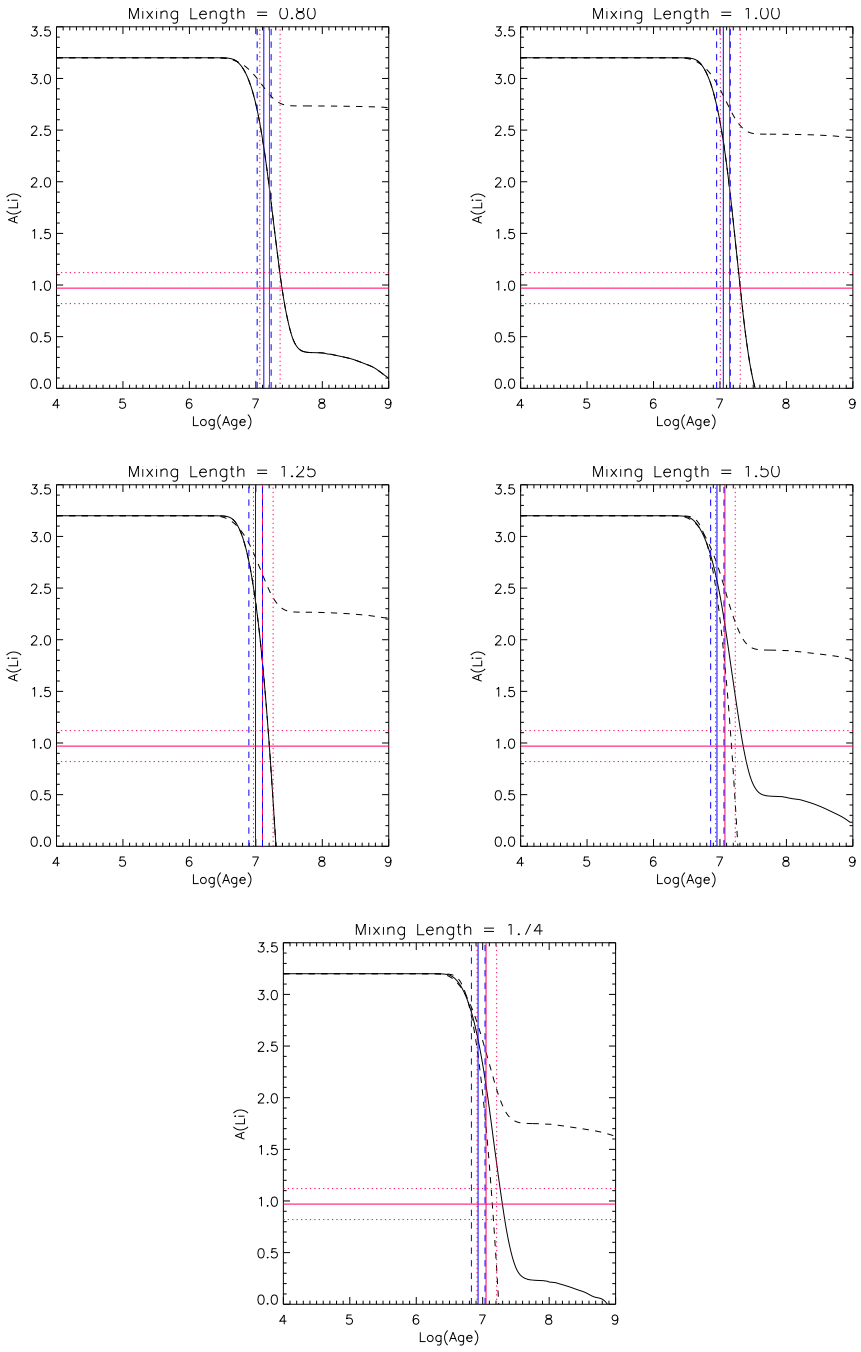

Figure A.24: HD98800 B lithium results for secondary component

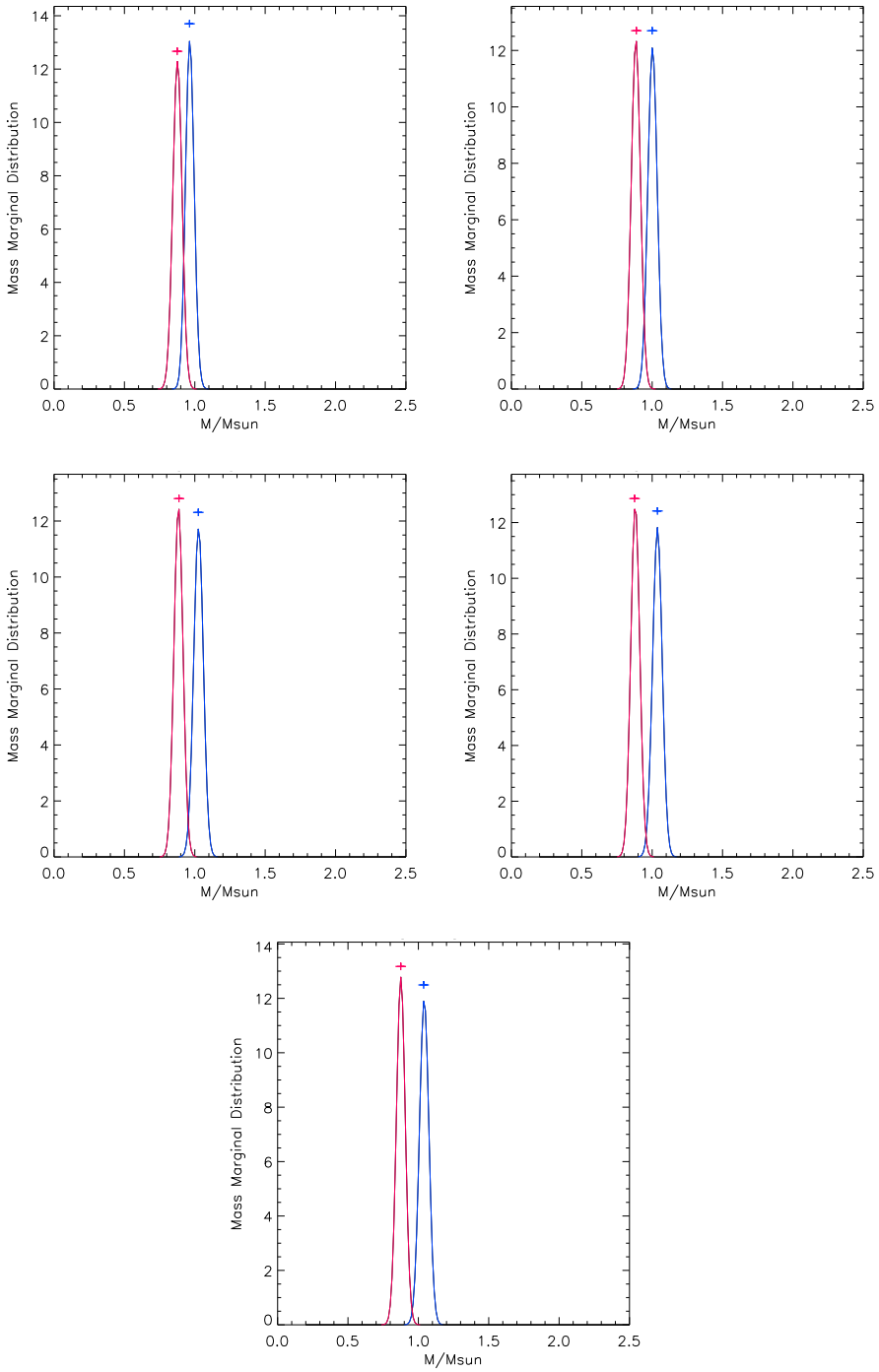

Figure A.25: MML 53 Mass Marginal Distribution for primary (blue) component and secondary (red) component.

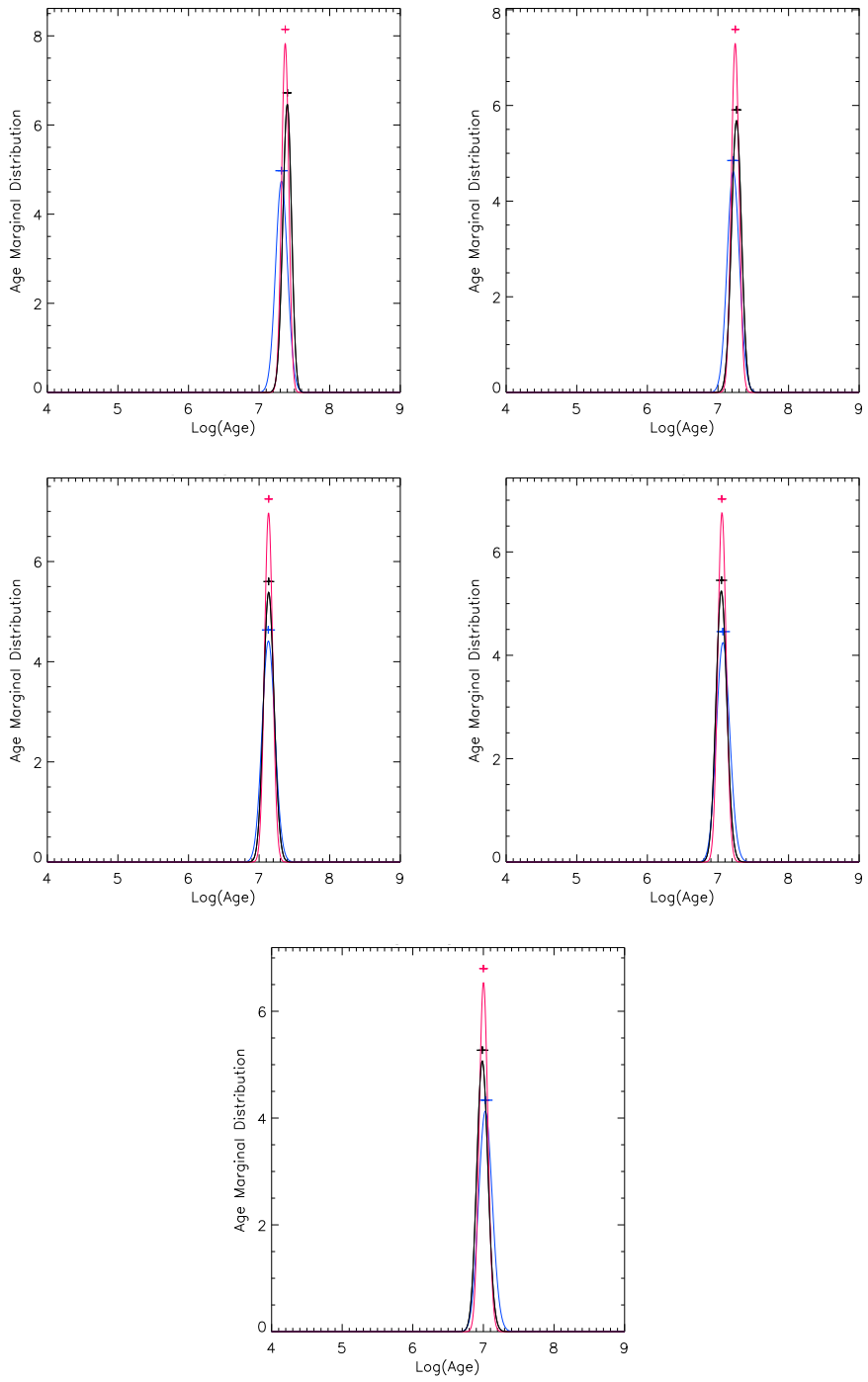

Figure A.26: MML 53 Age Marginal Distribution for the primary (blue) component, the secondary (yellow) component and for coevality (red).

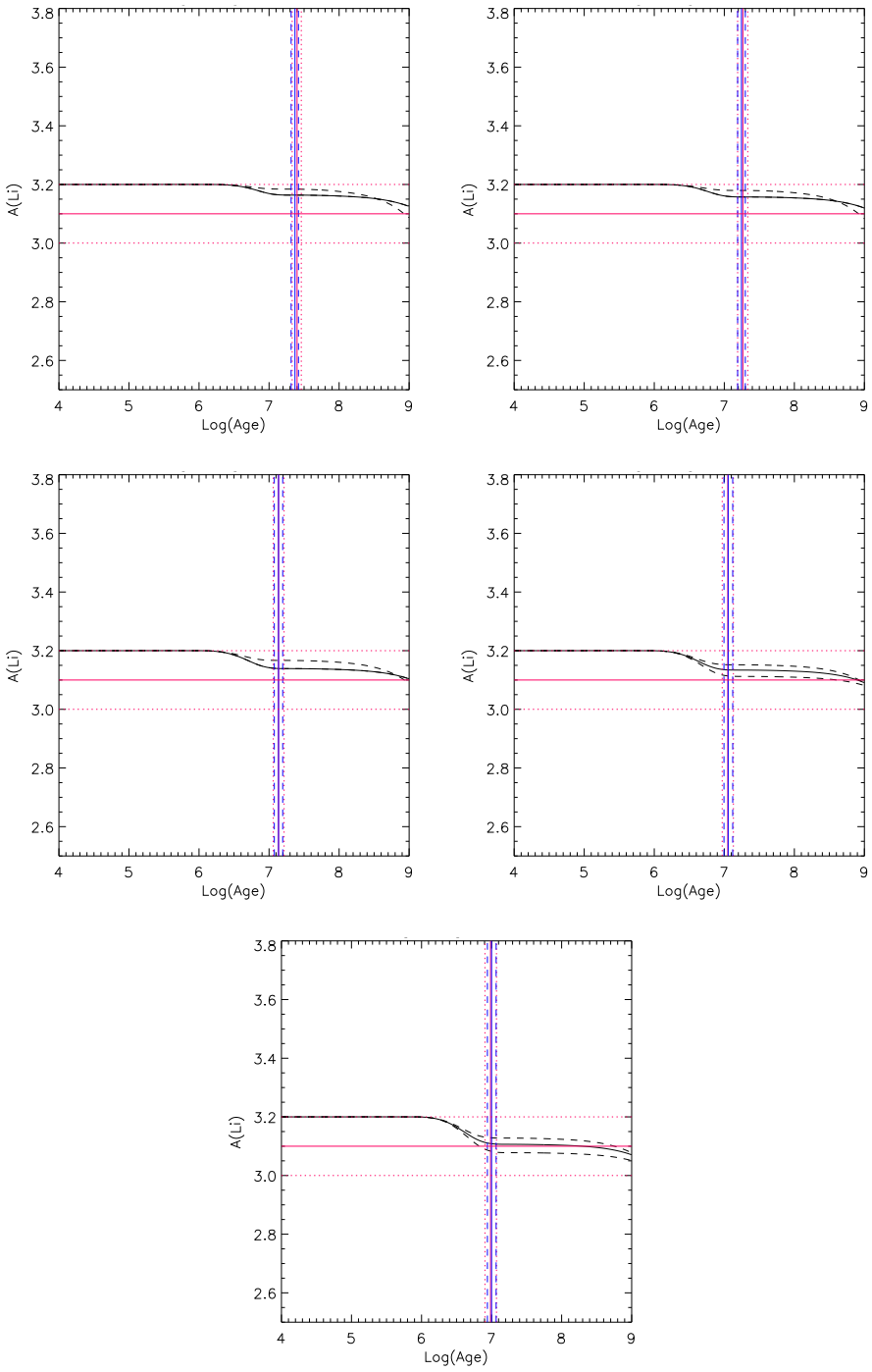

Figure A.27: MML 53 lithium results for primary component

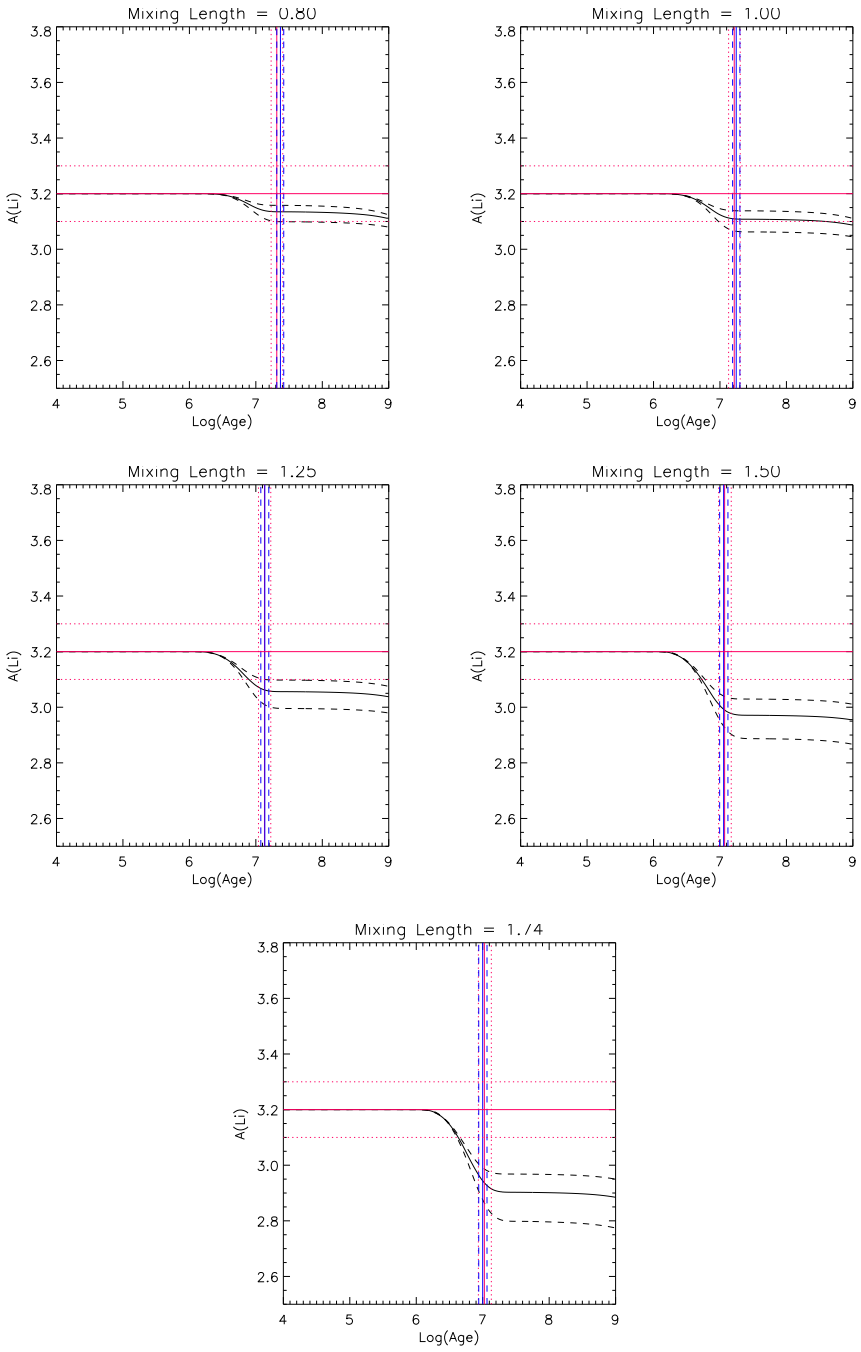

Figure A.28: MML 53 lithium results for secondary component

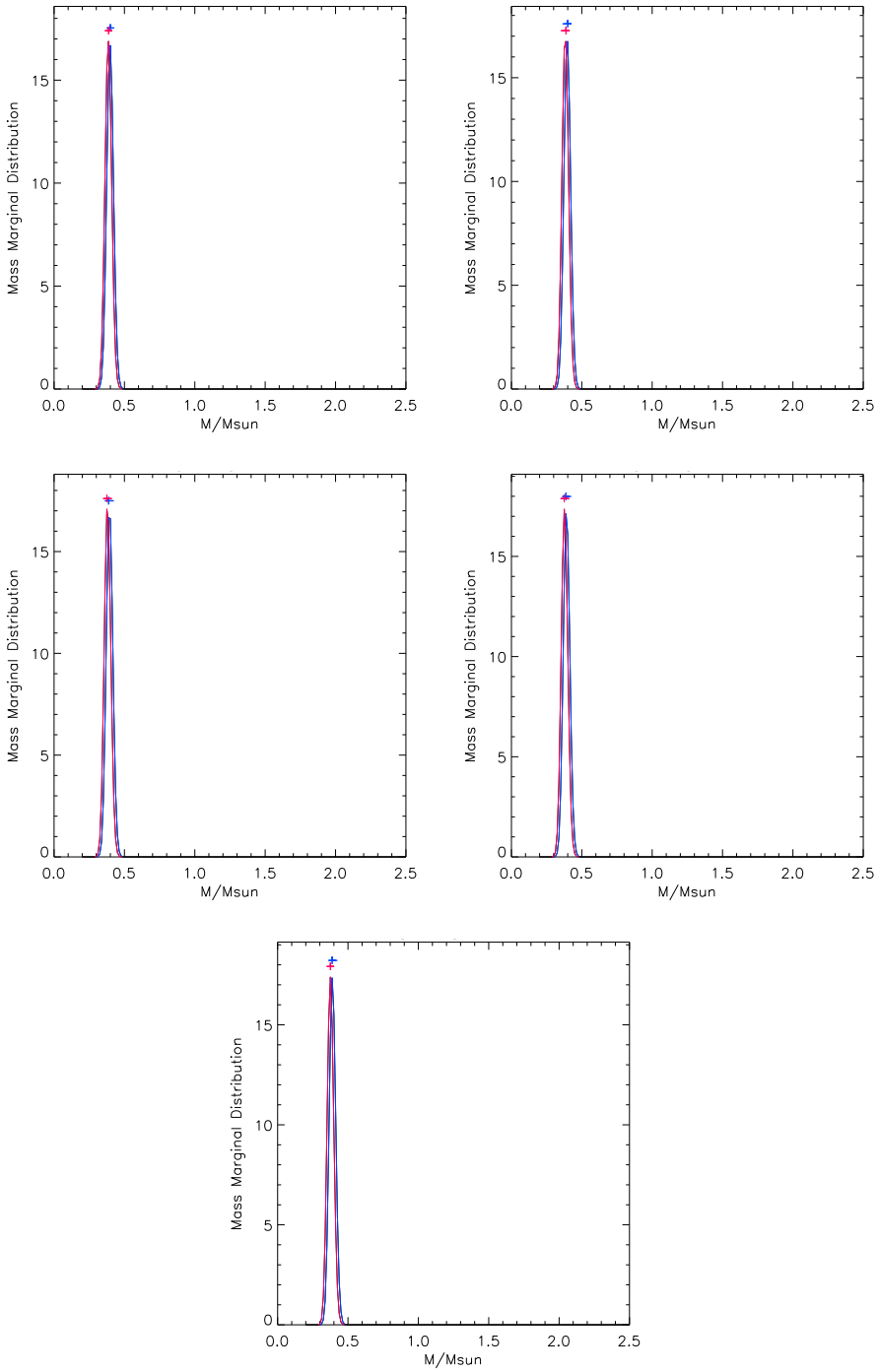

Figure A.29: PAR 1802 Mass Marginal Distribution for primary (blue) component and secondary (red) component.

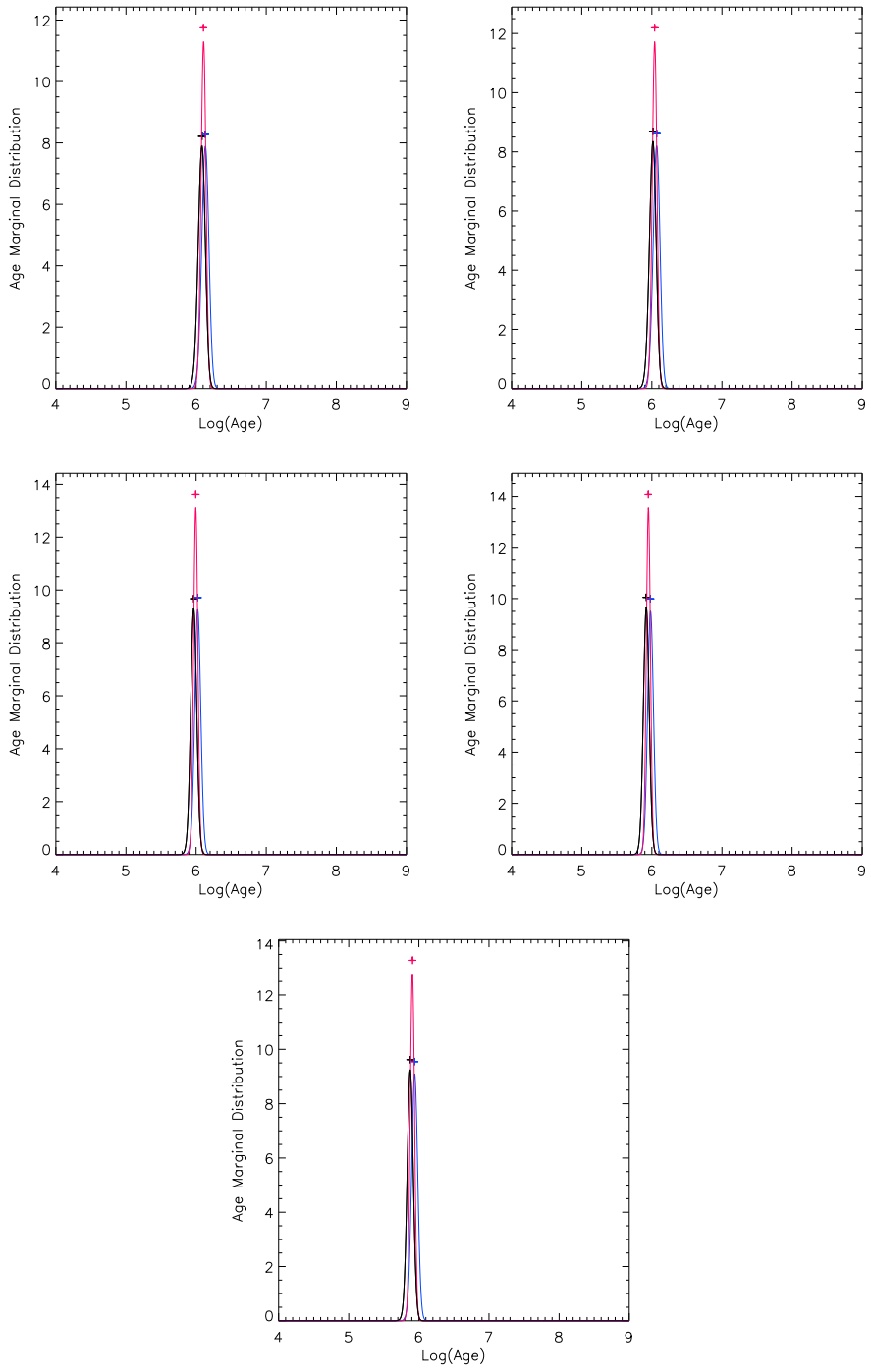

Figure A.30: PAR 1802 Age Marginal Distribution for the primary (blue) component, the secondary (yellow) component and for coevality (red).

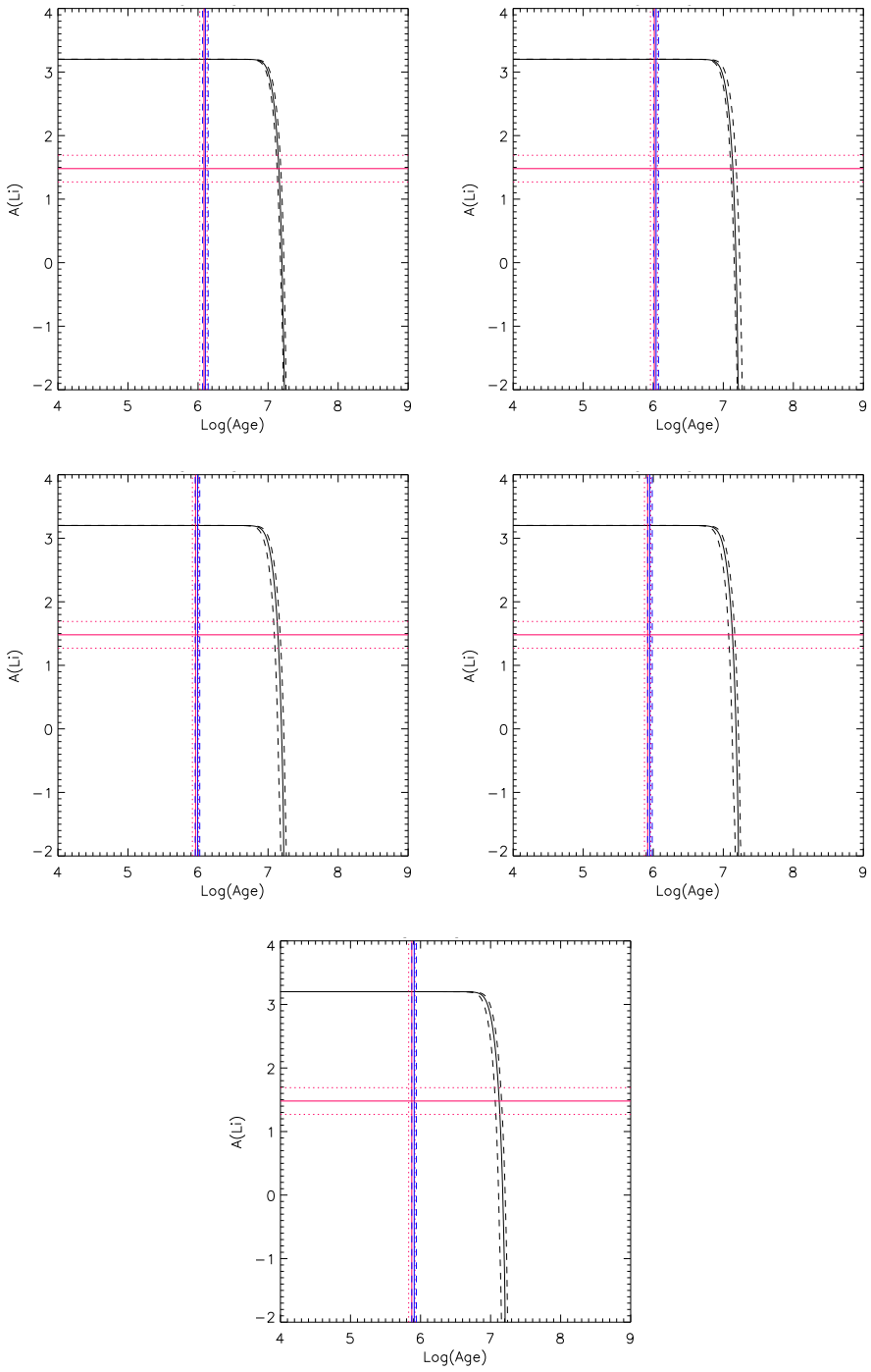

Figure A.31: PAR 1802 lithium results for primary component

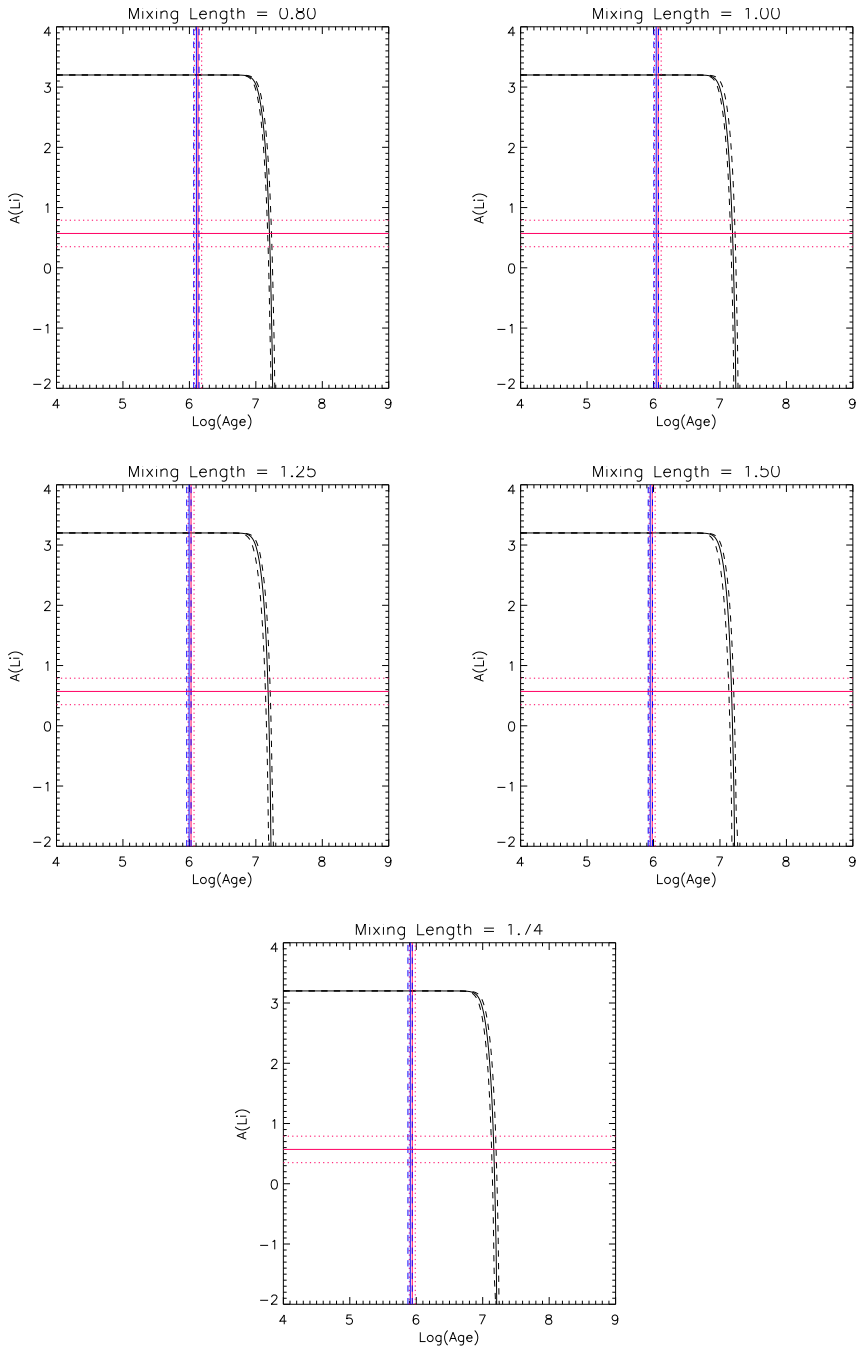

Figure A.32: PAR 1802 lithium results for secondary component

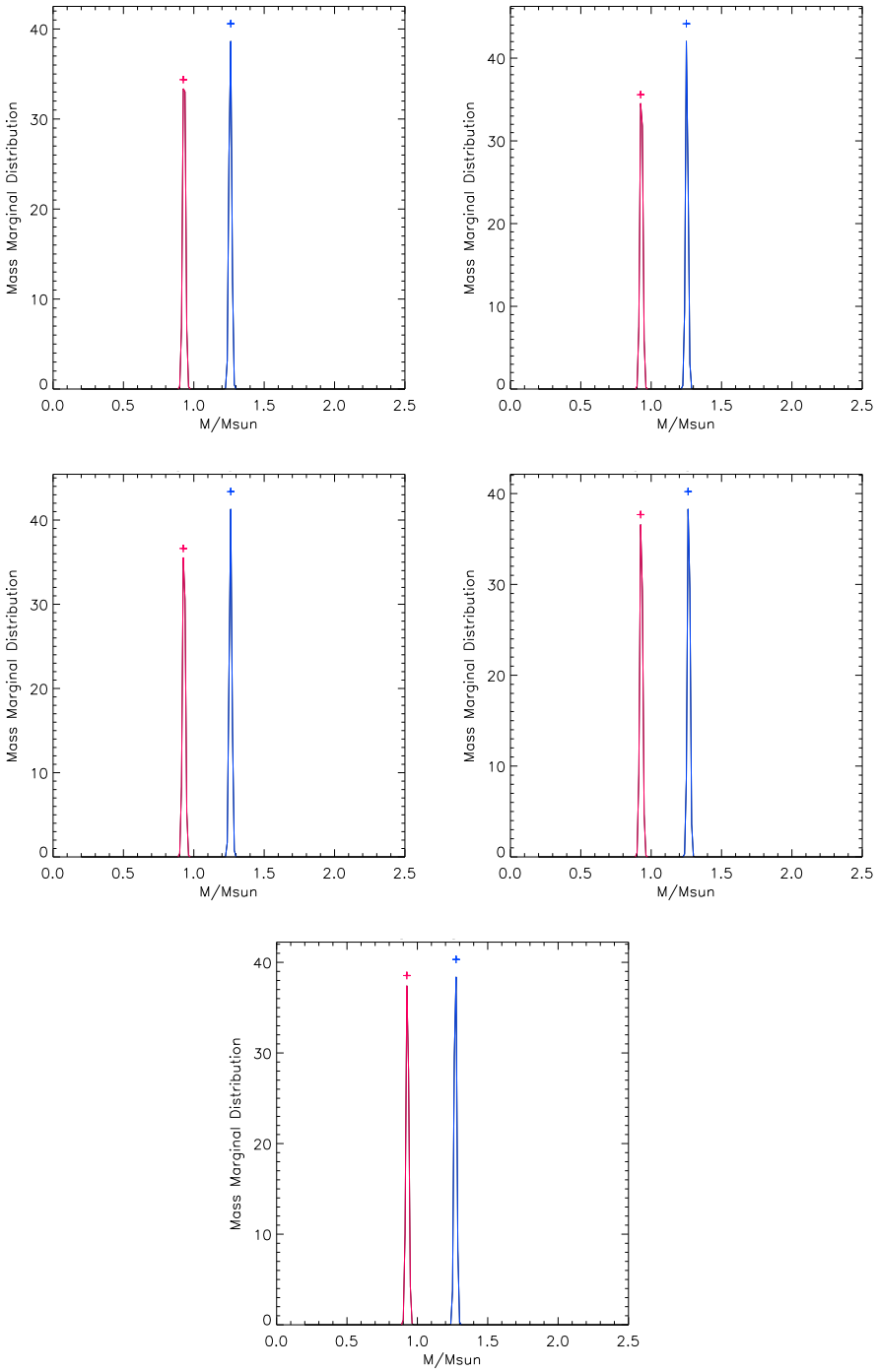

Figure A.33: RXJ0529.4+0041A Mass Marginal Distribution for primary (blue) component and secondary (red) component.

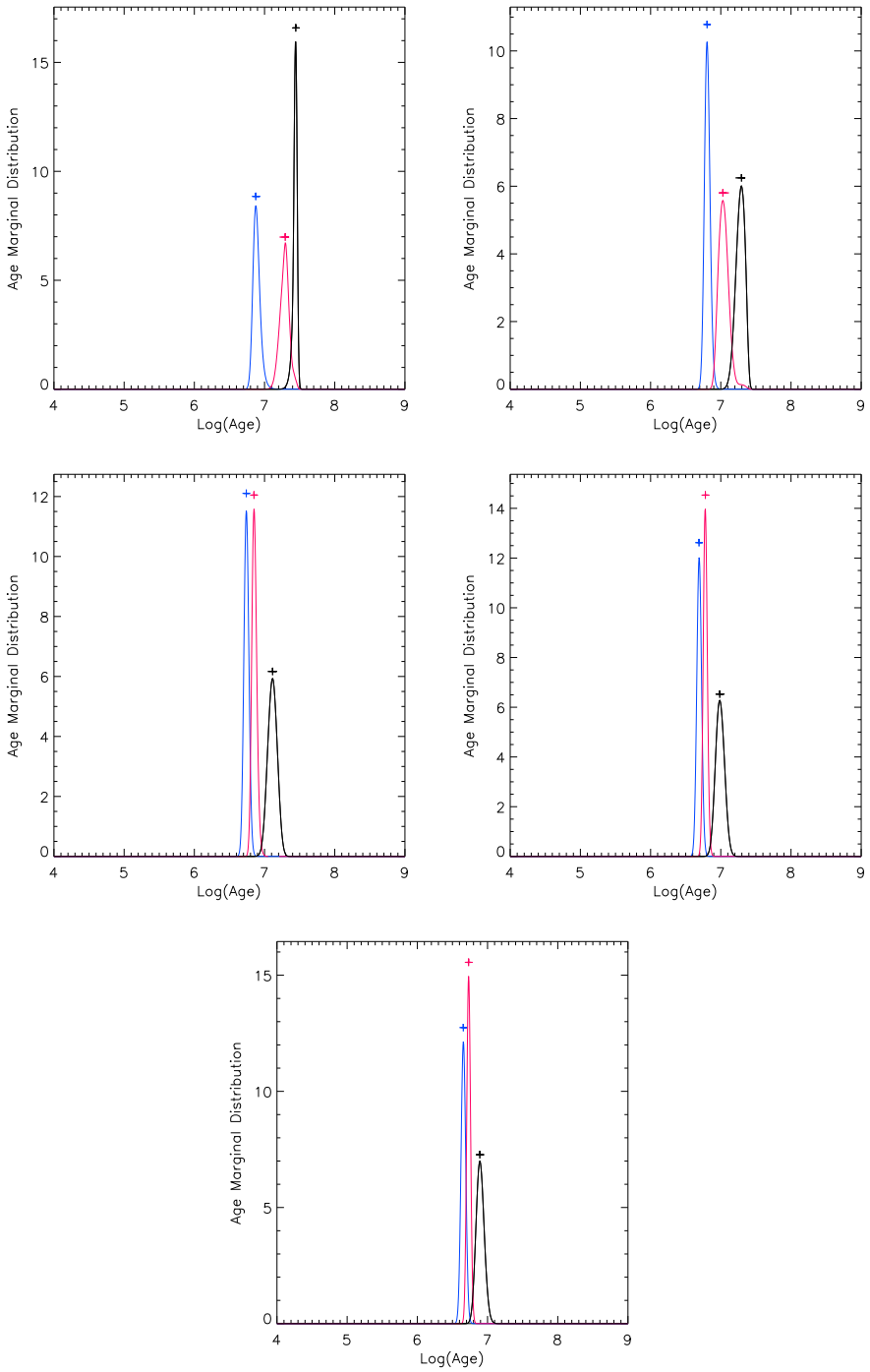

Figure A.34: RXJ0529.4+0041A Age Marginal Distribution for the primary (blue) component, the secondary (yellow) component and for coevality (red).

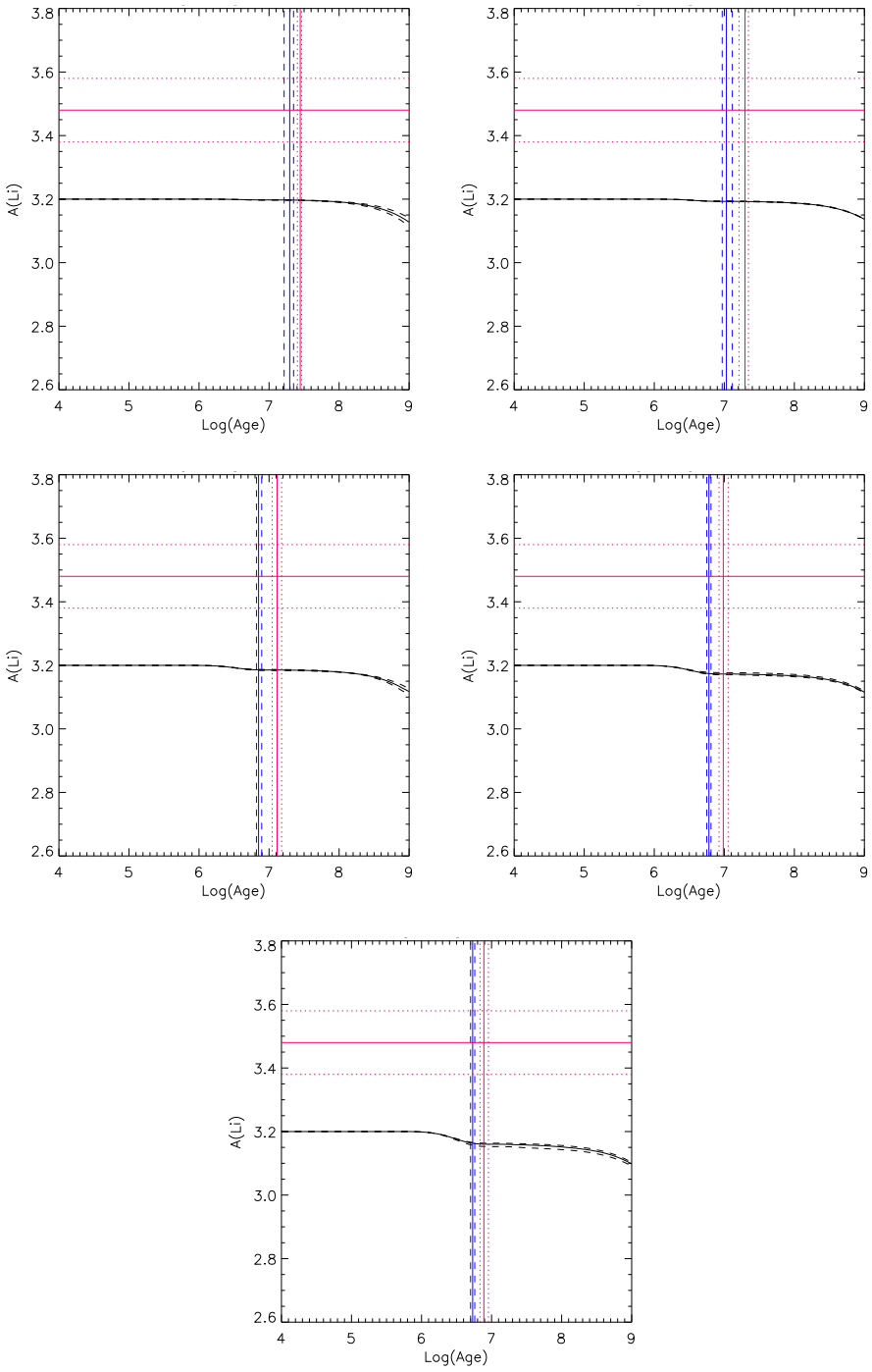

Figure A.35: RXJ0529.4+0041A lithium results for primary component

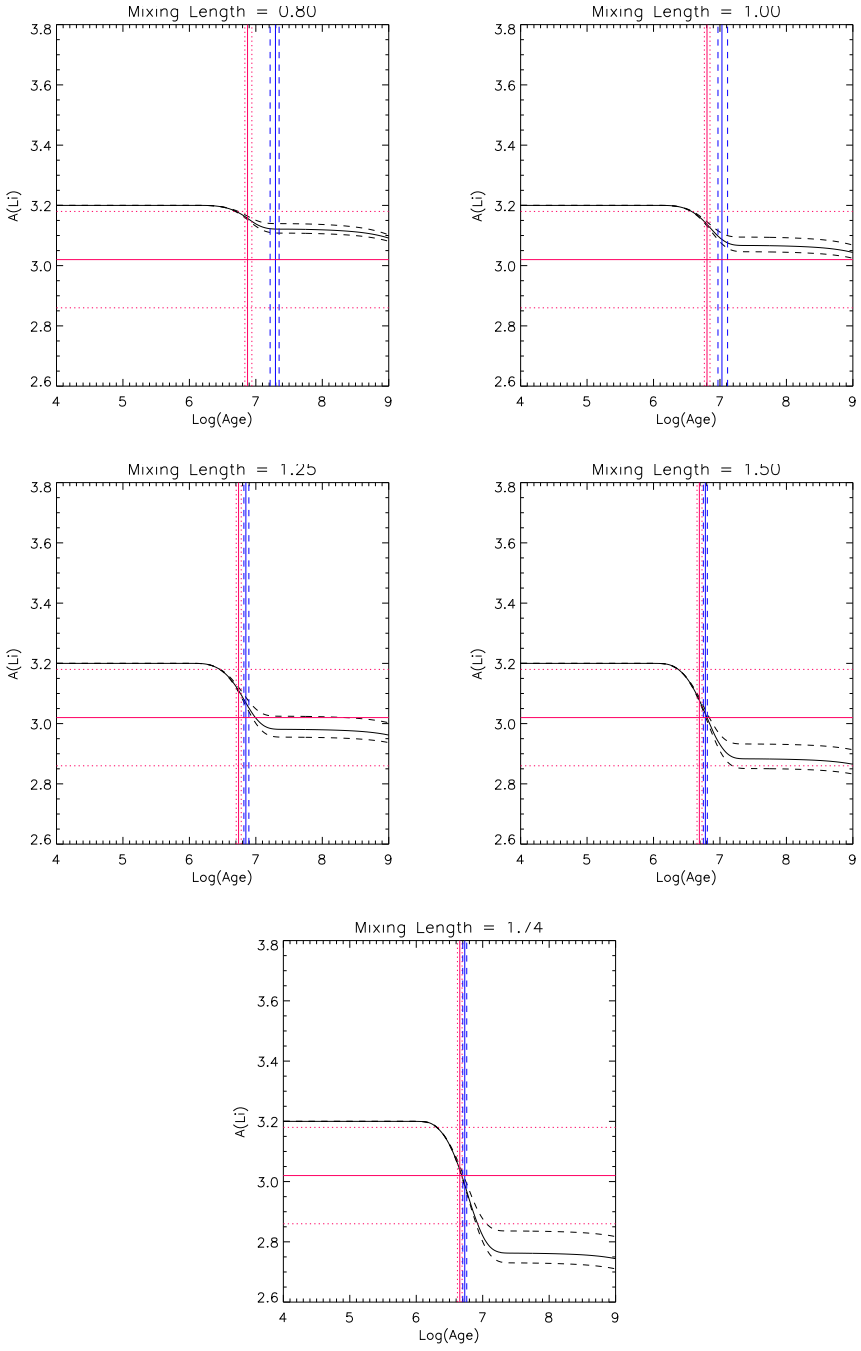

Figure A.36: RXJ0529.4+0041A lithium results for secondary component

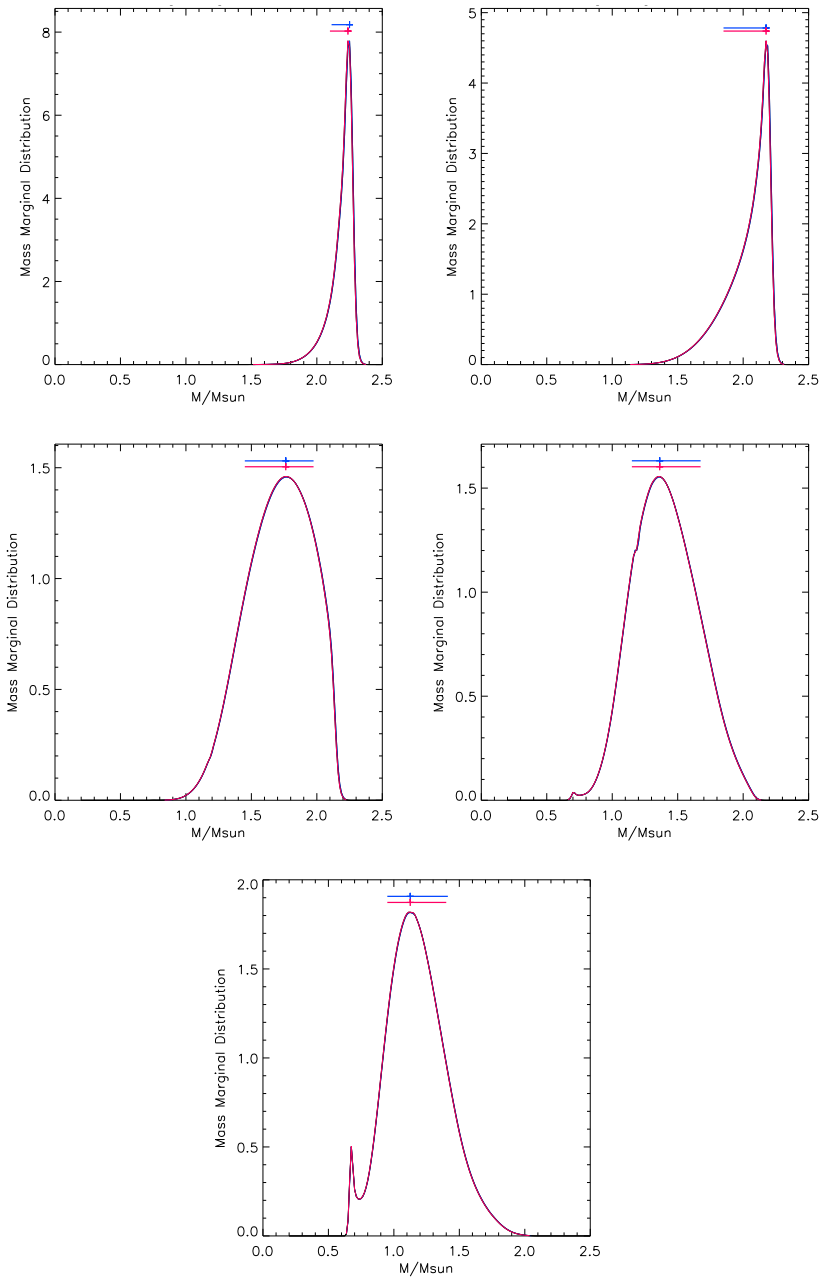

Figure A.37: RX J0530.7-0434 Mass Marginal Distribution.

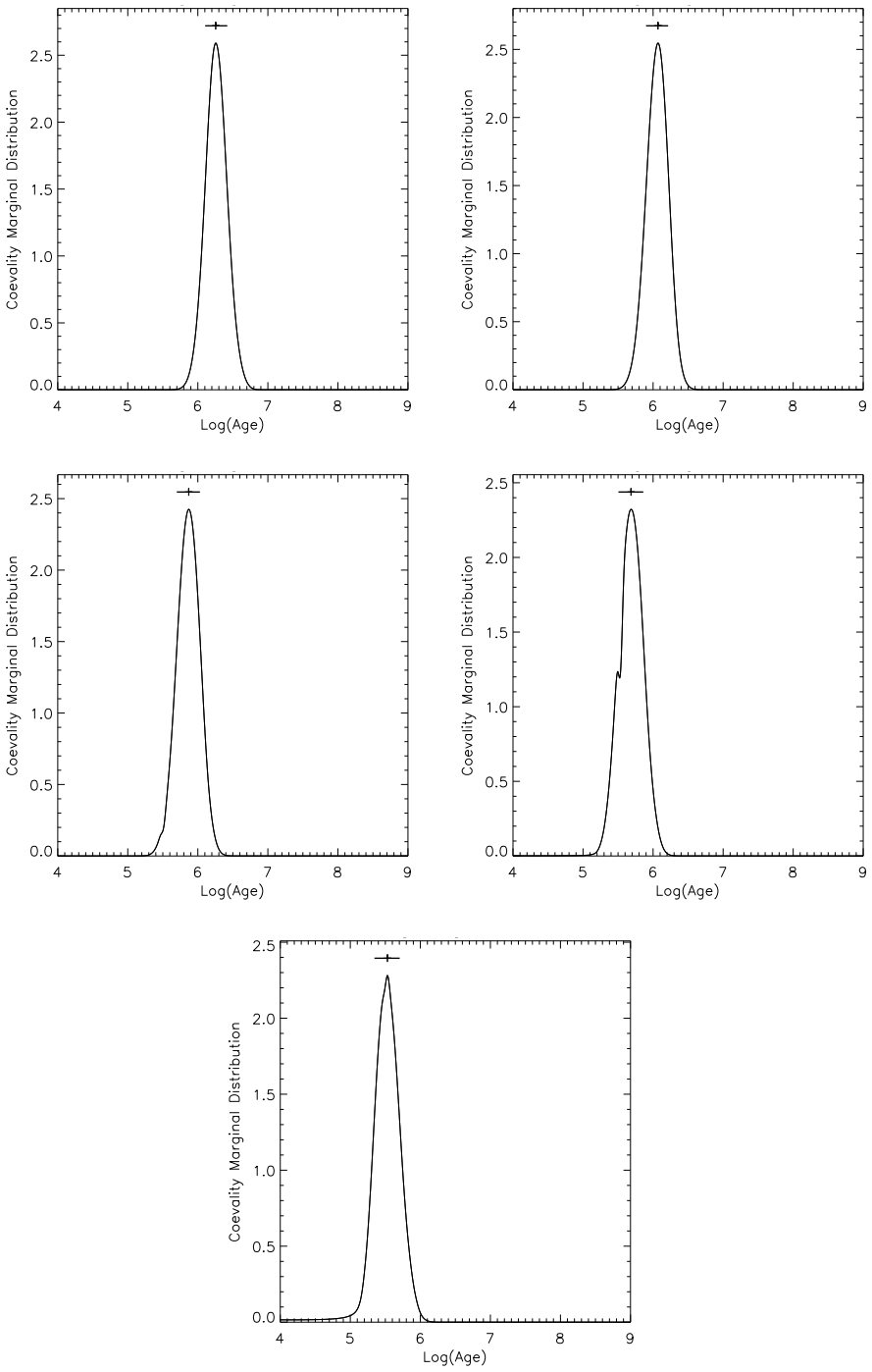

Figure A.38: RX J0530.7-0434 Age Marginal Distribution.

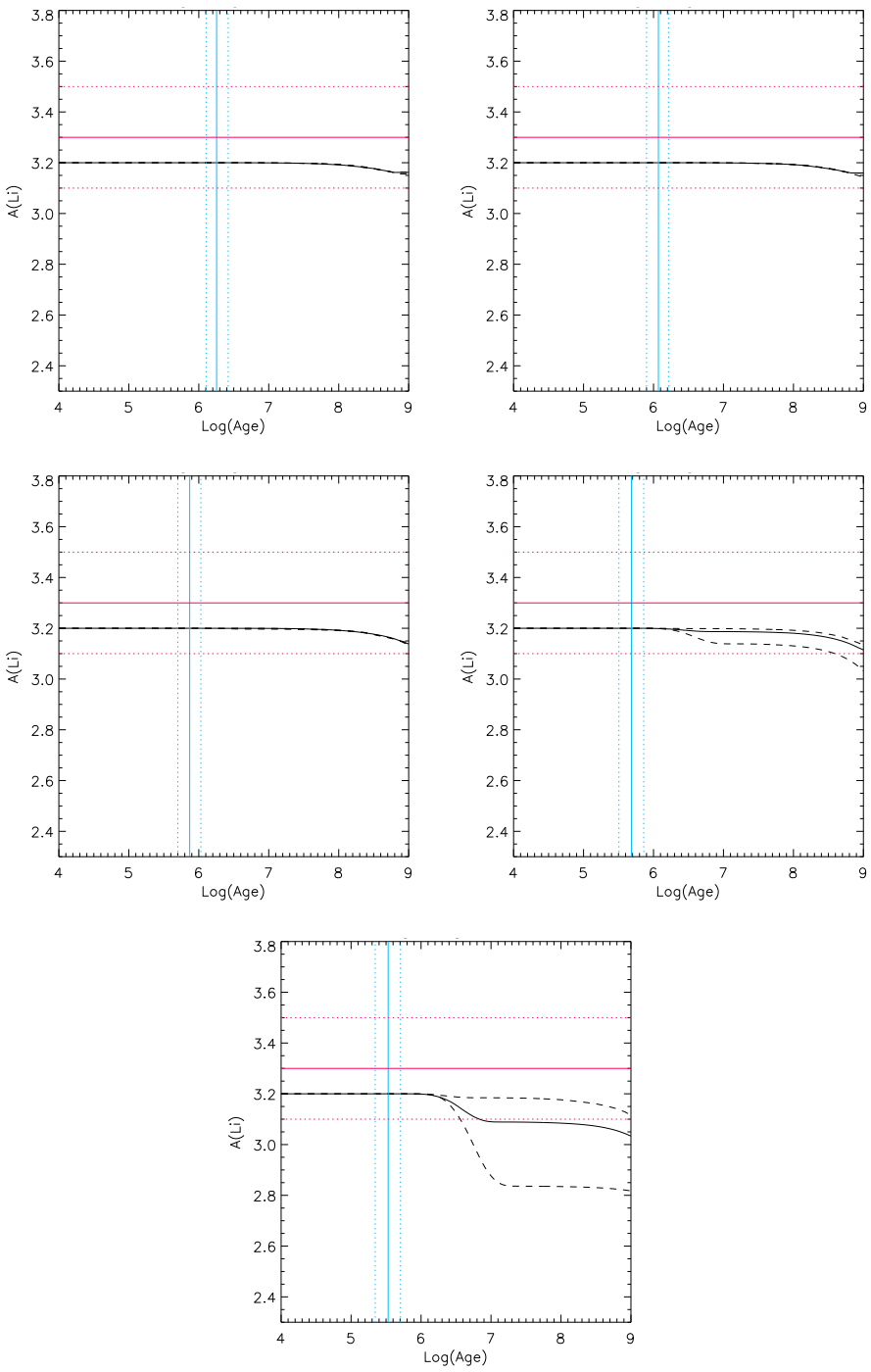

Figure A.39: RX J0530.7-0434 lithium results for primary component.

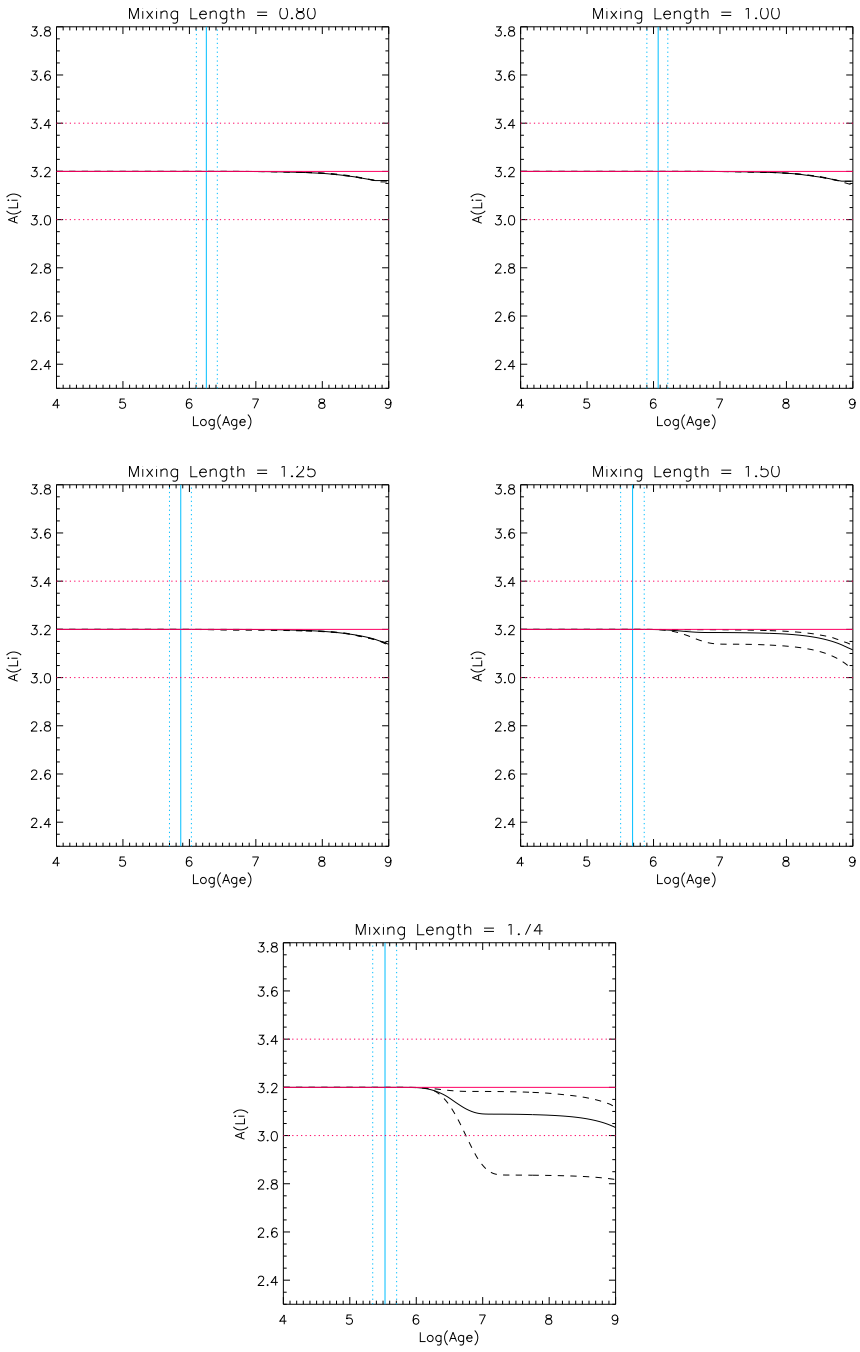

Figure A.40: RX J0530.7-0434 lithium results for secondary component.

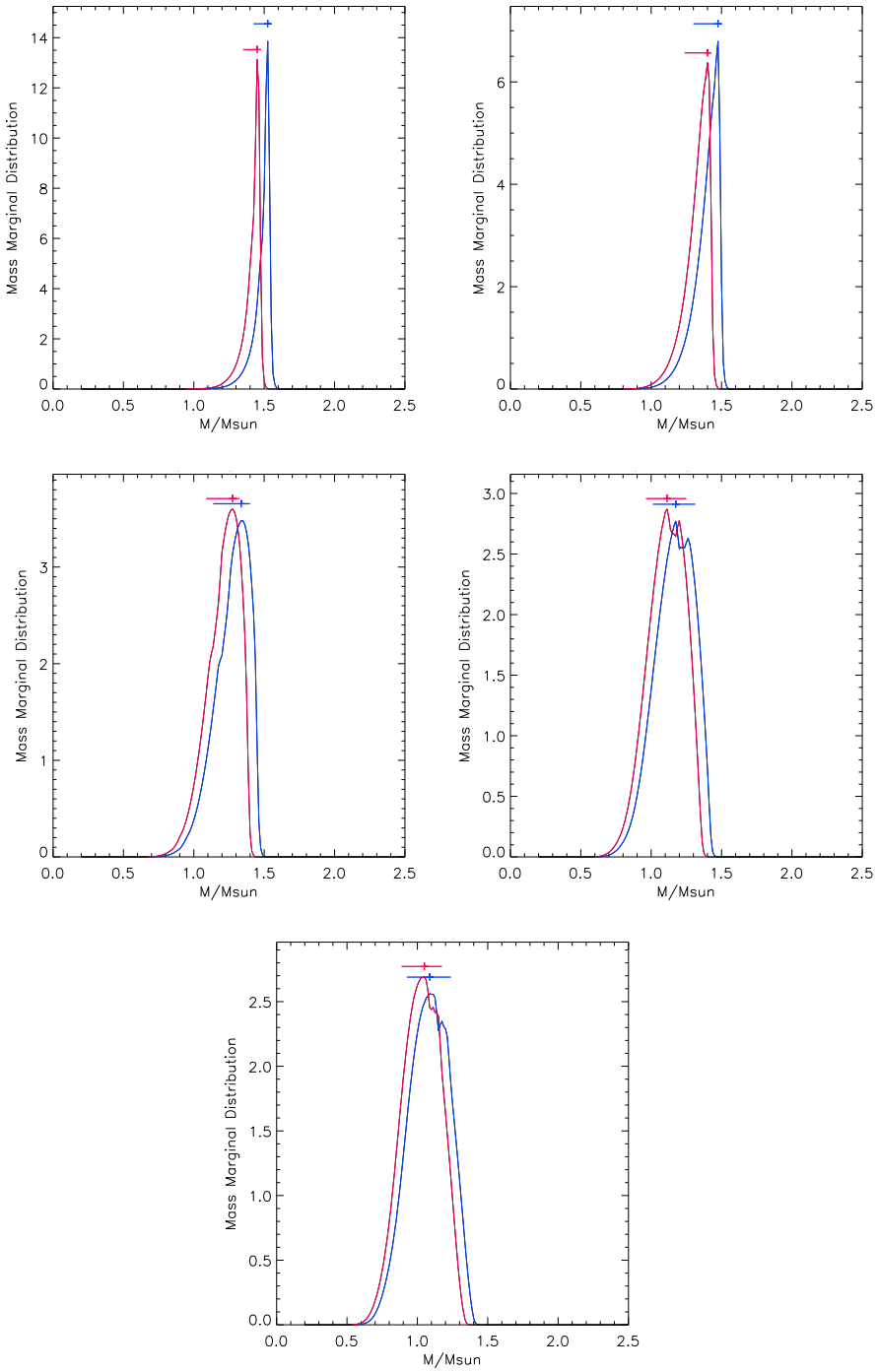

Figure A.41: RX J0532.1-0732 Mass Marginal Distribution for primary (blue) component and secondary (red) component.

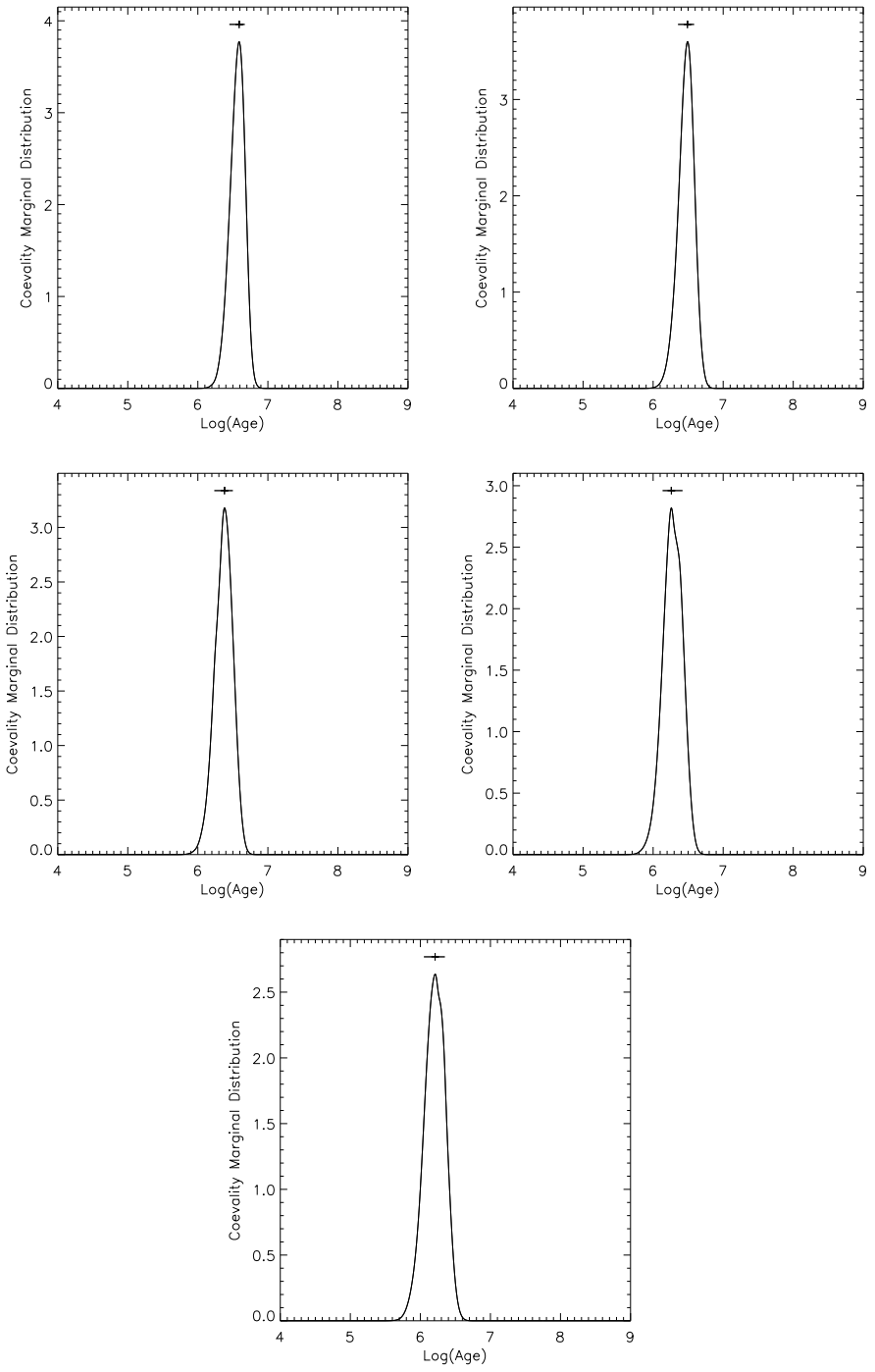

Figure A.42: RX J0532.1-0732 Age Marginal Distribution for the primary (blue) component, the secondary (yellow) component and for coevality (red).

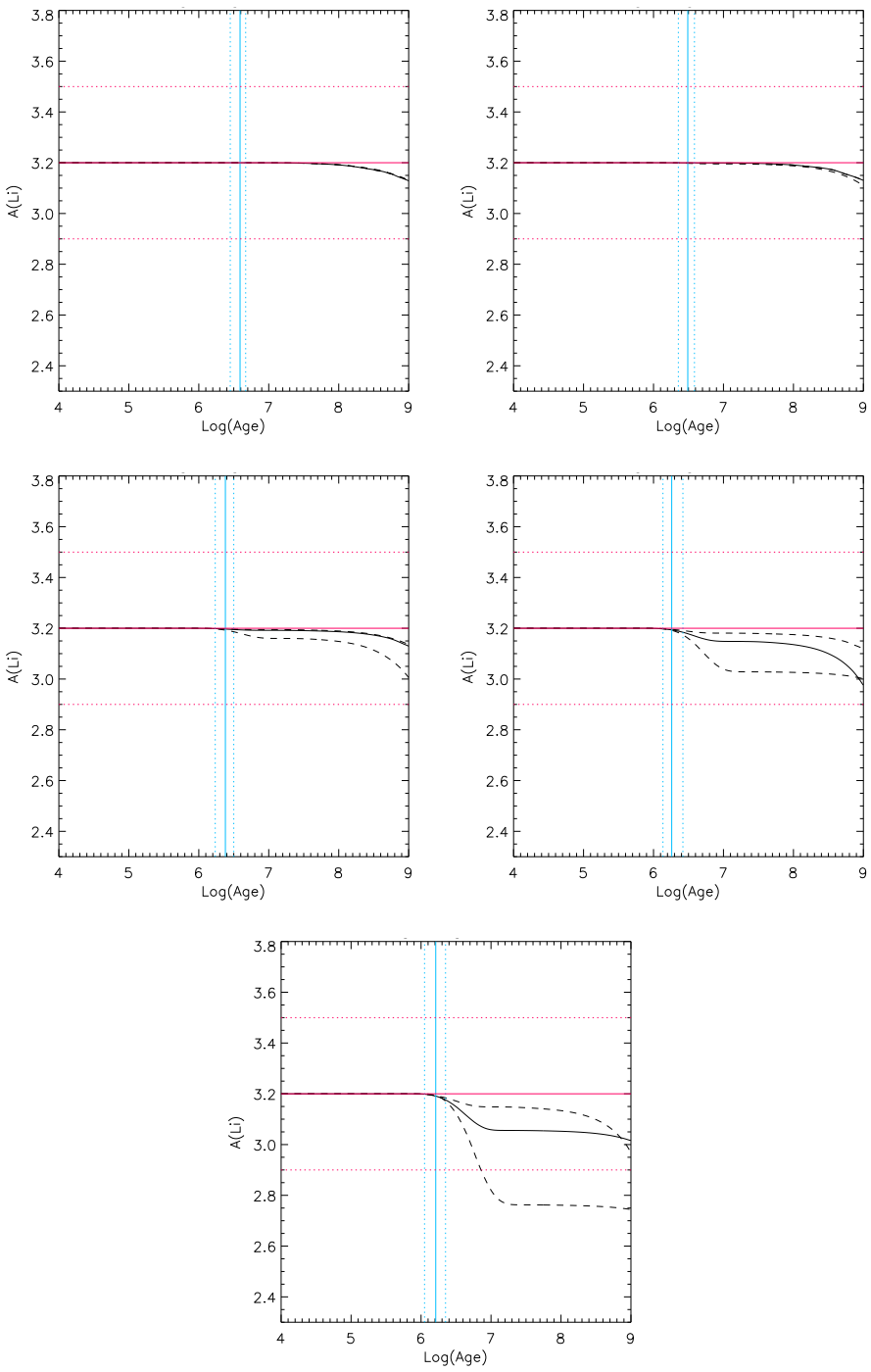

Figure A.43: RX J0532.1-0732 lithium results for primary component

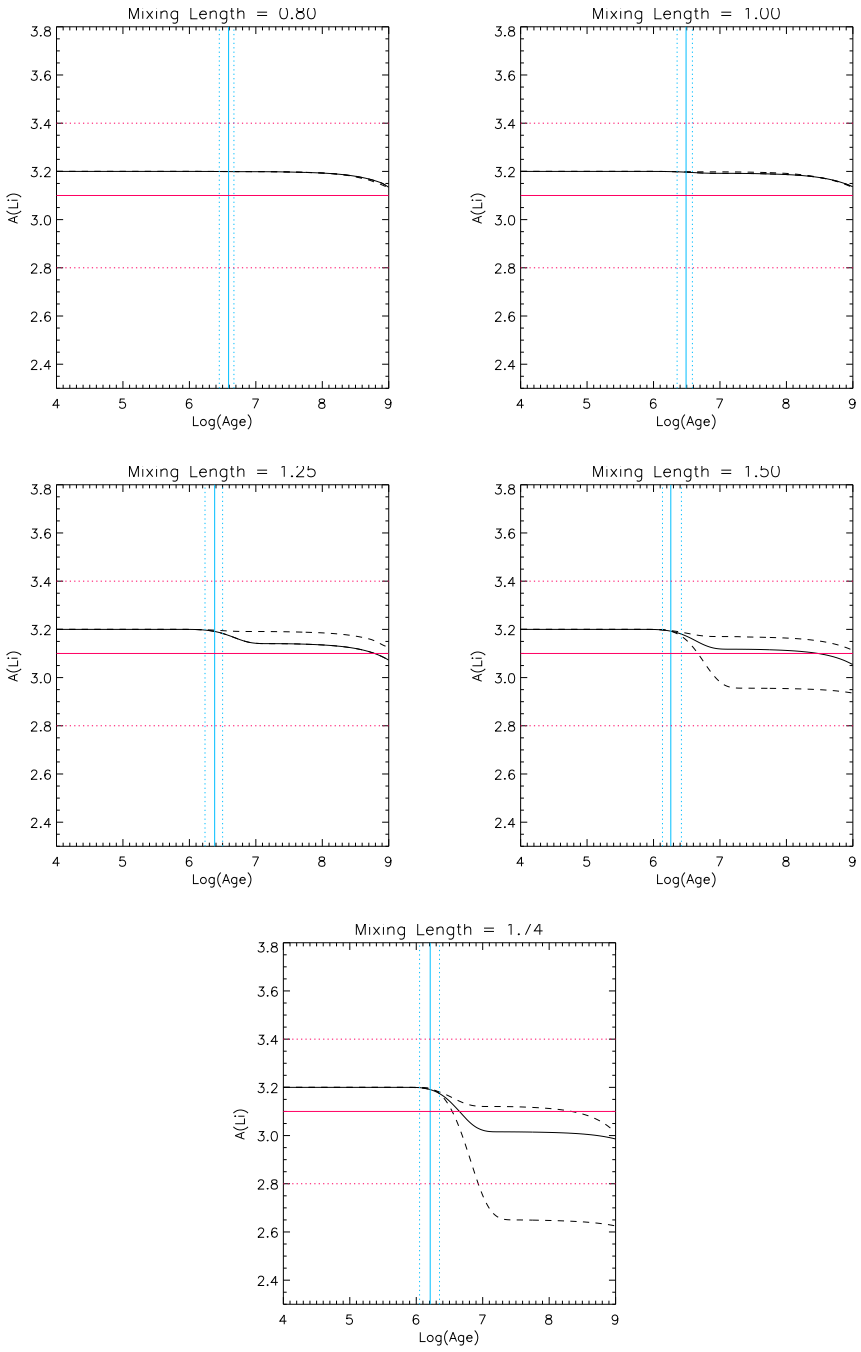

Figure A.44: RX J0532.1-0732 lithium results for secondary component

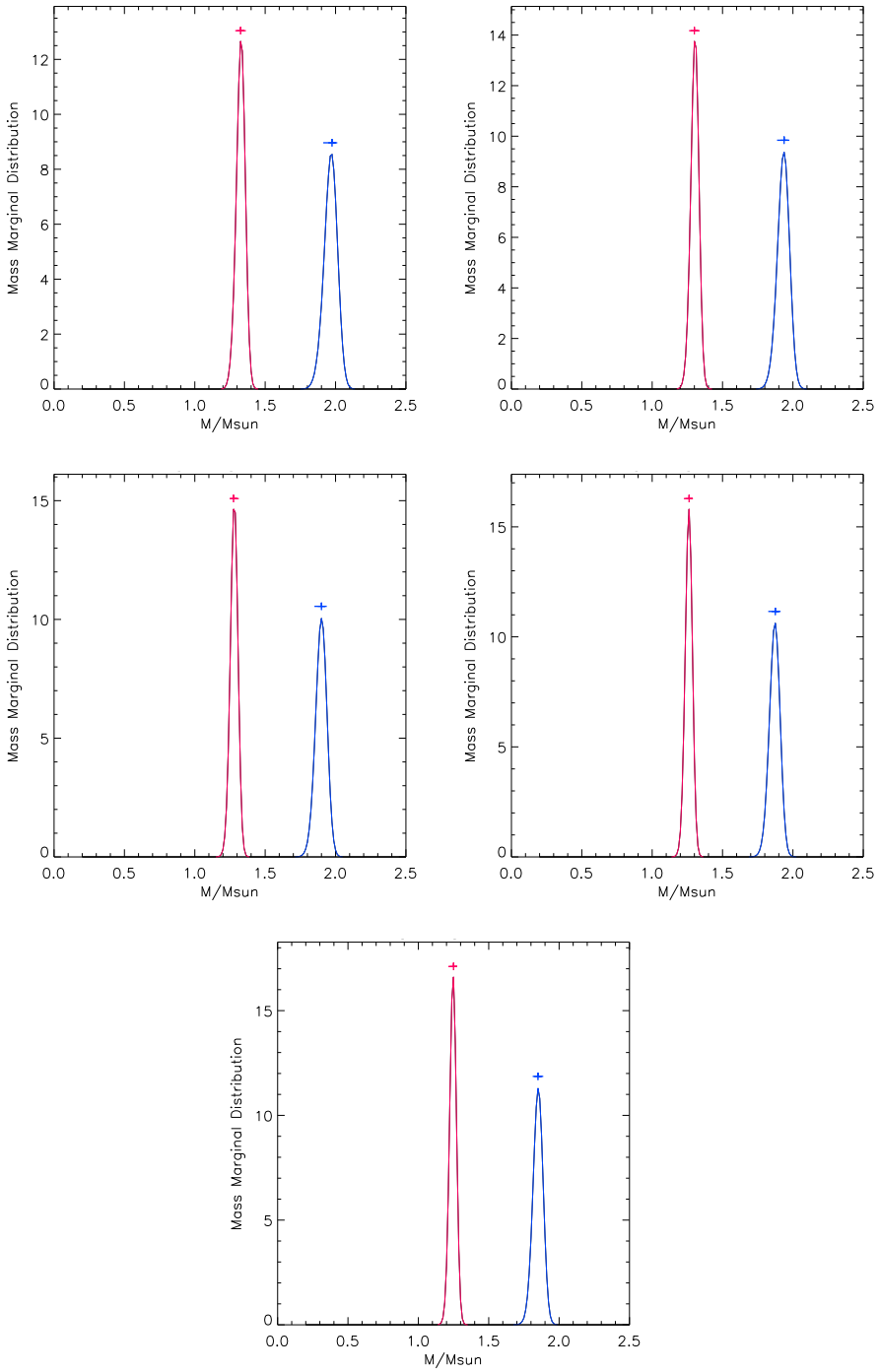

Figure A.45: RX J0541.4-0324 Mass Marginal Distribution for primary (blue) component and secondary (red) component.

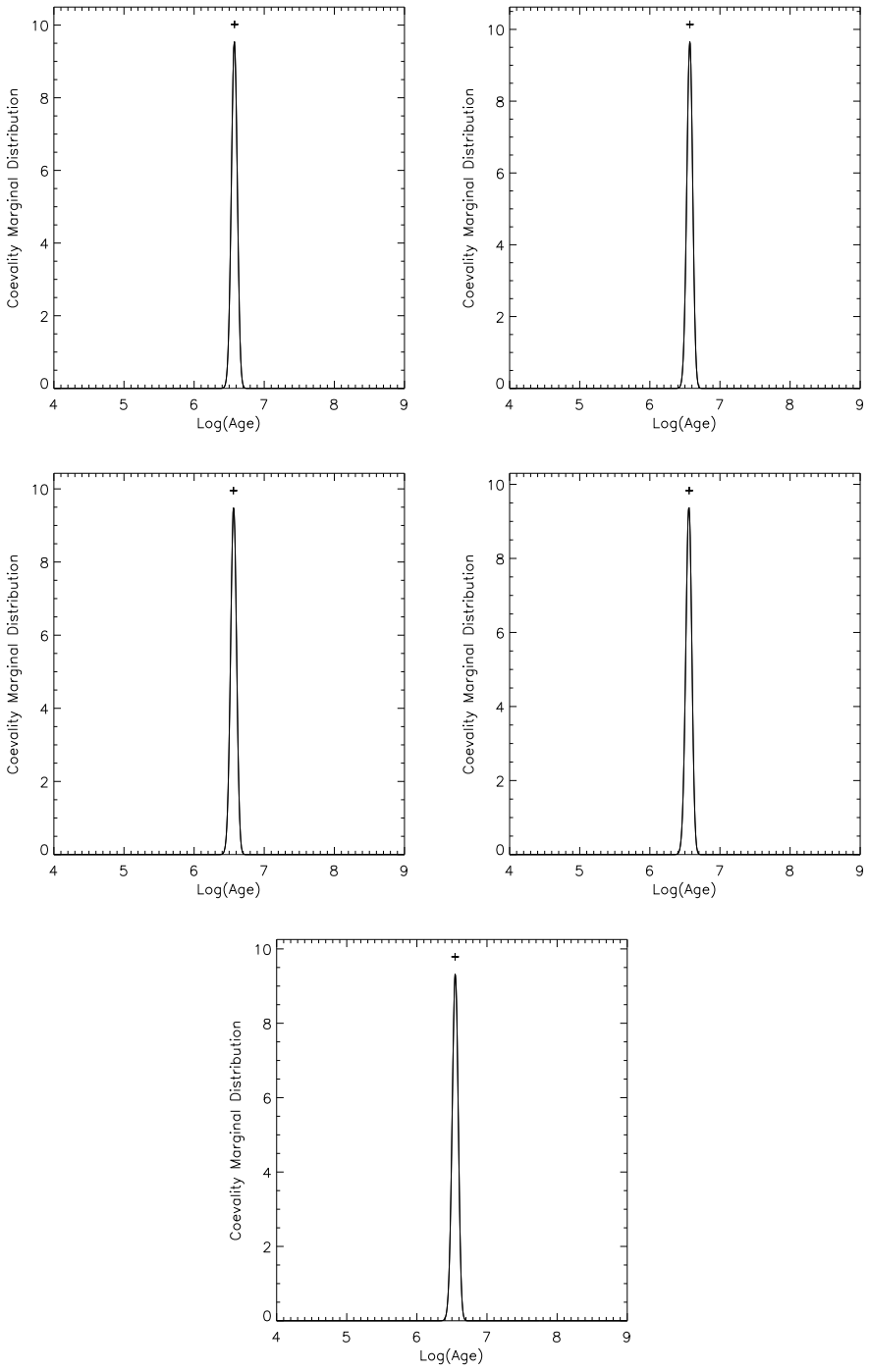

Figure A.46: RX J0541.4-0324 Age Marginal Distribution for the primary (blue) component, the secondary (yellow) component and for coevality (red).

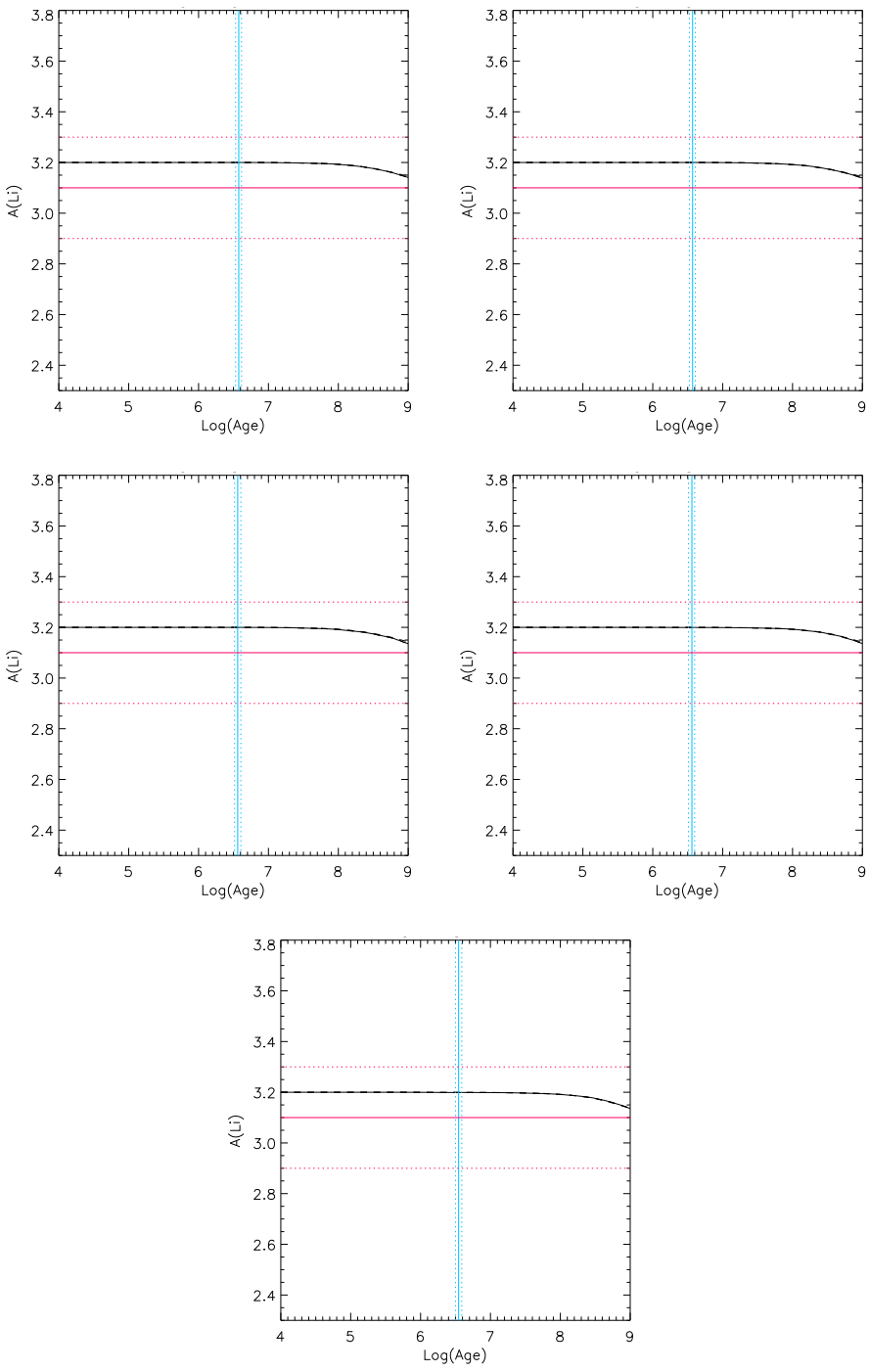

Figure A.47: RX J0541.4-0324 lithium results for primary component

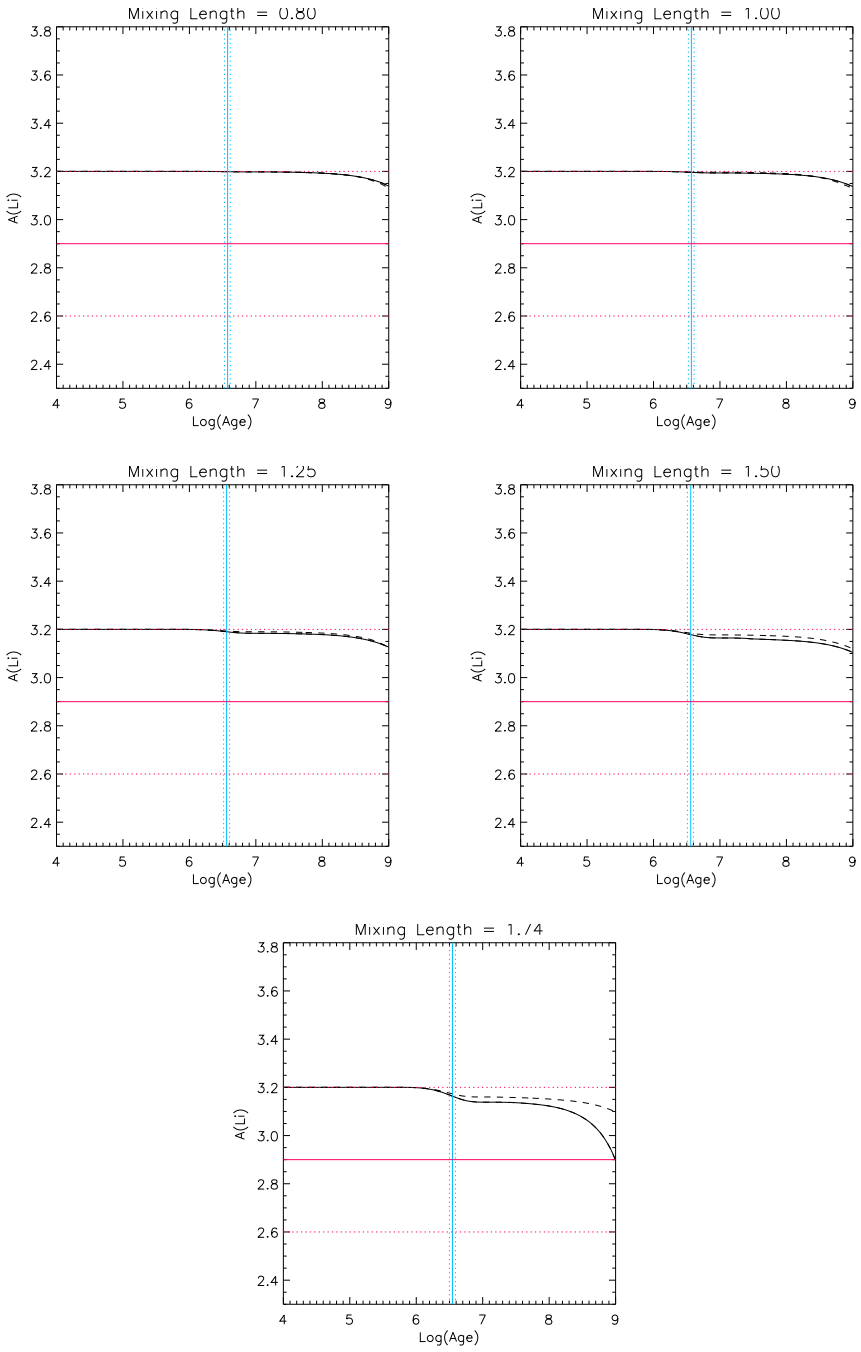

Figure A.48: RX J0541.4-0324 lithium results for secondary component

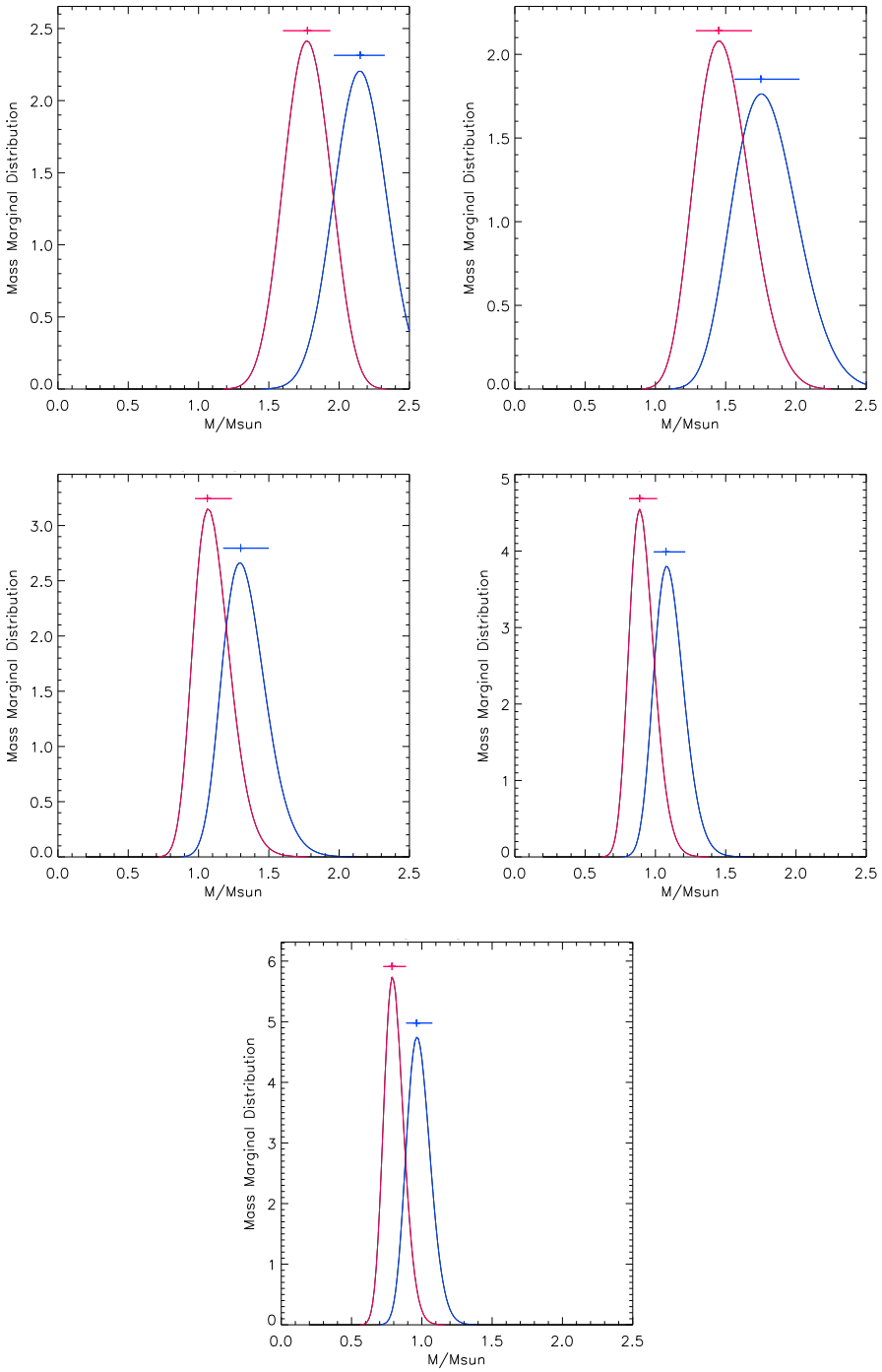

Figure A.49: V773 TauA Mass Marginal Distribution for primary (blue) component and secondary (red) component.

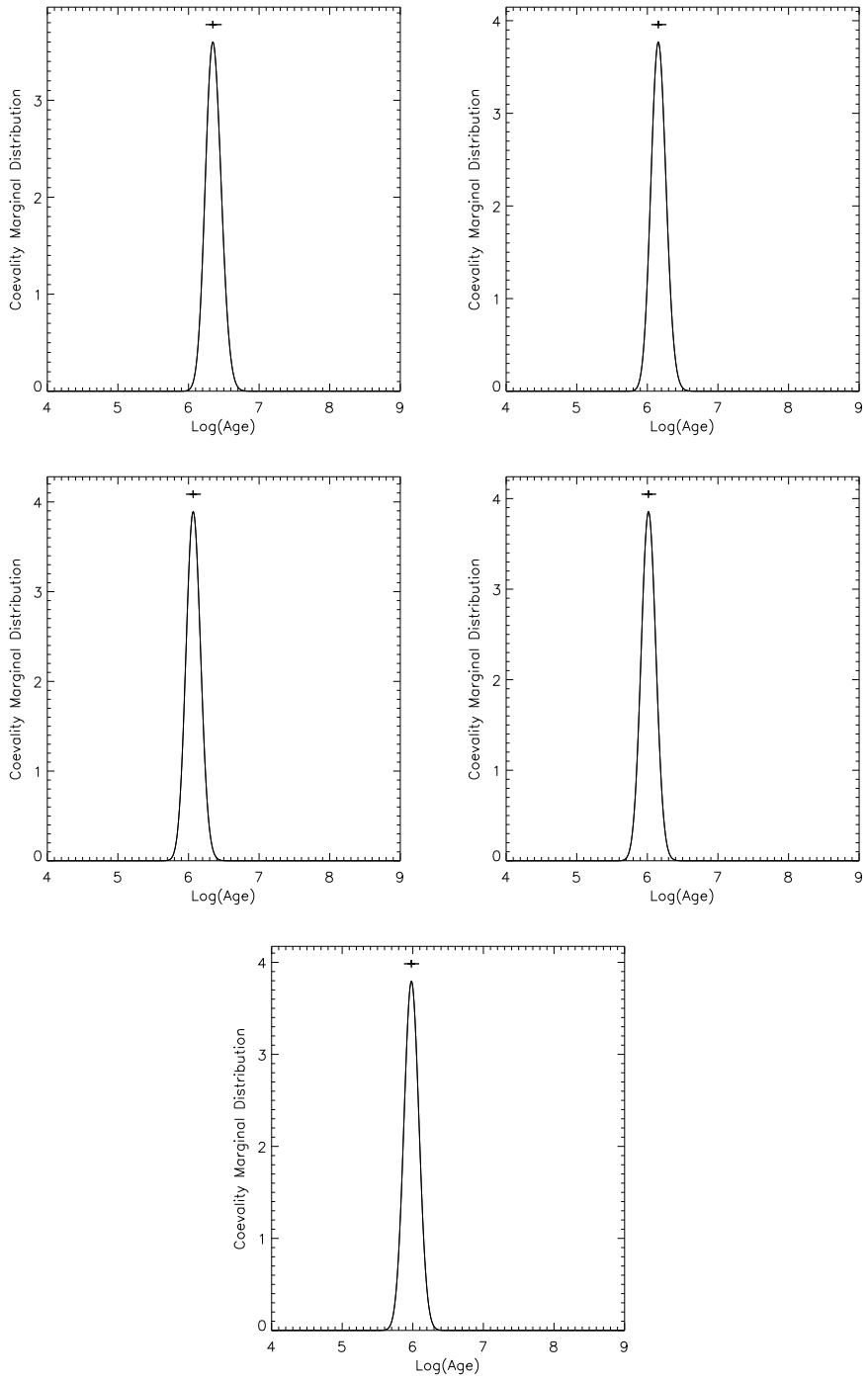

Figure A.50: V773 TauA Age Marginal Distribution for the primary (blue) component, the secondary (yellow) component and for coevality (red).

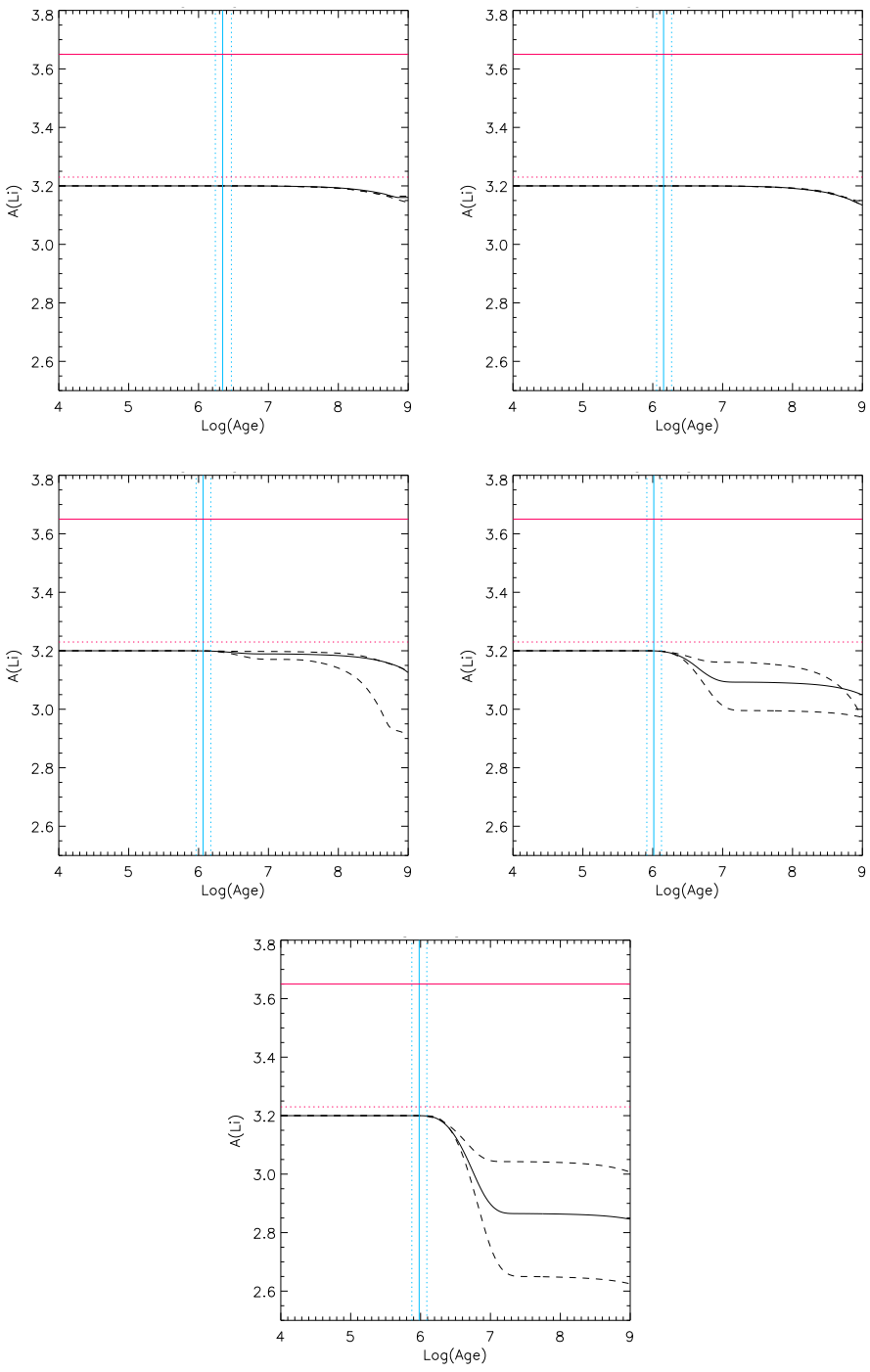

Figure A.51: V773 TauA lithium results for primary component

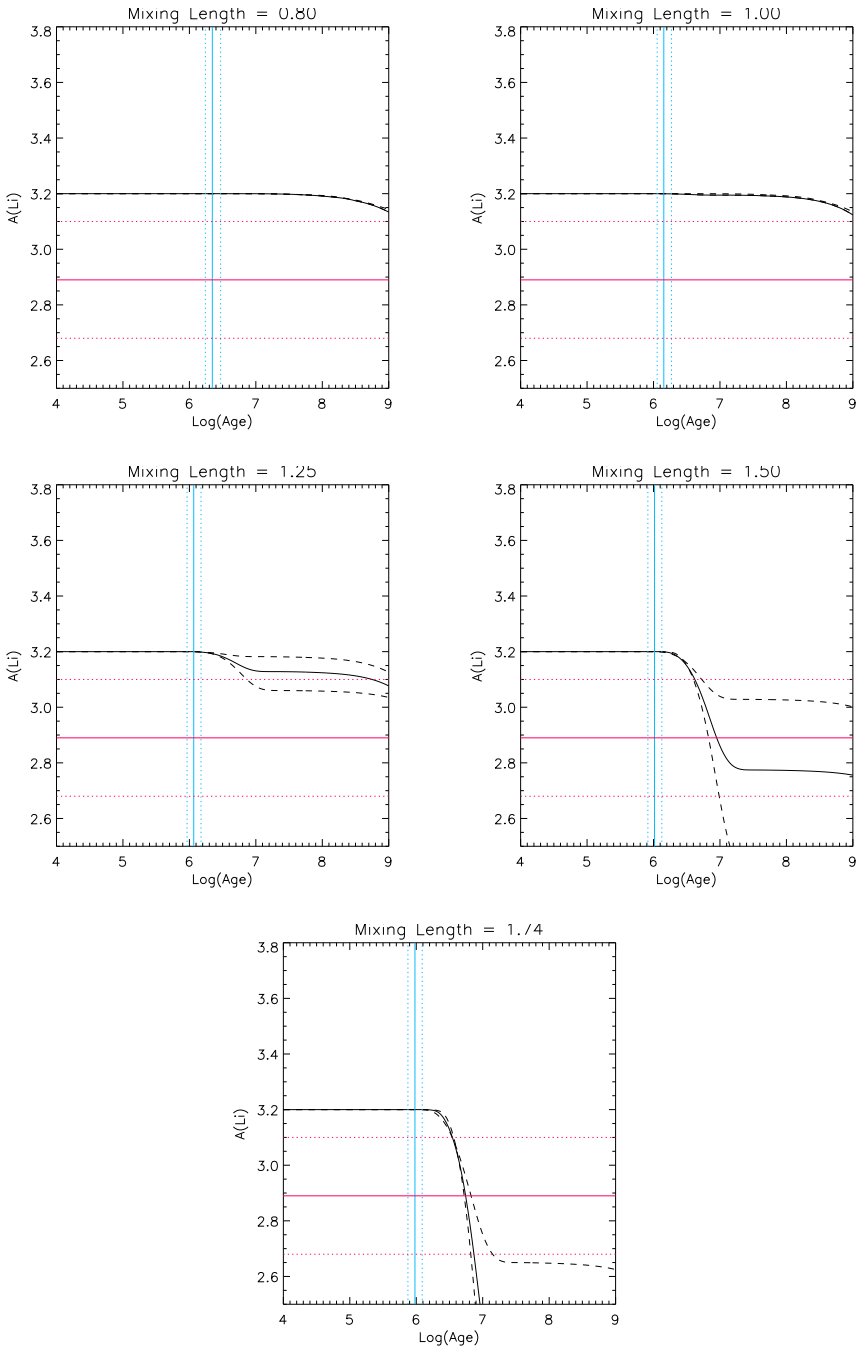

Figure A.52: V773 TauA lithium results for secondary component

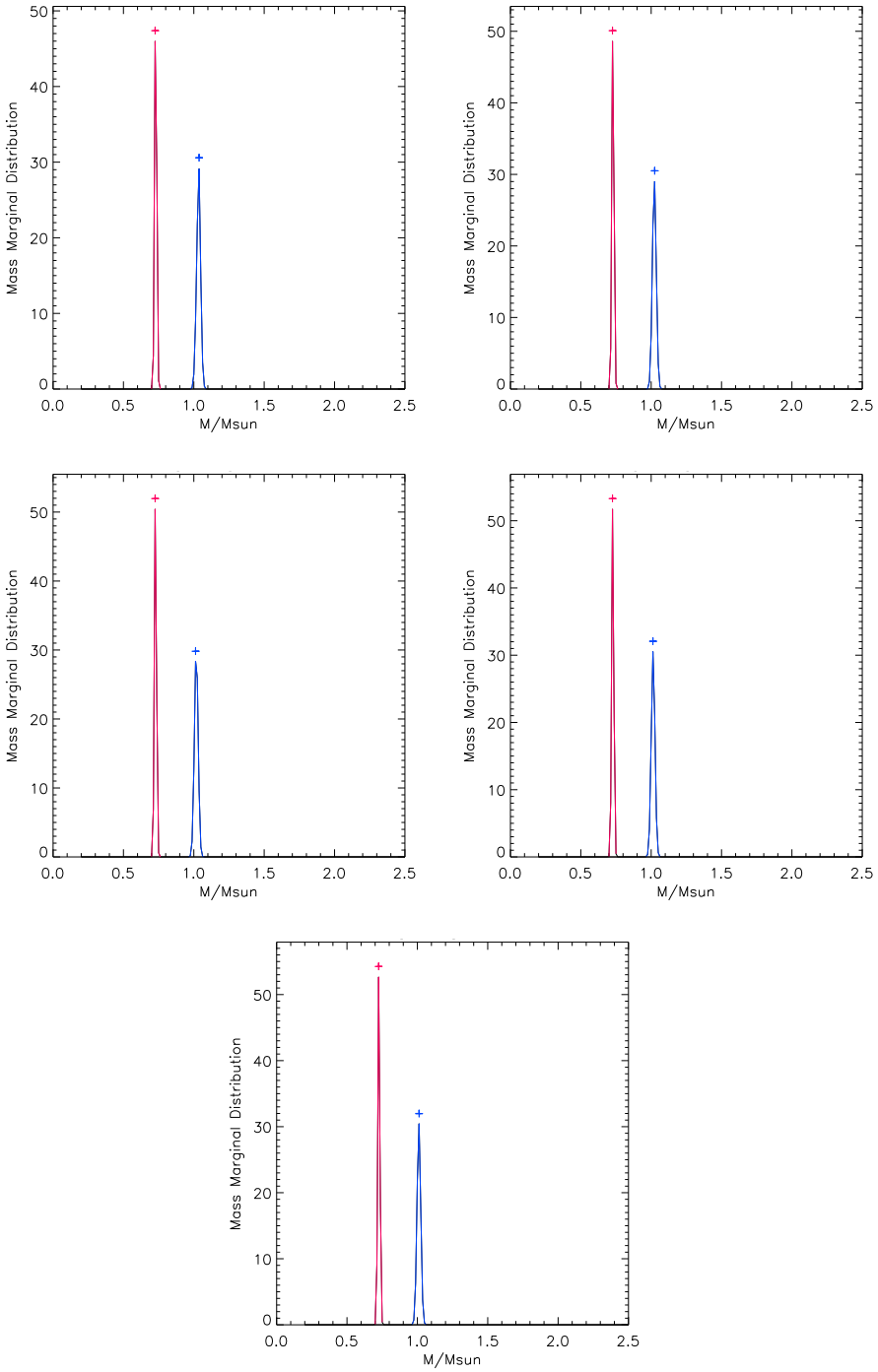

Figure A.53: V1174 Ori Mass Marginal Distribution for primary (blue) component and secondary (red) component.

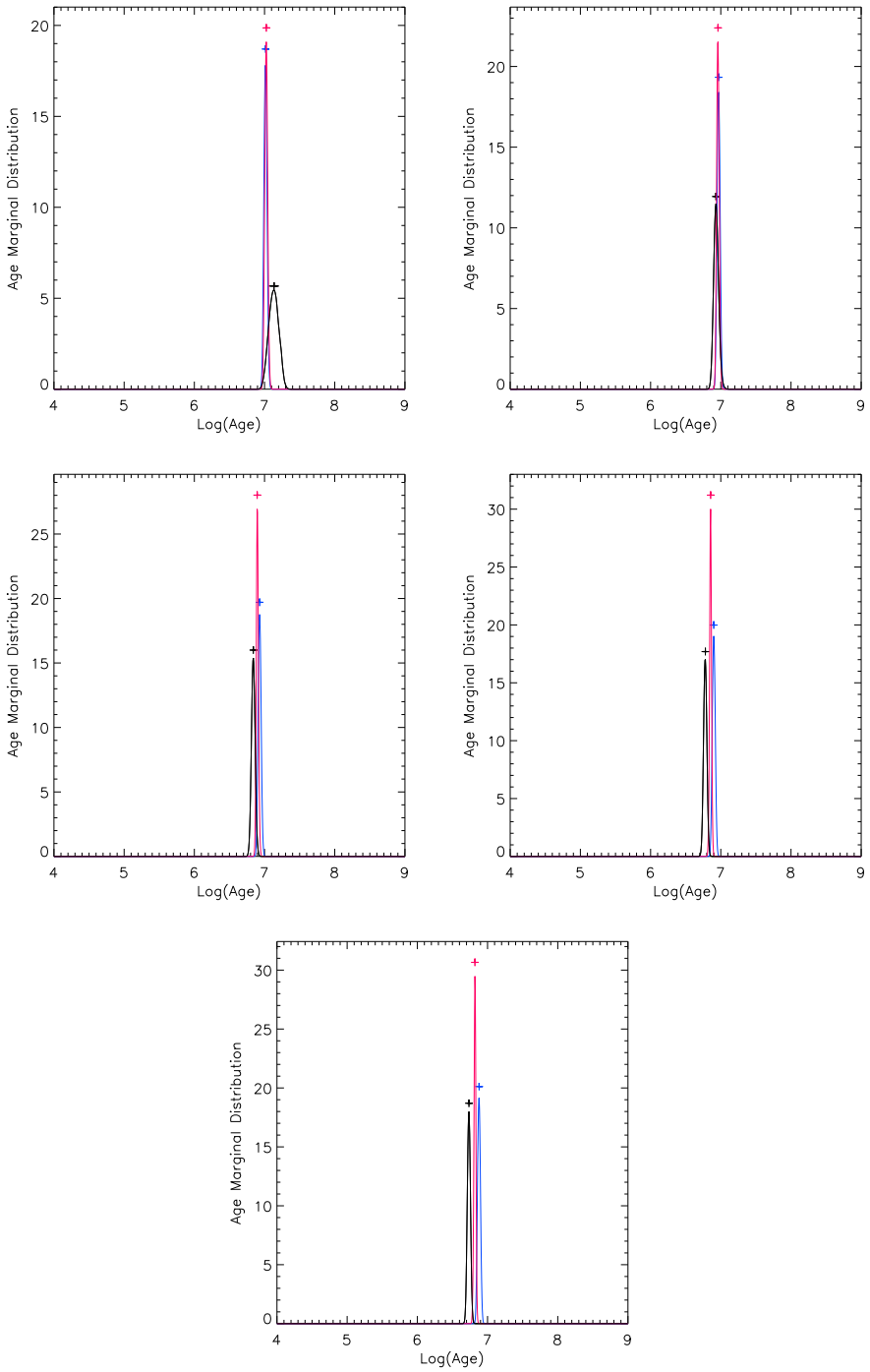

Figure A.54: V1174 Ori Age Marginal Distribution for the primary (blue) component, the secondary (yellow) component and for coevality (red).

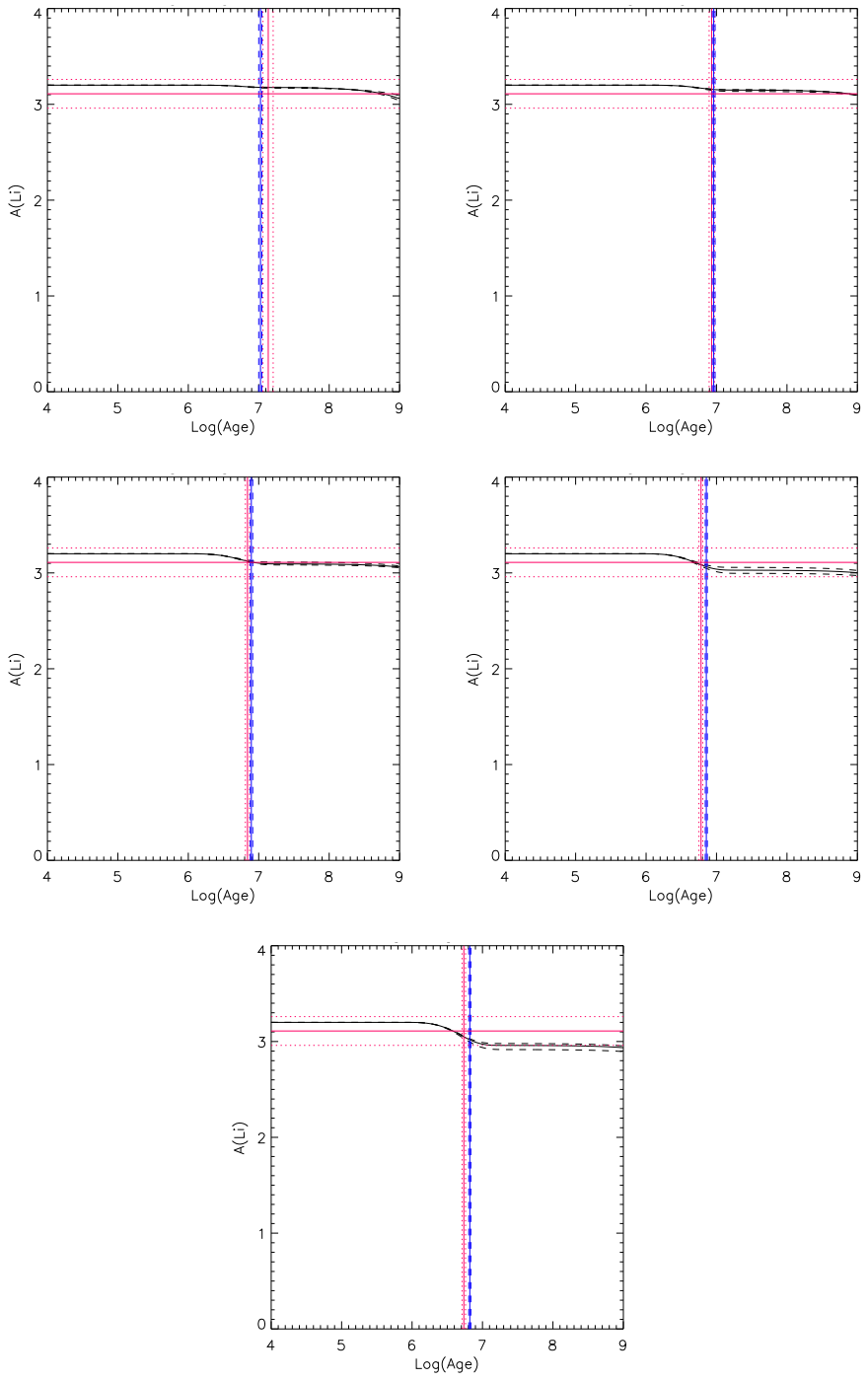

Figure A.55: V1174 Ori lithium results for primary component

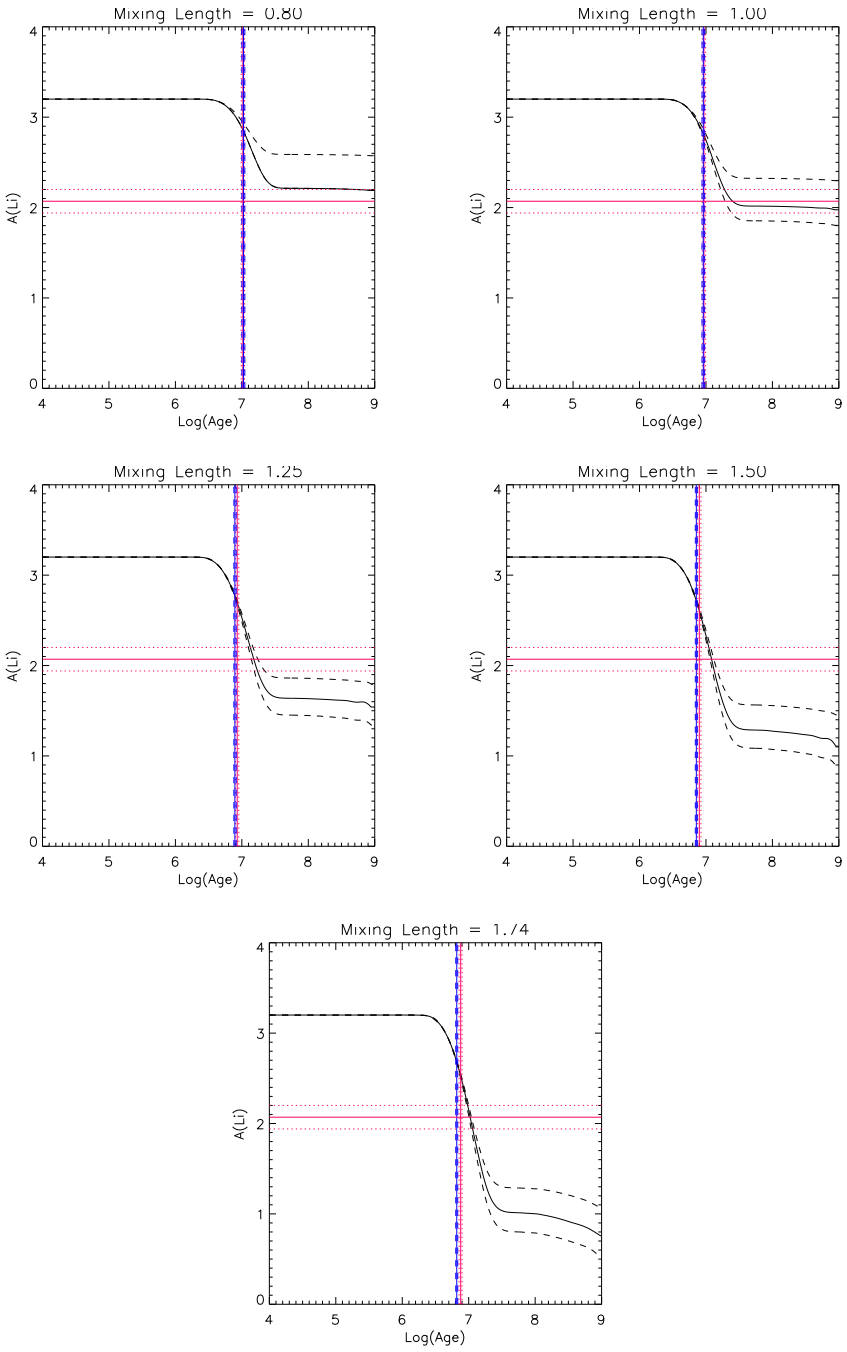

Figure A.56: V1174 Ori lithium results for secondary component

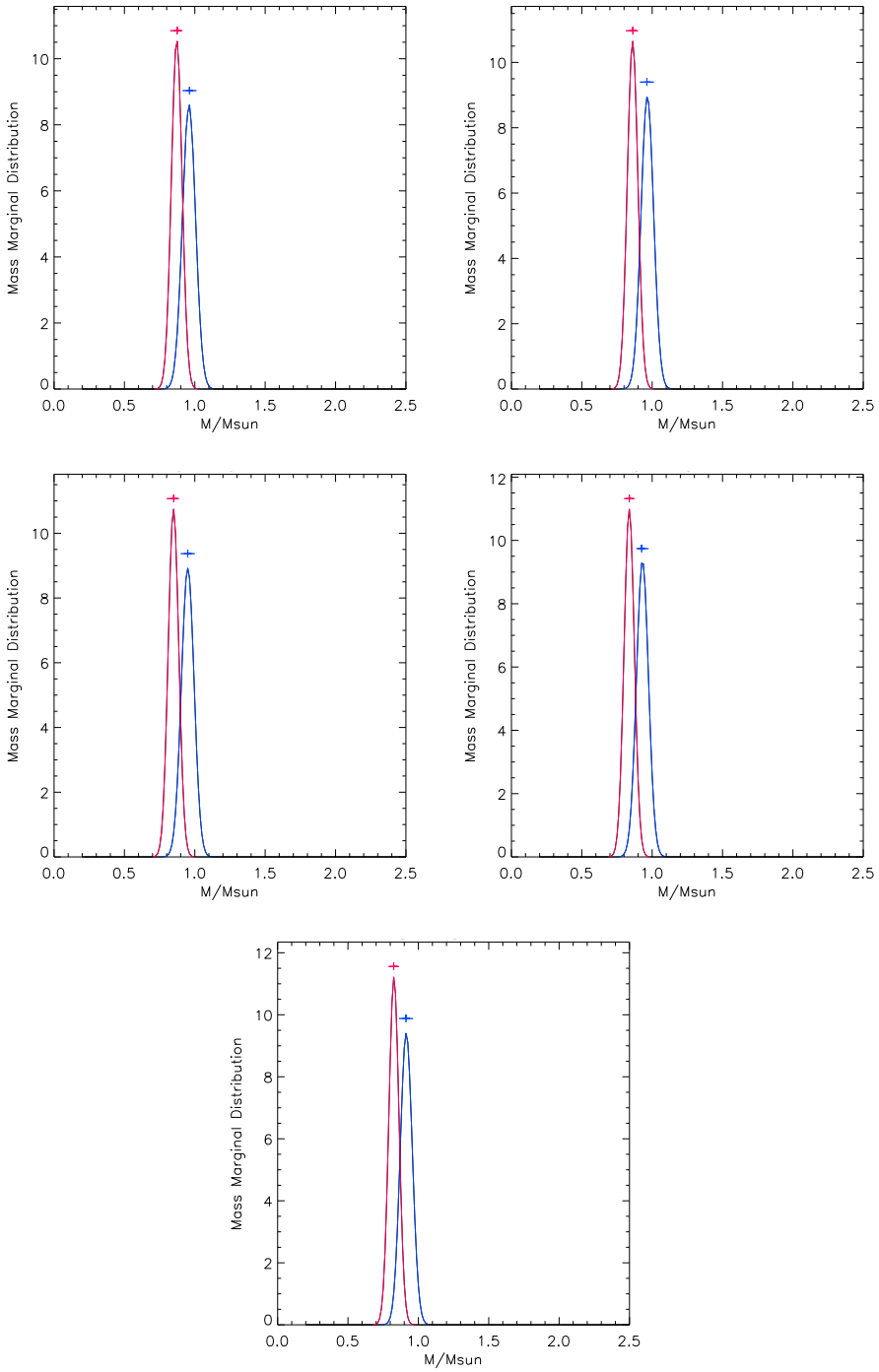

Figure A.57: V4046 Sgr Mass Marginal Distribution for primary (blue) component and secondary (red) component.

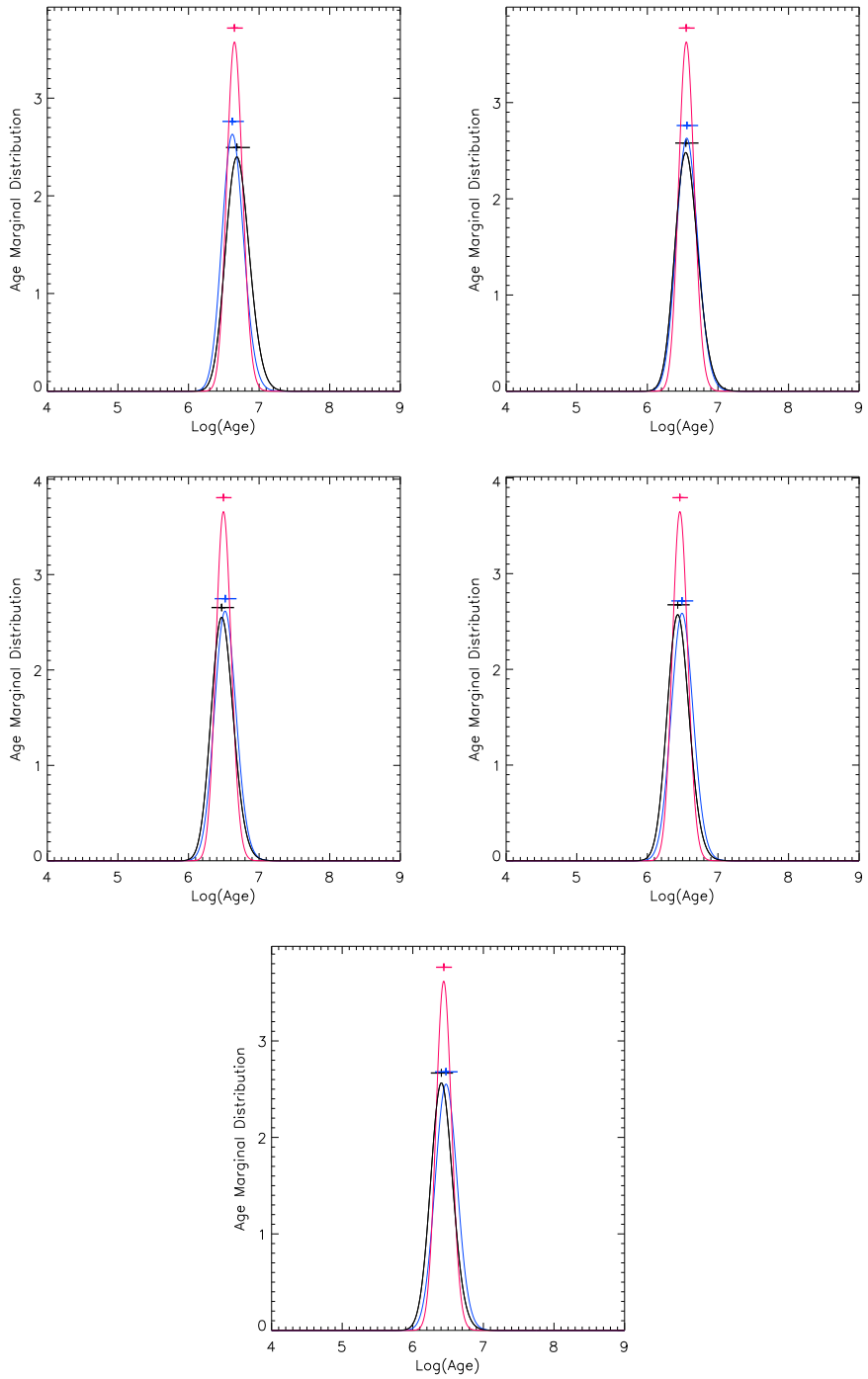

Figure A.58: V4046 Sgr Age Marginal Distribution for the primary (blue) component, the secondary (yellow) component and for coevality (red).

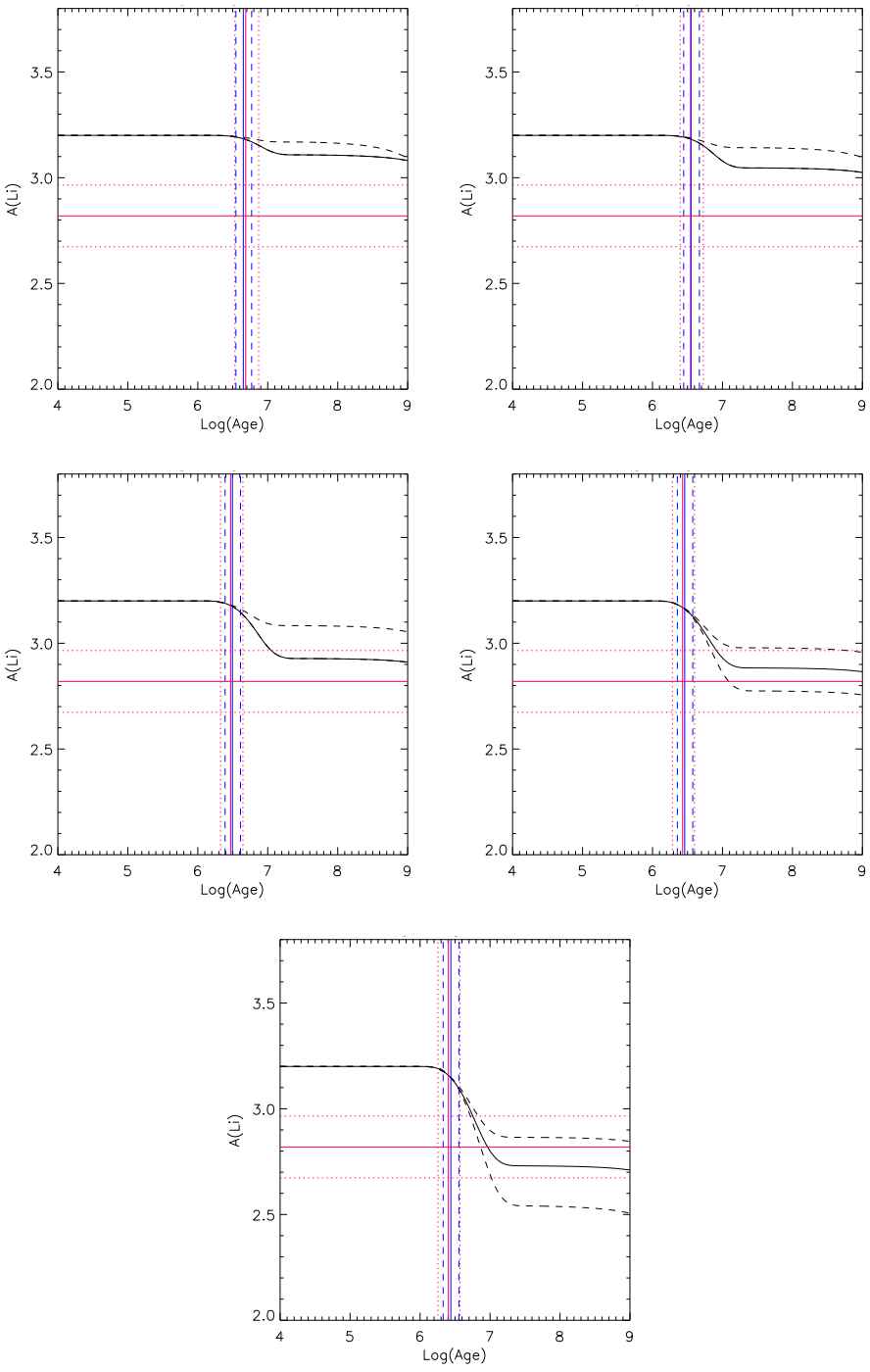

Figure A.59: V4046 Sgr lithium results for primary component

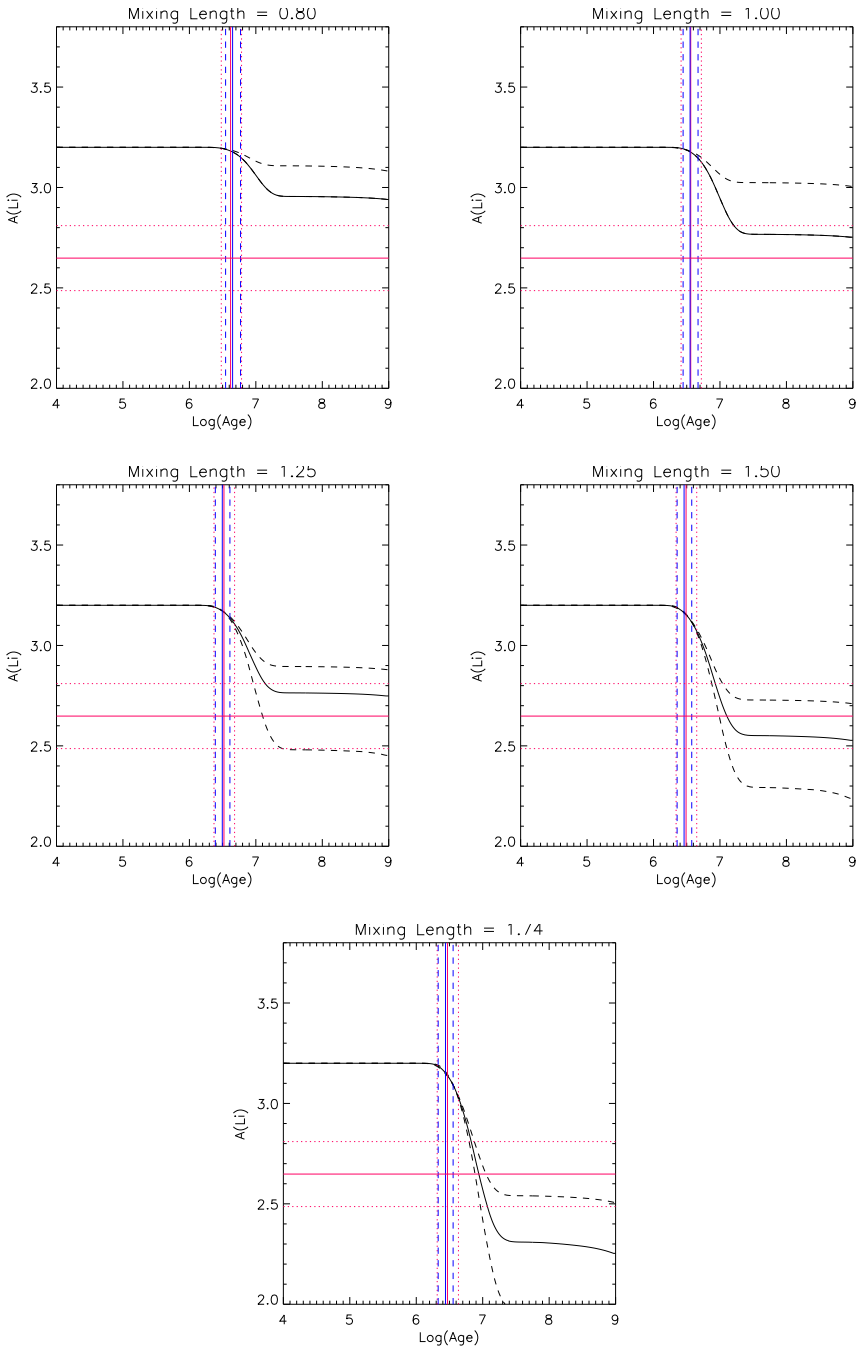

Figure A.60: V4046 Sgr lithium results for secondary component

APPENDIX B

Instruments

The here attached paper describes the high resolution Catania Astrophysical Observatory Spectropolarimeter (CAOS) that I have used to collect the observationald data. CAOS was installed in 2013 and tested in 2014, so that indeed I have partecipated to the Science Verification phase. The other instrument I used, *High Accuracy Radial velocity Planet Searcher for the Northern emisphere* (HARPS-N) is described in Cosentino et al. (2012).

However, a large part of this PhD project has been dedicated to the science verification of CAOS not only as a spectrograph but also as a spectropolarimeter. And I have partecipated to the installation and Science Verification of a polarimetric unit for HARPS-North and for the Low Resolution Spectrograph of the Telescopio Nazionale Galileo.

After Babcock (1948), it is well known that stellar magnetic fields can be detected and measured only on the basis of spectropolariemtric measurements. Thus, the main driving for my partecipation to these technological projects is the convinciment that

magnetic fields largely influence the structure of stars and their evolution. Morover, it is not yet completely understood the effect of these fields on spectral line desaturation (Babcock 1948).

A polarimetric unit for HARPS-North at the Telescopio Nazionale Galileo

Francesco Leone[ab], Massimo Cecconi[c], Rosario Cosentino[c], Adriano Ghedina[c], Marina Giarrusso[ab], Vania Lorenzi[c], Matteo Munari[b], Hector Perez Ventura[c], Luis Riverol[c], Jose San Juan[c], Salvatore Scuderi[b]

[a]Università di Catania, Dipartimento di Fisica e Astronomia, Sezione Astrofisica, Via S. Sofia 78, 95123, Catania;
[b]INAF / Osservatorio Astrofisico di Catanita, Via S. Sofia n. 78, Catania, Italy;
[c]INAF / Fund. Galileo Galilei, Rambla Jos Ana Fernndez Perez 7, 38712 Brea Baja (La Palma), Canary Islands, Spain;

ABSTRACT

Usually observational astronomy is based on direction and intensity of radiation considered as a function of wavelength and time. Despite the polarisation degree of radiation provides information about asymmetry, anisotropy and magnetic fields within the radiative source or in the medium along the line of sight is commonly ignored . Because of the importance of high resolution spectropolarimetry to study a large series of phenomena related to the interaction of radiatino with matter, as in the stellar atmospheres or more genrally stellar envelopes, we designed and realized a dual beam polarimeter for HARPS-N that is in operation at the Telescopio Nazionale Galileo (TNG). The polarisation degree is measured from the combination of a series of measurements and accuracy is limited by the instrumental stability. The great stability (0.6 m/s) and spectral resolution (R=115000) of the HARPS-N spectrograph should result in an accuracy in the measurements of Stokes parameters as small as 0.01%. Here we report on the design, realization, assembling and testing of the polarimetric unit whose first light is planned in August 2014.

Keywords: Manuscript format, template, SPIE Proceedings, LaTeX

1. INTRODUCTION

Physical mechanisms responsible for polarisation in Astrophysics are: reflection from solid surface and small grains, Thomson scattering Rayleigh scattering, Halle effect, Zeeman effect, gyro-resonance and gyro-synchrotron emission. So that, polarimetry as a role in almost all fields of Astrophysics as it can measure: 1. size, shape, orientation, and composition of dust particles (often critical for the determination of extinction values, the uncertainty of which dominates many error analyses), 2. weak reflected-light signatures (e.g., extra-solar planets, hidden nuclei of AGNs, deeply embedded protostars, massive stars with optically thick ejected envelopes), 3. scattering properties of light-reflecting screens (e.g., planetary atmospheres, dust shells, surfaces of rocky bodies, albedos for density measurements), 4. 3-dimensional shapes of point sources independently of distance and separately for physically distinct regions (e.g. physics of supernova explosions and aspect-angle dependency of their apparent luminosities), 5. formation of structure at very early epochs (e.g., AGNs, GRBs, dust grains), 6. stellar magnetic fields and their geometry (e.g., star formation, rotational braking, mass loss, convective processes, genealogy of advanced stages of stellar evolution, nature of soft gamma-ray repeaters).

The importance of polarimetry in Astrophysics and the prospective of characterise the atmosphere of esoplanets justifies the technological effort to update the present instrumentation in order to include a polarimetric capability. As well, new instrumentations are designed including polarimetric modules.

Further author information: (Send correspondence to F. Leone)
Francesco.Leone@oact.inaf.it, Telephone: +39 095 73322 229

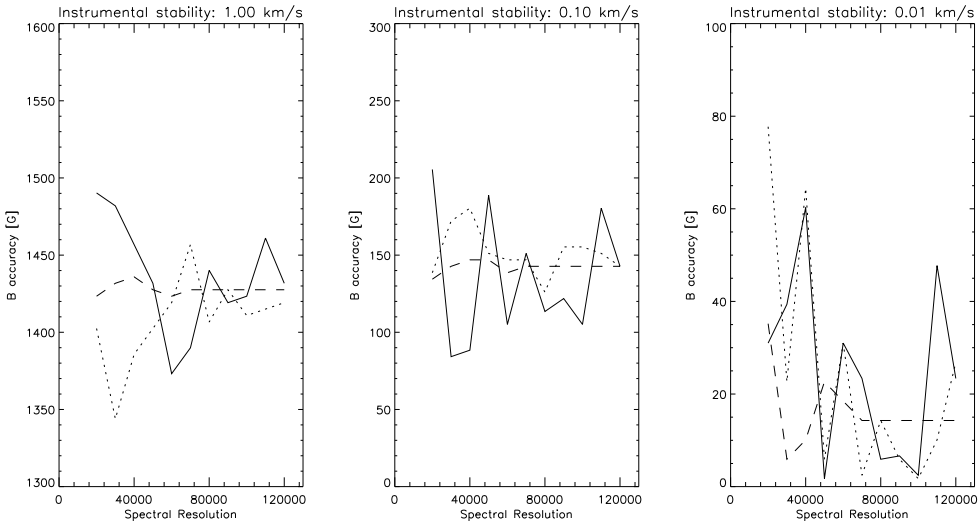

Figure 1. Expected accuracy in measuring the effective magnetic field[?] on the basis of Stokes V parameters by combining to consecutive spectra is reported as a function of S/N = 50 (continuous lines), 100 (dotted lines) and 500 (dashed lines) for three values of the instrumental stability given in $\mathrm{km\,s^{-1}}$.

2. IMPORTANCE OF INSTRUMENTAL STABILITY IN SPECTROPOLARIMETRY

Important Astrophysical problems, as the detection and measuring of magnetic fields, can be faced only on the basis of high resolution spectropolarimetry. For such a reason during the last ten years several (R $\geq$ 100 000) spectrographs have been updated with a polarimetric module, UCLES at AAT (Semel et al. 1993), SARG at TNG (Leone et al. 2003) and finally HARPS at ESO (Snik et al. 2011).

Recently, Bagnulo et al. (2013) explained how the discovery of longitudinal magnetic fields in FORS 2 data (Leone et al. 2011, 2014) can be due to non-photon noise, more specifically due to small offsets in the parallel and perpendicular beams, or non-predictable instrument instabilities or flexures, evidenced by changes in the individual spectra.

As in Leone et al. (2000), we have simultated the measurements of a magnetic field from the wavelength distance of σ components in left and right circular polarised light. Fig. 1 shows the accuracy dependence on signal-to-noise ratio, spectral resolution and instrumental stability as given in velocity stability. HARPS-N is expected to measure magnetic fields with an accuracy of tenths of gauss in a single line.

3. THE POLARIMETER

Two methods are commonly used to perform spectropolarimetry, one is based on a $\lambda/2$ and a $\lambda/4$ retarder that can be alternatively inserted along the optical path and rotated with reference to a beam displacer to measure the linear and the circular polarisation respectively. The polarimeters of the AAT (Hough & Bailey[13]) and WHT (Tinbergen & Rutten[18]) are based on this concept. The other method to measure the light polarisation, often called *dual-waveplate* method, is based on a $\lambda/2$ and a $\lambda/4$ retarders both inserted along the optical beam. The optical axes of these two retarders are opportunely rotated with respect to a beam displacer to measures the linear and the circular polarisation, as for the William-Wehlau spectropolarimeter (Eversberg et al.[10]).

It has to be noted that both methods need the same number of exposures to measure the linear and the circular polarisation. The advantage of the *dual-waveplate* method is the absence of mechanisms necessary to exchange the retarders, however this method **adds** all the defects of the two retarders. Thus we decide not to follow the *dual-waveplate* method having no space to use a K-prism as a $\lambda/4$ retarder and a Fresnel prism as $\lambda/2$ retarder that would be ideal items for their phase retardation with wavelengths (Leone et al.[1]).

3.1 Optical design

As it is usual for an Alto-Azimuthal mounting, the polarisation analyser (Fig. 2) is located after the tertiary mirror and an optical system that supplies a plane parallel beam.

Designing our polarimeter, we had to overcome three main problems:

a) the large spectral range covered and high spectral resolution of HARPS-N.

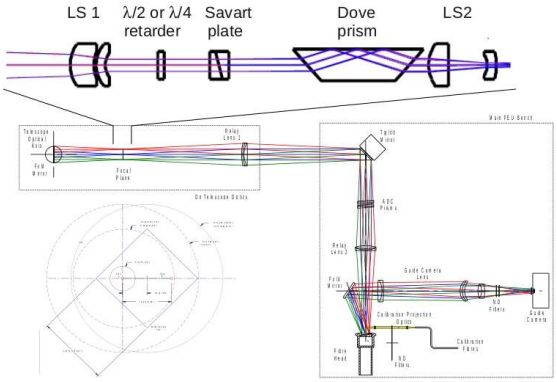

Figure 2. Optical scheme of the polarimeter. **Sostituire con nuova figura**

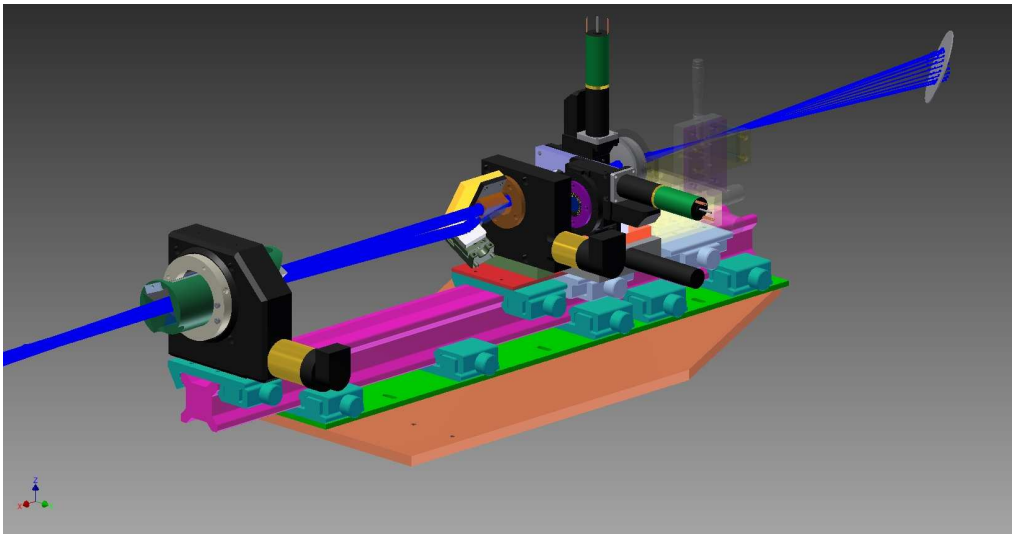

Figure 3. Scheme of the polarisation analyser. Longward the tertiary mirror, a $\lambda/2$ and a $\lambda/4$ retarder can be inserted along the beam. A Foster prism displaces the ordinary and extraordinary beams. A $\lambda/2$ retarder has been glued onto the Foster prism to rotate the polarisation plane of the extraordinary beam and optimise the reflectivity on mirror that bends this beam towards the second fiber of HARPS-N. Foster and retarders rotate continuosly to fix their optical axes onto the sky reference systems rotating because of the alto-azimuthal mounting. A Dove prism compensates such a rotation and feed both HARPS-N fibers.

b) the alto-azimuthal mounting that let the sky be apparently rotating when the polarimetry natural reference system is the equatorial one,

c) the instrumental polarisation, changing with the telescope position, due to the tertiary mirror that feeds the spectrograph,

The polarisation analyser consists of an achromatic $\lambda/4$ retarder, an achromatic $\lambda/2$ retarder and a Foster prism as beam displacer.

As to point a), Pancharatnam superachromatic retarders in principle were acceptable within the covered spectral range (Goodrich et al.[11] However, Donati et al.[9] reported that super-achromatic wave plates generate ripples. Such ripples are expected to limit the polarimetric capability at high resolution. For this reason we selected achromatic Quartz and MgF2 retarders by the *Bernhard Halle Nachfl. GmbH* whose path-difference is correct within $\pm 3\%$ in the spectral range of 450 - 700 nm.

Retarders are mounted on rotary stages, so that when the $\lambda/4$ retarder is inserted along the telescope beam and its axis forms a $\pm 45^o$ angle with respect to the beam displacer optical axis, the Stokes V parameter is measured. While the $\lambda/2$ retarder can assume the 0, 22.5, 45 and 67.5^o angles to measure the Stokes Q and U parameters. To face the field rotation, previous point b), also the Foster prism is mounted in rotary stages in order to have their optical axis fixed on the sky along the acquisiton time. In principle Stokes parameters could be acquired at any angle between the Foster axis and sky reference system being possible to rotated them, however we prefer to synchronously rotate the Foster and retarders to avoid any smearing of Stokes Q and U within the exposure time.

The ordinary and the extraordinary beams emerging from the Foster prism are subsequently *derotated* by a Dove prism to be aligned with respect to two fixed fibers feeding the HARPS-N spectrograph.

All rotary stages can be positioned with an angular precision of 10^{-3} degrees.

3.1.1 Optics Alignment

To align the optical axis of retarders with respect to the Savart plate optical axis, we have followed Goodrich et al.[11]

To align the retarders with respect to the Foster prism, a linear polariser was located along a simulated the beam telescope at an angle estinguishing the extraordinary beam emerging from the Foster prism. The intensity of the emerging beam was then measured as a function of the DMT100 position, and the Savart plate axis was fixed at that angle where the intensity was *null*.

Then the $\lambda/4$ retarder was inserted after the linear polariser and the beam intensity recorded during its rotation. The $\pm 45^o$ angles were fixed determining the maximum intensity of the emerging beam.

Similarly, we have determined the position of $\lambda/2$ retarder optical axis to be coincident with the beam displacer axis (Fig. 4).

3.2 Mechanics

To be filled

4. INSTRUMENTAL POLARISATION

HARPS-N is fed by means of the tertiary telescope mirror ($\mathbf{M_3}$) and a further folding mirror ($\mathbf{FM_1}$), so that the instrumental polarisation has to be determined as a function of the target position in the sky. A theoretical study of the TNG tertiary mirror has already been carried out by Giro et al. (2003) where it has been shown that such a polarization can be easily managed by means of the Muller calculus, considering that: the Stokes parameters describing the polarisation state of the observed target have to be rotated from the equatorial to the alto-azimuthal reference system and than multiplied for the Muller reflection matrix R(pa) because of the tertiary mirror $\mathbf{M_3}$ where the polarisation is changed according to the reflection matrix T. Finally being the

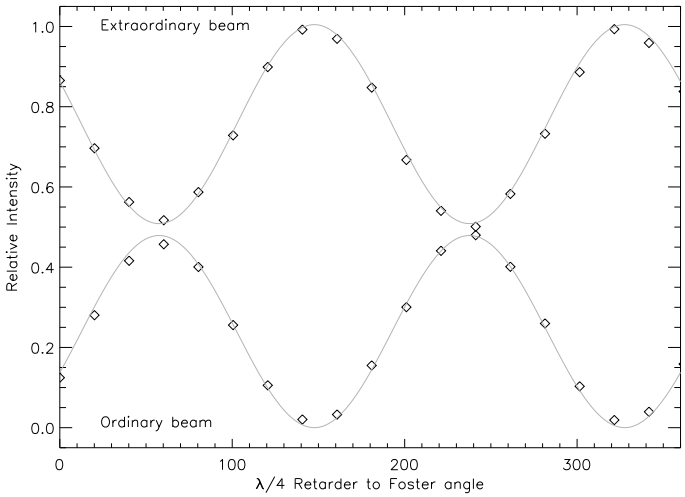

Figure 4. The relative angle between retarders and Foster axes has been

polarimeter always oriented to the north, we have to perform a further passage from the alto-azimuthal to the equatorial system:

$$IP = R(pa)R(\pi/2 - el)T(\mathbf{M_3})R(pa)$$

A successfully application of this method is given in Covino et al.[3] as to the polarimetric unit of the low resolution spectrograph and camera of the TNG.

ACKNOWLEDGMENTS

This unnumbered section is used to identify those who have aided the authors in understanding or accomplishing the work presented and to acknowledge sources of funding.

REFERENCES

[1] Leone, F., Bruno, P., Calì, A., Cosentino, R., Gentile, G., Gratton, R. Scuderi, S. 2003, SPIE, 4843, 465-475
[2] Giro, E., Bonoli, C., Leone, F., Molinari, E., Pernechele, C., Zacchei, A. 2003, SPIE, 4843, 456
[3] Covino, S., Molinari, E., Bruno, P., Cecconi, M., Conconi, P., D'Avanzo, P., di Fabrizio, L., Fugazza, D., Giarrusso, M., Giro, E., Leone, F., Lorenzi, V., Scuderi, S. 2014, AN, 335, 117
[4] Leone, F., Catanzaro, G., Catalano, S. 2000, A&A, 355, 315-326
[5] Leone, F., Catanzaro, G. 2004, A&A, 425, 271-280
[6] Leone, F., Martìnez Gonzáles, M. J., Corradi, R. L. M., Privitera, G., Manso Sainz, R. 2011, ApJ
[7] Leone, F., Corradi, R. L. M., Martìnez Gonzáles, M. J., Asensio Ramos, A.;, Manso Sainz, R. 2014, A&A 563, 43
[8] Capitani, C., Cavallini, F., Ceppatelli, G., Landi degl'Innocenti E., Landi degl'Innocenti M., Landolfi, M., Righini, A., 1989, Solar Physics 120, 173
[9] Donati, J.-F., Catala, C., Wade, G.A., Gallou, G. &, Delaigue, G., Rabou, P. 1999, A&AS 134, 149
[10] Eversberg, T. Moffat, A.F.J., Debruyne, M., Rice, J,B., Piskunov, N, Bastien, P., Wehlau, W.H., Chesneau, O. 1998, PASP 110, 1356
[11] Goodrich, R.W., Cohen, M.H., Putney, A. 1995, PASP 107, 179
[12] Harries, T. J., Howarth, I. D. 2002, A&A 361, 139
[13] Hough, J., Bailey, J. 1994, in Spectropolarimetry at the AAT (The AAT User's manual 24.2)
[14] Kawabata, K. S., Akitaya, H., Hirakata, N., Hirata, R., Ikeda, Y., Isogai, M., Karube, T., Kondoh, M., Matsumura, M., Nakayama, S., Okazaki, A., Seki, M. 2001, ApJ 552, 782

[15] Semel, M., Donati, J.-F., Rees, D.E., 1993 A&A 278, 231
[16] Schmid, H. M., Appenzeller, I., Camenzind, M., Dietrich, M., Heidt, J., Schild, H. & Wagner, S. 2001 A&A 372, 59
[17] Solanki, S.K., Stenflo J.O. 1986, A&A 170, 120
[18] Tinbergen, J., Rutten, R. 2000, in Measuring polarization with ISIS users' manual. The Isaac Newton Group of Telescopes.
[19] Snik, F. et al. 2011, ASPC 437, 237
[20]

D O 17, 2015
Preprint typeset using LaTeX style emulateapj v. 08/22/09

A METHOD TO CALIBRATE THE HIGH-RESOLUTION CATANIA ASTROPHYSICAL OBSERVATORY SPECTROPOLARIMETER

F. L [1,2], G. A [3], G. B [2], P. B [2], S. C [2], R. D B [2], A. D S [2], M. G [1,2], M. G [1,2], V. G [2], E. M [2], M. M [2], M. M [2], C. P [4], C. S [1,2], S. S [2], P. S [3]
[1]Università di Catania, Dipartimento di Fisica e Astronomia, Sezione Astrofisica, Via S. Sofia 78, I–95123 Catania, Italy
[2]INAF - Osservatorio Astrofisico di Catania, Via S. Sofia 78, I–95123 Catania, Italy
[3]ESO, Karl-Schwarzschild-Straße 2, 85748, Garching bei München, Germany
[4]INAF - Osservatorio Astrofisico di Arcetri, Largo E. Fermi 5, I-50125 Firenze, Italy
(Dated: Received TBD / Accepted TBD)
Draft version October 17, 2015

ABSTRACT

The Catania Astrophysical Observatory Spectropolarimeter (CAOS) is a white-pupil cross-dispersed échelle spectrograph with a spectral resolution up to R=55 000 in the 375-1100 nm range in a single exposure, with complete coverage up to 856 nm. CAOS is linked to the 36 inch telescope, at Mount Etna Observatory, with a couple of 100μm optical fibres and it achieves a signal-to-noise ratio better than 60 for a V=10 magnitude star in one hour. CAOS is thermally stabilized in temperature within a 0.01 K r.m.s., so that radial velocities are measured with a precision better than of 100 m s^{-1} from a single spectral line. Linear and circular spectropolarimetric observations are possible by means of a Savart plate working in series with a half-wave and a quarter-wave retarder plate in the 376-850 nm range. As it is usual for high resolution spectropolarimeters, CAOS is suitable to measure all Stokes parameters across spectral lines and it cannot measure the absolute degree of polarisation. Observations of unpolarised standard stars show that instrumental polarisation is generally zero at 550 nm and can increase up to the 3% at the other wavelengths. Since polarised and unpolarised standard stars are useless, we suggest a method to calibrate a high resolution spectropolarimeter on the basis of the polarimetric properties of spectral lines formed in presence of a magnetic field. As applied to CAOS, observations of magnetic chemically peculiar stars of the main sequence show that cross-talk from linear to circular polarisation is smaller than 0.4% and that conversion from circular to linear is less than 2.7%. Strength and wavelength dependences of cross-talk can be entirely ascribed, via numerical simulations, to the incorrect retardance of achromatic waveplates.

Subject headings: Instrumentation: polarimeters, Instrumentation: spectrographs

1. INTRODUCTION

In the same way the high resolution spectropolarimetry has given a deep comprehension of solar magnetism (Trujillo-Bueno et al. 2002), any field of the astrophysical research would greatly benefit from this observational technique. Many theoretical predictions are hidden in the polarised spectral line profiles, with a fashionable example given by exoplanets whose atmosphere, by analogy with the Earth (Sterzik et al. 2012), could be unveiled by polarimetric studies, particularly looking at the Raman scattering (Clarke & Naghizadeh-Khouei 2000). Regrettably, most of the available polarimetric facilities are nowadays limited to linear photopolarimetry and low resolution spectropolarimetry. In fact, the extention of high resolution spectropolarimetry beyond the Sun has been limited by the weakness, usually few per cent, of the polarised signal and faintness of astronomical sources.

With reference to the circular polarisation, Solanki & Stenflo (1986) have already discussed the limits of spectropolarimetry due to the spectral resolution. These authors have pointed out that the area and amplitude of a Stokes V profile across spectral lines strongly decreases with instrumental smearing. Resolution effects can be quantified by numerically computing the Stokes profiles for the FeI5250.4 Å line as formed in the solar atmosphere assuming a uniform 0.1 Tesla field, tilted of 45^o with respect to the observer line of sight and aligned with respect to the equatorial reference system. Radiative transfer equation has been solved in presence of a magnetic field with *Codice per la Sintesi Spettrale nelle Atmosfere Magnetiche* (Stift et al. 2012). Fig.1 shows computed Stokes Q/I profiles for different instrumental resolution and signal-to-noise (S/N) ratios. It appears that at typical resolution of solar spectrographs (R = 500 000) even at very low Signal-to-Noise ratio (S/N= 30), the Stokes parameters are correctly recovered. Decreasing the instrumental resolution, the Stokes profile progressively disappears and becomes almost null at R = 20 000, despite a huge S/N ratio. Fig.1 shows that present spectrographs, working at R = 115 000 (e.g. HARPS), can measure a few percent polarisation, getting easily the necessary S/N ratio, for targets with V $\leq$10. And that, the same is possible at R = 50 000 and S/N$\sim$ 200 with a one meter class telescope for objects brighter than V$\sim$8.

The facilities available to perform high resolution spectropolarimetry are very limited in number and all at medium size class telescopes. Full Stokes polarimeter is possible with ESPADONS (R = 68 000) at the 3.6 m Canadian-France-Hawaii Telescope, NARVAL (R = 65 000) at the 2 m Bernard Lyot Telescope and HARPS (R = 115 000) at the ESO 3.6m telescope. New facilities will be soon available, i.e. PEPSI (R = 120 000) at Large Binocular Telescope (Strassmeier et al. 2015) and HARPS-North Polarimeter (R = 115 000) at the Telescopio Nazionale Galileo (Leone et al. 2014). In such a context, where long temporal coverages or large surveys cannot be easily accomplished, we decided to realise a new white-pupil échelle spectrograph for the 36 inch telescope of the *Osservatorio Astrofisico di Catania* basically devoted to spectropolarimetry. Because of the limited size of the tele-

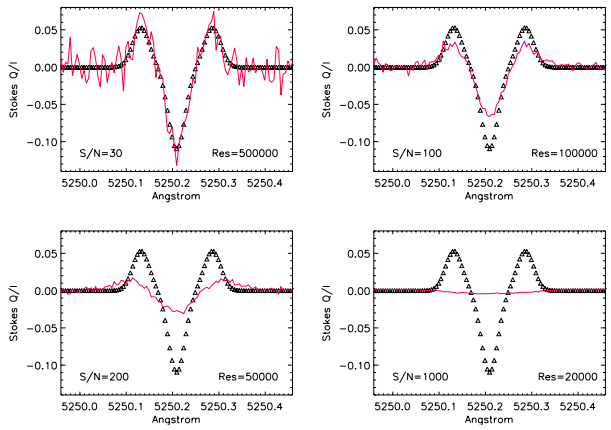

F . 1.— Theoretical (△'s) Stokes Q/I line profile of the FeI5018Å, for a solar spectral region assuming a uniform 0.1 Tesla magnetic field tilted with respect to the observer line of sight and clockwise rotated with respect to the equatorial reference system of 45°, and their appearance with instrumental smearing and signal-to-noise.

scope, resolution was fixed at R = 55 000 as a compromise between spectral smearing and observability of faint targets.

Accuracy in polarimetry is not only a matter of photon statistics (Bagnulo et al. 2013) but it depends on what Serkowski (1974) defined *instrumental polarisation*. A kind of *an observer effect* due to the interaction of the incoming radiation with the instrumentation that modifies just that polarisation status to be measured. Instrumental polarisation, for photopolarimeters and low resolution spectropolarimeters, is usually determined by observing unpolarised and polarised standard stars (Covino et al. 2014) or more recently observing the Earth sky (Harrington et al. 2011). Unfortunately, high resolution spectropolarimeters cannot measure the absolute fluxes with the necessary accuracy to be calibrated by observing standard stars and new methods are required for their calibration.

In the next sections, the *Catania Astrophysical Observatory Spectropolarimeter* (here after CAOS) is described with reference to commissioning results. We present also a method to determine the instrumental polarisation of a high-resolution spectrograph based on the full Stokes polarimetry of magnetic stars. We show how the variety of polarimetric properties presented by spectral lines formed in a magnetic field can be used to calibrate these instruments.

2. CATANIA ASTROPHYSICAL OBSERVATORY SPECTROPOLARIMETER

CAOS has been built to replace the old spectropolarimetric facility of the Catania Astrophysical Observatory (Leone et al. 2000, 2001). The main design requirements of CAOS were (Spanò et al. 2006):

- Linear and circular spectropolarimetry;
- Spectral resolution up to R = 60 000;
- Full spectral coverage in one exposure in the region: 388 - 725 nm, that is from calcium to lithium lines;
- Fibre fed. Both integral light mode and polarimetric mode will feed two fibres for simultaneous measurements of source+sky or two independent polarimetric components, respectively.

TABLE 1
L - .

Surface	Radius mm	Thickness mm	Material	Diam. mm
Fibre exit		28.263		
First doublet	60.310	2.00	SF2	15
	17.600	4.90	BK7	15
	-23.395	7.426	Air	15
Second doublet	41.400	3.700	BK7	15
	-30.153	2.000	SF2	15
	-103.800	97.538	Air	15
Field lens	38.760	2.700	BK7	15
	∞	15.00	Air	15

2.1. *Optical design*

In order to match the requirements, we designed a bench-mounted, fibre-fed, cross-dispersed échelle spectrograph. As trade-off between resolution and cost, the spectrograph had a 10 cm collimated beam dispersed by a R4 échelle grating in white-pupil configuration (Dekker et al. 2000), with an optimized all-dioptric camera focusing the dispersed spectrum onto a CCD detector. Fig. 2 shows the optical layout of the spectrograph as seen from the top.

2.2. *Fibre link and pre-slit optics*

CAOS spectrograph is fed with two 100um, multimode, high OH radicals optical fibres which are optimised for UV transmission. One fibre is for the target and the other for simultaneous calibration and/or sky substraction. At the Cassegrain focal plane, a couple of gradient-index lenses are glued on the input fibre ends projecting the pupil of the telescope on them. The lenses (by *Melles Griot*) have 1 mm focal distance, 1 mm diameter, a 0.37 numerical aperture and 0.25 fractional pitch. The fibre aperture projected on the sky is about 3", with a typical 2" seeing value at Mount Etna Observatory. The lenses convert the F/15 telescope beam into a F/4 beam into the fibres to reduce the so-called focal ratio degradation (Avila 1998). To convert the large F/4 exit optical aperture of the fibres into F/10 beams, two achromatic doublets and a single lens by *Optosigma* are used (Table 1). At the slit plane the two fibres appear with a diameter of 285um. The total efficiency of the fibre link, without considering seeing losses at the fibre input end is about 66%.

2.3. *Collimator mirrors*

An F/2.4 paraboloidal mirror in Astrosital, with 400 mm clear area and a focal length of 1000 mm has been shaped and cut in two off-axis portions as shown in Fig. 3 by *Costruzioni Ottico Meccaniche Marcon*. Both portions have been coated with protected silver for high reflectivity (> 97% at 0.5-1 μm) by *Gestione SILO*.

The larger portion has been used off-axis as a F/10 collimator. The mirror is used a second time creating an intermediate focal plane with light dispersed by the échelle grating. The second portion has been used to collimate the light towards the cross disperser.

It is worth to note that the adopted solution is slightly different than classical white-pupil spectrographs, like UVES, SARG or FEROS as there is no folding mirror at the return focus. This is to minimise the number of reflections, that is to reduce the image quality degradation and light losses.

2.4. *Grating*

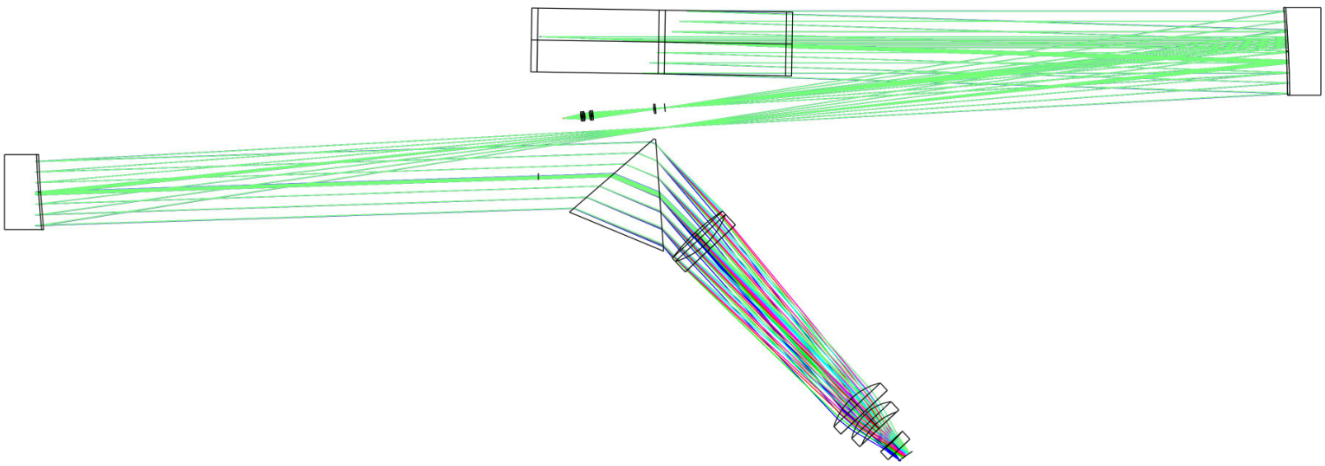

F . 2.— Optical layout of CAOS.

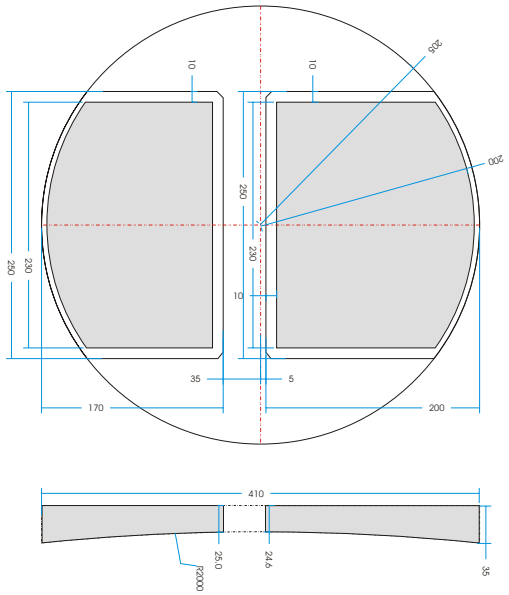

F . 3.— Collimators have been extruded from a 400 mm parabolic mirror. Measures are given in millimeter.

The échelle grating supplied by the *SPECTRA PHYSICS Richardson Gratings* presents 41,59 rules mm^{-1} with a blaze angle of 76^o (R4). Ruled area is 102×408 mm with an aluminum reflection coating. The grating works on Littrow configuration with a small (0.9^o) off-plane angle. Such a small angle introduces a small line tilt, below 0.2 pixel on the CCD (sect. 2.7) focal plane.

2.5. *Cross-disperser*

The *Gestione SILO* produced a 140x160x160 mm prism, made of Schott SF1, with an apex angle of 53.1^o that has been adopted as cross-disperser. A/R coatings give an average throughput better than 90%. An analysis of the wavefront shows a deformation compatible with a degradation of the resolution equal to 8%. Degradation was ascribed to the non homogeneous optical properties within the huge block of glass.

Fibres are rotated to have a projected distance with respect to the grating grooves equal to 570 μm. So that, when both fibres are illuminated, light overlapping is not present up to 856nm.

TABLE 2
L .

Surface	Radius mm	Thickness mm	Material	Diam. mm
Object		∞		
Pupil		15.000		106
1	299.957	25.000	S-FPL51	112
2	−131.845	1.000		112
3	−130.009	10.000	S-BSL7	112
4	∞	344.586		112
5	91.285	30.000	S-BSL7	104
6	∞	1.000		104
7	64.249	23.000	S-BSL7	90
8	66.993	32.393		70
9	-194.150	8.000	S-BSL7	54
10	∞	15.000		54

2.6. *Camera*

The F/2.1 camera (Fig. 4) was produced by *Société Européenne de Systèmes Optiques* and consists of five lens mounted in three groups: a doublet, two separate lenses, and a field flattener acting also as dewar window. All surfaces are spherical or plane.

Due to the fixed spectral format, axial chromatism has been corrected by tilting the focal plane. To assure the correct tilting of the focal plane the last lens of the camera is also the window of the Dewar stopper and the detector is mounted on the tilted focal plane screwed on the internal side of the dewar flange at the focal distance.

Optical prescription for the camera is given in Table 2. First order parameters are:
- Entrance diameter: 100 mm
- Effective focal length: 213 mm
- F/number: F/2.1
- Field of view (diameter) : 7.4^o
- Optimised wavelength range: 388-725 nm

2.7. *Detector*

The sensor used is an E2V42-40 Thinned and Back Illuminated High Performance Charge Coupled Device. It has a

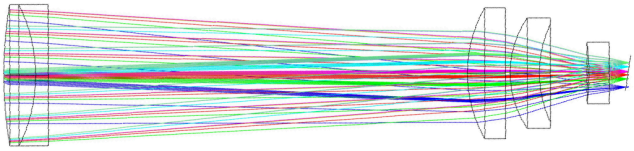

F . 4.— Camera layout. Spherical surfaces and standard glasses ensure high transmission and low-cost. Note the tilted focal plane to correct for axial chromatism.

TABLE 3

F

.

O	λ_i	λ_f	O	λ_i	λ_f	O	λ_i	λ_f
	nm	nm		nm	nm		nm	nm
44	1103	1121	72	662	673	100	472	480
45	1077	1095	73	652	663	101	468	476
46	1053	1070	74	643	654	102	463	471
47	1029	1046	75	634	645	103	458	466
48	1007	1023	76	626	636	104	454	462
49	986	1002	77	618	628	105	449	457
50	965	981	78	609	619	106	445	453
51	945	961	79	601	611	107	441	448
52	926	942	80	594	604	108	437	444
53	908	923	81	586	596	109	433	440
54	891	905	82	579	588	110	429	436
55	874	888	83	572	581	111	425	432
56	858	872	84	565	574	112	421	428
57	842	856	85	558	567	113	417	424
58	827	841	86	551	560	114	413	420
59	813	826	87	545	554	115	410	417
60	799	812	88	538	547	116	406	413
61	785	798	89	532	541	117	402	409
62	772	785	90	526	535	118	399	406
63	759	772	91	520	529	119	396	402
64	747	759	92	515	523	120	392	399
65	735	747	93	509	517	121	389	396
66	724	736	94	503	512	122	386	392
67	713	724	95	498	506	123	382	389
68	702	713	96	493	501	124	379	386
69	691	703	97	487	496	125	376	383
70	681	692	98	482	490			
71	671	682	99	477	485			

2048 by 2048 pixel format, with 13.5 mm square pixels yielding an image area of 27.6 mm × 27.6 mm.

The CCD controller is a generation 3 CCD controller developed, built and integrated on one of our cryostat at the Niels Bohr Institute in Copenhagen.

Reading the CCD at 100 kHz, the read-out noise is 3.5e$^-$, 4e$^-$ at 200 kHz, and 6e$^-$ at 400 kHz.

Table 3 shows the limits for any order of the echellogram imagined on the CCD. The resulting échelle spectral format covers 374-1100 nm range in 81 orders, with only a 5% uncovered spectrum longword of 856 nm due to not complete order overlapping.

2.8. *Ghosts and Straylight*

To locate ghosts in our echellogram we have illuminated the fibres with a 633 nm laser light close to the CCD saturation. Fig. 5 shows that there is not a ghost series in CAOS spectra due to periodic errors in grating rulings (Griffin 1968) or any other feature at a level of 10^{-4} of the peak.

Light dispersed by the grating out of the collimator, scattering on non-ideal optical elements and reflection on mechanical parts give origin to the straylight that hits the CCD irrespective of the diffraction law. Usually straylight is estimated by fitting the background signal present in the inter-order pixels and then subtracted it to the echellogram. In high resolution spectroscopy, this is an important step in the data reduction procedure to obtain a spectrum with correct equivalent widths. As for CAOS, it results that stray light is less than 1% of the total light recorded by the CCD.

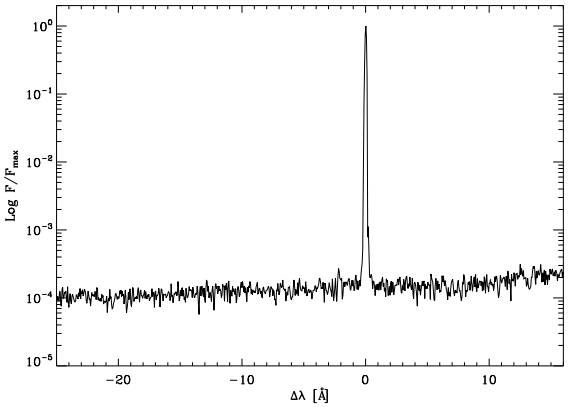

F . 5.— Observations of the laser line at 633 nm show no spurious lines due to imperfections in the gratings or other ghosts at a level of 10^{-4} of the peak.

2.9. *CAOS Stability*

Spectrographs are limited in their accuracy by changes of the echellogram projection on CCD in time.

To handle the various sources of vibration noise (e.g. continuous Etna seismic activity, or Building oscillation due to the Dome rotation), CAOS is mounted on a 2.4x1.2m TMC optical table that provides dry dumping vibration cancellation.

Thermal variations change the optical path within a spectrograph resulting in transverse movements of the echellogram on the CCD and longitudinal variations responsible of not in focus echellogram. Transverse variations are at the basis of errors in radial velocity measurements being the pixel-to-wavelength association no longer correct. If the thermal variation temporal scale is longer then typical exposure times, then it is still possible to correct the wavelength scale. Historically, echellogram movements have been traced with an absorption cell, or simultaneously recording the echellogram of a calibration lamp. Often telluric lines are used to set a zero point for wavelengths. Thermal variations shorter then exposure times result not only in a reduced wavelength calibration accuracy, but also in a decreased spectral resolution.

To reduce as much as possible the effects due to thermal variations and improve the instrument stability, CAOS is located in a thermally insulated room whose temperature is kept constant within an r.m.s.<0.01 K.

As a test of stability during the instrument commissioning in 2014, we have obtained spectra of Vega with a Signal-to-Noise Ratio of ∼100. The barycenter of single spectral lines was found constant in time within an accuracy of ∼100 m s^{-1}. This value can be compared with the accuracy of HARPS North, 60 m s^{-1} for a S/N∼50, that has the same 0.01 K temperature stability but a double spectral resolution. During the commissioning, the well known star *τBoo* hosting an exoplanet has been monitored. A simple correlation between chunks of spectra at limited signal-to-noise (< 50) a synthetic

spectrum[1] shows that radial velocities are accurate better then few hundred meters per second and in agreement with expectation (Fig. 6). Velocities were analysed using the *Image Reduction and Analysis Facility* (Tody 1986) packages, however *ad hoc* algorithms are under development for an optimal measurement of radial velocities.

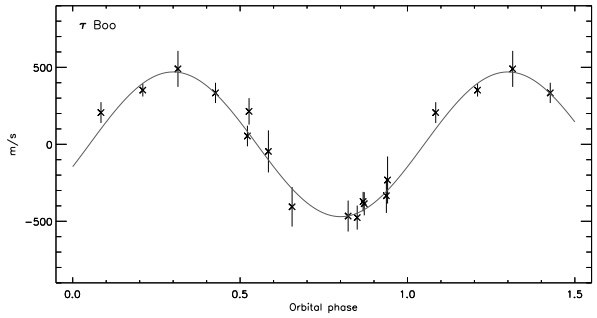

F . 6.— A simple correlation between chunks of CAOS (S/N~50) spectra and a synthetic spectrum highlights the radial velocity variations of τ*Boo*. Continuum line has been drawn according the ephemeris listed by Drummond (2014).

3. THE POLARIMETER

CAOS polarimeter follows the design we adopted for the polarimetric unit of the high resolution spectrograph (SARG) of the *Telescopio Nazionale Galileo* (Leone et al. 2003). The polarimeter is based on the double-beam technique and dual-waveplate method and it consists of a $\lambda/2$ or $\lambda/4$ retarder and a Savart plate working as beam displacer. The polarimeter is located along the converging *F/15.5* beam of the telescope.

The polariser is made from calcite, size 15x15 mm^2, with a total length of the two cemented parts of 32 mm resulting in a beam separation of 2.5 mm in the visible range; both sides are AR coated for the 350-900 nm interval range. The Savart plate has been chosen because gives null difference between the optical paths of the ordinary and extraordinary converging beams.

The retarders are achromatic ones. Because of the very large spectral interval covered by the CAOS in polarimetric mode (380 - 850 nm), low order or zero order retarders were not suitable, see figure 2 in Leone et al. (2003). Super-achromatic retarders were discarded being source of ripples already at resolution $R = 35\,000$ (Donati et al. 1999). Unfortunately, the ideal Fresnel rhombs as $\lambda/2$ plate a K-prism as $\lambda/4$ plate are too big to be located along the telescope converging beams.

To align the fast axis of retarders with respect to the Savart plate acceptance axis, we have applied the Goodrich et al. (1995) method as described in Leone et al. (2003).

3.1. *Observational strategy and data reduction*

The signal after the polariser (Landi Degl'Innocenti & Landolfi 2004) is a function of the angle α between the retarder fast-axis and polariser acceptance axis, the angle β that the polariser acceptance axis forms with the celestial meridian and the wave-plate retarder δ:

$$\begin{aligned} S(\alpha,\beta,\delta) = 0.5\{ & I + (Q\cos 2\alpha + U\sin 2\alpha)\cos[2(\beta-\alpha)] \\ & -(Q\sin 2\alpha - U\cos 2\alpha)\sin[2(\beta-\alpha)]\cos\delta \\ & +V\sin[2(\beta-\alpha)]\sin\delta\} \end{aligned} \quad (1)$$

As it is usual, CAOS measures the Stokes parameters on the basis of a finite numbers of α values. Stokes V is measured with a quarter wave-plate retarder ($\delta = \pi/2$) at $\alpha = +45^o$ and -45^o. By means of a half wave-plate retarder ($\delta = \pi$), Stokes Q is measured with at $\alpha = 0^o$ and 45^o, while Stokes U for $\alpha = 22.5^o$ and 67.5^o. To combine the *o*-rdinary and *e*-xtraordinary S beams emerging from the polariser and measure the Stokes parameters, we follow the ratio method as introduced by Tinbergen (1992). It is assumed that there is a time independent instrumental sensitivity $G(\lambda)$ (e.g. pixel-by-pixel efficiency) together with a time dependent sensitivity $F(\lambda)$ of spectra (e.g. variation of sky transparency). So that, a photon noise dominated Stokes parameter $P(\lambda)$ can be obtained from the recorded spectra at $\alpha = \alpha_1$ and α_2:

$$S_{\alpha_1,o}(\lambda) = 0.5\,[\,I(\lambda) + P(\lambda)\,]G_o(\lambda)F_{\alpha_1}(\lambda) \quad (2)$$
$$S_{\alpha_1,e}(\lambda) = 0.5\,[\,I(\lambda) - P(\lambda)\,]G_e(\lambda)F_{\alpha_1}(\lambda) \quad (3)$$
$$S_{\alpha_2,o}(\lambda) = 0.5\,[\,I(\lambda) - P(\lambda)\,]G_o(\lambda)F_{\alpha_2}(\lambda) \quad (4)$$
$$S_{\alpha_2,e}(\lambda) = 0.5\,[\,I(\lambda) + P(\lambda)\,]G_e(\lambda)F_{\alpha_2}(\lambda) \quad (5)$$

Hence:

$$\frac{P(\lambda)}{I(\lambda)} = \frac{R_P(\lambda)-1}{R_P(\lambda)+1} \qquad \text{with} \quad R_P^2(\lambda) = \frac{S_{\alpha_1,o}(\lambda)/S_{\alpha_1,e}(\lambda)}{S_{\alpha_2,o}(\lambda)/S_{\alpha_2,e}(\lambda)} \quad (6)$$

In addition, we compute the *Noise* polarisation spectrum:

$$\frac{N(\lambda)}{I(\lambda)} = \frac{R_N(\lambda)-1}{R_N(\lambda)+1} \qquad \text{with} \quad R_N^2(\lambda) = \frac{S_{\alpha_1,o}(\lambda)/S_{\alpha_2,e}(\lambda)}{S_{\alpha_2,o}(\lambda)/S_{\alpha_1,e}(\lambda)} \quad (7)$$

to check possible errors in Stokes $P(\lambda)/I(\lambda)$ due to the alignment of ordinary and extraordinary spectra in wavelength. In such a context, it is worth to point out the importance of the heliocentric velocity correction. For full Stokes polarimetry a minimum of six exposures are necessary. Often a series of four exposures with a sequence α_1, α_2, α_2, α_1 is obtained to measure a Stokes parameter by subtracting any possible derivative in time. A 100 m s^{-1} radial velocity shift between the ordinary and extra-ordinary beams could let Stokes V/I be interpreted as a magnetic field of one hundred gauss (Leone & Catanzaro 2004). Unchecked alignements have been wrongly interpreted as the presence of magnetic fields on the central star of Planetary Nebulae (Leone et al. 2011).

CAOS Stokes profiles of γEqu have been compared with similar spectra obtained with ESPADONS and HARPS-POL. Already reduced ESPADONS data have been obtained from CFHT archive, whereas CAOS and HARPS-POL spectra have been extracted with the procedures previously described. Fig.7 shows that differences are within the spectral resolution and noise. This means that CAOS operativity and data reduction extraction procedures are within the present standard of worldwide polarimetric capabilities.

4. HIGH RESOLUTION SPECTROPOLARIMETRY AND INSTRUMENTAL POLARISATION

Generally speaking, three are the sources of instrumental polarisation for a high resolution spectropolarimeter:

[1] The SYNTHE (Kurucz & Avrett 1981) spectrum has been computed assuming the ATLAS9 (Kurucz 1993) model atmosphere with: $T_{\rm eff}$ = 3687 K, log g = 4.26 (Valenti & Fischer 2005), solar metal opacity scale and the atomic line list given by Kurucz (1993).

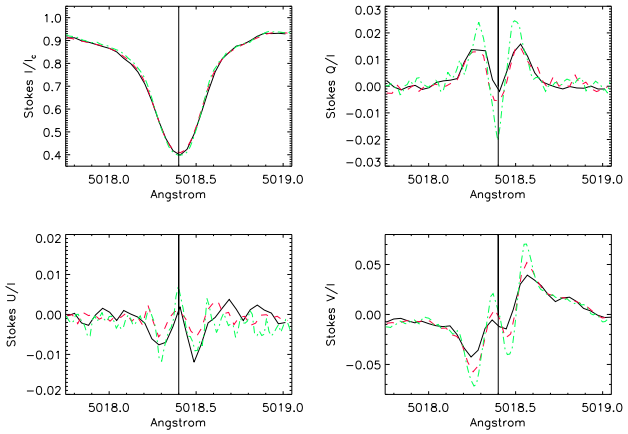

F . 7.— Stokes profiles of the FeI5018Å line as observed with CAOS (solid line), ESPADONS (red dashed line) and HARPS-POL (green dot-dashed line) are coincident within resolution and signal-to-noise.

a) Optics and mechanics collecting photons and feeding the instrument. Polarisation can be due to reflections and transmissions along the optical path before the polarimeter.

CAOS has no opto-mechanical elements whose polarisation changes continuously, like the tertiary mirror of an Alto-Azimuthal telescope (Giro et al. 2003). Indeed, there are no plane mirrors feeding the polarimeter and, because of the telescope axial symmetry, polarisation is expected to be negligible. Sen & Kakati (1997) have shown that the polarisation at a f/13 Cassegrain focus goes from 0.0018% to 0.016% for an unpolarised source observed in the range 10 to 90 arcsecs from the optical axis. And that a 100% linear polarised source would be measured at a 99.998334% on axis up to 99.998184% if observed 90 arcsec off-axis.

b) Polarimeter components, that in real life are far from being *ideal*.

Polarisers are characterised by an *extinction rate*, that is the fraction of a fully polarised light traveling along the wrong path. Nominal extinction rate for the CAOS Savart plate is 10^{-5}. Whatever this extinction ratio with the wavelength is for CAOS, the swapping strategy of beam paths within the polariser correct for.

Retarders present the nominal retardance only for few wavelengths so that at the other wavelengths a fraction of a polarised state proceed along the "wrong" path of the polariser. According to Bernhard Halle Nachfolger GmbH, CAOS retarders induce a retardance within ±3% of the nominal value in the 450-700 nm range with a correct value only at 488 and 633 nm. From eq. (1), (2) and (3), the expected Stokes Q, U and V for a fully linear polarised radiation (I=1, Q = 1, U=1 and V=0) because of a retardance error equal to −3% are: Q=0.998, U=0 and V=0, while a fully circular polarised radiation (I=1, Q = 1, U=1 and V=0) would be observed as Q = 0.047, U=0.0 and V = 0.999. At high resolution, retardance errors would slightly modify the Zeeman shaped spectral lines. Fig. 8 shows the expected profiles for negative and positive differences on retardance.

c) Fault of the assumption that the instrumental sensitivity is constant in time. According to eq. (2), the *o*-rdinary and *e*-xtraordinary beams emerging from the polariser should feed the spectrograph with an efficiency whose ratio

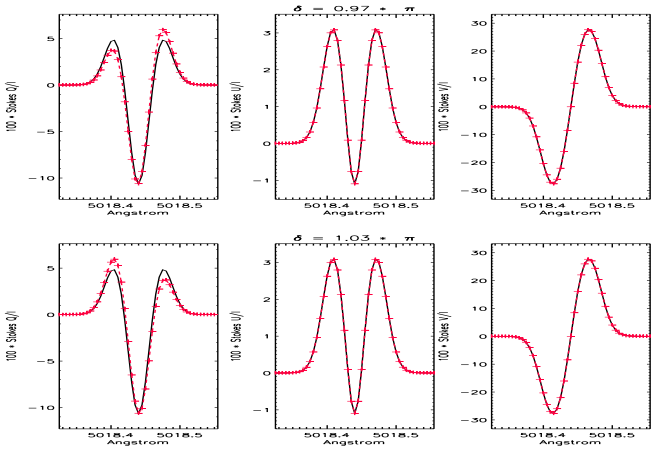

F . 8.— Cross-talk at high spectral resolution, due to a ±3% incorrect retardance of wave-plates, can be quantified from line profiles shaped by the Zeeman effect. Intrinsic (solid) and expected (dashed) Stokes profiles of the FeI5018Å line.

$(G_o(\lambda)/G_e(\lambda))$ is constant in time at any wavelength.

In standard spectroscopy, *Atmospheric Dispersion Correctors* or derotators, together with a telescope guiding system, are used to feed continuously the slit or the fibres with all wavelengths despite the terrestrial atmospheric refraction. Otherwise, certain wavelengths fall outside the slit or fibres and the resulting spectrum does not capture all the light from the object. Thus only low resolution spectroscopy can measure the absolute fluxes, by using slits much larger than the target image on the focal plane. At high resolution, when the slit is smaller then the target image, the combination of errors on autoguiding, alignement with the parallactic angle, and roughness of slit edges only the flux relatively to the continuum can be accurately measured. Fibre injection errors are related to the optical apertures and alignements.

The Earth atmospheric refraction, optical aberration and polariser chromatism[2] result in a rather complex distribution of the wavelengths on the focal plane, possibly without any preferred direction. And, the separation between the ordinary and extraordinary beams is certainly variable in time and wavelengths. As a consequence, it is difficult to get $G_o(\lambda)/G_e(\lambda)$ constant in time at the level that polarimetry requires. The parameter N in eq. (4) can also measures the fault of this hypothesis in two exposures at time t_1 and t_2:

$$\frac{(G_o/G_e)_{t_1}}{(G_e/G_o)_{t_2}} = \frac{1+N}{1-N} \tag{8}$$

then it is appears that a fault of only 1% results in an instrumental polarisation of 0.5%.

Cases **a)** and **b)** are generally handled by observing polarised standard stars. Differently, the time variability of the instrumental sensitivity, case **c)**, cannot be modeled neither quantified on the basis of standard stars. It can be evaluated a posteriori from the *Noise* spectrum. On the basis of eq. (5), CAOS *Noise* spectra are usually null at 550 nm and increases up to 3% at the other wavelengths. Probably this is due to the guiding camera whose maximum of the sensitivity is just at

[2] In a simple Calcite or Foster prism (e.g. HARPS polarimeter), only the extraordinary beam is chromatically dispersed along the two beams direction. As to the two beams emerging from a Savart plate (e.g. ESPADONS or CAOS), the chromatism directions are mutually orthogonal and both are orthogonal to the conjunction of the two beams. Chromatism in a wollaston prism for both beams is along the separation direction.

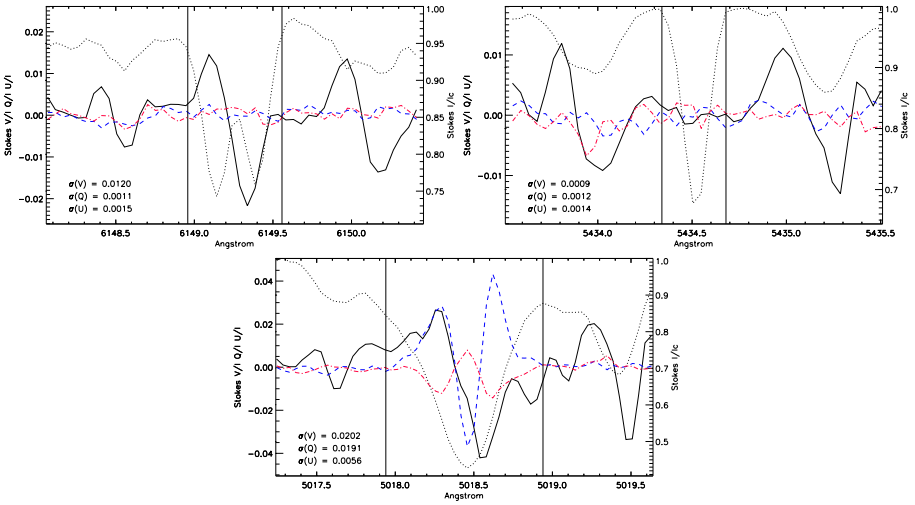

F . 9.— CAOS observations of βCrB. Relative intensity (black dotted), Stokes Q/I (red dot-dashed), U/I (blue dashed) and V/I (black solid) profiles for the FeII6149.2λ line (left panel) whose second order effective Landé factor is null and produces no linear polarisation, FeI5434.5λ line (central panel) whose effective Landé factor is null and produces no circular polarisation and FeI5018.4Å line (right panel) presenting one of the largest second order effective Landé factor G = 3.67.

the visible wavelengths.

5. CALIBRATION

As stated before, photopolarimeters and low resolution spectropolarimeters measure the absolute flux and are commonly limited to the linear polarisation. Assuming that targets present no circular polarisation, the instrumental polarisation is determined on the basis of unpolarised and polarised standard stars.

To calibrate a high resolution full Stokes spectropolarimeter, without reference to the polarised standard stars and including the possible conversion of a polarisation state into the other, new methods have to be defined. Following Kuhn et al. (1994), that have modeled the instrumental polarisation of the National Solar Observatory Vacuum Tower Telescope by observing the sunspot, we suggest to calibrate high resolution spectropolarimeters by observing the magnetic chemically peculiar (MCP) stars of the main sequence (Wolff 1983).

5.1. *Magnetic Chemically Peculiar Stars*

The impossibility to resolve the visible disk of magnetic stars, let Babcock (1947) to define the effective magnetic field i.e. the line-intensity weighted average over the visible stellar disk of the line-of-sight component ($B_\parallel$) of the magnetic field vector:

$$\mathrm{B_{eff}} = \frac{1}{\mathrm{W}\mathcal{F}_{I_c}} \int_0^{2\pi} \mathrm{d}\phi \int_0^{\pi/2} \mathrm{B}_\parallel \cos\theta \, \sin\theta \, \mathrm{d}\theta \int [\mathrm{I_c} - \mathrm{I}_\lambda] \mathrm{d}\lambda \quad (9)$$

where W is the line equivalent width, $\mathcal{F}_{I_c}$ is the flux in the continuum at the line wavelength, ϕ and θ define in the usual way the coordinates on the stellar surface. I_c and I_λ are the respective intensities in the continuum and in the line at the point (θ, ϕ).

By analogy, it is possible to define the transverse component of the magnetic field vector:

$$\mathrm{B_{tra}} = \frac{1}{\mathrm{W}\mathcal{F}_{I_c}} \int_0^{2\pi} \mathrm{d}\phi \int_0^{\pi/2} \mathrm{B}_\perp \cos\theta \, \sin\theta \, \mathrm{d}\theta \int [\mathrm{I_c} - \mathrm{I}_\lambda] \mathrm{d}\lambda \quad (10)$$

The relations between stellar magnetic fields and Stokes parameters have been given by Landi Degl'Innocenti & Landolfi (2004) for a weak line emerging from a small surface element:

$$V(\lambda) = \quad -4.67 \times 10^{-13} \bar{g} \lambda^2 B_\parallel \frac{\partial I}{\partial \lambda} \quad (11)$$

$$Q(\lambda) = -5.45 \times 10^{-26} \bar{G} \lambda^4 B_\perp \cos 2\chi \frac{\partial^2 I}{\partial \lambda^2} \quad (12)$$

$$U(\lambda) = -5.45 \times 10^{-26} \bar{G} \lambda^4 B_\perp \sin 2\chi \frac{\partial^2 I}{\partial \lambda^2} \quad (13)$$

with λ in angstroms, χ is the orientation angle of $B_\perp$ in a given reference system, $\bar{g}$ is the effective Landé factor and $\bar{G}$ is the second order effective Landé factor. Stokes profiles, in principle could be inverted and, supply the geometry of magnetic field (Bagnulo et al. 2001).

Up to now, the most extensive catalogue of observed Stokes I, V, Q and U profiles for MCPs has been supplied by Wade et al. (2000) at R = 35 000.

5.2. *The method*

Stokes parameters can be recovered by the observed ones via a Mueller matrix M characterising the instrumental polarisation so that $[I, Q, U, V]_{obs} = M_\lambda [I, Q, U, V]_{inp}$. Since CAOS works at a Cassegrain focus, M_λ does not present variation with the telescope position and it is constant in time as along the telescope mirrors do not change their properties. Following Kuhn et al. (1994), the inverse Mueller matrix is equal to:

$$M_\lambda^{-1} = \begin{pmatrix} 1 & 0 & 0 & 0 \\ 0 & 1 + a_\lambda c_\lambda & a_\lambda d_\lambda & -a_\lambda \\ 0 & c_\lambda b_\lambda & 1 + d_\lambda b_\lambda & -b_\lambda \\ 0 & -c_\lambda & -d_\lambda & 1 \end{pmatrix} \quad (14)$$

As a consequence of the large variety of Zeeman patterns (Stift & Leone 2003) very different Stokes profiles are observed in MCP stars. Fig. 9 shows how different can be the Zeeman effect on three iron lines of the MCP star βCrB. Particularly important for our goals are lines, like the FeII 6149.258 Å, with no linear polarisation that immediately gives the cross-talk from circular to linear polarisation. While, simple Zeeman triplets are expected to present no Stokes V signal at the central wavelength, and measured signal is due to cross-talk from linear to circular polairsation. To determine the coefficients of the Mueller matrix, we have carried out

full Stokes spectropolarimetry of the very long period, P>70 years (Leroy et al. 1994), MCP star γEqu and of the MCP star βCrB along its 18.4868 day period (Bagnulo et al. 2001). γEqu has been selected for the neglible rotational broadening, that let Stokes V profiles be very narrow, and Stokes Q and U profiles usually embedded in the noise. The few exceptions are lines with a very large second order Landé factor, like the FeI5018.4Å (G = 3.67, see Fig. 10). Differently, βCrB presents well defined Stokes Q and U, as well Stokes V profiles. The monitoring along the rotational period averages any possible wavelength shift of the zero value of Stokes V profiles.

We have then determined the c_λ and d_λ coefficients of the CAOS inverse Mueller matrix assuming that the input Stokes Q and U line profiles presented by γEqu are null. After correction for the cross-talk from Stokes V to Q and U in the spectropolarimetric data of βCrB, we determined the cross-talk from linear to circular polarisation, that is a_λ and b_λ coefficients, assuming that that the observed V_{obs} profiles have to be null at the wavelengths of π components. It results that coefficients of Mueller matrix show a quadratic dependence on wavelengths:

$$a_\lambda = -0.161 + 5.55 \times 10^{-5}\lambda - 4.60 \times 10^{-9}\lambda^2$$
$$b_\lambda = -0.131 + 4.80 \times 10^{-5}\lambda - 4.42 \times 10^{-9}\lambda^2$$
$$c_\lambda = +0.031 - 8.13 \times 10^{-6}\lambda + 5.04 \times 10^{-10}\lambda^2$$
$$d_\lambda = -0.370 + 1.33 \times 10^{-4}\lambda - 1.18 \times 10^{-8}\lambda^2$$

It appears that CAOS cross-talk is almost negligible. A maximum of 0.4% of Stokes Q and U is converted in V. While the upper-limit of cross-talk from V to U is 2.7% at 400 nm. The quadratic dependence of inverse matrix coefficients on the wavelength closely resembles the behavior of the retardance of achromatic retarders (Leone et al. 2003) and it suggests that most of cross-talk is due to the incorrect retardance of wave-plates. According to the Bernhard Halle Nachfolger GmbH, CAOS retarders induce a retardance within ±3% of the nominal value in the 450-700 nm range with a correct value only at 488 and 633 nm. It is worth to note that $d_{488nm} = -0.20\%$ and $d_{633nm} = -0.09\%$.

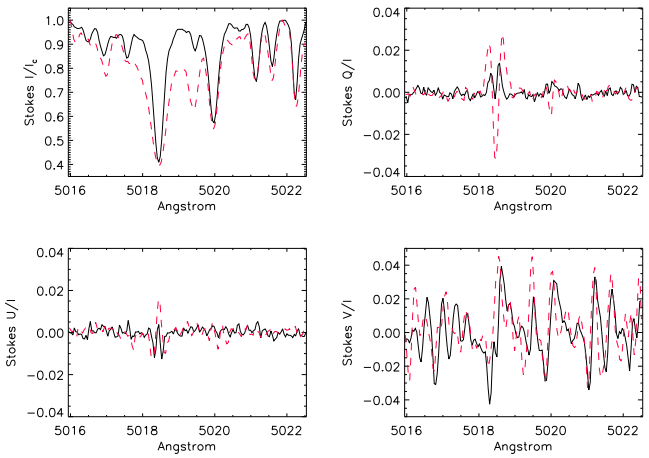

F . 10.— Stokes I, Q, U and V profiles for γEqu (solid line) and βCrB (dashed line).

6. SUMMARY

We have presented the new Catania Astrophysical Observatory Spectropolarimeter based on a fibre-fed white-pupil spectrograph able to perform full Stokes polarimetry. The $\tan\theta = 4.0$ échelle grating and a glass prism cross-disperser record in a single exposure wavelength from 375 to 1100 nm with a resolution up to R = 55 000. Small uncovered spectral regions are longword to 856 nm.

Linked at the 36 inch telescope with fibres whose FoV is 3 arcsec, CAOS is able to achieve, at R = 55 000, a S/N = 60 for a V=10 star in one hour. About 30% of the light has been estimated to be lost because of the telescope guiding system. A new telescope interface with a tip-tilting mirror for guiding is under development.

Thermalised with an r.m.s. smaller than 0.01 K, CAOS echellogram is stable to guarantee radial velocity measurements better than 100 m s^{-1} from a single spectral line of Vega acquired with S/N= 100.

With the exception of the achromatic retarders, CAOS polarimeter is a copy of the polarimetric unit of SARG, the former high resolution spectrograph of the Telescopio Nazionale Galileo. CAOS Stokes spectral line profiles are consistent within errors with the results of similar instruments, like ESPADONS and HARPS-South.

As it is expected for any high resolution spectrograph, CAOS cannot measure absolute fluxes and, as a consequence, unpolarised and polarised standard stars cannot be used to determine the instrumental polarisation. Measurements of unpolarised standard stars can present a signal up to 3%. After subtracting the spurious continuum polarisation, a method has been implemented to measure the cross-talk on the basis of spectral lines formed in presence of magnetic fields. Observations of the chemically peculiar stars βCrB and γEqu show that the cross-talk can be ascribed to the incorrect retardance of waveplates and that it is limited to few percent.

ACKNOWLEDGMENTS

We thank Dr. Andersen and Dr. Preben for their help with the CCD controller.

REFERENCES

Avila, G. 1998, ASPC 152, 329

Babcock, H.W. 1947, ApJ 105, 105

Bagnulo, S. et al. 2001, A&A 369, 881
Bagnulo, S., Fossati, L., Kochukhov, O., Landstreet J. D., 2013, A&A, 559, 103
Covino S., et al., 2014, AN, 335, 117
Clarke, D., Grainger, J.F. 1971, Polarized light and optical measurement, Pergamon Press
Clarke D., & Naghizadeh-Khouei J., 2000, P&SS, 48, 285
Dekker, H., D'Odorico, S., Kaufer, A., Delabre, B., Kotzlowski, H. 2000, SPIE 534, 4008
D'Odorico, S., & Tanné, J.F. 1984, *Messenger* 37, 24
Donati J.-F., Catala C., Wade G. A., Gallou G., Delaigue G., Rabou P., 1999, A&AS, 134, 149
Drummond, J.D. 2014, AJ 65, 147
Giro, E., Bonoli, C., Leone, F., Molinari, E., Pernechele, C., Zacchei, A. 2003, SPIE 4843, 456
Goodrich, R.W.; Cohen, M.H.; Putney, A. 1995, PASP, 107, 179
Griffin, R. F. 1968. A photometric atlas of the spectrum of Arcturus, lambda lambda 3600 - 8825 Å.. Publications of the Astronomical Society of Australia.
Harrington D. M., Kuhn J. R., Hall S., 2011, PASP, 123, 799
Hough, J., Bailey, J. 1994, in Spectropolarimetry at the AAT (The AAT User's manual 24.2)
Kuhn, J.R., Balasubramaniam, K.S., Kopp, G., Penn M.J. 1994, SoPh 153, 143
Kurucz R.L. 1993, A new opacity-sampling model atmosphere program for arbitrary abundances. In: M.M. Dworetsky, F. Castelli, R. Faraggiana (eds.) IAU Col. 138, Peculiar versus normal phenomena in A-type and related stars. A.S.P Conferences Series Vol. 44, p.87
Kurucz R.L., & Avrett E.H., 1981, SAO Special Rep. 391
Landi Degl'Innocenti, E. & Landolfi, M. 2004 Astrophysics and Space Science Library, 307
Leone, F. 2007, MNRAS 382, 1690
Leone, F., Bruno, P., Calì, A., et al. 2003, SPIE 4843, 465
Leone, F., Catalano, S. & Catanzaro, G. 2000, A&A 355, 315
Leone, F. & Catanzaro, G. 2001, A&A 365, 118
Leone, F. & Catanzaro, G. 2004, A&A 425, 271
Leone, F., Manso & Privitera, G. 2011, ApJ
Leone, F., Cecconi, M., Cosentino, R. Ghedina, A., et al. 2014, SPIE, 2, 9147
Leroy, J.L., Bagnulo, S., Landolfi, M., Landi Degl'Innocenti E. 1994, A&A 284, 174
Serkowski, K. 1974, Polarization techniques.. Astrophysics. Part A: Optical and infrared
Sterzik, M.F., Bagnulo, S., Palle, E. 2012, Nature 483, 64
Solanki, S.K. & Stenflo, J.O. 1986, A&A 170, 120
Spanò, P., Leone, F., Bruno, P., Catalano, S., Martinetti, E., Scuderi, S. 2006, MSAIS, 9, 481
Stift, M.J. & Leone, F. 2000, A&A 398, 411
Stift, M.J., Leone, F. & Cowley, C.R. 2012, MNRAS 419, 2912
Strassmeier, K. et al. 2015, AN 336, 324
Tinbergen, J. & Rutten, R. 1992, A User's Guide to WHT Spectropolarimetry (ING; La Palma User Manual No. 21)
Tody, D. 1986, The IRAF Data Reduction and Analysis System, in Proc. SPIE, Instrumentation in Astronomy VI, ed. D.L. Crawford, 627, 733
Trujillo-Bueno J., Moreno-Insertis F., & Sanchez Martinez F., 2002, assp.book,
Valenti, J.A., & Fischer, D.A. 2005, ApJ 159, 141
Wade, G.A, Donati, J.-F., Landstreet, J.D. & Shorlin S.L.S. 2000, MNRAS 313, 823
Wolff,S.C. 1983, The A-type stars, NASA SP-463, 33

Astron. Nachr. / AN **335**, No. 2, 117 – 123 (2014) / **DOI** 10.1002/asna.201311954

PAOLO: A Polarimeter Add-On for the LRS Optics at a Nasmyth focus of the TNG⋆

S. Covino[1,⋆⋆], **E. Molinari**[2,3], **P. Bruno**[4], **M. Cecconi**[2], **P. Conconi**[1], **P. D'Avanzo**[1], **L. di Fabrizio**[2], **D. Fugazza**[1], **M. Giarrusso**[5,4], **E. Giro**[6], **F. Leone**[5,4], **V. Lorenzi**[2], and **S. Scuderi**[4]

[1] INAF / Brera Astronomical Observatory, Via Bianchi 46, 23807, Merate (LC), Italy
[2] INAF / Fund. Galileo Galilei, Rambla José Ana Fernández Perez 7, 38712 Breña Baja (La Palma), Canary Islands, Spain
[3] INAF / IASF-MI, Via E. Bassini 15, 20133, Milano, Italy
[4] INAF / Osservatorio Astrofisico di Catania, Via S. Sofia 78, 95123, Catania, Italy
[5] Università di Catania, Dipartimento di Fisica e Astronomia, Sezione Astrofisica, Via S. Sofia 78, 95123, Catania, Italy
[6] INAF / Padova Astronomical Observatory, Vicolo dell'Osservatorio 5, 35122, Padova, Italy

Received 2013 May 2, accepted 2013 Aug 30
Published online 2014 Feb 3

Key words instrumentation: polarimeters – methods: data analysis – techniques: polarimetric

We describe a new polarimetric facility available at the Istituto Nazionale di AstroFisica / Telescopio Nazionale Galileo at La Palma, Canary islands. This facility, PAOLO (Polarimetric Add-On for the LRS Optics), is located at a Nasmyth focus of an alt-az telescope and requires a specific modeling in order to remove the time- and pointing position-dependent instrumental polarization. We also describe the opto-mechanical structure of the instrument and its calibration and present early examples of applications.

© 2014 WILEY-VCH Verlag GmbH & Co. KGaA, Weinheim

1 Introduction

Polarimetry is a powerful diagnostic tool for studying astrophysical sources. Radiation mechanisms that produce similar radiation output can be disentangled by means of their polarization signatures. Also, polarization provides unique insights into the geometry of unresolved sources, hidden in the integrated light, even at cosmological distances.

Polarization and wavelength are the bits of information attached to every photon that reveal the most about its creation and subsequent history. In an observational science such as astronomy, polarimetry is especially important because it goes directly to the heart of the problem, i.e. the underlying physical process. The elementary processes include, among others:

- scattering (e.g. by dust particles in the interstellar medium);
- absorption by aligned, intrinsically asymmetric particles (e.g. in molecular clouds);
- scattering by asymmetrically distributed particles (e.g. in disks);
- coherent scattering in spectral lines (e.g. in magnetospheres);
- emission or scattering by asymmetric sources (e.g. supernova explosions);
- cosmic magnetic and electric fields through observation of Zeeman-, Stark-, and Paschen-Pack effects (e.g. on stellar surfaces);
- cyclotron or synchrotron radiation, inverse-Compton process and relativistic jets (e.g. active galactic Nuclei, AGNs; gamma-ray bursts, GRBs; etc.);
- reflection (e.g. by extra-solar planets);
- quantum gravity modification of standard dispersion relation (e.g. for cosmological sources).

The increasing importance of polarimetry in many astrophysical contexts is witnessed by the proportional increase in recent years of the number of scientific publications based on optical/NIR polarimetric observations at the European Southern Observatory (ESO)[1] (Schmid 2008).

With these considerations in mind, we designed, built, commissioned and calibrated a polarimetric add-on for the DOLORES[2] (Device Optimized for the LOw RESolution) instrument, LRS in short) at the INAF/Telescopio Nazionale Galileo (TNG)[3]. The main scientific goal of our project is to deliver a flexible all-purpose polarimetric facility hosted by a well calibrated and reliable instrument with a particular attention to provide polarization measurements of rapidly variable sources as GRB afterglows, blazars, and in general any high-energy transients.

⋆ Based on observations made with the Italian Telescopio Nazionale Galileo (TNG) operated on the island of La Palma by the Fundacin Galileo Galilei of the INAF (Istituto Nazionale di Astrofisica) at the Spanish Observatorio del Roque de los Muchachos of the Instituto de Astrofisica de Canarias.

⋆⋆ Corresponding author: stefano.covino@brera.inaf.it

[1] http://www.eso.org
[2] http://www.tng.iac.es/instruments/lrs/
[3] http://www.tng.iac.es

© 2014 WILEY-VCH Verlag GmbH & Co. KGaA, Weinheim

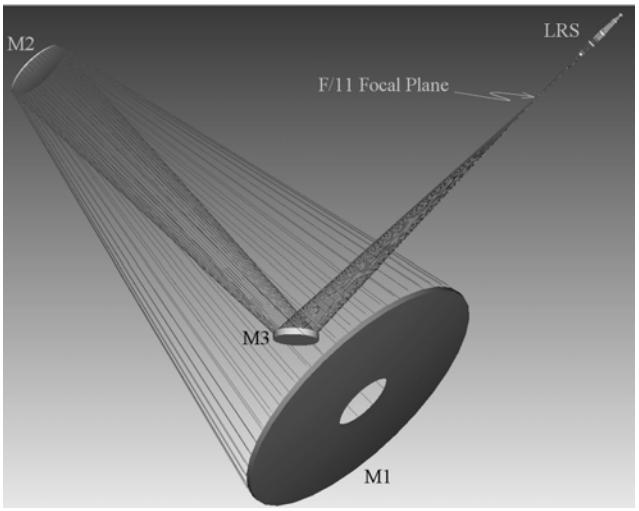

Fig. 1 Primary (M1) and secondary (M2) mirrors of the TNG. The M3 flat mirror can rotate by 180° to direct light to scientific instruments sited in Nasmyth A or Nasmyth B room.

In this paper we describe the technical design of the instrument in Sect. 2 and the polarimetric model adopted for PAOLO calibration in Sect. 3. Examples of typical PAOLO observing runs are briefly proposed in Sect. 4.

2 Opto-mechanical design

PAOLO is integrated in the LRS instrument, which is mounted on the Nasmyth B interface of the TNG. Primary (M1) and secondary (M2) mirrors of the TNG form an optical system with a 3580 mm aperture and a 38 500 mm equivalent focal length with a corrected $15\,\mathrm{arcmin}^2$ field of view (FoV). The corresponding F/11 focal plane (FP) matches the LRS one (see Fig. 1).

A set of six custom lenses set collimates the beam coming from the F/11 FP (see Fig. 2). A Gravitational Eccentric Correction Optics (GECO; Conconi et al. 2002) then reduces the beam tilting caused by mechanical flexures during FoV derotation by the mechanical derotator. The collimated beam can then either a) pass through a filter mounted on a filter wheel or b) pass through a grism/volume holographic grating mounted on a grism wheel. A set of seven custom lenses set following the grism wheel forms the LRS camera which focuses the FoV or the spectra onto the 2048×2048 E2V4240 thinned back-illuminated, deep-depleted, Astro-BB coated CCD with a pixel size of 13.5 μm (0.″252/pixel plate scale).

To optimize the trade-off between scientific goals and technical feasibility, we decided to mount the polarizer (a Double Wollaston, DW) on the filter wheel and the filters (for photo-polarimetry) and the grism/volume holographic gratings on the grism wheel. A rotating $\lambda/2$ or, alternatively, $\lambda/4$ wave plate can be set before the F/11 FP in the optical path to allow circular polarimetry measurement.

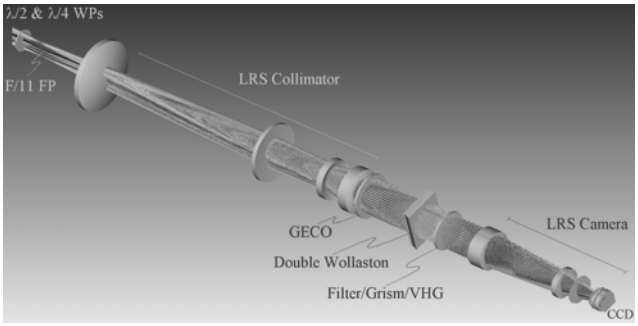

Fig. 2 PAOLO integrated in LRS setup at TNG.

The DW opto-mechanical design was optimized based on an earlier study for its application on LRS (Oliva 1997). The goal was to simultaneously obtain four polarization states of the FoV/spectra. A simple Wollaston polarizer outputs two polarization states so two Wollaston were used. A special wedge was glued in front of them to tilt and separate the corresponding images onto the CCD (see Fig. 3). A $80\times6\,\mathrm{mm}^2$ field stop was set on the F/11 FP in photo-polarimetric mode to obtain four $430''\times33''$ separated FoV strips on the detector. A $0.''7\times33''$ slit was set in the same focal plane to work in spectro-polarimetric mode.

The adopted configuration allows us to measure the polarization status of any, even rapidly varying, source in "one-shot" at the expense of some unavoidable aberration in the PSF shape. We can easily compensate for this aberration for the analysis of point-like object. But the aberration makes the instrument less suitable for extended source polarimetric studies. DW polarimeters also make it easier to correct the time-dependent instrumental polarization that is an intrinsic feature of Nasmyth focus polarimeters, as discussed later in Sect. 3.

The 73 mm collimated beam exiting from GECO enters the DW. In principle, two $73\times35\,\mathrm{mm}^2$ Wollaston glued to each other should have been the best solution but it was difficult and expensive to find polarizing crystals of these sizes. Therefore the final choice was to glue two $45\times45\,\mathrm{mm}^2$ identical Wollastons to form the 0-90 block and other two Wollastons to form the 45-135 one (see Fig. 4).

An hexagonal shape has been obtained to mount the DW in the mechanical interface to the LRS filter wheel (see Fig. 5).

A test campaign has been made in optical laboratory. The A1/A2 and B1/B2 crystals have been separately analyzed with a collimated entering beam. The corresponding exiting collimated beam pairs have been focused and analyzed to single out aberration effects. On-sky images show a 0.″2 (1 pixel) difference in their FWHMs. Throughput tests showed a 95 % transmittance by the DW except in few small bubbled areas where it decreases by less than a 2 %.

A setup with a polaroid and a rotating $\lambda/2$ wave plate in front of the DW has allowed us to measure the orientation between the polarization states of its crystal blocks. The beam exiting from $\lambda/2$ wave plate has been collimated

© 2014 WILEY-VCH Verlag GmbH & Co. KGaA, Weinheim

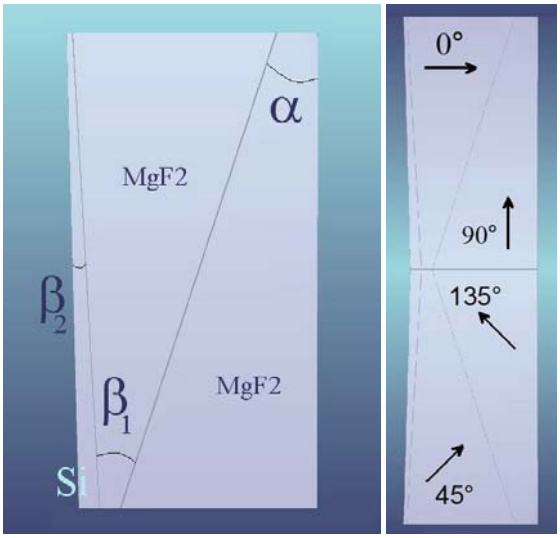

Fig. 3 One of the two Wollaston (left side) forming the Double Wollaston polarizer (right side) glued along the center line. The front Si wedge with a β_1 angle allows for tilting the collimated beam to separate the FoV images corresponding to the two polarization state pairs (a pair for each Wollaston). $\alpha = 18\overset{\circ}{.}00$, $\beta_1 = 3\overset{\circ}{.}41$, and $\beta_2 = 1\overset{\circ}{.}80$.

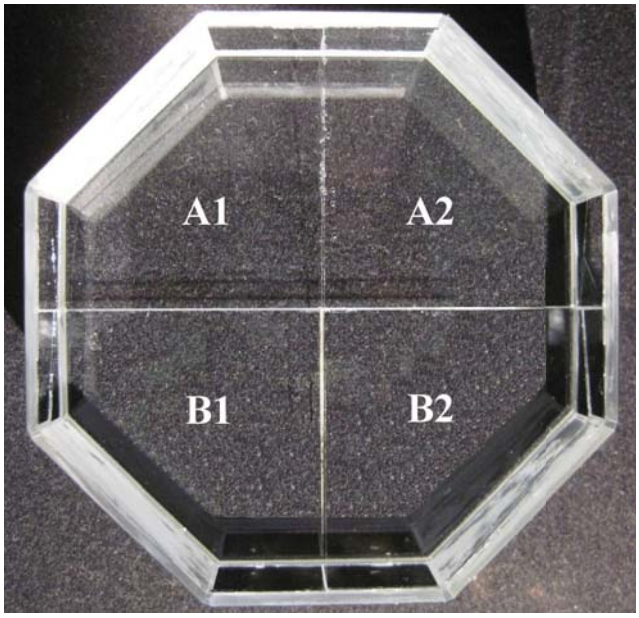

Fig. 4 The final DW of PAOLO. A1/A2 and B1/B2 crystals pairs, glued to each other, form the two Wollaston with 0-90 and 45-135 polarization states, respectively. The tilting wedges were then glued in front of them to separate the corresponding spot pairs. Then the two blocks are then glued to form the final DW.

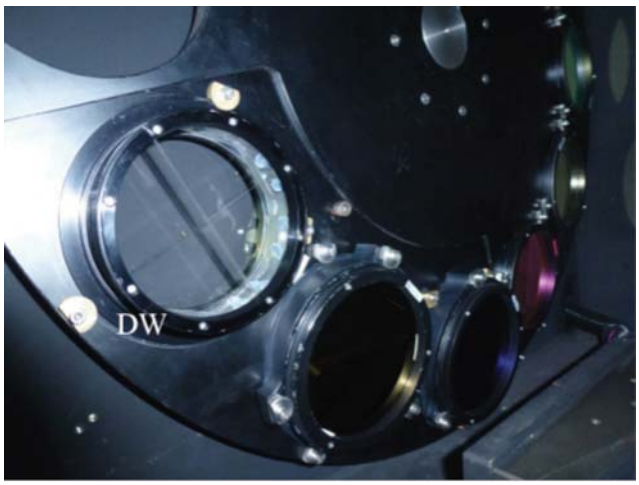

Fig. 5 The DW mounted on the LRS filter wheel at TNG.

by means of a simple optical setup that outputs a ~ 40 mm collimated beam centered on the DW (the intersection point of all the glued faces). The four polarized beams coming out the DW have been focused on the CCD by means of another optical setup. The four spot intensities have been measured for each rotation step of $\lambda/2$ wave plate. There is a $89\overset{\circ}{.}89$ angle between 0-90 beams. A $90\overset{\circ}{.}29$ one between 45-135 beams and $45\overset{\circ}{.}13$ angle between the two couples.

3 PAOLO polarimetric model

From the opto-mechanical point of view, PAOLO is a relatively standard instrument. However, it has been designed to work at one of the Nasmyth foci of the TNG. Polarimeters at a Nasmyth focus are rather uncommon since they require a careful modeling of the optical path in order to remove the important, often dominant, instrumental polarization.

On the other hand, considerable experience in the management of polarimeters located at Nasmyth foci has been gained in recent years, as demonstrated by the publications devoted to the subject: e.g. Giro et al. (2008), Joos et al. (2008), Selbing (2010), Tinberger (2007), and Witzel et al. (2011).

We do not discuss here in detail the various pros- and cons- of placing instruments at a Nasmyth rather than at a Cassegrain focus. Clearly, factors related to mass distribution, control of flexures, etc. play a fundamental role. Polarimetric instruments are indeed typically placed on a Cassegrain focus to avoid the modification of the incoming light beam polarization state by folding mirrors. In addition, for an alt-az telescope such as the TNG, the orientation of folding mirrors with respect to the sky reference changes with time due to field rotation and the reference system of the telescope is of course in turn rotated compared to the sky reference by a time dependent quantity, i.e. the parallactic angle (see, e.g., Fig. 2 in Giro et al. 2008).

The goal of a polarimetric model is to compensate for the instrumental effect enabling one to know the incoming polarization state from the measured polarization on the detector. Both rotations and folding mirrors effects can be modeled building an appropriate set of Mueller matrices. We remind the readers to the quoted references for details about the mathematical treatment. In principle all the parameters (rotation angles, complex refraction index of the metallic mirror surface, etc.) involved in the model can be

© 2014 WILEY-VCH Verlag GmbH & Co. KGaA, Weinheim

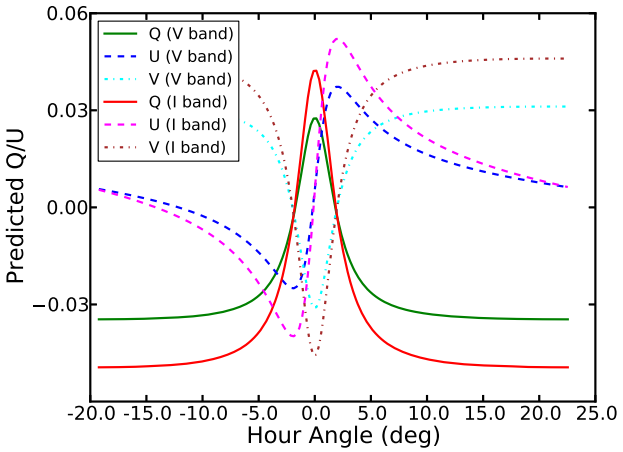

Fig. 6 Simulation of the instrumental polarization in two filters, V and I, introduced by the TNG folding mirror for the observation of a non-polarized standard star BD +30°3639 on 2012 October 5. For circular polarization a $\lambda/4$ wave plate at 45° was assumed.

accurately measured. However, as it is well known (e.g. Giro et al. 2008), metallic mirrors tend to accumulate dust and other polluting factors with time that can modify their reflective performances and induced polarization. The best solution is to leave the complex refraction index be a free parameter of the model and to observe of a suitable number of standard stars well distributed during an observing night. A best-fit solution can then be readily obtained.

The availability of a polarimetric model allows any observer to study in advance the expected instrumental polarization induced by the whole system. We show in Fig. 6 a simulation of the instrumental polarization introduced by the TNG M3 folding mirror for the observation of a non-polarized standard star.

Typical values for the instrumental polarization for an unpolarized source observed at three different hour angles are also presented in Table 1. The computed circular polarization is obtained assuming to observe a source with 1% linear polarization and 0° position angle, and is totally due to the cross-talk of the 45° reflection on the M3 metallic mirror surface.

Once the main parameters of a polarimetric model are determined, for a typical observational run it is sufficient to secure the observation of a small number of polarimetric standard stars in order to update the best-fit values. Our experience at the TNG shows that for a quick-look analysis, models a few weeks old are still perfectly adequate. A set of software tools to manage PAOLO observations, derive a polarimetric model, compensate for instrumental polarization and performing simulations is freely available.[4] This package, developed for internal use, is offered without any warranty, although we will gladly provide help to any user who requests it. Some more information about how this package works is given in Appendix A.

[4] https://pypi.python.org/pypi/SRPAstro.TNG/

Table 1 Typical instrumental polarization for an unpolarized source observed at the hour angles: $\sim 0, 15$, and $45°$ in the optical band. The circular polarization is computed for a source with 1 % and 0° position angle and no intrinsic circular polarization. The resulting instrumental circular polarization is due to the cross-talks induced by the 45° reflection on the M3 metallic mirror.

	U	B	V	R	I
Hour angle $\sim 0°$					
Polarization (%)	2.57	2.65	2.92	3.24	4.49
Position angle (°)	6.4	6.2	5.6	4.9	3.4
Stokes V (%)	0.00	0.00	0.00	0.00	0.00
Hour angle $\sim 15°$					
Polarization (%)	3.35	3.44	3.71	4.04	5.31
Position angle (°)	80.6	80.7	81.0	81.4	82.3
Stokes V (%)	0.04	0.03	0.03	0.02	0.02
Hour angle $\sim 45°$					
Polarization (%)	3.09	3.17	3.44	3.77	5.03
Position angle (°)	–88.1	–88.0	–87.5	–87.0	–85.7
Stokes V (%)	–0.09	–0.08	–0.07	–0.06	–0.05

4 Examples of PAOLO observations

The field of view of the PAOLO polarimeter, in imaging mode, is shown in Fig. 7. To perform imaging polarimetry, one must analyse photometrically the sources of interest in the field of view and then properly match these sources in the four slices to derive instrumental polarization as described, e.g., in Witzel et al. (2011). In case of spectro-polarimetry each spectrum has to be analyzed and wavelength calibrated separately. After that, the procedure is the same, and even for spectro-polarimetry a polarimetric model based on standard star observations has to be derived.

It is possible to roughly estimate PAOLO performances basing on the available DOLORES calibration information[5], simply considering that the collected light is split in four quadrants and taking into due account the expected degree of polarization. However, given the main scientific goal of the project, most of the tests performed so far have been devoted to observations of rapidly variable objects in linear polarimetry rather than sources down to the polarimetric detection limits. Circular polarimetry calibration will be carried out in the near future although in principle the polarization model should work without modifications.

Simultaneously with scientific target observations a few polarized and/or non-polarized standard star observations must be performed. During the commissioning phase we extensively tested the behavior of the instrument for linear polarimetry and some results are shown in Fig. 8.

The standard stars observed during these tests are listed in Table 2. Exposure times were typically 1–10 s, depending on the object magnitude and reduction, was carried out following standard recipes. Photometric analysis was performed with the DAOPHOT code (Stetson 1987) and 1σ er-

[5] http://www.tng.iac.es/instruments/lrs/

© 2014 WILEY-VCH Verlag GmbH & Co. KGaA, Weinheim

Star	Magnitude (V band)	Polarization (%, V band)	Position Angle (°)	Reference
BD +28°4211	10.5	0.05 ± 0.03	54.2	Schmidt et al. 1992
HD 204827	7.9	5.39 ± 0.04	60.0	Schulz & Lenzen 1983
GD 319	12.3	0.09 ± 0.09	140.2	Schmidt et al. 1992

Table 2 Parameters for the standard star observation discussed in this paper.

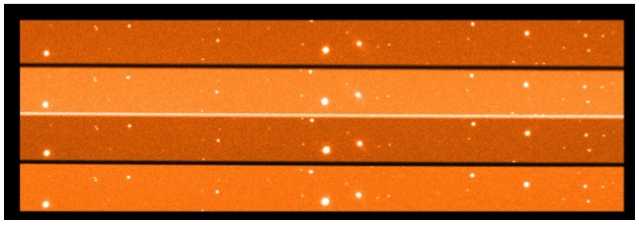

Fig. 7 The PAOLO field of view, in imagine mode, is formed by four slices providing four position angles for linear or circular polarization measurements. The availability of all the information to properly determine Stokes parameters in one shot is an important feature for instruments affected by rapidly varying instrumental polarization.

rors were derived taking into account photon statistics and background determination.

The errors associated with the catalogue standard star polarizations are of the order of a few times 0.01 %, while the photometric errors for the bright (with a 3.6 m telescope) observed objects for differential measurements are low enough to give Stokes parameters measurements with comparable uncertainties. The scatter around the best-fit curves reported in Fig. 8 is typically an order of magnitude larger and therefore, from the rms error evaluated comparing the observations to model predictions, we can infer that the removal of instrumental polarization can be performed at the 0.2% level, although relative measurements can be more accurate (see also Wiltzer et al. 2011). The model best fit components of the complex refractive index of the M3 mirror were typically about 90 % the values tabulated for pure Aluminium.[6]

An example of a real scientific observation, although performed as a system test, is shown in Fig. 9. On 2012 September 1 we carried out a continuous linear polarimetric and photometric monitoring of BL Lac. BL Lac is one of the most intensively studied AGNs even in polarimetry, and long time-series covering a few decades are available (e.g. Hagen-Thorn et al. 2002). We tried to study its linear polarization characteristics on short time-scales, typical integration times were of 20 s. The polarization degree during the slightly less than eight hour monitoring decreased from about 11 % to 6 %, while the position angle on the contrary increased from about 15° to less than 30°. Some relevant short-term activity is indeed present in the data (see an analogous study in Andruchow, Romero & Cellone 2005 for other AGNs) and a detailed scientific analysis will be presented elsewhere.

[6] http://www.filmetrics.com/refractive-index-database/Al/Aluminium

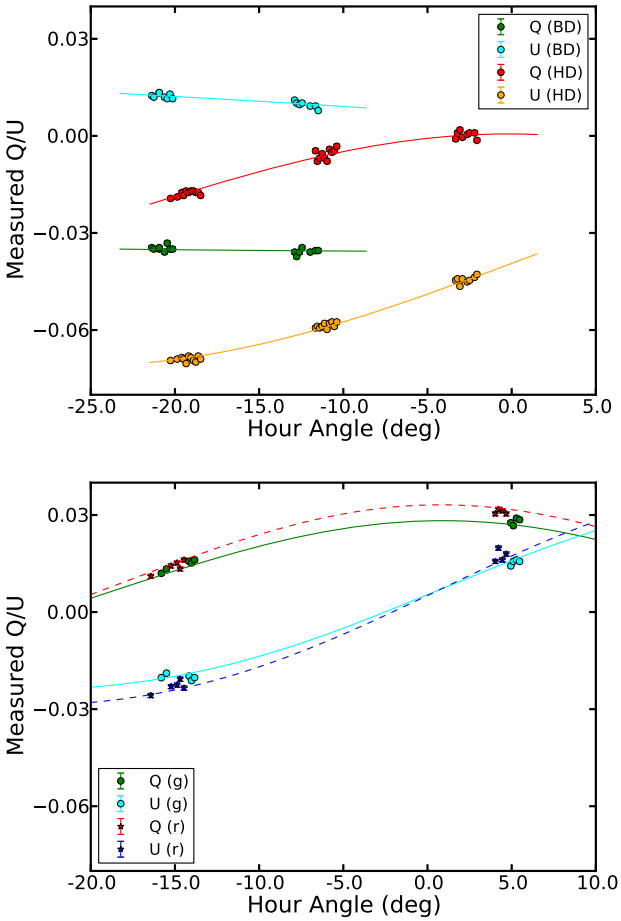

Fig. 8 Polarimetric standard star observations (BD +28°4211 and HD 204827) carried out on 2012 October 5 (*upper panel*) and (GD 319) on 2013 January 27 and 28 (*lower panel*). We show our best-fit model superposed on the measured instrumental polarizations. The wavelength dependance of the instrumental polarization in this limited range is also well reproduced by the model.

5 Conclusions

In this paper we have presented a new polarimetric facility, PAOLO, available at the INAF/TNG. TNG is an alt-az telescope and PAOLO is located at one of its Nasmyth foci. This positioning introduces time- and pointing position-dependent polarization. We described the methodology followed to model the instrumental polarization and remove it from scientific data. A set of software tools to analyze PAOLO polarimetric data have also been developed.

A few examples of possible applications have also briefly described. PAOLO is now offered to the general community as part of the instrument set of the INAF/TNG.

© 2014 WILEY-VCH Verlag GmbH & Co. KGaA, Weinheim

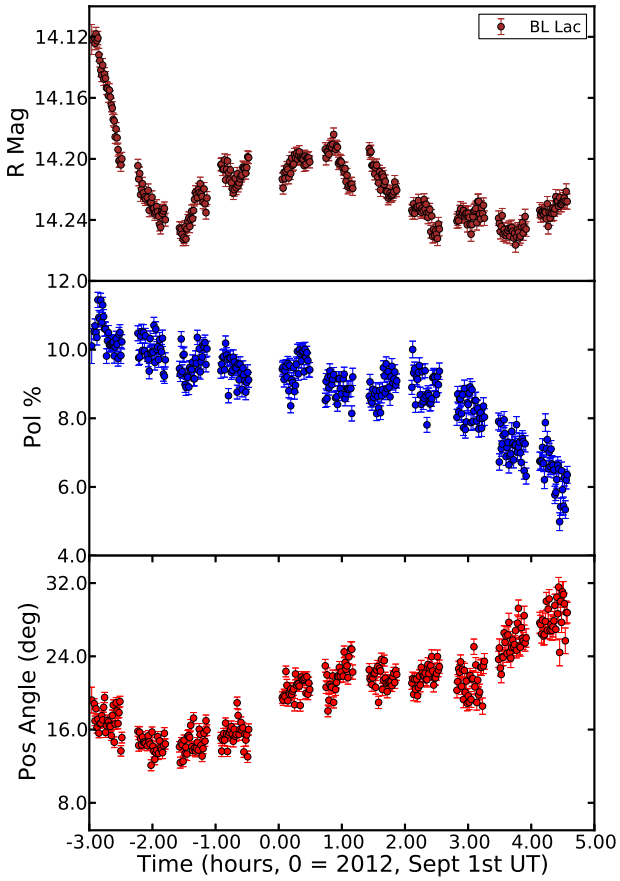

Fig. 9 Linear polarimetric and photometric monitoring of BL Lac carried out on 2012 September 1.

Acknowledgements. This work was made possible by a grant from the INAF TecnoPRIN 2009. We thank G. Pareschi for his continuous encouragement and for having created the acronym of the project. We also thanks L. Foschini and A. Treves for useful discussions and J. Schwarz for editorial assistance. We thank the anonymous referee as well for her/his very useful comments.

References

Andruchow, M., Romero, G.E., & Cellone, S.A. 2005, A&A, 442, 97
Conconi, P., Molinari, E., & Crimi, G. 2002, Applied Optics, 41, 193
Giro, E., Claudi, R.U., Antichi, J., et al. 2008, Proc. SPIE, 7014, 117
Hagen-Thorn, V.A., Larionova, E.G., Jorstad, S.G., Björnsson, C.-I., & Larionov, V.M. 2002, A&A, 385, 55
Joos, F., Buenzli, E., Schmid, H.M., & Thalmann, C. 2008, Proc. SPIE, 7016, 48
Oliva, T. 1997, A&AS, 123, 589
Schmid, H.M. 2008, Polarimetry with ESO Instruments, in The 2007 ESO Instrument Calibration, ed. A. Kaufer & F. Kerber (Springer, Berlin/Heidelberg), 499
Schmidt, G.D., Elston, R., & Lupie, O.L. 1992, AJ, 104, 1563
Schulz, A., & Lenzen, R. 1983, A&A, 121, 158
Selbing, J. 2010, astro-ph/1010.4142
Smith, R.J., Lucey, J.R., Hudson, M.J., & Steel, J. 1997, MNRAS, 291, 461
Stetson, P.B. 1987, PASP, 99, 191
Tinbergen, J. 2007, PASP, 119, 1371
Witzel, G., Eckart, A., Buchholz, R.M., et al. 2011, A&A, 525, A130

A The PAOLO software tools

In order to aid the calibration and commissioning activities for PAOLO we have developed a set of command-line tools for managing the main phases of a typical polarimetric analysis session. These tools are thought to match the PAOLO instrumental features, nevertheless some of them may be of general use or interest. The package is entirely written in the PYTHON language[7] and is based on the standard numerical and scientific libraries NUMPY[8] and SCIPY[9]. Here we briefly describe how the package works. An user's manual, mainly devoted to installation and with some recipe for analysis is also available.[10]

1. PAOLO can work both in imaging and spectro-polarimetric modes. Photometry can be derived by means of any suitable tool, and it is only required that as output a file with as many entries as the number of objects analyzed be produced. Each entry must contain at least an Id, pixel position on the detector and instrumental magnitudes. The `SRPTNGPAOLOSourceMatch` command takes care of matching the different sources in the four quadrants constituting the PAOLO field of view in imaging (see Fig. 7). In case of spectroscopy, again spectral extraction and wavelength calibration can be carried out with any suitable tool. The `SRPTNGPAOLOSpectrumMatch` imports the extracted spectra and rebins them if required in order to have the same number of pixels. Both commands also compute the total magnitude for each detected source and the sum of fluxes for spectroscopy. A FITS[11] table managed with the ATPY tool[12] containing all the imported data is generated as output.
2. Once data are properly imported instrumental polarization Stokes parameters are computed with the command `SRPTNGPAOLOInstrStokes` following standard recipes (e.g. Giro et al. 2008). Errors are correctly propagated. In case one is managing observations of polarimetric standard stars catalogued polarization Stokes parameters can be provided. In addition parameters from the original observation frames such as pointing direction, epoch, exposure times, etc. are obtained.
3. The most important step is the derivation of the best-fit parameters for the instrument polarimetric model (see Sect. 3). The command `SRPTNGPAOLOParamFit` will perform this fit using one or more parameters as chosen by the user. At present the available parameters are the offset in the detector position angle, real and complex refraction indices of the metallic mirror surface, and Stokes parameter instrumental polarization. The best-fit is computed by χ^2 minimization by using the downhill (Nelder-Mead) simplex algorithm as coded

[7] http://www.python.org
[8] http://www.numpy.org
[9] http://www.scipy.org
[10] http://pythonhosted.org/SRPAstro.TNG/
[11] http://fits.gsfc.nasa.gov
[12] http://atpy.readthedocs.org/en/latest/

© 2014 WILEY-VCH Verlag GmbH & Co. KGaA, Weinheim

in the SCIPY library, v. 0.12.0. This is not the most efficient algorithm, yet it is simple and easy to manage.

4. Once best-fit parameters for the polarimetric model are obtained, one can remove the time-dependent instrumental polarization with the command `SRPTNGPAOLOCalStokes`. It generates a new table with instrumental and corrected Stokes parameters, together with information about the pointing direction, epoch, etc. for each epoch.
5. There is also the possibility to generate simulated sets of instrumental polarization in order to compare with standard star observations, plan future observations, etc. The command is `SRPTNGPAOLOStokesSim`.

The package is part or a larger set of tools we developed for generic astronomical data analysis[13]. Again these tools are freely available, although they have been developed without following a specific strategy, i.e. to solve detailed and often unrelated problems in dealing with astronomical datasets.

[13] https://pypi.python.org/pypi/SRPAstro

© 2014 WILEY-VCH Verlag GmbH & Co. KGaA, Weinheim

APPENDIX C

Data reduction

Spectroscopic data have been reduced by means of the *Image Reduction and Analysis Facility* (IRAF) code. That is "a general purpose software system for the reduction and analysis of astronomical data" written by IRAF group at the National Optical Astronomy Observatories (NOAO). A standard procedure has been applied to the data reduction of all Echelle spectra, despite these were acquired with HARPS, FEROS, UVES, ISIS, HARPS-North or CAOS. In the following the HARPS-North case is presented.

– Debiasing:
  To define the zero level of any CCD pixel, a series (> 5 of BIAS exposures is obtained with the shutter closed and a null exposure time. The BIAS shows the electronic noise of the camera and possible systematics. It can look like the one in Fig. C.1. This pattern is also in SCIENCE actual imaging data. BIASes are combined into a MASTER BIAS, using outlier rejection. Anomalous values, usually are due

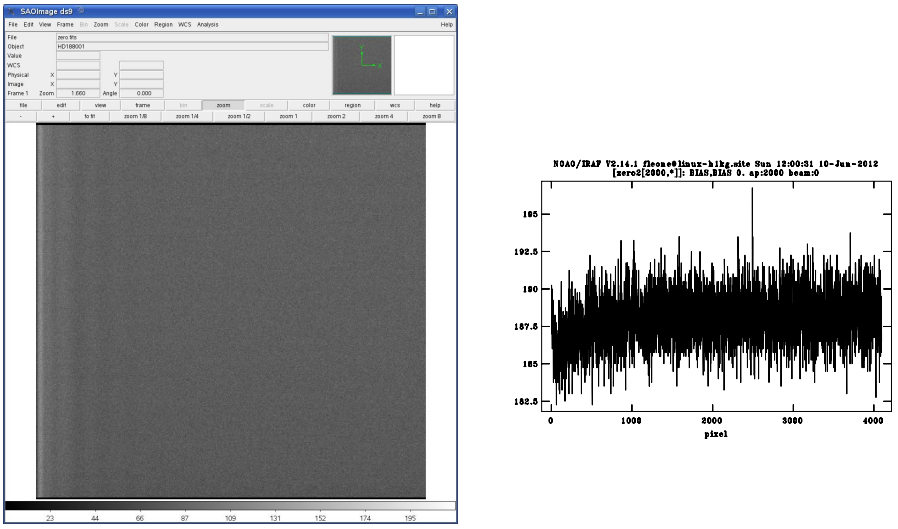

Figure C.1: Left: typical master BIAS frame, as dispaly on DS9. Right: plot of the central column with a r.m.s. equal to 1.588 ADU.

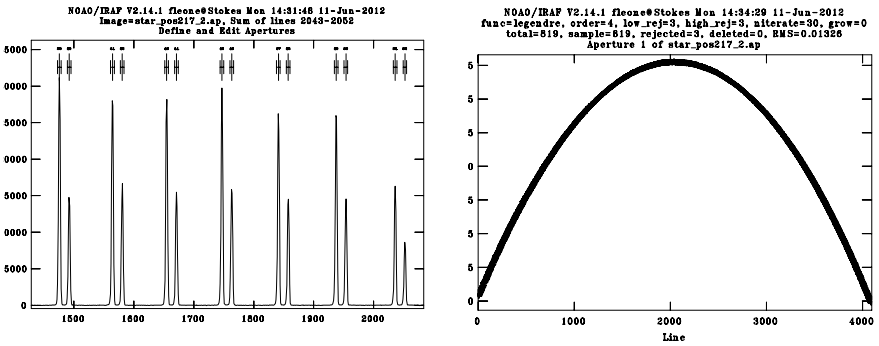

Figure C.2: Aperture identification.

to cosmic rays. The master BIAS is then subtructed from any SCIENCE frame.

– Aperture identification:
To identify orders, columns of the echellogram have been extracted to define the position of maxima as it is shown in Fig.C.2. Orders are than traced following the maxima along

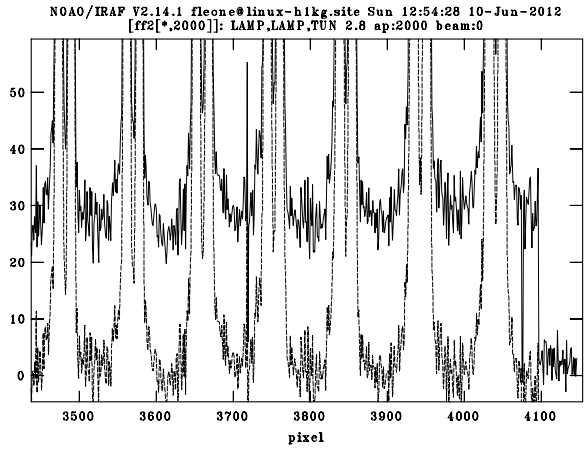

Figure C.3: Section of a frame before and after scattered light removal.

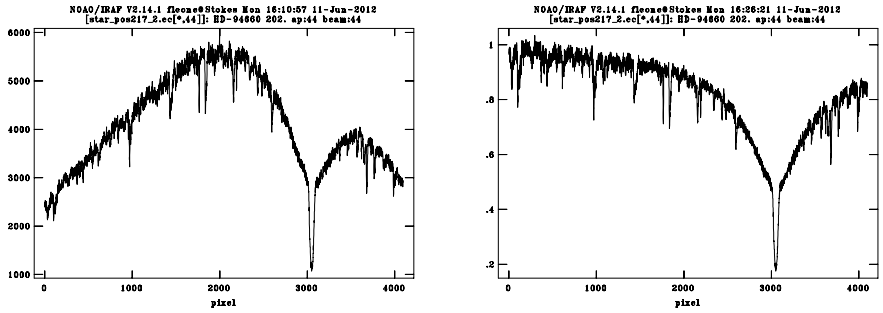

Figure C.4: Top panel: Extracted order of HARPS echellogram containing the Hα line. Bottom panel: Flux distribution after flat-fielding.

the CCD (Fig.C.2).

– Scattered light subtruction:
Some of the light entering the spectrograph appears on the detector well away from the *proper* position expected for the wavelength. These scattered photons may have been deflected by imperfections present in the optical items or in the air dust. More important, gratings disperse light within

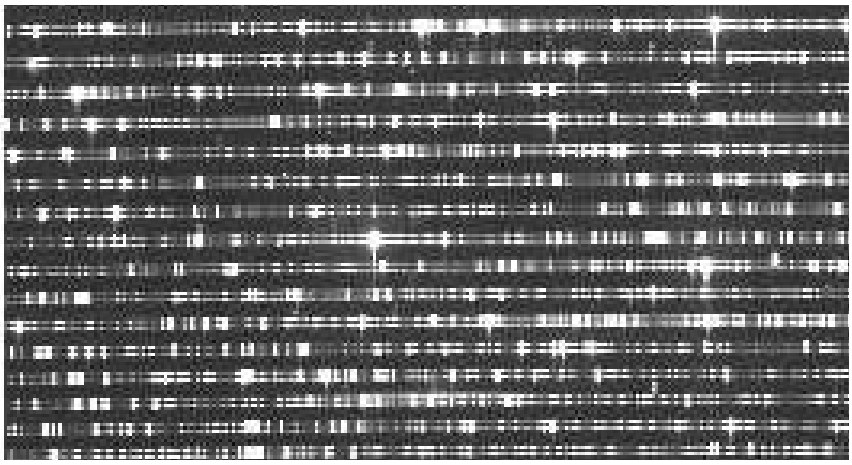

Figure C.5: Echellogram of the ThAr lamp.

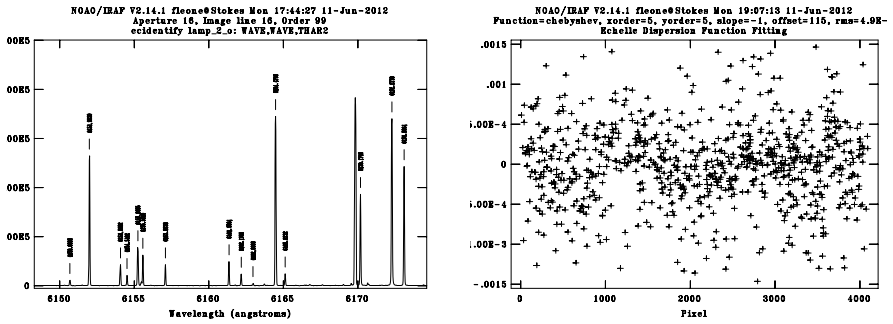

Figure C.6: Top panel: Example of identified ThAr lines. Bottom panel: Polynomial fitting of wavelength dispersion. Plase note the very high accuracy of the wavelength calibration stated by rms = $4.9\,10^{-4}$.

an angle that is much wider than any acceptance angle of other optical part and is scattered by mechanical mountings. As a result, up to 1% of light entering a spectrograph forms an almost smooth surface under the echellogram. As an example, Fig. C.3 shows the cut of the HARPS echellogram before and after the scatered light subtruction.

– Spectrum extraction:
Pixels transversally to any aperture have been added to ob-

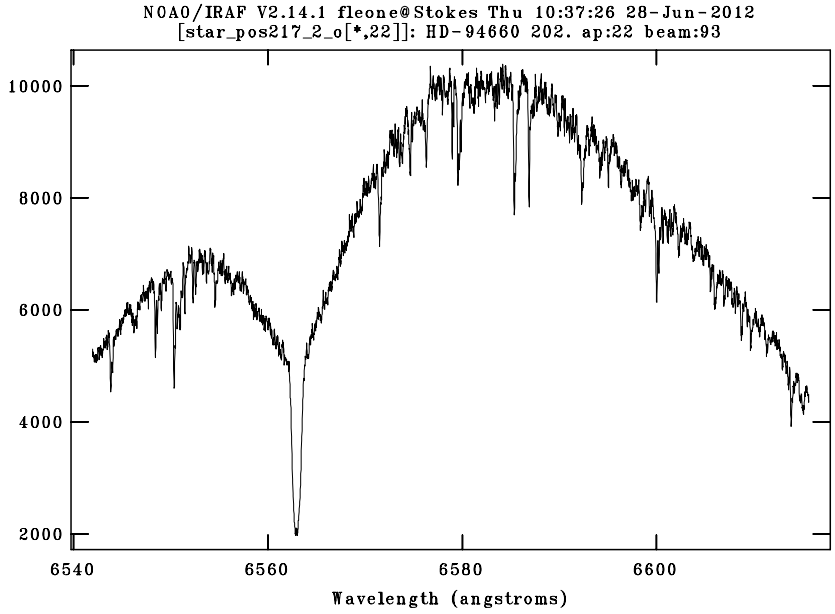

Figure C.7: The extracted order calibrated in wavelength that contains the Hα line.

tain the relative flux per wavelength. Fig.C.4 shows the HARPS order containg the Hα spectral line.

– Flat fielding:
The quanum efficiency of the CCD itself is also not necessarily the same for all pixels. A series of FLAT exposures of a light source with an almost constant flux with the wavelength are subtructed of the MASTER BIAS and than combined into a MASTER FLAT. SCIENCE frames are then corrected for the pixel-to-pixel efficiency by the division for the MASTER FLAT. Fig.C.4 shows also the flat-fielding effect on the Hα spectral line.

– Wavelength calibration:
Hollow Thorium Argon lamps are commonly used to define

the wavelength calibration in Echelle spectrographs.

– Radial velocity correction:
After the wavelength calibration, the observed radial velocity is corrected for the motion of the observer in the direction of the observation. The components of the observer's motion corrected are those due to the Earth's rotation (diurnal velocity), the motion of the Earth's center about the Earth-Moon barycenter (lunar velocity), the motion of the Earth-Moon barycenter about the center of the Sun (annual velocity), and the motion of the Sun (solar velocity) relative to some specified standard of rest. Spectral lines after that the heliocentric velocity correction not yet at the laboratory wavelengths because the intrinsic radial velocity of stars with respect to the Sun.

Bibliography

Abt H. A., Levy S. G., 1976, ApJS, 30, 273

Abt H. A., 1983, ARA&A, 21, 343

Alencar S. H. P., Melo C. H. F., Dullemond C. P., Andersen J., Batalha C., Vaz L. P. R., Mathieu R. D., 2003, A&A, 409, 1037

Andersen J., Lindgren H., Hazen M. L., Mayor M., 1989, A&A, 219, 142

Asplund M., Grevesse N., Sauval A. J., Scott P., 2009, ARA&A, 47, 481

Angulo C., et al., 1999, NuPhA, 656, 3

Babcock, H.W. 1949, ApJ, 110, 126

Bahcall, J.N. 1989 *Neutrino Astrophysics*, Cambridge: Cambridge University Press.

Bailey, J. I. III, White, R. J., Blake, C. H., Charbonneau, D., Barman, T. S., Tanner, A. M., Torres, G. 2012, ApJ, 749, 16

Baraffe I., Chabrier G., Allard F., Hauschildt P. H., 1998, A&A, 337, 403

Batten, A.H. 1973, *Binary and Multiple Systems of Stars*. London: Pergamon

Baur G., 1986, PhLB, 178, 135

Boden, A. F., Sargent, A. I., Akeson, R. L., Carpenter, J. M., Torres, G., Latham, D. W., Soderblom, D. R., Nelan, E., Franz, O. G., Wasserman, L. H. 2005, ApJ, 635, 442

Boden, A. F., Torres, G., Sargent, A. I., Akeson, R. L., Carpenter, J. M., Boboltz, D. A., Massi, M., Ghez, A. M., Latham, D. W., Johnston, K. J., Menten, K. M., Ros, E., ApJ, 670, 1214

Böhm-Vitense E., 1958, ZA, 46, 108

Brott I., Hauschildt P. H., 2005, ESASP, 576, 565

Cargile, P. A., Stassun, K. G., Mathieu, R. D. 2008, ApJ, 674, 329

Casagrande L., Flynn C., Portinari L., Girardi L., Jimenez R., 2007, MNRAS, 382, 1516

Castellani, V. 1985, Astrofisica stellare, Bologna: Zanichelli,

Castelli F., Kurucz R. L., 2003, IAUS, 210, 20P

Cesaroni R., Galli D., Lodato G., Walmsley C. M., Zhang Q., 2007, prpl.conf, 197

Catanzaro G., Leone F., Leto P., 2003, A&A, 407, 669

Catanzaro G., et al., 2015, MNRAS, 451, 184

Cherubini S., Kondratyev V. N., Lattuada M., Spitaleri C., Miljanic D., Zadro M., Baur G., 1996, ApJ, 457, 855

Gómez, Maqueo Chew, Y. G. M., Stassun, K. G., Prsa, A., Stempels, E., Hebb, L., Barnes, R., Heller, R., Mathieu, R. D. 2012, ApJ, 745, 58

Conti P. S., 1970, A&A, 7, 213

Cosentino R., et al., 2012, SPIE, 8446, 84461V

Covino, E., Catalano, S., Frasca, A., Marilli, E., Fernández, M., Alcalá, J. M., Melo, C., Paladino, R., Sterzik, M. F., Stelzer, B. 2000, A&A, 361, L49

Covino, E., Melo, C., Alcalá, J. M., Torres, G., Fernández, M., Frasca, A., Paladino, R. 2001, A&A, 375,130

Covino, E., Frasca, A., Alcalá, J. M., Paladino, R., Sterzik, M. F. 2004, A&A, 427, 637

Covino, S., et al., 2014, AN, 335, 117

Cox, J.P. & Giuli, R.T. 1968 *Principles of Stellar Astrophysics* (Gordon and Breach, N w York)

Cyburt R. H., Fields B. D., Olive K. A., 2004, PhRvD, 69, 123519

Czekala I., Andrews S. M., Jensen E. L. N., Stassun K. G., Torres G., Wilner D. J., 2015, ApJ, 806, 154

Deeming T. J., 1960, MNRAS, 121, 52

Degl'Innocenti S., Prada Moroni P. G., Marconi M., Ruoppo A., 2008, Ap&SS, 316, 25

de Zeeuw P. T., Hoogerwerf R., de Bruijne J. H. J., Brown A. G. A., Blaauw A., 1999, AJ, 117, 354

di Criscienzo M., Ventura P., D'Antona F., 2009, A&A, 496, 223

D'Orazi, V., Randich, S., Flaccomio, E., Palla, F., Sacco, G. G., Pallavicini, R. 2009, A&A, 501, 973

D'Orazi, V., Biazzo, K., Randich, S. 2011, A&A, 526, 103

Dotter A., Chaboyer B., Ferguson J. W., Lee H.-c., Worthey G., Jevremović D., Baron E., 2007, ApJ, 666, 403

Dunham M. M., Vorobyov E. I., 2012, ApJ, 747, 52

Dunstone, N. J., Hussain, G. A. J., Collier Cameron, A., Marsden, S. C., Jardine, M., Stempels, H. C., Ramirez Velez, J. C., Donati, J.-F. 2008, MNRAS, 387, 481

Durisen R. H., Gingold R. A., Tohline J. E., Boss A. P., 1986, ApJ, 305, 281

Ferguson J. W., Alexander D. R., Allard F., Barman T., Bodnarik J. G., Hauschildt P. H., Heffner-Wong A., Tamanai A., 2005, ApJ, 623, 585

Gennaro M., Prada Moroni P. G., Degl'Innocenti S., 2010, A&A, 518, A13

Gennaro M., Prada Moroni P. G., Tognelli E., 2012, MNRAS, 420, 986

Gillen, E., Aigrain, S., McQuillan, A., Bouvier, J., Hodgkin, S., Alencar, S. H. P., Terquem, C., Southworth, J., Gibson, N. P., Cody, A., Lendl, M., Morales-Calderón, M., Favata, F., Stauffer, J., Micela, G. 2014, A&A, 562, A50

Gray, D.F., 1992 *The observation and analysis of stellar photospheres* Cambridge Astrophysics Series

Guenther, E. W., Torres, G., Batalha, N., Joergens, V., Neuhäuser, R., Vijapurkar, J., & Mundt, R. 2001, A&A, 366, 965

Guenther, E., Aigrain, S., McQuillan, A., Bouvier, J., Hodgkin, S., Alencar, S. H. P., Terquem, C., Southworth, J., Gibson,

N. P., Cody, A., Lendl, M., Morales-Calderón, M., Favata, F., Stauffer, J., Micela, G. 2014, A&A, 562, A50

Hartigan P., Kenyon S. J., Hartmann L., Strom S. E., Edwards S., Welty A. D., Stauffer J., 1991, ApJ, 382, 617

Henyey L. G., Forbes J. E., Gould N. L., 1964, ApJ, 139, 306

Herbig G. H., Kameswara Rao N., 1972, ApJ, 174, 401

Hillenbrand L. A., Carpenter J. M., Feigelson E. D., 2001, ASPC, 243, 439

Hoyle F., 1953, ApJ, 118, 513

James D. J., Melo C., Santos N. C., Bouvier J., 2006, A&A, 446, 971

Jeffries R. D., 2000, ASPC, 198, 509

Iben I., Jr., 1965, ApJ, 142, 421

Iglesias C. A., Rogers F. J., 1996, ApJ, 464, 943

Jensen E. L. N., Mathieu R. D., 1997, AJ, 114, 301

Johns-Krull, C. M., Hatzes, A. P. 1997, ApJ, 487, 896

Jørgensen B. R., Lindegren L., 2005, A&A, 436, 127

Joy, A.H. 1949, ApJ 110, 424

Kastner J. H., Zuckerman B., Weintraub D. A., Forveille T., 1997, Sci, 277, 67

King, Jeremy R., Soderblom, David R., Fischer, Debra, Jones, Burton F. 2000, ApJ, 533, 944

Kurucz R. L., 1993, KurCD, 1,

Kurucz R. L., 2005, MSAIS, 8, 14

Kurucz R. L., Avrett E. H., 1981, SAOSR, 391,

Lamia, L., Spitaleri, C., La Cognata, M., Palmerini, S., Pizzone, R. G. 2012, A&A, 541, A158

Lamia, L., Spitaleri, C., Pizzone, R. G., Tognelli, E., Tumino, A., Degl'Innocenti, S., Prada Moroni, P. G., La Cognata, M., Pappalardo, L., Sergi, M. L. 2013, ApJ, 768, 65

Laskar, Tanmoy, Soderblom, David R., Valenti, Jeff A., Stauffer, John R. 2009, ApJ, 698, 660

Leone F., 2007, ApJ, 667, L17

Leone et al. , AJ, submitted

Lind, K., Asplund, M., Barklem, P. S. 2009, A&A, 503, 541

Linsky J. L., et al., 2006, ApJ, 647, 1106

Lucy L. B., Ricco E., 1979, AJ, 84, 401

Magazzu A., Martin E. L., Rebolo R., 1991, A&A, 249, 149

Malo, L., Doyon, R., Feiden, G. A., Loïc, A.,Lafreniére, D., Artigau, É., Gagné, J., Riedel, A. 2014, ApJ, 792, 37

Manara C. F., Robberto M., Da Rio N., Lodato G., Hillenbrand L. A., Stassun K. G., Soderblom D. R., 2012, ApJ, 755, 154

Martin E. L., 1997, A&A, 321, 492

Masunaga H., Miyama S. M., Inutsuka S.-i., 1998, ApJ, 495, 346

Masunaga H., Inutsuka S.-i., 2000, ApJ, 531, 350

Mathieu R. D., Baraffe I., Simon M., Stassun K. G., White R., 2007, prpl.conf, 411

Melo, C. H. F., Covino, E., Alcalá, J.M.,& Torres, G. 2001, A&A, 378, 989

Mentuch, E., Brandeker, A., van Kerkwijk, M. H., Jayawardhana, R., Hauschildt, P. H. 2008, ApJ, 689, 1127

Merrill P. W., 1952, ApJ, 116, 21

Mora A., et al., 2001, A&A, 378, 116

Muzerolle, J, Clvet, N., Hartmann, L. 2001, ApJ, 550, 944

Palla F., Stahler S. W., 1992, ApJ, 392, 667

Palla F., Stahler S. W., 1991, ApJ, 375, 288

Pavlenko, Ya. V., Magazzú, A. 1996, A&A, 311, 961

Pecaut M. J., Mamajek E. E., Bubar E. J., 2012, ApJ, 746, 154

Pereira C. B., Franco C. S., de Araújo F. X., 2003, A&A, 397, 927

Prantzos N., 2012, A&A, 542, A67

Prato L., et al., 2001, ApJ, 549, 590

Quast G. R., Torres C. A. O., de La Reza R., da Silva L., Mayor M., 2000, IAUS, 200, 28P

Rice, ,J. B., Strassmeier, K., G. 1996, A&A, 316, 164

Ripepi V., Balona L., Catanzaro G., Marconi M., Palla F., Giarrusso M., 2015, MNRAS, 454, 2606

Rogers F. J., Nayfonov A., 2002, ApJ, 576, 1064

Rosenfeld K. A., Andrews S. M., Wilner D. J., Stempels H. C., 2012, ApJ, 759, 119

Ruíz-Rodríguez, D., Prato, L., Torres, G., Wasserman, L. H., Neuhäuser, R. 2013, AJ, 145, 162

Rigliaco E., Natta A., Testi L., Randich S., Covino E., Alcalá J. M., 2011, AN, 332, 249

Sestito P., Palla F., Randich S., 2008, A&A, 487, 965

Sestito P., Randich S., 2005, A&A, 442, 615

Shu F. H., Adams F. C., Lizano S., 1987, ARA&A, 25, 23

Siess L., Dufour E., Forestini M., 2000, A&A, 358, 593

Soderblom, D. R., Henry, T. J., Shetrone, M. D., Jones, B. F., Saar, S. H. 1996, ApJ, 460, 984

Soderblom D. R., 2010, ARA&A, 48, 581

Somers G., Pinsonneault M. H., 2014, ApJ, 790, 72

Spitaleri C., 1997, nuig.conf, 32

Spitaleri C., et al., 1999, PhRvC, 60, 055802

Spitaleri C., Mukhamedzhanov A. M., Blokhintsev L. D., Cognata M. L., Pizzone R. G., Tumino A., 2011, PAN, 74, 1725

Stahler S. W., 1983, ApJ, 274, 822

Stahler S. W., Palla F., 2005, The Formation of Stars. Wiley-VCH

Stassun, K. G., Mathieu, R. D., Vaz, L. P. R., Stroud, N., Vrba, F. J. 2004, ApJS, 151, 357

Stassun, K. G., Mathieu, R. D., Cargile, P. A., Aarnio, A. N., Stempels, E., Geller, A. 2008, Nature, 453, 1079

Stempels, H. C., Piskunov, N., A&A, 408, 693

Stempels, H. C., Gahm, G. F. 2004, A&A, 421, 1159

Stempels, H. C., Hebb, L., Stassun, K. G., Holtzman, J., Dunstone, N., Glowienka, L., Frandsen, S. 2008, A&A, 481, 747

Stempels H. C., Hebb L., 2011, ASPC, 448, 747

Sterzik M. F., Melo C. H. F., Tokovinin A. A., van der Bliek N., 2005, A&A, 434, 671

Strom, S. E., Strom, K. M., Grasdalen, G. L. 1975, ARA&A, 13, 187

Tajitsu A., Sadakane K., Naito H., Arai A., Aoki W., 2015, Natur, 518, 381

Tognelli E., Prada Moroni P. G., Degl'Innocenti S., 2011, A&A, 533, A109

Tognelli E., Degl'Innocenti S., Prada Moroni P. G., 2012, A&A, 548, A41

Tohline J. E., 2002, ARA&A, 40, 349

Tomida K., Tomisaka K., Matsumoto T., Hori Y., Okuzumi S., Machida M. N., Saigo K., 2013, ApJ, 763, 6

Torres G., 2004, AJ, 127, 1187

Tribble R. E., Bertulani C. A., La Cognata M., Mukhamedzhanov A. M., Spitaleri C., 2014, RPPh, 77, 106901

Tumino A., et al., 2007, PhRvL, 98, 252502

Tumino A., et al., 2008, PhRvC, 78, 064001

Tumino, A., Spartá, R., Spitaleri, C., Mukhamedzhanov, A. M., Typel, S., Pizzone, R. G., Tognelli, E., Degl'Innocenti, S., Burjan, V., Kroha, V., Hons, Z., La Cognata, M., Lamia, L., Mrazek, J., Piskor, S., Prada Moroni, P. G., Rapisarda, G. G., Romano, S., Sergi, M. L. 2014, ApJ, 785, 96

van Leeuwen F., 2007, A&A, 474, 653

Vorobyov E. I., Basu S., 2006, ApJ, 650, 956

Walter, F. M. 1986, PASP, 98, 1100

Wen, Qun-Gang, Li, Cheng-Bo, Zhou, Shu-Hua, Meng, Qiu-Ying, Zhou, Jing, Li, Xiao-Mei, Hu, Shou-Yang, Fu, Yuan-Yong, Spitaleri, C., Tumino, A., Pizzone, R.G., Rapisarda, G.G. 2008, Phys. Review C., 78, 3

Wichmann, R., Covino, E., Alcalà, J.M., Krautter, J., Allain, S., & Hauschildt, P.H. 1999, MNRAS, 307, 909

Wuchterl G., Tscharnuter W. M., 2003, A&A, 398, 1081

Yee, J. C., Jensen, E. L. N. 2010, ApJ, 711, 303

Yi S., Demarque P., Kim Y.-C., Lee Y.-W., Ree C. H., Lejeune T., Barnes S., 2001, ApJS, 136, 417

Zuckerman B., Forveille T., Kastner J. H., 1995, Natur, 373, 494